
DESEMBER
2001

EVALUATION OF A COMMERCIAL RADIATION ONCOLOGY TREATMENT PLANNING SYSTEM AGAINST MONTE CARLO SIMULATED DOSE DISTRIBUTIONS

BY

WILLIAM SHAW

Thesis submitted to comply with the requirements for the M.Med.Sc. degree in the Faculty of Health Sciences at the University of the Free State

November 2007

Study Leader: Dr. FCP du Plessis

Abstract

A method is described in this study whereby dose distributions calculated by a treatment planning system (TPS) were evaluated by using dose distributions calculated with Monte Carlo (MC) simulations. The MC calculated dose data were used as a benchmark. A generic Siemens MD 2 linear accelerator was simulated with the BEAMnrc MC code to obtain beam specific dynamic variables in a phase space file (PSF) related to particle fluence in a plane at a known distance from a water phantom. Dose distributions from various field sizes were produced by simulations with the DOSXYZnrc MC code. Two datasets were produced consisting of percentage depth dose (PDD), profiles and diagonal profile data for 6 and 15MV x-ray beams. The CadPlan TPS was commissioned with these datasets for both energies. Analyses of TPS calculated dose distributions were done in a water phantom and dose distributions for various clinical cases on patient CT data.

Patient CT datasets were transformed into patient CT models that were suitable for dose calculations with DOSXYZnrc. These models consisted of various media with various densities for which interaction cross section data is available. Dose distributions for a number of clinical treatment plans could be devised on both the TPS and DOSXYZnrc. These included head and neck, breast, lung, prostate, oesophagus and brain plans. Calculations on the TPS were done for the Single Pencil Beam (SPB) and in some cases the Double Pencil Beam (DPB) convolution algorithms in combination with the Batho and ETAR (Equivalent Tissue-air ratio) inhomogeneity correction algorithms. Dose distributions were normalized to the depth of maximum dose (d_{max}) for single fields and

to the ICRU reference point in full treatment plans. The location of these points was the same for the TPS and DOSXYZnrc distributions.

PDD curves, beam profiles, dose-volume histograms (DVHs) and equivalent uniform doses (EUDs) were produced to aid in the evaluation of the TPS dose calculation accuracy. Results demonstrated that the assumptions in the convolution models used to produce beam penumbra regions, especially in blocked field cases, fail to account for scattered dose contributions outside the treatment field and overestimated the dose underneath small or thin shielding blocks. The PB algorithms in combination with the inhomogeneity corrections show total disregard for lateral and longitudinal electron transport through heterogeneous media. This effect is pronounced in regions where electronic equilibrium is not found, like low density lung. This region, in combination with high density bone nearby, proved even larger discrepancies as dose absorption decreases in low density media and increases in high density media. A small 15 MV field passing through lung tissue exhibited large dose calculation errors by the PB algorithms.

The dataset produced here is flexible enough to be used as a benchmark for any TPS utilizing commissioning measurements in water. This method can address commissioning results as well as any clinical situation requiring dose calculation verification.

Key words: Treatment planning system, pencil beam algorithm, Monte Carlo, BEAMnrc, DOSXYZnrc, dose distributions, inhomogeneity, water phantom, electronic equilibrium, fluence

Opsomming

In hierdie studie word ‘n metode bespreek waardeur dosis distribusies wat met ‘n behandelingsbeplanning sisteem (TPS) bereken is, ge-evalueer kan word met dosis distribusies wat deur middel van Monte Carlo (MC) simulasies bereken word. Die MC berekende dosis data was as verwysings data gebruik. Die BEAMnrc MC kode was gebruik om ‘n Siemens MD2 lineêre versneller te simuleer sodat bundel spesifieke dinamiese veranderlikes gestoor kon word in ‘n faseruimte-lêer. Hierdie faseruimte-lêer was geskep op ‘n bekende afstand vanaf ‘n water fantoom. Dosis distribusies was bereken vir verskeie veld groottes met die DOSXYZnrc MC kode. Twee datastelle was geskep wat bestaan uit persentasie diepte dosis (PDD), bundel profiele, en diagonale profiel data vir 6 en 15MV x-straal bundels. Die CadPlan TPS was in gebruik gestel met hierdie datastelle vir beide energië. Die analiese van die TPS berekende dosis distribusies was op water fantoom data uitgevoer en die distribusies van verkeie kliniese gevalle was met behulp van rekenaartomografie (RT)- gebasseerde data uitgevoer.

Die pasiënt RT beelddata was omgeskakel na pasiënt RT modelle wat geskik was om berekeninge met behulp van DOSXYZnrc uit te voer. Hierdie modelle het bestaan uit verskeie media met verskillende digthede waarvoor daar interaksie deursnit data beskikbaar is. Dosis verspreidings kon nou bereken word vir ‘n aantal kliniese behandelings gevalle met die TPS en DOSXYZnrc. Hierdie gevalle het bestaan uit ‘n kop en nek, bors, long, prostaat, esofagus en brein plan. Die berekeninge op die TPS was uitgevoer met behulp van die Enkel Dun Bundel (SPB) en Dubbel Dun Bundel (DPB)

konvolusie algoritmes gekombineer met die Batho en ETAR (Ekwivalente Weefsel-lug verhouding) heterogeniteitskorreksie algoritmes. Die dosis verspreidings was genormaliseer by die diepte waar die maksimum dosis verkry word (d_{max}) vir enkel velde en by die ICRU verwysingspunt in geval van die gesommeerde dosis distribusies.

PDD krommes, bundel profiele, dosis-volume histogramme (DVHe) en ekwivalente uniforme dosisse (EUDe) was geskep om die TPS se dosis berekening akkuraatheid mee te evalueer. Die resultate toon dat die aannames wat gemaak word in die konvolusie modelle om die bundel penumbra mee te skep, veral in die geval van afgeskermde (geblokte) velde, nie daarin slaag om vir verstrooide dosis bydraes buite die behandelings veld te korrigeer nie en oorskat ook die dosis onder klein en dun afskermings blokke. Dit bleik dat die PB algoritmes, gekombineer met die heterogeniteitskorreksies, geensins oorweging skenk aan die laterale en longitudinale elektron voortplanting binne heterogene media nie. Hierdie effek word veral beklemtoon in areas waar daar nie elektron ekwilibrium teenwoordig is nie, soos in die geval van lae digtheid long weefsel. Verskille was groter in sulke areas wat gekombineer is met nabygeleë hoë digtheid been aangesien dosis absorbsie afneem in lae digtheid media en toeneem in hoë digtheid media. ‘n Ondersoek na ‘n klein 15 MV veld wat deur long dring het getoon dat groot foute in dosis berkening deur die PB algoritmes gemaak word.

Die datastelle wat tydens hierdie studie geskep was, is universeel genoeg om as verwysings data vir enige TPS gebruik te word wat van gemete water fantoom data

gebruik maak tydens ingebruikneming. Hierdie metode kan resultate van sulke ingebruiknemings toetse aanspreek, asook die dosis verifikasie van enige kliniese gevalle.

Sleutelwoorde: Behandelingsbeplanning sisteem, dun bundel algoritme, Monte Carlo, BEAMnrc, DOSXYZnrc, dosis distribusie, heterogenieteit, water fantoom, elektron ekwilibrium, tydvloed

Table of contents

Glossary		**15**
Chapter 1	**Introduction**	**18**
1.1.	Biological principles for radiation treatment planning justification	18
1.1.1.	Dose response curves	19
1.1.2.	Particles used in radiation therapy	20
1.2.	The radiation therapy treatment chain	21
1.3.	The treatment planning system (TPS)	22
1.3.1.	Summary of the treatment planning process	24
1.3.1.1.	Beam Data Characterization	25
1.3.1.2.	Patient Data Characterization	29
1.3.1.2.1.	Electron densities	29
1.3.1.2.2.	Delineation of volumes of interest	30
1.4.	Accuracy requirements in external beam treatment planning	31
1.5.	Aim	32
	References	34
Chapter 2	**Treatment Planning Systems**	**42**
2.1.	Introduction	42
2.2.	Isodose curves	43

2.3.	Treatment planning accuracy	44
2.4.	Computation of absorbed dose	45
2.4.1.	Current dose calculation techniques	46
2.5.	The convolution process	49
2.5.1.	Pencil Beam convolution algorithms	53
2.5.2.	Superposition Algorithms: Collapsed Cone Algorithm	55
2.6.	The CadPlan TPS	56
2.6.1.	The Regular Beam Model (RBM)	56
2.6.2.	Double Pencil Beam Algorithm	65
2.6.2.1.	Calculation of the dose in a blocked region and outside the radiation field	68
2.6.2.2.	Calculation of the pencil kernels	69
2.6.2.3.	Calculation of the boundary kernels	71
2.6.3.	Single Pencil Beam Algorithm	73
2.6.3.1.	Calculation of the pencil beam kernel	75
2.7.	Inhomogeneity Corrections	79
2.7.1.	Effective attenuation correction method	81
2.7.2.	The ratio of tissue-air ratios	82
2.7.3.	Effective SSD method	83
2.7.4.	The Batho Power Law method	84
2.7.5.	The Equivalent Tissue-Air Ratio method	87
2.7.6.	Differential scatter-air ratio method	93
2.8.	Dose calculation verification	97

2.9. Treatment plan evaluation by means of the Equivalent Uniform Dose (EUD) 98

References 101

Chapter 3 Monte Carlo Simulations 116

3.1. Overview 116

3.2. Accuracy of MC simulations 117

3.3 PEGS4 and the user codes 121

3.4. Random numbers 110

3.5. Photon interactions 122

3.6. Electron interactions 125

3.7. The Monte Carlo simulation process 126

3.7.1. Photon transport 126

3.7.1.1. Pathlength selection through random sampling 126

3.7.1.2. Choosing an interaction type 129

3.7.2. Electron transport 130

3.7.2.1. Electron-step algorithms 131

3.7.2.2. Electron spin algorithm 134

3.8. EGSnrc MC user codes 134

3.8.1. BEAMnrc 134

3.8.2. DOSXYZnrc 135

3.9. Limitations of the MC code 136

3.10.	Efficiency and variance reduction	137
3.11.	Role of MC simulations in this study	141
	References	143
Chapter 4	**Methods**	**150**
4.1.	Introduction	150
4.2.	Construction of a Siemens MD2 based generic accelerator	153
4.2.1.	Modeling of the accelerator components	157
4.2.1.1.	The brehmstrahlung target	157
4.2.1.2.	The primary collimator and flattening filter	157
4.2.1.3	The ion chamber	158
4.2.1.4.	The mirror	158
4.2.1.5.	The collimating jaws	159
4.2.1.6.	The reticle	159
4.2.1.7.	The cerrobend blocks	160
4.2.1.8.	The block tray	160
4.2.1.9	Air gaps	160
4.2.1.10.	Variance reduction	161
4.2.2.	Cross section data for the flattening filter mixture of materials	163
4.3.	Calculation of absorbed dose in a water phantom using DOSXYZnrc	164
4.3.1.	Construction of the water phantom	165

4.3.2. Transport control parameters for the water phantom 166
4.3.3. Data analyses 167
4.4. Commissioning of the TPS input data 169
4.4.1. Water phantom dose calculations 169
4.5. Conversion of CT based patient models into a suitable DOSXYZnrc format 173
4.6. Preparing and executing DOSXYZnrc with compatible patient models for absorbed dose calculations 176
4.6.1. Patient study cases 176
4.6.2. CT data conversion from TPS to egsphant files 178
4.6.3. The DOSXYZnrc input file 179
4.6.4. DOSXYZnrc simulations 179
4.6.5. DOSXYZnrc transport control parameters 181
4.6.5.1. Open fields 181
4.6.5.2. Blocked fields 181
4.7. Absorbed dose calculations for clinical cases on the TPS 182
4.7.1. Absorbed dose calculations 182
4.8. Comparison of DOSXYZnrc and TPS calculated dose distributions 185
4.8.1. Normalization of the dose distributions calculated with DOSXYZnrc 185
4.8.2. Evaluation of treatment plans with dose volume histograms 186
4.8.3 Evaluation of treatment plans with the Equivalent Uniform Dose (EUD) 187

References 190

Chapter 5 Results and Discussion 192

5.1. Introduction 192

5.1.1. Analysis of the BEAMnrc generated PSFs for open and blocked beams 192

5.1.2. Input beam data for the CadPlan TPS generated with DOSXYZnrc 198

5.1.2.1. Open Fields 198

5.1.2.2. Blocked fields – CadPlan transmission and beam penumbra dose modeling 213

5.1.3. Evaluation of the TPS dose calculations accuracy in a homogeneous water equivalent phantom 218

5.1.4 Transformation of CT based patient models into a format suitable for DOZXYZnrc 234

5.1.5. Comparison between the dose distributions calculated by DOSXYZnrc and theTPS for the SPB and DPB dose calculation algorithms in combination with the BATHO and ETAR inhomogeneity correction algorithms 235

5.1.5.1. Open field percentage depth dose and profile data for various clinical cases 235

5.1.5.1.1. Head and Neck plans 236

5.1.5.1.2. Breast plans 252

5.1.5.1.3. Lung plans 262

5.1.5.1.4. Prostate plans 272

5.1.5.1.5. Oesophagus plans 275

5.1.5.1.6. Brain plans 280

References 284

Chapter 6 Conclusion 286

6.1. Similar studies on lung geometries 290

6.2. Similar studies on head and neck and missing tissue geomtries 296

6.3. Similar studies on breast and head and neck geometries 297

References 308

Acknowledgements 312

Glossary

1D	one dimensional
2D	two dimensional
3D	three dimensional
3DCRT	three dimensional conformal radiotherapy
BCA	boundary crossing algorithm
CAX	central axis
CCC	collapsed cone convolution
CF	correction factor
CM	component module
CPE	charged particle equilibrium
CSDA	continuous slowing down approximation
CT	computed tomography
CTV	clinical target volume
D	dose
D_{max}/d_{max}	maximum buildup dose
DPM	double pencil beam
dSAR	differential scatter-air-ratio
DVH	dose volume histogram
ECUT	electron cut-off energy
EGS	electron gamma shower
ETAR	equivalent tissue-air-ratio

EUD	equivalent uniform dose
eV	electron volt
FS	field size
Gy	gray
GTV	gross tumor volume
ICRU	international commission on radiological units
ISQR	inverse square correction
IMRT	intensity modulated radiotherapy
keV	kilo electron volt
MC	monte carlo
MLC	multileaf collimator
MR(I)	magnetic resonance (imaging)
MSKCC	Memorial Sloan Kettering Cancer Centre
MU	monitor unit
MeV	mega electron volt
MV	mega volt
NTCP	normal tissue complication probability
OAR	organ at risk
PB	pencil beam
PCUT	photon cut-off energy
PDD	percentage depth dose
PET	positron emission tomography
PSF	phase space file

PTV	planning target volume
PWLF	piecewise linear fit
QA	quality assurance
RBM	regular beam model
SAR	scatter-air-ratio
SBS	selective bremsstrahlung splitting
SD	standard deviation
SOP	standard operating procedure
SPB	single pencil beam
SSD	source-surface distance
SST	stainless steel
SPECT	single photon emission computed tomography
TAR	tissue-air-ratio
TCP	tumor control probability
Terma	total energy released per unit mass
TLD	thermo luminescent dosimeter
TMR	tissue-maximum-ratio
TPR	tissue-phantom-ratio
TPS	treatment planning system
TUC	treatment unit characterization
UBS	uniform brehmsstrahlung splitting
VOI	volume of interest

Chapter 1

Introduction

1.1 Biological principles for radiation treatment planning justification

Radiotherapy is based on the principle of using ionizing radiation to cause irreparable damage to the DNA of tumor cells and inhibition of their duplication. Normal tissue cells suffer the same type of damage, but have better capacity to repair and control mechanisms. As a consequence of this damage, doses to tumors have to be maximized through strategic treatment planning methods, while at the same time limiting the dose to normal healthy tissue to as low as possible.

Some methods of achieving tumor control and limiting normal tissue damage is by fractionating the treatment to obtain the total tumor dose. In utilizing fractionated treatment, healthy tissues or organs at risk (OARs) can be spared due to better repair mechanisms while eradication of the tumor is not necessarily significantly influenced. Some tumors or cancerous lesions are not treated with fractionated radiotherapy when they exhibit late responses to radiation[1].

Radiosensitizers can also be used in conjunction with radiotherapy to enhance the radiosensitivity of cells, leading to quicker breakdown of the living tissue due to radiation damage. Another method is optimizing the radiation dose distribution through treatment

planning and ensuring that the dose is conformed to the tumor, with minimal dose to OARs. Individualized tailoring of high doses to the tumor volume and lower doses to OARs is thus a necessity for curative radiotherapy treatment. Normal tissue is expected to always receive a reasonable dose which should be kept within well defined limits.

During the past century there have been numerous developments in the treatment of cancer and specifically in the field of radiation therapy [1-13]. These developments include the determination of absorbed dose to an absorbing tissue or medium, higher levels of accuracy achieved in absorbed dose calculations for treatment planning, as well as fractionation regimes and the use of tissue response models in optimizing planned dose distributions for treatment. Radiotherapy is not the only common modality used for the treatment of cancer but can be combined with surgery, hormonal treatment or chemotherapy.

1.1.1. Dose response curves

The response of tissue to radiation treatment can be described by dose-response curves. These curves show that when the radiation dose is increased, there will be a tendency for tumor and normal tissue response to increase. The response of a tumor and the associated control of tumor tissue both show a sigmoidal relationship with dose. Normal tissue damage can also be quantified with a sigmoidal curve to indicate an increase in toxicity

with increased radiation dose. Normal tissues have upper limits of radiation dose that can be tolerated[14].

The radiobiological concept of the therapeutic index plays an important role and describes the tumor response for a fixed level of normal-tissue damage[1]. Radiation response happens on a molecular level when ionizing radiation causes irreparable damage to DNA of tumor cells, thus inhibiting their duplication. Secondary charged particles and free radicals, created when ionizing radiation interacts in the tissue, are produced in the cell nucleus and inflict a variety of damage to DNA. Radiation lethality correlates most significantly with unrepaired double-strand breaks in cell DNA.

1.1.2. Particles used in radiation therapy

In radiotherapy, patients with benign and malignant tumors can be treated with medium energy x-ray-, high energy x-ray-, neutron-, proton- or electron beams. The use of x-rays for the treatment of the hairy nevus with medium energy x-rays dates back to 1896 in Vienna. Treatment units have developed to what we know as Linear Accelerators (Linacs) today and these units are used to produce high energy, well collimated x-ray or electron beams. With modern advanced collimating systems incorporated in a linac, these radiation beams can be shaped or conformed to a volume of interest inside the patient. This volume is usually defined by radiation oncologists and is known as the planning target volume (PTV)[15].

Some guidelines have been set to aid in the treatment planning of radiotherapy patients and specifically refer to prescribing and reporting of radiotherapy treatments to have meaningful comparisons of treatment outcomes[15]. Ellis[16] indicated that relatively small differences in treatment schedules can result in easily detectable differences in the effects on the patient and that precision in dosage and treatment planning is essential to the outcome of the treatment.

Inaccuracies in dose delivery can also have serious consequences which might have potentially lethal effects[1,17]. Developments based on radiobiology have shown that inaccurate dose determination may have a significant impact on the prediction of tissue survival, or normal tissue complication probability (NTCP) and tumor control probability (TCP).

Radiation dose, defined as the energy deposited in a known mass (Joules per kilogram) and measured in the SI unit Gray (Gy), is influenced by the energy or quality spectrum of the beam, as well as the medium in which the dose is determined.

1.2 The radiation therapy treatment chain

Once a patient has been diagnosed with cancer, extensive clinical tests are done to determine the type and staging of the tumor, its size etc. A radiation oncologist then decides on the type of radiation treatment and the treatment regime for the case where

radical x-ray radiotherapy treatment is to be given. The treatment onset starts with the acquisition of 3D anatomical and functional images of the tumor and normal tissues through a combination of Computed Tomography (CT) imaging, Magnetic Resonance (MR) imaging and other imaging modalities such as Single Photon Emission Computed Tomography (SPECT) or Positron Emission Computed Tomography (PET). Ultra Sound imaging is often also used for brachytherapy treatment planning. Anatomical structures can be defined on a computer treatment planning system (TPS) to aid in conforming treatment beams to the PTV, while keeping the dose contribution to the OARs as low as possible. Radiation treatment can only start once the radiation beam and patient configuration has been determined. Sophisticated mathematical algorithms and computers are used for this purpose.

1.3. The treatment planning system (TPS)

During the treatment planning phase the treatment setup and dose distributions inside a patient can be visualized. 3D planning tools can be used to graphically design radiation beams that are directed and shaped to the geometrical projection of the target in the plane of interest. The software of the TPS allows the user to create dose distributions to conform to the PTV. Fast dose calculation algorithms allow the display of the dose distribution to evaluate the conformity of a beam, or the added effect of other beams. Once a suitable dose distribution has been reached, various other parameters relevant to the treatment can be calculated, such as monitor units and patient setup parameters.

During the actual radiation treatment phase, the beam parameters calculated by the treatment planning system (TPS) can be used for the patient and the linac setup. Any deviation in these planned beam parameters would lead to a difference in the dose delivered to the patient. This would have a direct impact on the treatment outcome and treatment effectivity and such deviations should be minimized under all circumstances.

Taking all the above mentioned factors into account, one can easily understand that it is critically important to know the accuracy of treatment, and thus the accuracy of the dose delivered to all tissues in the beams, whether they be normal or malignant. Only then could any estimation of treatment outcome or effectivity of treatment be made.

The TPS represents the way in which the patient will be treated and estimations of treatment outcome are usually based on the resulting dose distribution. This emphasizes the importance of dose calculation accuracy because if the radiation dose is not calculated correctly the use of guidelines such as the ICRU report 50[15] would be meaningless. Inhomogeneities present in the CT based patient data are usually taken into account during dose calculation. The TPS used in this study is the CadPlan TPS, External Treatment Planning version 6.3.6 (Varian Medical Systems, Inc., Palo Alto, CA 94304).

Parameters used for the evaluation of the merit for delivering a treatment plan and estimating possible outcomes of local tumor control and normal tissue complication, like Dose Volume Histograms (DVHs), rely heavily on the accuracy of dose calculation algorithms.

Treatment planning systems show a trade-off between dose calculation accuracy and computational speed. The more accurate dose calculation algorithms usually take longer to calculate the dose in a patient model compared to simpler, less accurate algorithms. For example, the Collapsed Cone Superposition algorithm takes longer to calculate dose distributions in such models compared to the simpler Pencil Beam Convolution model.

1.3.1 Summary of the treatment planning process

Treatment planning starts of with the acquisition of relevant patient (anatomical) data, definition of target volumes and prescription of target absorbed doses (ICRU report 50[15]). From this required treatment volume, the iterative process of defining beam arrangements starts as well as subsequent dose distribution calculations. If the speed at which calculations are done permits, different beam arrangements and energies can be compared with dose distributions of other arrangements to find the optimal treatment plan. Once the optimal plan and associated dose distribution has been identified, the plan protocol can be produced. It contains all the relevant parameters for daily use in setup procedures on the linac (including monitor units for each beam). A plot of the relevant information regarding the dose distribution on one or two CT can also be supplied.

1.3.1.1. Beam Data Characterization

The TPS algorithms require measured input beam data to set up its beam model for the linac of interest. In a modern TPS a set of physical radiation parameters will be calculated

from the input linac beam dataset, e.g. primary fluence profiles, kernels and phantom- and collimator scatter factors.

Beam data characterization usually consists of the use of normalized 2D dose distributions that have been measured in water equivalent phantoms[18-20], to calculate the beam characteristic radiation parameters. The measurements are usually done with an electronically positioned ionization chamber in a large watertank. The most important measurements are percentage depth dose (PDD) and off-axis or profile data of a number of square fields. Other related dosimetric quantities are derived, like Tissue-Air-Ratios (TARs), Tissue-Phantom-Ratios (TPRs) and Scatter-Air-Ratios (SARs). Some of these quantities can also be measured.

In this study, however, the characterization data was not measured with conventional dosimetry equipment, but was generated with the Monte Carlo (MC) codes BEAMnrc[21] and DOSXYZnrc[22] and will be discussed in detail later on. Once the radiation beams used in the TPS have been modeled from this characterization process, the data needs to be validated before clinical use. The characterization process can only be completed once the model has been tested and found to be within acceptable limits of accuracy.

The advantage of using MC codes to simulate the radiation transport process of the high energy x-rays produced in the linac head, and the subsequent scoring of the dose in a simulated waterbath model, is that any measurement discrepancies are eradicated[23,24]. Any discrepancies in measured beam data will be incorporated into the planning system

unless there is a safety net of data verification checks that could clearly identify discrepancies and inaccuracies. In this regard it is also evident that simulated MC data can contribute significantly to consistent beam/linac data as there are no electronic, mechanical or output dependencies on the measured data.

Once validated, the TPS should be able to perform calculations of dose distributions in a homogeneous water phantom to replicate the conditions under which the measurements (or simulations) were done[25-28]. The calculations can then be compared to the original measurements to evaluate the accuracy of the calculations. It is also done to make sure the entered beam data was read in correctly and that the TPS calculations correspond to measurements within allowable tolerances[27,29-32]. The AAPM[28] and IAEA[33] have proposed very comprehensive guidelines that can be used at the discretion of the user for TPS commissioning and quality assurance (QA) programs. Other authors have also shown what goals should be achieved when these QA tests are carried out[27,29,31,34].

Commissioning of the TPS involves commissioning of the software for each treatment machine, energy, and modality. Calculated dose distributions for a selected set of treatment conditions in standard phantoms are usually compared to measured dose distributions for the same phantoms. Comparisons of the calculated and measured dose distributions can be carried out for conditions which are meant to simulate those used in clinical situations. The dose in the phantom should be independently calculated at selected points, using alternative algorithms. The accuracy of dose distribution

calculations depends on machine input data, the dose calculation algorithms and patient data.

Venselaar et al.[27] have proposed to express dose differences as a percentage of the dose measured locally. Normalization to local dose values was preferred instead of to the dose at d_{max} as the local dose eventually determines the success of a radiation treatment of a tumor and is therefore clinically more relevant. The criteria applied for acceptability of dose calculations are related to uncertainties which are present in dose measurements as well as errors which follow from the dose calculation model. Evaluations of dose profiles and percentage depth dose curves typically include regions in the beam with small dose gradients and other regions with large dose gradients. Criteria for the small dose gradient regions are expressed as percentages, while regions with large dose gradients are expressed in shifts of the relevant isodose line in units of millimeter. A tolerance of 2% in the dose value or 2 mm in the position of an isodose line, whichever is smaller, is usually recommended for overall accuracy in dose calculations. Special attention is paid to increasing complexity of the geometry, typically in the presence of inhomogeneities.

Comparison of dose distributions are not limited to the evaluation of differences between calculated and measured dose values. Acceptance tests should confirm that the TPS performs according to its design specification. The specification of the algorithm accuracy, planning capabilities and functional utilities of the system must be verified using appropriate tests.

Examples of quality assurance tests include setting up reference sets of treatment planning cases to be used for yearly recommissioning of the TPS. A subset of this reference set can be used for monthly QA in which the reproducibility of the calculations can be compared. Checksums must be done to verify consistency in beam data parameters or other indicators that verify that the data and application files have not changed. Monitor unit calculation verifications should be done on all treatment plans to ensure that not only were the TPS dose calculations were carried out correctly, but also that it conformed to the clinician's prescription. In addition to absolute dose measurements, the computer-calculated monitor units for all energies and modalities should be compared with an independent calculation.

3D TPS tests should confirm the spatial accuracy of beam's eye-view projections, digitally reconstructed radiographs and other spatial displays. Data transfer from diagnostic units including simulators, CT, MRI, and ultrasound should be evaluated at regular intervals to verify the consistency. Data transfer errors can occur because of digitizer nonlinearities and malfunctions. Digitizers should also be checked regularly.

Although good agreement between measured dose distributions and the ones produced by the TPS in a water phantom is achievable, accurate dose computations in the presence of tissue inhomogenieties is challenging and many algorithms exhibit limitations[35-38].

The TPS sometimes use dose calculation algorithms in combination with inhomogeneity correction models. Correction based algorithms include the equivalent path length method, the Batho – and modified Batho Power law methods and the ETAR

method[20,36,39,40]. The ETAR and Batho Power Law methods will be discussed in more detail in the theory part of this thesis as they are used in the CadPlan TPS.

1.3.1.2 Patient Data Characterization

1.3.1.2.1. Electron densities

Patient specific data need to be acquired to serve as input for the TPS. The data must reflect geometrically correct patient anatomy. CT based transverse, sagittal and coronal images can be used for the planning process.

The CadPlan TPS uses electron densities relative to water (ρ_e^w) to calculate changes in dose distributions for different types of media since it is used during inhomogeneity correction calculations[20,36,40]. Whenever kernels in convolution/superposition algorithms are scaled for inhomogeneities, the relative electron densities are also used[36,41-43].

When pixel sizes in one plane (cross sectional slice) as large as 4 mm^2 are used in the reconstructed CT image for dose calculations, the uncertainty in determining an individual particle path length would result in approximately 2% uncertainty in dose and would be less if the dose calculation involved the determination of many particle path lengths[45]. Image resolution required for dose calculation is much less stringent than for

object localization, but one should bear in mind that this is true where few and small heterogeneities are involved and where the body outline does not change rapidly.

1.3.1.2.2. Delineation of volumes of interest

The TPS uses CT slices and delineation tools for definition of the target and sensitive structures to produce volumes of interest (VOIs). All delineated structures are three dimensional and examining the dose distributions on a treatment planning system by making use of CT data must be carried out on several images so that the whole of the irradiated volume is considered.

These structures allow optimization of a treatment plan to obtain effective tumor control and few treatment complications. Sontag et al[44] have said: “The most severe errors in computing the dose distribution are caused by inaccurate delineation of the geometric outlines of tissue inhomogeneities. Less severe errors in the dose calculation are caused by using an inaccurate relative electron density for the imhomogeneity, provided the outline is accurate”. This stresses the fact that VOIs must be drawn in accurately while making provision for setup errors and organ movement.

Once the volumes of interest have been identified and specified, the treatment plan can be created by an iterative process (in 3D conformal radiotherapy [3DCRT]). This process involves the identification of angles at which the radiation should be incident on the

patient, the field sizes to be used, the energy (quality) of the x-ray beam and the number of treatment beams that will give a suitable dose distribution so as to effectively treat the tumor volume. Immobilization devices should be included in the body outline if they influence the dose distribution.

The distance between a true contour of an organ and its representation should not give rise to errors in dosage in excess of one percent of peak absorbed dose per beam[27]. For high energy photon beams, this requires a geometric accuracy of better than 3 mm. 3D structures are usually acquired and displayed as a series of parallel body sections. Volumetric images can be derived if sufficient closely spaced sections are obtained and this allows 3D treatment planning techniques with no limitation on beam geometry.

1.4. Accuracy requirements in external beam treatment planning

The AAPM TG40[37] protocol recommends that a TPS should undergo rigorous acceptance tests and commissioning as well as the implementation of a QA program. Some of the general recommendations for acceptance testing are found in ICRU 42[45]. Van Dyk et al[46] have also given detailed procedures for commissioning and QA protocols for TPSs. Other publications specific to QA and commissioning of TPSs include AAPM Report 40[26], Venselaar et al[27] and Fraass et al[28].

ICRU 24[47] recommended a minimum accuracy of ±5% in absorbed dose to the target volume. This level was further refined by ICRU 42[45] by stating a limit of 2% or 2 mm difference in high dose gradient regions in dose distributions when these dose distributions are calculated by a TPS.

Ahnesjö and Aspradakis[41] found that the beam delivery accuracy for currently employed and most often used techniques was 4.1% at best. These inaccuracies include the uncertainty in absorbed dose at the calibration point, as well as other points. It also includes treatment unit parameters and patient related uncertainties. However, this figure excludes any uncertainties in the TPS. Brahme[48] concluded that a realistic demand or accuracy level for photon beams in the range of 3% (or 3 mm in position) could be achieved which would result in an overall uncertainty of 5.1% (1 SD).

1.5. Aim

The aim of this study was to:

1.) Produce full input beam datasets with the Monte Carlo codes BEAMnrc and DOSXYZnrc for 6 and 15 MV x-ray beams of a generic accelerator based on the design of a Siemens MD2 accelerator for commissioning of the CadPlan.

2.) Generate 3D dose distributions for typical treatment plans with both energies for the following clinical cases: Head and Neck, Oesophagus, Breast, Lung, Brain and Prostate.

The dose distributions were mostly done for open fields, but blocked fields were also included in the study.

3.) Evaluate the CadPlan dose calcualtion algorithms by comparing the dose distributions calculated by CadPlan with the dose distributions produced with DOSXYZnrc. Comparisons of dose volume histograms and equivalent uniform dose was also used to aid in the evaluation of the CadPlan TPS.

References

1. Steele G.G., “Basic Clinical Radiobiology”, Third edition, Arnold, London (2002).

2. Greene D. and Williams P.C., “Linear Accelerators for radiation therapy”, Institute of Physics Publishing, Bristol and Philadelphia, Second Edition (1997).

3. Karzmark C.J. “Advances in linear accelerator design for radiotherapy”, Med. Phys. **11**, 105-128 (1984).

4. Karzmark C.J. and Pering N.C., “Electron linear accelerators for radiation therapy: history principles and contemporary developments”, Phys. Med. Biol. **18**, 321-354 (1973).

5. Alber M. and Belka C., “A normal tissue dose response model of dynamic repair processes”, Phys. Med. Biol. **51**, 153–172 (2006).

6. Alber M. and Nüsslin F., “A representation of an NTCP function for local complication mechanisms”, Phys. Med. Biol. **46**, 439–447 (2001).

7. Warkentin B., Stavrev P., Stavreva N., Field C. and Fallone B.G., “A TCP-NTCP estimation module using DVHs and known radiobiological models and parameter sets”, J. Appl. Clin. Med. Phys., **1**, 50-63 (2004).

8. Engelsman M., Damen E.M.F., Koken P.W., van `t Veld A.A., van Ingen K.M., and Mijnheer B.J., “Impact of simple tissue inhomogeneity correction algorithms on conformal radiotherapy of lung tumors”, Rad. Onc. **60**, 299-309 (2001).

9. Milker-Zabel S., Zabel A., Thilmann C., Schlegel W., Wannenmacher M., Debus J., “Clinical results of retreatment of vertebral bone metastases by stereotatic conformal radiotherapy and intensity-modulated radiotherapy ”, Int. J. Radiat. Oncol. Biol. Phys., **55**, 162–167 (2003).

10. Fippel M., “Fast Monte Carlo dose calculation for photon beams based on the VMC electron algorithm”, Med. Phys. **26**, 1466 – 75 (1999).

11. IAEA International Atomic Energy Agency, “Absorbed dose determination in external beam radiotherapy: An international code of practice for dosimetry based on standards of absorbed dose to water”, Technical Report Series no. **398**, IAEA, Vienna (2001).

12. AAPM American Association of Physicists in Medicine, “Clinical reference dosimetry of high energy photon and electron beams”, Report no. **51,** Medical Physics Publishing, Madison, USA (1999).

13. Intensity Modulated Radiation Therapy Collaborative Working Group (ICWG), “INTENSITY-MODULATED RADIOTHERAPY: CURRENT STATUS AND ISSUES OF INTEREST”, Int. J. Radiat. Oncol. Biol. Phys., **51**, 880–914 (2001).

14. Emami B., Lyman J., Brown A., Coia L., Goitein M., Munzenrider J.E., Shank B., Solin L.J. and Wesson M., “ Tolerance of normal tissue to therapeutic irradiation”, Int. J. Radiat. Oncol. Biol. Phys. **21**, 109 – 122 (1991).

15. International Commission on Radiological Units and Measurements. “Prescribing, Recording and Reporting Photon Beam Therapy,” ICRU Report **50**. Bethesda, MD: ICRU (1993).

16. Ellis F., “Time, Fractionation and Dose Rate in Radiotherapy”, Front. Radiation Ther. Onc. **3**, 131-140 (1969).

17. Hall E.J., “Radiobiology for the radiologist”, Fifth Edition, Lippincott Williams and Wilkins, Philadelphia, (2000).

18. Storchi P. and Woudstra E., “Calculation models for determining the absorbed dose in water phantoms in off-axis planes of rectangular fields of open and wedged photon beams”, Phys. Med. Biol. **40**, 511-527 (1995).

19. Storchi P. and Woudstra E., “Calculation of the absorbed dose distribution due to irregularly shaped photon beams using pencil beam kernels derived from basic beam data” , Phys. Med. Biol. **41**, 637-656 (1996).

20. CadPlan 6.0 (Varian Medical Systems, Inc., Palo Alto, CA 94304), External Beam Modelling Physics Manual (1999).

21. Rogers D.W.O., Ma C., Walters B., Ding G.X., Sheikh-Bagheri D. and Zhang G., “BEAMnrc Users Manual”, NRCC Report **PIRS-0509**, NRC Canada, (2001).

22. Walters B. R. B. and Rogers D.W.O., “DOSXYZnrc Users Manual”, NRCC Report **PIRS-794**, NRC Canada (2002).

23. Wieslander E. and Knöös T., “A virtual linear accelerator for verification of treatment planning systems”, Phys. Med. Biol. **45**, 2887–2896 (2000).

24. Paena J., Franco L., Gomez F., Iglesias A., Lobato R., Mosquera J., Pazos A., Pardo J., Pombar M., Rodriguez A. and Sedon J., “Commissioning of a medical accelerator photon beam Monte Carlo Simulation using wide-field profiles”, Phys. Med. Biol **49**, 4929 – 4942 (2004).

25. CadPlan 6.0 (Varian Medical Systems, Inc., Palo Alto, CA 94304), External Beam Utility Programs Manual (1999).

26. AAPM American Association of Physicists in Medicine “COMPREHENSIVE QA FOR RADIATION ONCOLOGY”, Report No. **40**, College Park, USA (1994).

27. Venselaar J., Welleweerd H. and Mijnheer B., “Tolerances for the accuracy of photon beam dose calculations of treatment planning systems”, Rad. Onc. **60**, 191-201 (2001).

28. Fraass B., Doppke K., Hunt M., Kutcher G., Starkschall G., Stern R. and Van Dyke J., “Quality assurance for clinical radiotherapy treatment planning”, AAPM American Association of Physicists in Medicine, Radiation Therapy Committee Task Group 53, Med. Phys. 25, 1773-1829 (1998).

29. International Commission on Radiation Units and Measurements (ICRU) “Use of computers in external beam radiotherapy procedures with high-energy photons and electrons”, ICRU Report 42, Baltimore, MD: ICRU (1987)

30. American Association of Physicists in Medicine. Report of Task Group 23 of the Radiation Therapy Committee, “Radiation treatment planning dosimetry verification” AAPM Report No. **55**, Woodbury, NY: American Institute of Physics (1995).

31. Mijnheer B.J., “Dose Calculations in Megavoltage Photon Beams: The Role of NCS”, Klinische Fysica, **3**, 10-14 (2002).

32. Venselaar J. and Welleweerd H., “Application of a test package in an intercomparison of the photon dose calculation performance of treatment planning systems used in a clinical setting”, Rad Onc **60**, 203-213(2001).

33. IAEA International Atomic Energy Agency, “Commissioning and Quality Assurance of Computerized Planning Systems for Radiation Treatment of Cancer”, Technical Report Series no. 430, IAEA, Vienna (2004).

34. Mayles W.P.M., Lake R., McKenzie A., Macaulay E.M, Morgan H.M., Jordan T.J. and Powley S.K., “Physics Aspects of Quality Control in Radiotherapy”, Institute of Physics and Engineering in Medicine (IPEM), Fairmount House, 230 Tadcaster Road York (1999).

35. Arnfield M.R., Siantar C.H., Siebers J., Garmon P., Cox L. and Mohan R., “The impact of electron transport on the accuracy of computed dose”, Med Phys **27**, 1266-1274 (2000).

36. Metcalf P., Kron T. and Hoban P., “ The Physics of Radiotherapy X-Rays,” Medical Physics Publishing, Madison, Wisconsin, (1997).

37. Butts J.R. and Foster A.E., “Comparison of commercially available three-dimensional treatment planning algorithms for monitor unit calculations in the presence of heterogeneities”, J. Appl. Clin. Med. Phys. **2**, 32-41 (2001).

38. Hurkmans C., Knoos T., Nilsson P., Svahn-Tapper G. and Danielsson H., “Limitations of a Pencil Beam approach to photon dose calculations in the head and neck region”, Rad. Onc **37**, 74 – 80 (1995).

39. Du Plessis F.C.P., Willemse C.A., Lötter M.G. and Goedhals L., “The indirect use of CT numbers to establish material properties needed for Monte Carlo calculation of dose distributions in patients”, Med. Phys. **25**, 1195 – 1201 (1998).

40. Sontag M.R. and Cunningham J.R., “Corrections for absorbed dose calculations for tissue inhomogeneities”, Med. Phys. **4**, 431-436 (1977).

41. Ahnesjö A. and Aspradakis M.M., “Dose calculations for external photon beams in radiotherapy”, Phys. Med. Biol. **44,** R99–R155 (1999).

42. Ahnesjö A. and Andreo P., “Determination of effective brehmsstrahlung spectra and electron contamination for photon dose calculations”, Phys. Med. Biol. **34**, 1451-1464 (1989).

43. Ahnesjö A., “Collapsed cone convolution of radiant energy for photon dose calculation in heterogeneous media”, Med. Phys. **16**, 577 – 92 (1989).

44. Sontag M.R., Battista J.J., Bronskill M.J. and Cunningham J.R., “Implications of computed tomography for inhomogeneity corrections in photon beam dose calculations”, Radiology **124**, 143 – 149 (1977).

45. ICRU Report 42, “Use of Computers in External Beam Radiotherapy Procedures with High Energy Photons and Electrons”, Bethesda, Maryland USA (1987).

46. Van Dyk J., Barnett R.B., Cygler J.E. and Shragge P.C., “Commissioning and quality assurance of treatment planning computers”, Int. J. Radiat. Oncol. Biol. Phys. **26,** 261–73 (1993).

47. International Commission on Radiation Units and Measurements. “Determination of absorbed dose in a patient by beams of X or Gamma rays in radiotherapy procedures,” ICRU Report **24**, Bethesda, MD: ICRU (1976)

48. Brahme A., Ed., “Accuracy requirements and quality assurance of external beam therapy with photons and electrons”, Stockholm, Acta Oncologica, ISBN 1100-1704 (1988).

Chapter 2

Treatment planning systems

2.1 Introduction

The role of the treatment planning system (TPS) is to utilize the input accelerator beam data during the commissioning process in order to derive parameters that can be used to calculate dose distributions with acceptable accuracy. In 3D conformal radiotherapy (3DCRT) treatment planning, an iterative process of finding suitable beam angles and apertures is used to find an optimal dose distribution that would lead to acceptable tumor control and manageable normal tissue complication.

Therapeutic gain can only be achieved through accurate knowledge of the respective doses to the tumor and healthy tissues. Integral doses to healthy organs pose limitations on deliverable doses when a treatment plan is devised. Indications for tolerance doses for different organs are available in the literature[1]. Tumor dose uniformity is another aspect which should be considered during radiation treatment planning. It is not always possible to achieve a homogeneous dose throughout a well defined tumor volume. This may have a significant impact on the outcome of the treatment, especially if clonogen densities vary inside this volume[2-5]. If all factors mentioned here are addressed in the treatment plan, the outcome of treatment will rely on the response of the different tissues and organs presented by CT data to the planned dose distribution.

Factors influencing the TPS dose calculation accuracy are the calculation algorithms, patient setup accuracy and repeatability, as well as variations in target and organ at risk (OAR) volumes due to organ movement and beam data inaccuracies associated with the mechanical tolerance of the linac[4,8]. Considering all three of these aspects, the accuracy in dose distribution calculation should be within at least 3% [6-11].There are generally accepted recommendations made by the ICRU[2] that the dose in the PTV should not deviate by more than -5 to +7% of that which is prescribed for treatment planning. Mijnheer et al[9] proposed a standard deviation of the uncertainty in the delivered dose that should not be greater than 3.5%. This considers the fact that only a part of the overall uncertainty arises from the process of dose calculations in treatment planning.

2.2 Isodose curves

The dose distribution can be visualized on the TPS using isodose curves superimposed on the patient data and can be displayed on transverse, sagital and coronal slices of the CT based patient model. The isodose lines can be assigned the actual dose values or the percentage dose values. When different treatment plans are compared, the two different isodose distributions can be displayed on the same CT data set. The target volume can also be displayed along with any other annotations or delineations such as OARs. Isodose curves aid in finding suitable gantry, collimator and couch angles, as well as field sizes and beam modulation and shaping.

2.3 Treatment planning accuracy

Errors on the TPS may also be caused in defining the positioning of the measurement detector in the waterbath, over or under response in the measurement signal, variations in linac output during measurements, or dose calculation errors[12-15]. These may result in the patient receiving a dose that differs from what was planned. Other errors may result from the incorrect use of the TPS, or from transferring incorrect parameters to the treatment sheet or protocol. The verification of the correct calculation of monitor units (MU) by the TPS is also a very important aspect of quality control in radiotherapy. All radiotherapy departments should have some standard operating procedures (SOP's) to reduce dose delivering inaccuracies to an absolute minimum[16,17].

The accuracy of dose calculation algorithms can be verified by comparing isodose distributions and monitor unit calculations with measurements and independent calculations[18-20]. Good comparisons are usually found in homogeneous areas like prostate and cervix plans and the dose distributions can usually be calculated with great levels of accuracy[18] in these treatment regions. Differences between the verification calculations and film, TLD and ionchamber measurements compared to the TPS results may be found where large heterogeneities are involved. These can be low densities, high densities or missing geometries. Dose discrepancies may also be the result of sharp changes in the exterior patient contours.

2.4 Computation of absorbed dose

Dose computations should consider the fact that patients are irregularly shaped, heterogeneous in composition, and irradiated in various positions. For a good correlation between the planned treatment with external radiation beams and internal patient dose distributions, a coordinate system is set up for the radiation beam and the patient to establish a relationship between the two.

A number of factors have modifying influences on the commissioning dose data and these changes should be reflected during treatment planning dose calculations. They include the source surface distance (SSD) that affects the percentage depth dose (PDD), divergence of the beam and the penumbra.

In some dose calculation algorithms dose correction factors can be calculated to take density variations or tissue inhomogeneities into account. Examples are the effective depth corrections, power law, tissue-air-ratio methods and corrections for mass energy absorption coefficients for the medium in which the calculation is made. With the aid of CT scanned 3D patient datasets, the lateral extent of inhomogeneities can be accounted for in the density correction algorithms if the separation of primary and scattered radiation is possible. Scatter-air ratio methods utilize small elements of the patient volume and assume that the scattered radiation emerging from each element is proportional to its electron density. The Equivalent tissue-air-ratio (ETAR) method

attempts to separate primary and scattered doses by making use of the CT density data. These methods will be discussed later on in detail.

Dose distributions are calculated at discrete coordinate points (mostly a Cartesian grid) and doses at points that do not coincide exactly with those on the grid are usually obtained by interpolation or extrapolation. When combinations of stationary beams are used they can be weighted to describe the relative contribution of each beam to a reference (or prescription) point. The dose distribution can also be normalized to allow intercomparison of different plans. This normalization can refer all doses to a specification point[2], maximum dose in the total distribution, minimum target absorbed dose or even the isocenter. For better comparison, the ICRU beam reference point is recommended especially for reporting purposes. A true three dimensional dose calculation algorithm would involve integration over the entire (3D) scattering volume for each grid point used in the display.

2.4.1. Current dose calculation techniques

A summary of dose calculation methods can be found in Ahnesjö and Aspradakis[21] where, for example, descriptions of tissue-air-ratios (TAR), tissue-phantom-ratios (TPR) and tissue-maximum-ratios (TMR) can be found. These techniques have also been explained in detail in other sources[13,22-25]. Along with the development of faster computers, better software and the use of CT and MRI, a whole shift from the manual

type of calculations to computerized calculations followed, and more explicit modeling of radiation transport started to appear. When the complexity of the calculation increases, and the accuracy of determining scattered dose contributions to the calculation point, the time associated with dose determination also increases[26,27]. The characteristics of high energy photon interactions in matter could be better approximated[27-28] and simulated[29-39] leading to a gain in accuracy for dose calculations in hetero- and homogeneous media. This was due to the use of physical characteristics in the form of the tissue density of matter, and specifically the use of relative electron densities in combination with correction for heterogeneities, patient outline and curvature. More advanced inhomogeneity correction techniques[3] like the Scatter-air-ratio (SAR), Equivalent-tissue-air-ratio (ETAR), and differential Scatter-air-ratio (dSAR) have also shown some improvements to these basic techniques to account for scattered dose contributions or shielded areas that lessen dose at a specific point when shielding blocks or MLCs are used.

It is important to know that dose deposited is due to secondary charged particles that are set in motion by photon interactions. Thus, for accuracy improvement, the inhomogeneity corrections should not only be applicable to primary and scattered photon radiation, but also electron fluence perturbation as they are transported through the media. Electron transport can only be ignored when electronic equilibrium exists[40]. In this case, the change in dose caused by an inhomogeneity is proportional to the change in the photon fluence.

In radiotherapy dose calculations the radiation field fluence functions can be convolved with pencil beam kernels to obtain dose distributions in irregularly shaped fields[41-48]. This is done by considering dose deposited by secondary charged particles in the dose calculation process. The pencil beam kernels describe the fractional energy that is imparted when the incident photon fluence is absorbed in an attenuating medium and this imparted energy is a result of electrons put in motion and absorbed through various atomic interactions.

The pencil kernels are usually obtained by MC calculations and are calculated in water or can be derived from measured waterbath data. MC calculations are based on the physics of radiation transport and thus the use of these kernels require that the appropriate energy spectrum and the primary fluence of the photon beam as a function of the off-axis position must be utilized. The photon and electron contamination component of the beam should also be known[49-51]. This approach has some difficulties because the model needs to be fitted against measured data requiring adjustment of some of the parameters if the fit is not good enough. Convolution algorithms use physical principals to determine the energy deposited per unit mass. To determine the dose delivered at a specific point, the beam model algorithms are used in conjunction with inhomogeneity corrections to account for changes in dose distributions due to inhomogeneities. Many of the proposed algorithms that do not attempt to take full physical simulations of primary and secondary radiation particles into account have shown limitations where electronic equilibrium has not been established. These algorithms are usually of the sort where pencil kernels are convolved with the primary fluence to obtain dose distributions.

Dose deposition kernels are also known as “dose spread arrays[52]”, “differential pencil beams[53]”, “point spread functions[27]” or “energy deposition kernels[54]”**.** In the current work they will be referred to as pencil beam kernels[28,55]. The resultant dose distribution is calculated by a convolution/superposition of these kernels with the energy released from the photon energy fluence. The methods described by Storchi et al[28,55] will be discussed in detail later on.

2.5. The convolution process

MC methods have been used to generate arrays, or kernels, representing the energy absorbed in water like phantoms from charged particles and scattered radiation set in motion by primary interactions at one location. Mackie et al[42] named them “dose spread arrays” and they were normalized to the collision fraction of the kinetic energy released by the primary photons. These arrays can be convolved with the relative primary fluence interacting in a phantom to obtain 3D dose distributions.

These algorithms attempt to take complex scattered radiation transport processes into account. It is usually in the circumvention of modeling scattering events, or approximation of these events, that the simpler algorithms start showing their limitations. The scattered radiation is a product of primary x-rays having interactions with the flattening filter and the collimators in the radiation head. As a result of scattered radiation, the energy spectrum of the radiation beam undergoes changes and also brings

about changes in the attenuation of the treatment beam. The scatter fluence must be taken into account in the calculation of the dose distribution in a given medium. It is well known that spectral changes have an influence on transmission factors as the penetration properties and dose deposition inside a medium is modified[56-58,60-64].

In the convolution dose calculation process, one needs to simplify it by referring to two essential components: One representing the energy imparted to the medium by the interactions of primary photons (called the terma) and one representing the energy deposited about a primary photon interaction site (the kernel)[3,65]. The total energy released per unit mass (terma) is the energy imparted to secondary charged particles and the energy retained by the scattered photon as a result of primary photons having interactions. Kernel values are measurements of energy deposited at a vectoral displacement from the interaction site, expressed as a fraction of the terma at that site.

The convolution method is sometimes, under special conditions, referred to as a superposition method of dose calculation. This special condition is when the kernels used in the convolution process are scaled to consider the density of the medium in which the dose calculation is done, such as in the case where inhomogeneities are found. Kernels do not consider changes in the vectoral displacement when calculations are done in inhomogeneous media. When the kernels are in fact scaled for different media densities, the calculation is not a true convolution because the kernels are not invariant. In these situations the scaled kernels will be modulated by the terma.

The terma is calculated by considering the exponential attenuation of the energy fluence of primary photons with depth in the medium. It also regards the polyenergetic nature of the beam and the radiological depth to the point of calculation. An expression that takes all these variables into account in calculating the terma in this case is given by

$$T(x', y', z') = ISQR(x', y', z')\sum_{n=1}^{N}\psi_n(x_0, y_0, z_0)e^{-\mu_{n,water}d_{eff}(x',y',z')}\left(\frac{\mu}{\rho}\right)_n \qquad (2.1)$$

ISQR is the inverse square correction at (x', y', z'), Ψ_n is the energy fluence of the primary photons at (x_0,y_0,z_0), $\mu_{n,water}$ is the associated linear attenuation coefficient in water for a specific energy bin and d_{eff} is the radiological depth at (x', y', z') due to the density ρ. $\left(\frac{\mu}{\rho}\right)_n$ is the mass energy absorption coefficient for each photon energy bin in an absorbing medium (n).

The terma (T) at point (x', y', z') is thus the attenuated primary fluence ψ_n as known on point (x_0,y_0,z_0) which is attenuated in the medium at effective depth d_{eff} calculated from the radiological pathlength to point (x', y', z'). This fluence ψ_n(x', y', z') is now multiplied by the mass energy absorption coefficient of water $\left(\frac{\mu}{\rho}\right)_w$ to determine the total energy released in water at (x', y', z'). The inverse square function is then applied to take beam divergence into account.

Convolution calculations are usually done on a component-by-component basis where terma and kernels are generated for multiple single energies, but polychromatic methods also exist.

The primary fractional energy imparted consists of energy from electrons ejected by primary photons through Compton collisions, photoelectric interactions and pair production events. Scattered kernels are also calculated from the energy deposited by charged particles set in motion by scattered photons and brehmstrahlung photons. The expression corresponding to a polyenergetic primary kernel value is

$$H_p(\Delta x \Delta y \Delta z) = \frac{\sum_{n=1}^{N} \psi_n \left(\frac{\mu}{\rho}\right)_n H_{p,n}(\Delta x \Delta y \Delta z)}{\sum_{n=1}^{N} \psi_n \left(\frac{\mu}{\rho}\right)_n} \qquad (2.2)$$

This equation constitutes a kernel value (H_p) calculated by dividing the primary energy deposited in a voxel at a vectoral displacement ($\Delta x \Delta y \Delta z$) from the terma primary interaction site, by the total energy imparted by primary photons. The primary kernels can be calculated separately for all the different energy bins in a photon beam spectrum and subsequently combined with appropriate weights to generate a polyenergetic kernel spectrum. The same expression as in 2.2 is valid for scattered kernels.

In inhomgeneous media the fractional energy distribution about the interaction site will depend on the relative position of the interaction site. The dose is calculated by summing

the dose contributions from each irradiated volume element. The total energy imparted to a unit mass at interaction site r' consists of the terma T(r') and the energy deposited in a unit volume at another point r. This imparted energy is given by T(r')H(r - r') with H(r - r') the kernel value for a displacement r - r' from the kernel origin. The total dose at r is given by integrating over unit masses in the irradiated volume and considers primary (H_p) and scattered (H_s) components. Since the energy loss is mainly due to electron-electron collisions and most photon interactions are Compton events, the average electron density can be scaled by the average density between r' and r for calculation in inhomogeneous media. When such a density scaling is applied to the kernels, the final expression for convolution calculations in a heterogeneous medium becomes:

$$D(r) = \frac{1}{\rho(r)} \int_{r'} T(r') \rho_e^w(r') \left[H_p(\rho_{ave}, r - r') + H_s(\rho_{ave}, r - r') \right] \frac{\rho_e^w(r')}{\rho_{ave}} d^3 r' \qquad (2.3)$$

The division by ρ(r) converts energy per unit volume to energy per unit mass. In such an implementation the kernels have to be generated for a range of different densities with the value corresponding to the average density being found through interpolation.

2.5.1. Pencil Beam convolution algorithms

The differential pencil beam algorithm is an example of a convolution correction algorithm and makes use of an infinitesimally small segment of a pencil beam (directed along a ray line from the beam source) where primary photons have interactions to create

a differential pencil beam dose distribution. It calculates dose in water by convolving polyenergetic pencil beams with a planar radiation fluence distribution[21]. There are various pencil beam algorithms discussed in the literature[3,21,39,41,42,43,44,46,55,65-69].

The two main accuracy limitations on pencil beam models are for heterogeneities[14] and for scatter calculations in medium volumes that deviate substantially from the size for which the pencil kernel is determined[15]. These models are not able to produce accurate changes in scatter from lateral heterogeneities, as well as a lack of scaling of the electron transport for the medium in which the calculation is done[68-70]. In pencil beam algorithms the kernels are usually calculated in water equivalent media, meaning that the secondary electron pathlength will not be accurate in higher or lower density media. Even if the algorithm uses polyenergetic kernels, they must still be scaled for different densities to accurately reflect secondary charged particle tracks.

The result of these limitations are errors in dose distribution when dealing with small irradiated volumes limited in the lateral and/or forward directions or when density changing boundaries are encountered, as well as inside inhomogeneities. It leads to over- or underestimations of scattered radiation inside the media and thus over- or underestimations of the calculated dose. Other problems might also surface when dealing with oblique patient curvature. It is important to realize that some algorithms do scale kernels, but still lack accuracy at inhomogeneity interfaces to account for forward and backscatter.

2.5.2. Superposition Algorithms: Collapsed Cone Algorithm

The Collapsed Cone convolution algorithm is a point kernel convolution (superposition) model[3,21,27,29,51]. This algorithm convolves a polyenergetic energy spectrum and a point kernel energy distribution. Polyenergetic energy deposition kernels are calculated from the energy spectrum of the beam using a database of monoenergetic kernels. The point kernel is represented analytically and combines primary and scatter contributions. It calculates the absolute dose per radiation energy fluence in a medium and the result is very accurate as it can determine the scattered kernels accurately.

These kernels are convolved with the total energy released per unit mass to yield dose distributions. The kernels are scaled during the convolution procedure to account for inhomogeneities and this is a major accuracy advantage of the algorithm. It can however slightly underestimate lateral scattered dose when large fieldsizes are used and in areas just downstream of high-to-low density interfaces.

The reason this algorithm is referred to as a Collapsed Cone algorithm, is that the 3D scatter point kernel distribution is represented by a number of discrete lines of a finite number of polar angles with respect to the primary beam along which the function is defined. Each of these lines is considered to be the axis of a cone. This means that the kernel is a discrete representation of a 3D dose distribution over solid angle $\Omega = 4\pi$. The kernel function along each line is actually the energy deposited within the entire cone at radius r, collapsed onto the line.

2.6. The CadPlan TPS

The CadPlan TPS can make use of two different inhomogeneity correction methods in combination with the PB algorithm. These are the Modified Batho-power law and the equivalent tissue-air-ratio (ETAR) method[3,59]. The ETAR method has been regarded as more accurate than the Batho method as it takes the size of the inhomogeneity into consideration. When an arbitrary square or rectangular beam is modeled by the CadPlan TPS the measured x-ray beam input data is used for dose calculation.

There are basically three dose calculation algorithms that can be utilized during dose calculations namely the Regular Beam Model (RBM), double pencil beam model (DPB) and the single pencil beam model (SPB) on which these inhomogeneity corrections can be implemented. They are based on the Milan-Bentley storage model[3,22,41,45,72] for dose calculation in an off-axis plane. Similar algorithms have been developed by Chui and Mohan[71] for rectangular fields. As their designs are based on the Milan-Bentley model, the TPS requires almost the same beam data as the Milan-Bentley model with some extra measurements.

2.6.1 The Regular Beam Model (RBM)

The RBM accounts for changes in SSD, surface curvature and inhomogeneities and makes use of measured central axis depth dose data for a number of different field sizes

and profile data for these fields at 5 different depths. The data originates from measurements in water at a reference SSD and can then be manipulated to account for patient and setup variations. The profiles are stored as off-axis ratios on a diverging grid formed by the intersections of ray lines originating from the photon source with points on the measured lines. Profile point spacing increases linearly with depth, in proportion to the distance from the source, thus forming a fan-line grid. Profile dose values are relative to that at d_{max} when multiplied by the central axis value at that depth. Data missing in-between the measurement points or ray lines are found through interpolation. Commissioning data for the TPS consists of the central axis depth dose curves for square fields, profiles perpendicular to the inline or crossline jaws for open and wedged beams at 5 recommended depths, and diagonal profiles for the largest open field size.

Some of the assumptions of this model include the equality of the off-axis ratios in the two main central planes while non-wedged planes in a wedged beam are assumed to be equal to open beam profiles (no beam hardening effects considered) resulting in the use of 1D functions rather than 2D functions.

The RBM can only be used for rectangular fields. When the field is partly outside the patient, the double pencil beam (DPB) model is used. This also applies when the field has an irregular shape due to the use of shielding blocks or MLCs. The Milan-Bentley model dose points are stored as infinite source surface distance (SSD) depth dose data, where the dose fall-off is that which would exist if there were no inverse square fall-off. Percentage depth dose (PDD) values are calculated throughout a calculation grid

superimposed on the patient CT data and the values are found by converting the infinite SSD PDD data to diverging field data (to accounting for inverse square dependence) and by multiplying with the off-axis ratio.

If an SSD, other than that where reference conditions apply, is used in a calculation, a different field size is found at the surface for the same jaw settings. If the field size changes to resemble the same area as at the reference field SSD (SSD_1), there can be a significant change in the dose contribution due to scattered photons leading to a change in the depth dose curve. Thus there will be a change in output at the new SSD (SSD_2) and if the PDD with respect to d_{max} at SSD_2 is required, a correction to the reference PDD is made through

$$\begin{aligned} P(d, FS_2, SSD_2) &= P(d, FS_1, SSD_1)\left(\frac{SSD_1 + d}{SSD_1 + d_{\max}}\right)^2\left(\frac{SSD_1 + d_{\max}}{SSD_2 + d}\right)^2 \\ &= C(d, FS_2)\left(\frac{SSD_2 + d_{\max}}{SSD_2 + d}\right)^2 \end{aligned} \tag{2.4}$$

$P(d,FS_1,SSD_1)$ is the measured PDD at depth d for a field size FS_1 on the surface of the phantom and $P(d,FS_2,SSD_2)$ the new PDD value at the depth d for fieldsize FS_2 on the surface of the phantom/patient. $C(d,FS_2)$ is the correction factor accounting for the change in scattered dose contribution.

When the surface curvature changes, the SSD corresponding to each ray line is considered separately. Both the position at which the ray line from the source intersects

the surface and the projected off-axis distance at the reference SSD must then be considered. These influence the effective field size for the ray line from the source affecting the PDD and the depth due to the off-axis inverse square dependence. The dose at an off-axis distance with the considered surface curvature is calculated through

$$D(x,y) = C(d, FS_2)R(x, y, d, FS_1)\left(\frac{SSD_1 + d_{\max}}{SSD_1 + x}\right)^2 \quad (2.5)$$

Here, $SSD_1 + x$ is equivalent to $SSD_2 + d$ in equation 2.4.

At isocentric treatments the SSD is always less than the source-isocenter distance of the linear accelerator. The calculation then becomes

$$D(x,y) = C(d, FS_2)R(x, y, d, FS_1)\left(\frac{SSD_1 + d_{\max}}{SAD}\right)^2 \quad (2.6)$$

The RBM calculates the dose distributions of rectangular fields in water equivalent media where the dose is a product of the corrected PDD of an equivalent square field size, and an off-axis ratio factor[73]. This factor is simply a product of open-field off-axis ratios and the PDD on the central axis. The simple multiplicative rule for an open beam is applied when the off-axis ratios are calculated:

$$R(x, y, d, FS) = R(x, 0, d, FS)R(0, y, d, FS) \quad (2.7)$$

with R the off-axis ratio (profile value at an arbitrary point) for an open beam with equivalent field size FS and x and y directional displacement from the central axis.

It is clear from equation 2.7 that there is no distinction between X and Y profiles. This could potentially be a problem when narrow rectangular fields are used where there is much less scatter in one direction compared to others. Some authors have also found an overestimation of the off-axis ratio at small depths in the case of over flattened beam profiles[74]. For wedged profile calculations, the multiplicative rule is used in the off-axis dose determination at a point in the wedge direction and the same point for an open field. These profiles are not equal in the non-wedge direction compared to the open field due to beam hardening.

Storchi and Woudstra[73] modified this rule for open beams by separating the measured profile into two factors called the envelope profile and boundary profile. The envelope profile represents the radial dose distribution of the beam, which should ideally be symmetric. The envelope profile is estimated from all input profiles for increasing field sizes in combination with a diagonal profile. The boundary profile describes the boundary of the profile and the penumbra created by the jaws. The product of these two factors gives the off-axis ratio of a square field

$$P_0(x, y, d, FS) = P_c(r, d)P_b(x, d, X)P_b(y, d, Y) \qquad (2.8)$$

To distinguish between the off-axis values in the boundary and envelope profile, the nomenclature is changed here so that P_0 is the open beam off-axis value; P_c represents R in equation 2.7 for the envelope part of the profile and P_b the boundary part of the profile. X and Y is the field size in the x and y direction. The distance is (r) from the point (x,y) to the beam axis and the value of P_b is unity on the beam axis. This equation does not have the multiplicative problem as long as P_b describes the boundary and is equal to unity inside the field. At any arbitrary point from the CAX, the off-axis ratio would thus be the product of the primary off-axis ratio and the boundary factors.

The envelope profile is determined from the measured diagonal profile of the largest possible field. It represents the profile of an infinite, uncollimated field and is the dose at a point (r) away from the CAX, relative to the value of the CAX at the same depth (d). Discrepancies between profiles in the x and y directions can very well be found if the beam, during measurement for commissioning, is not symmetrical. To circumvent this problem, the diagonal profile is only used in the extrapolated part of the envelope profile calculation for distances from the CAX larger than the largest measured fieldsize.

The beam profiles in the boundary region are described by the boundary factors and they are defined by the collimating jaws. From here the concept of boundary profile ($P_b(x,d,FS)$) arises as the boundary factors are the ratios of the dose at a point off-center in a finite field relative to the dose at the same point in an infinite field. This profile is a function of distance from the CAX (x or y), depth of the calculation point (d), and field size (FS).

In the situation where wedges are used, the influence of the wedge on the shape of the profile is achieved by translating the profile shape to an equivalent water thickness. It involves a method of finding the depth at which the profile of the corresponding open beam fits best. In order to compute the wedge envelope profiles in planes other than the central plane, a narrow beam attenuation coefficient in water is used to calculate relative transmission for different positions in the wedge direction as a function of equivalent water thickness. The boundary profiles of the wedged beam are interpolated from the available measured set in the same way as the open beam boundary profiles.

The boundary profiles are defined by dividing the input (measured) profile ($P_m(x,0,d,FS)$) with the envelope profile:

$$P_b(x,d,FS) = \frac{P_m(x,0,d,FS)}{P_c(x,d)} \tag{2.9}$$

With P_B the boundary profile, P_m the measured input profiles and P_c the envelope profiles.

The depth dose curves calculated for the equivalent square fields become

$$D(x,y) = C(d,FS_2)P_0(x,y,d,FS)CF_{inv} \tag{2.10}$$

With $C(d,FS_2)$ the modified PDD value for an equivalent field size FS at the point where the field intersects the body/phantom with a divergence correction and change in PDD due to a changed SSD, while CF_{inv} is the inverse square law factor.

The depth dose curve must be modified because the PDD shape changes when the central axis distance differs from the source-phantom distance (SPD) at which the measurements were done. The correction is achieved using:

$$CF_{dd}(d) = \left[\frac{T(d,FS_2)}{T(d,FS_1)}\right] \cdot \left[\frac{SSD_2 + d_{\max}}{SSD_2 + d}\right]^2 \cdot \left[\frac{SSD_1 + d}{SSD_1 + d_{\max}}\right]^2 \qquad (2.11)$$

FS_1 is the equivalent field size corrected for the changed SSD (SSD_1) and depth of the point of interest, and the same for the equivalent field size FS_2 corrected for SSD_2 and point of interest. T(d,FS) is the TAR/TMR value at depth d for field size (FS) and could be substituted with the respective PDDs. The correction needs to be done because the beam input data is measured at a reference SSD and these PDD curves are normalized to 100% at d_{max}. The inverse square correction factor is thus

$$CF_{inv} = \left[\frac{SSD_1 + d_{\max}}{SSD_2 + d_{\max}}\right]^2 \qquad (2.12)$$

with SSD_1 equal to the reference SSD of the input data. All fields are normalized to 100% at d_{max} whenever the SSD entry point is located on the body surface.

Off – axis dose points are calculated simply through the product of the envelope factor and the boundary factor which are all generated from the measured profiles. Only symmetrical fields are calculated this way, while asymmetrical fields have a geometrical field central axis and this is used as the reference for boundary profiles.

Off – axis dose points are calculated with the following equation:

$$OA_o(x, y, d_2) = P_c(r, d_2) \cdot P_b(x, d_2, FS_x) \cdot P_b(y, d_2, FS_y) \quad (2.13)$$

with P_c the envelope profile and P_B the boundary profile.

The divergence of the field is corrected for whenever a non reference SSD field is calculated simply by scaling the field size at the plane of interest for the difference in SSD.

For asymmetric fields the dose at an arbitrary point is calculated relative to the dose of the corresponding symmetric field at depth d_{ref} on the central axis (CAX). This method assumes that the effect of field position on the collimator scatter factor S_c and the phantom scatter factor S_p is negligible. The off-axis ratio is again determined by the product of the envelope profile and the respective boundary profiles (x or y plane). This is very similar to shifting the boundary profile of the corresponding symmetric field to the proper position. The same model is used for wedged beams.

2.6.2. Double Pencil Beam Algorithm

Irregularly shaped fields are often used in radiotherapy treatment such as multileaf collimator segments, beam shaping blocks and compensators. Convolution techniques allow computation of dose from irregular shaped photon fields in inhomogeneous media[40-42,48,54,65,75].

A simple way to understand the dose calculation at a point P in a calculation matrix is through the following:

$$D(p) = DD(d_2) \times OA(x_1, y_1, d_2) \times CO \times CF \qquad (2.14)$$

$DD(d_2)$ = depth dose value at depth d_2

$OA(x_1,y_1,d_2)$ = off-axis factor at point (x_1,y_1) in a plane perpendicular to the beam CAX at depth d_2

CO = correction factor for skin obliquity

CF = correction factor for tissue inhomogeneities

From the geometry of a radiation field, it can be understood that the product of the depth dose value and off-axis factor gives the dose value in a water-equivalent medium. The double – and single pencil beam algorithms suggested by Storchi and Woudstra et al[41,69], can be implemented for the calculation of this value.

As a 3D convolution calculation takes a lot of time, a 2D pencil kernel convolution process was adopted on the CadPlan TPS. In this case, the pencil beam kernels are calculated before the convolution process[43,44] and saved as a dataset. This pre-calculation is usually done in water which means that they cannot be applied in full 3D calculations where inhomogeneities are involved. The only way of scaling these kernels is by a correction along the fan lines of the beam through the use of media densities. These kernels are also calculated for specific beam qualities and do not vary as a function of the energy of primary x-rays incident on the medium being irradiated.

This pencil beam algorithm is based on measured data for a specific linear accelerator. The model is an extension to the regular beam model for dose calculation in off-axis planes where the input data is the same as required by the Milan-Bentley model. Some additional data is required in the form of phantom scatter factors at a reference depth which changes as a function of field size.

In the case of fields shaped irregularly through MLCs or shielding blocks, changes in the model for the rectangular fields are required. The absorbed dose D(x,y,z,FS) in an irregularly shaped photon beam is normalized to the absorbed dose of the $10x10cm^2$ field at a reference depth, z_{ref}. The changes are required to the depth dose as the equivalent field size changes, as well as a change in the boundary function. The depth dose change cannot be calculated through the equation proposed by Worthley[76] as the equivalent field size has changed. Another reason is that the CAX of the beam might be under a block or MLC leaf, or fall in the penumbra region. The boundary function can also not be

computed as before because the old method assumes that the field boundaries are perpendicular to the directions of the boundary profiles in the directions of the two main axes.

The method for calculating doses in irregular fields comprises of a convolution of a field intensity function, F(x,y), with two different types of pencil beam kernels which are derived from basic beam data. These are called the scatter- and boundary kernels respectively. If the central axis is obscured by blocks or MLCs, or lie very close to, or on the collimator defined beam edge, a different way of calculating the PDD profile along the CAX is by making use of an effective axis on a ray line through a point where the scatter dose of the field is maximal at a depth of 10 cm and normalized to the absorbed dose at a reference depth of the same open field area. In the case of a rectangular field, this effective axis coincides with the beam axis. The boundary function is also normalized to unity at this point.

The field intensity function, F(x,y), is a two-dimensional function and is equal to unity inside the contour of the field at the reference source-phantom distance. For irregularly shaped fields, this function changes to a value equal to the transmission through the block, MLC or jaw material under the blocks and becomes zero underneath the jaws.

2.6.2.1. Calculation of the dose in a blocked region and outside the radiation field

Underneath any field defining boundary created by jaws, MLCs or blocks, the value of the field intensity function will become very small. Here the boundary kernel is calculated from a strip kernel. The strip kernel (figure 2.1) is basically a pencil kernel divided into a number of parallel strips (from the beam's eye view). The number of strips determines their width. The value of a strip at a distance from the pencil beam axis is equal to the sum of the surface of the intersection of the n^{th} strip with rings representing the kernel at radial distances. These get multiplied by the boundary kernel. Outside these rings the strip kernel is zero and thus the boundary kernel will also be zero.

Any dose point outside the field will consist of a scattered dose contribution, produced in the phantom, inside the geometrical field. This contribution is calculated as the ratio of the depth dose at a point (x,y,z) outside the irregular field, $D_{\infty}(x,y,z;F)$, and the depth dose at the same depth, but on the effective axis of the irregular field. This approach would lead to a very sharp cut-off in dose in the penumbra region or near the field edge as the intensity function value drops rapidly in these regions. Because of this, a smoothing function is used to modify the boundary function to achieve a continuous and smooth transition from the boundary region to the region outside the field. One important factor explicitly pointed out by Storchi and Woudstra[41], is that this approach neglects the contribution of the transmission through the jaws and of the head scatter and will underestimate the absorbed dose for points outside the field.

In the case of wedged beams, the envelope and boundary profiles of the open beam are computed for depths including an equivalent water thickness which depends on the off-axis coordinates in the wedged direction to account for the influence of the flattening filter on the profile shape. Boundary kernels are only calculated for open beam data. This means that the model cannot distinguish between the open beam boundary profile and the wedged beam boundary profile. Thus the boundary function is not computed by the product of the two boundary profiles. In this case the irregular field multiplication of two boundary profiles is replaced by the boundary function of the open beam.

2.6.2.2. Calculation of the pencil kernels

The pencil kernel calculated from measured depth dose curves of regular square fields is called the scatter kernel. Depth doses and peak scatter factors are used for its determination. The scatter- and boundary kernels ($K_s(r,z)$ and $K_b(r,z)$) are rotationally symmetric. The distance from the axis of the kernel to a point (x,y) in the kernel is represented by variable r. The scatter kernel is considered as the dose contribution per unit area to the depth dose at a depth z for a narrow beam at distance r from the field axis. It resembles the TAR/SAR or TPR/SAR frequently used in dose determination. These quantities are usually derived for CAX PDDs for field sizes larger than $2x2cm^2$. The smaller field size values are determined through extrapolation to field size zero, which is inaccurate and subject to interpretation[41]. To calculate the dose close to the field edge correctly, the off-axis ratios need to be calculated using the boundary kernel, $K_b(x,y,d)$.

All calculations are performed in water-equivalent media at a reference source-phantom distance. Any change in SSD or skin obliquity is corrected in the patient model for the patient geometry. The associated changes in field size at the SSD through divergence, changes in PDD etc., are considered here.

The scatter kernels are calculated at five standard depths, z_i, from measured phantom scatter factors, S_p, and relative depth doses. S_p is measured at a reference depth, z_{ref}, and thus the dose can be expressed relative to the absorbed dose on the CAX of the 10x10cm^2 square field at the same reference depth. With the inverse square effect removed, the calculation is done using:

$$D_{\infty}(z_i; X) = S_p(X) D_a(z_i; X) \left(\frac{(SPD + z_i)^2}{(SPD + z_{ref})^2} \right) \tag{2.15}$$

Square field phantom scatter factors and depth doses are converted to circular field phantom scatter factors and PDDs and the scatter kernels can be calculated by taking the derivative of $D_{\infty}(z_i,R)$ relative to the radius R of the field. After applying a correction factor, the CAX dose of the square fields calculated through integration of the scatter kernel usually differs less than 0.5% from the input value.

2.6.2.3. Calculation of the boundary kernels

Boundary kernels are also calculated at the five standard depths. It is computed in two steps. A number of strip beam kernels are firstly calculated by numerical differentiation of the boundary profiles of a number of large square fields. A separate strip beam kernel is computed from the center of the field to the field boundary. To suppress any errors in measurement of the profiles of input data, the strip kernel is computed from the average of a number of computed strip beam kernels.

The second step is the calculation of the boundary pencil kernel from the strip beam kernel (Figure 2.1). The computed strip beam kernel has a finite range because the boundary profile of a large field is equal to unity inside the field. This means that there will be a number of δ's (δ being the resolution of the calculation) for which the strip beam kernel will be positive and the other δ's will have a zero value. The boundary kernel will be given for the same range of indices and the value of this boundary kernel for r = Nδ is calculated using:

$$K_b(N\delta, z_i) = S_b(N\delta, z_i)/a_{NN} \qquad (2.16)$$

where a_{NN} is the area of the intersection of the outer ring with the outer strip.

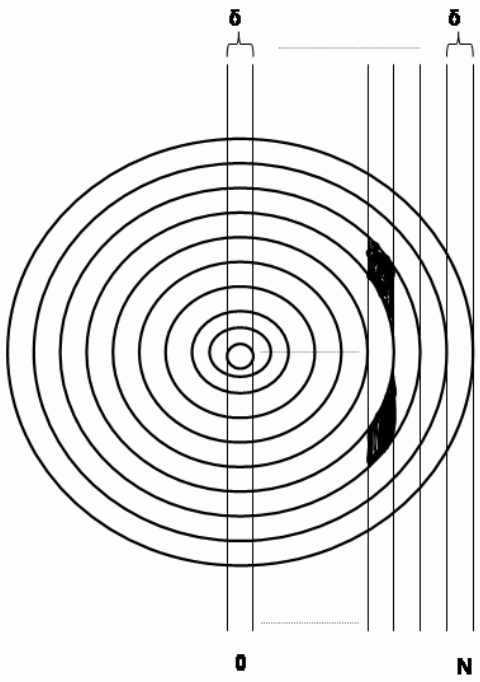

Figure 2.1: A schematic representation of how the boundary kernel is calculated from the strip kernel. The sum of the surface of the intersection of the nth strip with the rings with index n to N, multiplied by the value of the boundary kernel gives $S_b(n\delta)$. $S_b(n\delta)$ is calculated at a distance $r = n\delta$ from the CAX of the pencil beam. As $S_b(n\delta)$ and $K_b(n\delta)$ are zero for $n > N$, the boundary kernel can be computed recursively starting with the outer ring (reproduced from Storchi and Woudstra, 1996[41]).

According to Storchi and Woudstra[41] (Table 1), the algorithm showed a high level of accuracy in reproducing the input data after calculation of the kernels and subsequent convolution. They have however found that the tail outside the field is not properly reproduced and jaw transmission and phantom scatter from inside the field is over estimated. The reason for this effect is that the boundary kernel is calculated from the first part of the boundary profiles.

In the wedged beam case the algorithm underestimates the dose outside the field and this can possibly be, according to the authors, due to the fact that the scatter from the flattening filter and from the jaws is not taken into account. In comparison with the

regular beam model (rectangular field model) these effects are taken into account because the profile is computed by direct interpolation from measured data. In the wedge direction, the profile also differs from the rectangular field model because the pencil beam convolution algorithm uses the boundary kernel computed from the open beam data instead of the boundary kernel of the wedged beam.

The convolution of the boundary kernel K_b at depth, d, results in a 2D boundary profile of an irregular field. $P_b(x,y,d,F) = K_b(x,y,d) \times F(x,y)$ and this replaces the product of two one dimensional boundary profiles as shown earlier.

2.6.3. Single Pencil Beam Algorithm

In the new convolution model[69], the single pencil beam model in CadPlan V6.4.7, the dose is calculated through one single convolution equation. Storchi et al[69] recons that it is difficult to fully derive the pencil beam kernel from measured data because it is difficult to measure central axis doses for small fields in which lateral electron equilibrium does not exist. They propose another way of deriving pencil kernels from measured beam data. The method completes their previous work[41] where the inner part of the pencil beam corresponding to the region of electronic disequilibrium is not derived from the central axis dose of small fields, but from the penumbra region of the off-axis ratios. A correction factor is also used in combination with the pencil beam kernel that takes into

account the variation of the primary photon fluence as a function of depth and off-axis distance.

Their first pencil beam model[41] calculated the absorbed dose due to phantom scatter in an irregularly shaped photon beam. The dose is normalized to the absorbed dose of a 10x10 cm^2 field at a reference depth. The model consisted of a convolution of two pencil kernels that have been derived from measured beam data. The convolution was done between a depth dose function on an effective axis of the field, a boundary function at specific off-axis points and at different depths, which describes the penumbra region of the field, and an envelope profile which takes into account the non-flatness of the beam, as well as differences in beam attenuation as a function of off-axis distance. The off-axis ratios, with which the depth dose was modulated, were produced by the product of the envelope and boundary functions. The depth dose and boundary functions were computed by the convolution of a field intensity function and a scatter kernel and boundary kernel respectively. The irregular shape of the field influenced the field intensity function. This function had a value of 1 inside the irregular field, but became 0 underneath blocks, MLC leafs or jaws. The 0 value could be substituted with the transmission factor for the blocks, MLCs or jaws.

In the new model that utilizes only a single pencil kernel convolution, the equation for dose calculation changes to

$$D(x,y,z;F) = \frac{\left(f + z_{ref}\right)^2}{\left(f + z\right)^2} \int_{-\infty}^{+\infty}\int_{-\infty}^{+\infty} F(x',y') P_{\text{int}}(x',y',z) K(x-x',y-y',z)\,dx'\,dy' \qquad (2.17)$$

K(x,y,z) is the new pencil kernel, (K(r,z)) in cylindrical coordinates with $r = (x^2+y^2)^{½}$), a dose distribution of a narrow beam entering the water phantom along the z-axis. F(x,y) is the same field intensity function as was used in the DPB model. The variation in the primary fluence is given by a normalized fluence function, $P_{int}(x,y,z)$, of primary photons at depth z and is referred to as the intensity profile varying as a function of off-axis distance. This function is assumed to have rotational symmetry, just like P_c used in the DPB model. It accounts for the non-flatness of the beam and variations of the fluence as a function of depth in the phantom. The latter is due to variation in the energy spectrum of the beam as a function of the off-axis distance. The input data, from which the scattering kernel and intensity profile is calculated to satisfy equation 2.17, consists of the same measurement data set as mentioned for the double pencil beam algorithm. The multiplication of the field intensity function by P_{int} in this convolution replaces the multiplication by the envelope profile, P_c, that was used in the DPB algorithm.

2.6.3.1. Calculation of the pencil beam kernel

According to Storchi et al[69] the scatter kernel $K_s(r,z)$ from the phantom scatter at a reference depth is calculated for at least a $4x4cm^2$ field. It is computed by differentiation of the scatter dose, $D_{scat}(z,R)$, on the central axis of a circular beam with radius R. The field intensity function is now given by a field intensity profile $P_{int}(r,z)$ and is calculated from the envelope profile, P_c. In this calculation it is assumed that the intensity profile is equal to the envelope profile.

$$D_{scat}(z;R) = \int 2\pi r K_s(r,z) P_c(r,z) dr \qquad (2.18)$$

$D_{scat}(z;R)$ is firstly evaluated from the measured square field data set.

$$D_{scat}(z;X\pi^{\frac{1}{2}}) = \frac{(f+z)^2}{(f+z_{ref})^2} S_p(X) D_{a,N}(z;X) \qquad (2.19)$$

S_p is the phantom scatter factor at reference depth z_{ref} and $D_{a,N}$ is the normalized depth dose of the corresponding equivalent square field $X = \pi^{1/2}R$ (In Storchi and Woudstra[28] the symbol D_∞ was used for the scatter dose). For field sizes smaller than an equivalent 4x4 cm^2, the dose is extrapolated linearly. This will lead to a situation where electronic equilibrium is ignored at the small field sizes, but it is addressed to some extent later on in the following steps.

Through numerical differentiation, K_s can be calculated from equation 2.18:

$$K_s(0,z) = \frac{D_{scat}(z;0)}{14\pi\delta^2 P_c(0,z)} \qquad (2.20)$$

$$K_s(0,z) = \frac{D_{scat}(z;n\delta) - D_{scat}(z;(n-1)\delta)}{2\pi n\delta^2 P_c(n\delta,z)} \qquad n = 1,\ldots..,\ n_{max} \qquad (2.21)$$

δ is the resolution of the calculation. After this first evaluation, K_s is corrected for the fact that square fields are used and not circular fields, as pointed out in Storchi and

Woudstra[28]. This leads to a difference between the previous method of calculation and the single pencil kernel calculation. Before differentiation, $D_{scat}(z;R)$ is fitted by a double exponential function:

$$D_{scat}(z;R) = a_0 + a_1 e^{-b_1 R} + a_2 e^{-b_2 R} \tag{2.22}$$

Fitting parameters, a and b, depend on the depth, z. These variables are found through fitting of the data and any errors found through fitting the data is below the uncertainty in measurement.

The intensity profile, $P_{int}(x,z)$ is calculated next with a recalculation of the scatter kernel. The off-axis distance is denoted by x and the intensity profile is calculated through a convolution:

$$\begin{aligned} P_c &= \|K_s\|^{-1} K_s * P_{\text{int}} \\ &= \left(\int_{-\infty}^{+\infty}\int_{-\infty}^{+\infty} K_s\left(\sqrt{(x-x')^2 + y'^2}, z\right) P_{\text{int}}\left(\sqrt{x'^2+y'^2}, z\right) dx'\, dy' \right) \times \left(\int 2\pi r K_s(r,z) dr \right)^{-1} \end{aligned} \tag{2.23}$$

Through an iterative procedure, the intensity profile can then be calculated through

$$\begin{aligned} P_{\text{int}}^{(0)}(x,z) &= P_c(x,z) \\ P_{\text{int}}^{(n)}(x,z) &= P_{int}^{(n-1)}(x,z) + \left(P_c(x,z) - \|K_s\|^{-1} K_s * P_{\text{int}}^{(n-1)}(x,z) \right) \end{aligned} \qquad \text{n = 1, 2, 3,….} \tag{2.24}$$

Here, $P_{\text{int}}^{(n)}(x,z)$ is the intensity profile at the n$^{\text{th}}$ iteration. A threshold is set up, value usually 0.1%, for a mean absolute value of a correction term and when this threshold is reached, the iteration process is terminated. A fixed maximum number of iterations can also be reached which will stop the process. This is a way of speeding up the calculation process: only about 2-6 iterations are used. The intensity profile and scatter kernel is assumed to have rotational symmetry which changes a 2D integration to a 1D integration. The scatter kernel K_s is again computed but this time with the intensity profile. The intensity profile represents a scatter profile, while the envelope profile represents a fluence modulating profile.

The boundary kernel is then calculated so that it can be combined with the scatter kernel into a single pencil beam kernel. The boundary kernel is calculated from a boundary profile at the penumbra of the field. The scatter profile, $P_{scat}(x,z;X)$ is basically the off-axis ratio of a square field with sidelength X in the central axis plane of the beam. It is obtained when the field intensity profile is convolved with the scatter kernel. The boundary profile, which is corrected for phantom scatter, is calculated by dividing the measured profile P(x,z;X) by the scatter profile in the region inside the field boundary.

$$P_b(x,z;X) = \frac{P(x,0,z;X,X)}{P_{scat}(x,z;X)} \qquad \text{for } P_{scat}(x,0,z;X,X) > 0.6P_c(x,z) \tag{2.25}$$

$$P_b(x,z;X) = P(x,0,z;X,X) \qquad \text{for } P_{scat}(x,0,z;X,X) \leq 0.6P_c(x,z) \tag{2.26}$$

The scatter profile, P_{scat}, is calculated by

$$P_{scat}(x,z;X) = \frac{\int\int P_{\text{int}}(x',y',z')K_s(x-x',0-y',z)dx'\,dy'}{\int\int P_{\text{int}}(x',y',z')K_s(0-x',0-y',z)dx'\,dy} \tag{2.27}$$

It is assumed that the boundary profile, corrected for photon scatter, is the result of the convolution of the missing part of the pencil beam kernel (referred to as the boundary kernel, $K_b(r,z)$) with a uniform square field. This square field is described by a block function H(x,y,z;X) that is equal to 1 inside and 0 outside the field. This assumption is sufficient for the calculation of the boundary kernel as the non-uniformity of the field is already taken into account by the scatter profile. Strip kernels are calculated through numerical differentiation of the boundary profile of a number of fields and then the boundary kernel is calculated from the mean strip kernel. Once the scatter kernel and the boundary kernel have been computed separately, they can be combined into a single pencil beam kernel.

2.7. Inhomogeneity Corrections

Air cavities or regions with low densities cause disruptions of electronic equilibrium[77]. Some authors have investigated the effects of inhomogenieties[14,15,78-81] and have shown that ignoring electronic disequilibrium can lead to significant errors at high x-ray energies. This is especially true where low density inhomogeneities are encountered. In addition, the atomic number of the atoms in the various tissues tissues involved also influences the electron scattering pattern. The density differences result in a shift of

isodoses with depth, and the scattering perturbations affect the dose distribution local to the inhomogeneity.

Electrons are generated by Compton interactions in patient tissues. Inhomogeneities in tissue will cause these electrons to have a longer range in lower density tissue compared to high density tissues. Small inhomogeneities mainly affect the scatter distributions with a lesser effect on beam absorption. Dense media have higher scattering capabilities and will cause a larger number of electrons to leave the inhomogeneity rather than entering it from the surrounding low density medium.

Sontag et al[78] found that accurate dose calculations should especially be done when tissue inhomogeneities are present in the path of the beam. This, in combination with an accurate dose calculation algorithm, may reduce accuracies to within ±5%[22].

Cunningham et al[3,47] compared dose calculations in simple heterogeneous phantoms with measurements made with a Baldwin Farmer ionization chamber. The experiment clearly showed differences between measured and calculated dose points or distributions. Inhomogeneity correction algorithms can aid in achieving better accuracy in dose calculations in such heterogeneous media. These correction methods are usually applied by calculating the dose firstly in a water equivalent patient model and then employing a set of correction factors for the inhomogeneities. However, large differences are still found when absolute measurements are compared to calculations, even on the central axis (CAX) of the beam. Only when accurate calculation of first- and multiple scattered

electrons through convolution algorithms are considered is a more accurate result achievable.

2.7.1 Effective attenuation correction method

An inhomogeneity correction factor can be based on the use of the equivalent depth in water for the inhomogeneity by making use of an exponential function and an effective attenuation coefficient. It is assumed that the dose is increased by a certain fraction for each centimeter of water-equivalent material that is missing and that thickness represents an attenuation coefficient for the radiation beam:

$$CF = e^{\mu'(d-d')} \tag{2.28}$$

Here, μ' is the effective attenuation coefficient, d the depth to the point of calculation in a water equivalent medium, (d') the effective depth correcting for the density of the inhomogeneity and CF the correction factor. The correction does not take the scattering effects of the field size or depth of the inhomogeneity into account. It also does not consider the volume of the inhomogeneity, nor the position with respect to the beam CAX and edges.

The effective depth can also be calculated through a linear function by using the coordinates at which a rayline intersects the different tissue densities:

$$d_{eff} = (x_1 - x_0)\rho_1 + (x_1' - x_1)\rho_2 + (x_2 - x_1')\rho_3 + ... + (x_c - x_n)\rho_n \quad (2.29)$$

where x_i are the coordinates where 2 differing density media meet and ρ_i the corresponding densities, and x_c being the coordinate of the point of calculation in depth.

The regions of differing densities can also be devided into segments of lengths corresponding to CT pixel sizes. The effective depth (d') is then found through:

$$d' = \sum_{i=1}^{n} \Delta h'_i + \frac{\Delta h'_{n+1}(d - n\Delta h)}{\Delta h} \quad (2.30)$$

with ρ_i being the average density of an increment and the effective pathlength increment is $\Delta h' = \rho_i \Delta h$. The calculation point lies in the (n+1)th rayline segment.

2.7.2. The ratio of tissue-air ratios

The equivalent depth in water can be further explored by making use of two tissue-air-ratios (TAR):

$$C = \frac{T(d'; FS_d)}{T(d, FS_d)} \quad (2.31)$$

Again d is the depth to the point of interest and d' the water equivalent depth. FS_d is representative of the dimensions of the crossection of the beam at the depth d. The fieldsize is taken into account this time along with the depth through the use of TARs. The lateral dimension of the inhomogeneity is not considered, nor it's position with respect to the point of the calculation.

2.7.3. Effective SSD method

Similar to the ratio of TARs, PDD curves can also be used. These are employed in the effective SSD method where PDDs are basically shifted by changing the source to surface distance (SSD) to make the calculation point depth equal to the water equivalent depth. The new dose value at the point of interest should consider the changed SSD and requires an inverse square correction. The correction factor for the new SSD (SSD_1) becomes:

$$C = \frac{D(d', FS, SSD')}{D(d, FS, SSD)} \left(\frac{SSD + d_m}{SSD' + d_m} \right)^2 = \frac{D(d', FS, SSD)}{D(d, FS, SSD)} \left(\frac{SSD + d'}{SSD' + d} \right)^2 \quad (2.32)$$

Since the PDD can be related to the tissue-air ratios through

$$D(d,FS,SSD) = 100\frac{T(d,FS_d)}{T(d_m,FS_{d_m})}\left(\frac{SSD+d_m}{SSD+d}\right)^2$$
$$\therefore C = \frac{T(d',FS_d)}{T(d,FS_d)}\left(\frac{T\left(d_m,FS_{d_m}\right)}{T\left(d_m,FS'_{d_m}\right)}\right)^2 \quad (2.33)$$

The method is very similar to the ratio of TARs. A major advantage of this method over TARs is that off-axis calculation points can account for the lateral position of the point of calculation. This means that surface curvature can also be taken into account. The last term in equation 2.33 considers the ratio of backscatter factors and corrects for divergence of the beam.

2.7.4. The Batho Power Law method

Batho[3,45,82] proposed a method for inhomogeneity corrections by raising the TARs to a power that depends on density. Futher development of the method produced a general form for calculation of a correction factor (CF) that can be applied for dose calculation points within or beyond the inhomogeneity. These points are defined by the relative electron density values (ρ_i) of different anatomical structures:

$$CF = \frac{T(d_1;FS_d)^{\rho_1-\rho_2}}{T(d_2,FS_d)^{1-\rho_2}} \quad (2.34)$$

where ρ_1 is the relative electron density of the point of the material in which the calculation point lies and d_1 is the depth of the point. ρ_2 is the next medium density with

d_2 the depth below its upper surface. This method takes the position of the inhomogeneity with respect to the point of calculation into account. It proves to be in far better agreement with measured data compared to the previous inhomogeneity correction methods. Scattered photons are not explicitly modeled, but due to the nature of the model they are taken into account in a forward direction. On the CadPlan TPS the calculation of inhomogeneity correction factors is done by using either TARs or TMRs.

Pixel values (on patient CT slice data) for grid points are first converted to dose calculation grid coordinates. The total area of the dose distribution matrix depends on the grid size. After pixel values have been determined, a rayline is determined from the grid point of calculation to the beam focus. The pixels intersected by the line are taken into account. The system tracks homogeneity layers at 1 cm intervals and simultaneously calculates the mean electron density for each layer. The correction factor for each layer is then calculated and all CFs along the calculation line are multiplied together:

$$CF = K_N \cdot \prod_{m=1}^{N} T\left(d_m, FS\right)^{\left(\mu_m - \mu_{m-1}\right)/\mu_0} \qquad (2.35)$$

where μ_0 is the linear attenuation coefficient of water and μ_m, the linear attenuation coefficient of the m^{th} inhomogeneity layer. The distance between the gridpoint and the m^{th} inhomogeneity boundary is denoted by d_m with T the tissue-air ratio value at this depth. K_N is a scaling factor for the N^{th} material electron density relative to water and can be expressed as:

$$K_N = \frac{\left(\mu_{en}/\rho\right)_N}{\left(\mu_{en}/\rho\right)_0} = \left(\rho_e^w\right)_N \tag{2.36}$$

with $\left(\mu_{en}/\rho\right)_N$ the mass energy absorption coefficient for the Nth layer (the last layer) and $\left(\mu_{en}/\rho\right)_0$ the mass energy absorption coefficient for water. CF can also be expressed as:

$$CF = K_N \cdot \prod_{m=1}^{N} T\left(d_m, FS\right)^{\left(\rho_e^w\right)_m - \left(\rho_e^w\right)_{m-1}} \tag{2.37}$$

with $(\rho^w{}_e)_m$ the mth material electron density relative to water. T can be either TAR or TMR values that are normalized to a reference depth of D_{max}. Tissue maximum ratios are used for high energy beams. This method is refered to as the generalized Batho power law.

For the Modified Batho power law, the depth definition in TAR/TMR value starts from the surface layer. For high energy photon beams the build-up depth can be several centimeters and in this region the TAR/TMR value is not valid. The generalized Batho power law uses the TAR/TMR value at D_{max} in the buildup region, while modified Batho power law uses only the descending part of the TAR/TMR curve. Therefore the depth of D_{max} is added to the depth of d_m:

$$CF = K_N \cdot \prod_{m=1}^{N} T\left(d_m + D_{\max}, FS\right)^{\left(\rho_e^w\right)_m - \left(\rho_e^w\right)_{m-1}} \tag{2.38}$$

2.7.5. The Equivalent Tissue-Air Ratio method

The equivalent tissue-air ratio (ETAR), makes corrections for the change in radiological depth and the field size and considers the 3D shape of the structures using a ratio of tissue-air ratios[78]. With this method, all linear dimensions such as depth and field size are scaled in proportion to the electron density of the inhomogeniety. This way, dose data in a homogeneous medium can be scaled to fit the dose distribution in a heterogeneous medium. The scaled depth (d') to a calculation point is calculated using the average electron density of all elements along the beam ray up to the depth d.

The tissue-air ratio can be calculated from a radiation beam incident on a phantom such as figure 2, considering a monoenergetic radiation beam with fluence Φ

$$T(d, FS_d)_1 = \frac{\Phi\left(e^{-\mu d}\,\frac{\mu}{\rho}\,\overline{E}_{ab} + \int_V e^{-\mu a} n \frac{d\sigma}{d\omega}\frac{e^{-\mu' b}}{b^2}\frac{\mu'}{\rho}\,\overline{E}'_{ab}\,dV\right)}{\Phi\left(e^{-\mu d_m}\,\frac{\mu}{\rho}\,\overline{E}_{ab} + \int_v ds\right)} \tag{2.39}$$

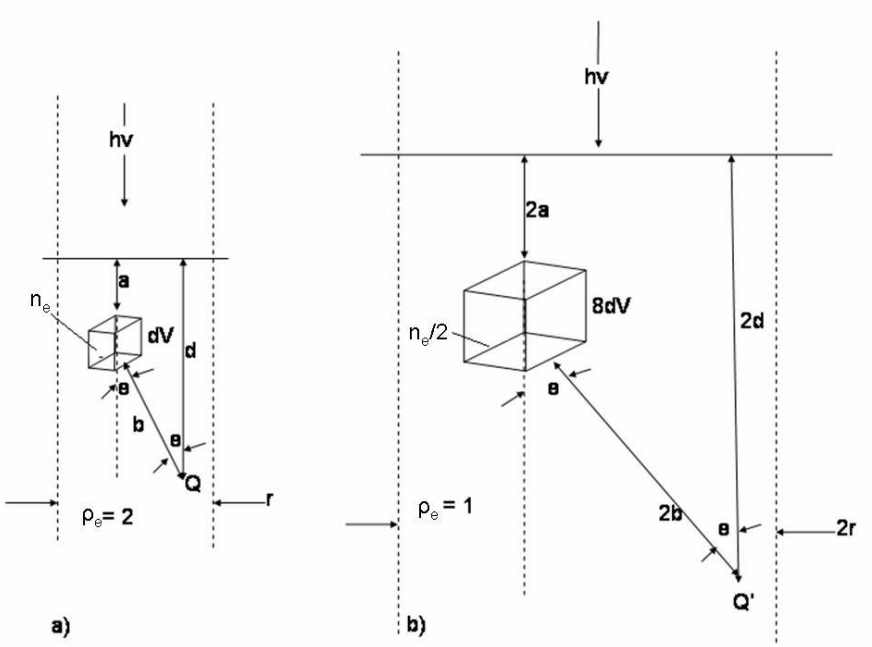

Figure 2.2: Parameters used in the calculation of absorbed dose from primary and single-scattered photons. a) A phantom with electron density twice that of water ($\rho_e = 2$) and an incident radiation beam. b) The conditions that would produce equal doses at points Q and Q' for the same incident radiation beam in a medium like water ($\rho_e = 1$).

From figure 2.2 and equation 2.39, the first term in the numerator is the absorbed dose from primary photons attenuated along the pathlength d. The linear attenuation coefficient is denoted by μ and μ/ρ the mass attenuation coefficient for these photons. $\overline{E}_{ab}$ is the average energy absorbed as a result of each photon interaction. The second term is the integration of dose from once-scattered photons over the irradiated volume. The distance to the point of interaction and site of scattering is denoted by (a), n_e the number of electrons per unit volume in the phantom, dσ/dω is the Klein-Nishina cross section for scattering a photon through angle ϴ expressed per electron and per unit solid angle. The linear attenuation coefficient for the scattered radiation is denoted by μ' and b

the path length from the scattering site to point Q. The mass attenuation coefficient for the scattered radiation is denoted by μ'/ρ and $\overline{E}'_{ab}$ is the average energy absorbed from each interaction of the scattered photons.

The denominator in equation 2.39 is the absorbed dose from primary and once-scattered photons in a small (reference) mass of phantom material of radius d_m in air. The integral $\int_v ds$ is the same as the integral in the numerator but the integration is over the small (reference) volume ν. If equation 2.39 is applied to the beam in figure 2.2a on the left with beam radius r and the phantom density is ε relative to water, the attenuation coefficients of the phantom material can be expressed in terms of the attenuation coefficients of water so that $\mu = \mu_w\varepsilon$. In the same way $n = n_w\varepsilon$, and μ/ρ, μ'/ρ, $\overline{E}_{ab}$, $\overline{E}'_{ab}$ are not altered. The exponents would then become $\mu_w\varepsilon d$, $\mu_w a$ and $\mu'_w\varepsilon b$. The scaling of all linear dimensions with ε is possible resulting in $\mu_w\varepsilon d = \mu_w d_w$, etc. The volume element dV may also become dV_w/ε^3. Rearrangement of equation 2.39 gives

$$T(d,r)_1 = T(d_w, FS_w)_1 = \frac{1}{A_{eq}}\left(e^{-\mu_w d_w} + \frac{1}{\frac{\mu}{\rho}\overline{E}_{ab}} \times \int_{V_w} e^{-\mu_w a_w} n_w \frac{d\sigma}{d\omega}\frac{e^{-\mu_w' b_w}}{b_w^2}\frac{\mu'}{\rho}\overline{E}'_{ab}\, dV_w \right) \quad (2.40)$$

This method assumes that it is possible to find an "equivalent" homogeneous medium for dose calculations in an inhomogeneous medium with a relative electron density $\rho_e^{'}$, and that a correction factor can be obtained accordingly using an "equivalent" tissue-air ratio

$$C = \frac{T(d', \hat{r})}{T(d, r)} \tag{2.41}$$

with d the depth of the point of calculation and r the radius of an equivalent circular field used in the calculation. Variables d' and $\hat{r}$ are the scaled versions of these two parameters. $T(d', \hat{r})$ can be determined by considering the primary and scattered components separately.

The ETAR is suited to utilize CT data. If one defines the beam radius as $\hat{r} = r\hat{\varepsilon}$ and $\tilde{\varepsilon} = \frac{\sum_i \sum_j \sum_k \varepsilon_{ijk} w_{ijk}}{\sum_i \sum_j \sum_k w_{ijk}}$ with ε_{ijk} the relative electron densities of pixels in a series of CT images of the irradiated volume. w_{ijk} is a set of weighted factors which express the relative importance of the ε_{ijk} elements (voxels) in affecting the dose due to scattered radiation at the point of calculation. The weighting factors are considered through integration over an area. The integration over the whole irradiated volume requires extensive calculation times, but can be significantly reduced by coalescing the CT slices into a single effective slice, which produces the same scattering as all the slices taken together. Figure 2.3 illustrates this procedure when the dose is calculated in the shaded CT slice. A weighting factor, w_k, is assigned to each slice resulting in the coalesced slice consisting of the weighted average of all pixels that have the same i and j indices:

$$\hat{\varepsilon}_{ij} = \frac{\sum_{k} \varepsilon_{ijk} w_k}{\sum_{k}^{s} w_k} \tag{2.42}$$

Weighting factors, w_k, are determined by the difference of two scatter-air ratio values.

$$w_k = SAR(d_{ref}, r_2) - SAR(d_{ref}, r_1) \tag{2.43}$$

with r_1 and r_2 the radii of equivalent circular beams and d_{ref} the reference distance to the point of measurement, being 10 cm in this case.

The coalesced plane is considered to be at an effective distance Z_{eff} from the plane of calculation. The weighted average density and thus the equivalent beam radius and the consequent equivalent tissue-air ratio, is performed for each of the points at which dose calculations are made:

$$\hat{r} = r\hat{\varepsilon} = r \frac{\sum_{i}\sum_{j} \hat{\varepsilon}_{ij} w_{ij} Z_{eff}}{\sum_{i}\sum_{j} w_{ij} Z_{eff}} \tag{2.44}$$

This method takes the densities and size of structures in an irradiated medium into account to some extent, as well as their position with respect to the point of calculation. It also considers the shape of the external contour on the exit side of the beam in the form of an inhomogeneity. Loss of electronic equilibrium is not modeled near interfaces

between structures and is the major remaining shortcoming of this method of dose calculation.

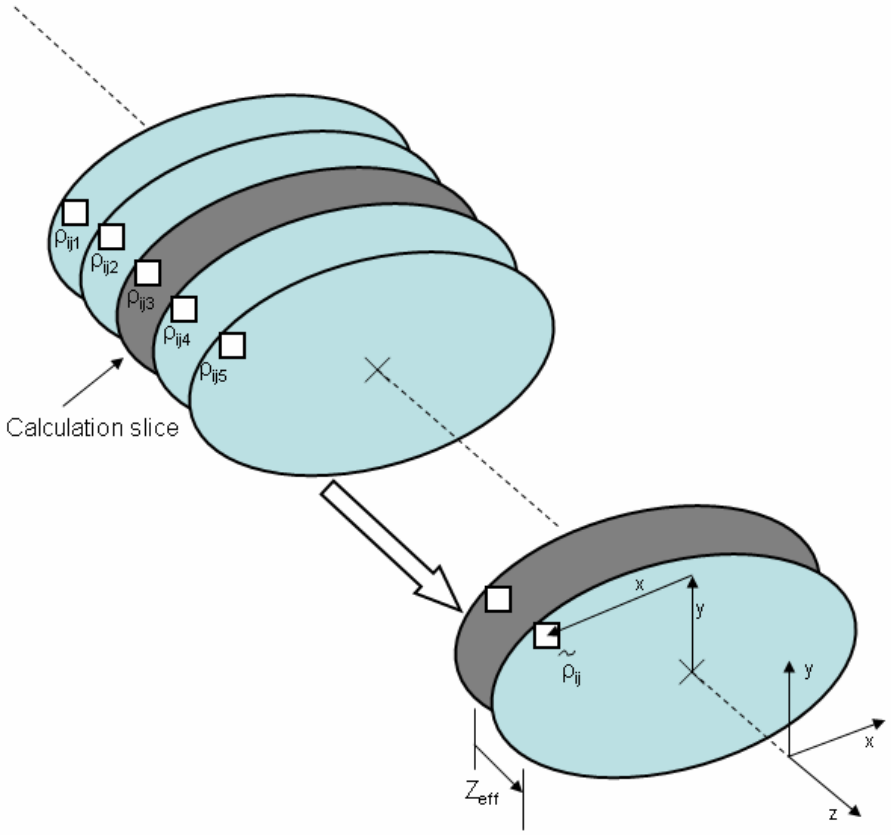

Figure 2.3: Schematic representation of the ETAR calculation methodology. A slice in which the dose is calculated is displayed along with the surrounding CT slices. A pixel at location i,j is shown on each slice. On the right it is shown that 5 slices can be coalesced into one effective slice at a distance Z_{eff} from the calculation slice. The effective density of the pixels depicted in the 5 slices becomes $\tilde{\rho}_{i,j}$.

2.7.6. Differential scatter-air ratio method

Cunningham[83] suggested, based on the work of Beaudoin[84], to use TARs to derive scatter-air ratios that can be used to calculate the absorbed dose at a point in an inhomogeneous medium. If the dose due to radiation having an interaction in a volume element at a distance above (or below) the point of interest is firstly calculated, as well as which fraction of that scattered dose reaches the point of interest, the total dose can be calculated. A differential of the scatter-air ratio (SAR) is calculated to describe the total amount of scattered radiation reaching a calculation point from this volume element. This method separates primary and scatter dose by explicitly summing the dose from scatter elements and adding this to the primary dose.

The ratio of the effective tissue-air ratio at the calculation point, $\overline{\overline{TAR}}$, to the tissue-air ratio for the equivalent square field size at d_{max}, $TAR(d_{max},r_{eq})$, is used to calculate the dose

$$D(P) = D_0 \frac{\overline{\overline{TAR}}}{TAR(d_{\max}, r_{eq})} \tag{2.45}$$

with D_0 the dose at d_{max} for the equivalent square field. $\overline{\overline{TAR}}$ is the sum of TAR(d',0) and an effective scatter-air ratio:

$$\overline{\overline{TAR}} = TAR(d',0) + \overline{\overline{SAR}} \tag{2.46}$$

The procedure is shown in figure 2.4 with the dose calculated at point P. The dose to point P as a result of scatter is the sum of scattered dose from all voxels in the irradiated volume.

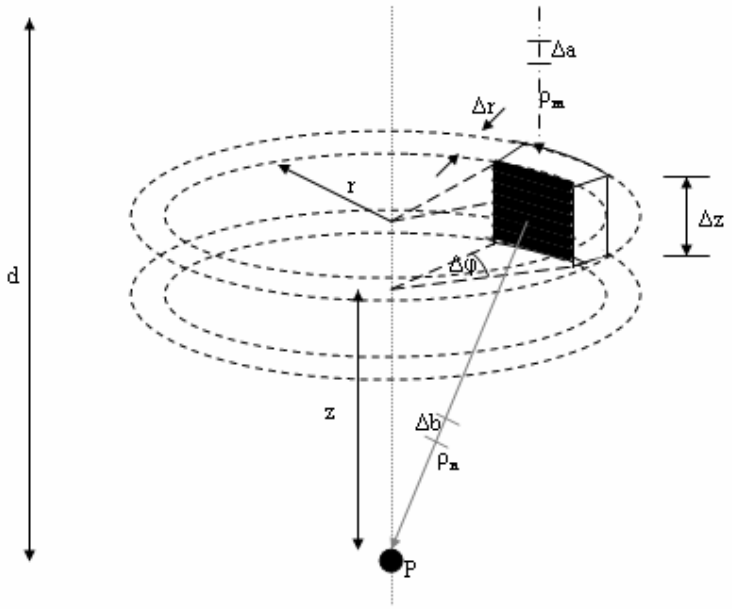

Figure 2.4: Schematic representation of the parameters involved in deriving the differential scatter-air ratio data. It shows a scattering element of volume $r\Delta\varphi\Delta z\Delta r$ at coordinates (z,r,φ) with respect to the dose calculation point P at a depth of z. Point P is on the axis of a circular beam with radius $r + \Delta r$. The differential scatter-air ratio for this value of z and r is a measure of the radiation that interacts first in this volume and eventually reaches point P. Attenuation corrections are made for primary photons reaching the scattering element and for scattered photons traveling to the calculation point using the density elements along these paths.

The second term in equation 2.46 is the sum of all differential scatter-air ratio values, $DSAR(d,z,r,\varphi)$, for elements within the volume. The depth of the calculation point is denoted by d with the scattering element a distance z above that point, at a radius r and

azimuthal angle φ. The scattering element has a density ρ(d,z,r,φ) and $\overline{SA}\overline{R}$ is calculated through:

$$\overline{SA}\overline{R} = \sum_{z}\sum_{r}\sum_{\varphi}\overline{D}\overline{SA}\overline{R}(d,z,r,\varphi) \tag{2.47}$$

An attenuation correction can be made to the effective differential scatter-air ratio for inhomogeneity effects on the primary fluence at the scattering element:

$$\overline{D}\overline{SA}\overline{R}(d,z,r,\varphi) = DSAR((d,z,r,\varphi)\times\rho(d,z,r,\varphi)\times\exp\left(\mu_0\Delta a\sum(1-\rho_m)\right) \tag{2.48}$$

where μ_0 is the attenuation coefficient of water, Δa is the incremental step size in a ray line tracing from the surface to the calculation point along the direction of the primary beam and ρ_m is the electron density of elements along this line. The perturbation in attenuation of scattered photons is also taken into account:

$$\overline{D}\overline{SA}\overline{R}(d,z,r,\varphi) = DSAR((d,z,r,\varphi)\times\rho(d,z,r,\varphi)\times\exp\left(\mu_0\Delta a\sum(1-\rho_m)\right)\times\exp\left(\mu_1\Delta b\sum(1-\rho_n)\right) \tag{2.49}$$

The attenuation coefficient of first-scattered photons in water is μ_1 and the density of element n with length Δb along a line from the scattering element to the calculation point is ρ_n. This results in treatment of all scatter as first scatter, but experimentally derived

SAR values are used and thus all orders of scattered radiation will be included in the DSAR value.

A further deficiency in this method is that perturbations in backscatter cannot be explicitly accounted for as the dose is calculated in a forward scatter manner.

The Delta Volume method[85] is similar to the DSAR method, but first and multiple scattered doses are separated. The main advantage here is seen at lower energies where multiple scattered dose makes a significant contribution to absorbed dose. First scatter is calculated analytically using Compton scattering cross sections to calculate the scattering angles of primary photons and the density of volume elements along a ray line from the scattering element to the dose calculation point to obtain the perturbation in scattered photon attenuation. The density values in pixels along a ray line from the surface to the scattering element is also used to account for modifications to the primary photon fluence. Multiple scatter dose is equivalent to multiple scatter dose in water. This is determined from the difference in measured SAR values and the calculated first scatter component. Total scatter is thus forced to be correct for a water medium. Perturbations to multiple scattered dose due to inhomogeneities are calculated via the measured perturbation caused by a small void at the position of the inhomogeneity and from the average density of the irradiated medium. Scatter from behind the dose calculation point can in this case be considered and is an improvement over the DSAR method. Unfortunately this method requires long computation times and electronic equilibrium is assumed leading to errors when electronic disequilibrium is found with inhomogeneities.

2.8. Dose calculation verification

Performing accurate dose measurements in phantoms are usually difficult and time consuming if an acceptable level of accuracy needs to be achieved. This is especially true where large dose gradients are found (like penumbra areas) as most detectors, electronic or solid state (like TLDs) have finite sizes[77]. Some researchers have opted to rather use film dosimetry which is suitable at higher x-ray energies[77,86-87] without a pronounced energy dependence resulting in over- or under responses. The error in the registration of the film to the treatment planning dose distributions would need to be <3 mm to clearly demonstrate a distance to agreement of 3 mm. On the other hand, TLD measurements are accurate in the order of 3-5%[88]. Orientations of film with respect to the CT scanning plane can also sometimes differ by a few degrees and setup uncertainty with phantoms may also be of the order of 1-2 mm. As shown by McDermott et. al.[89] a comparison of a TPS dose distribution with MC dose distributions, the accuracy of dose distribution registration is excellent compared to other measuring methods.

Many authors have suggested that MC simulations could be used as a method of dose calculation verification. Some institutions are now using MC methods for treatment planning[30,31,33,35,37,39,90,91]. The advantage of using MC simulations for verification purposes is the flexibility of the software to use patient CT data to simulate particle interactions for a large range of absorbing media. The accuracy achievable with these simulations makes MC methods the method of choice in this study, especially the fact

that 3D dose distributions produced on the CadPlan TPS and those by MC can be compared on the patient CT dataset, as if comparing to different TPSs.

2.9. Treatment plan evaluation by means of the Equivalent Uniform Dose (EUD)

Niemierko[92] stated that for any homogeneous dose distribution delivered to a volume of interest according to a certain fractionation scheme, there exists a unique uniform dose distribution delivered in the same number of fractions, over the same total time, which causes the same biological effect. Models of TCP and NTCP provide a quantitative biophysical measure of dose distributions, but their predictive power has not yet been proven clinically[93-95]. Their application without full understanding of the underlying biological mechanisms, the assumptions and the range of their application, could be discouraged if they are not robust against the population averages applicable to experimental data and should be invariant under scaling operations of the dose and the irradiated volume.

The Equivalent Uniform Dose (EUD) is a phenomenological concept that can be used to address the problem of reporting and quantitatively comparing inhomogeneous dose distributions for target volumes. The EUD concept is very useful, especially in a study like this one where differences between 3D dose distributions and 2D DVHs are compared and summed up in a single value to address differences in dose calculations and could even be used for calculation of therapeutic ratios using TCP and NTCP data. It

is defined as the dose, when distributed uniformly across the target volume, causes the survival of the same number of clonogens as the survival from a non-uniform dose distribution. Each non-uniform dose distribution must thus have such an Equivalent Uniform Dose. The formula for the EUD is:

$$EUD(Gy) = D_{ref} \frac{\ln\left[\sum_{i=1}^{N} \upsilon_i \cdot (SF_2)^{D_i / D_{ref}}\right]}{\ln(SF_2)} \tag{2.50}$$

or

$$EUD(Gy) = D_{ref} \frac{\ln\left[\frac{1}{N}\sum_{i=1}^{N} (SF_2)^{D_i / D_{ref}}\right]}{\ln(SF_2)} \tag{2.51}$$

Equation 2.50 is used when the EUD is calculated from a DVH where υ_i is the partial volume corresponding to dose D_i in that partial volume. SF_2 is the survival fraction of the clonogens at a reference dose D_{ref} of 2 Gy. If equation 4.12 is used utilizing the target dose calculation points within the target volume, N is the total number of dose calculation points. The summation in both equations is to incorporate the overall survival fraction as a weighted average of the survival fractions taken over N near-homogeneously irradiated subvolumes or dose calculation points of the target.

The EUD calculation can be extended to include absolute volume effects, non-uniform spatial distribution of clonogens, dose-per-fraction effects, cell proliferation effects and inhomogeneity of patient populations. This simplest one parameter model (equation 2.50)

shows predictions very similar to the predictions of the more complex models that include the dose per fraction effect and inter patient heterogeneity. The EUD concept stems from basic radiobiological principles and is simple and easy to use for reporting doses actually delivered to patients under actual treatment conditions and takes into account the unavoidable inhomogeneity of clinical dose distributions. It seems to be a better single predictor of outcome of radiotherapy than several other strictly dosimetric measures commonly used[92]. The dose volume histogram data from the CadPlan and DOSXYZnrc distributions were used for calculation of the EUD in the clinical cases.

References

1. Emami B., Lyman J., Brown A., Coia L., Goitein M., Munzenrider J.E., Shank B., Solin L.J. and Wesson M., " Tolerance of normal tissue to therapeutic irradiation", Int. J. Radiatiation Oncology Biol. Phys. **21**, 109 – 122 (1991).

2. International Commission on Radiological Units and Measurements. "Prescribing, Recording and Reporting Photon Beam Therapy," ICRU Report 50. Bethesda, MD: ICRU (1993).

3. Metcalf P., Kron T. and Hoban P., "The Physics of Radiotherapy X-Rays," Medical Physics Publishing, Madison, Wisconsin, (1997).

4. Niemierko A., "Reporting and analyzing dose distributions: A concept of equivalent uniform dose", Med. Phys. **24**, 103 – 110 (1997).

5. Brahme A., Agren A.K., "Optimal dose distribution for eradication of heterogeneous tumors", Acta Oncologica 26, 337 – 385 (1987).

6. Mijnheer B.J., "Dose Calculations in Megavoltage Photon Beams: The Role of NCS", Klinische Fysica **2**, 10-14 (2002).

7. Venselaar J., Welleweerd H., “Application of a test package in an intercomparison of the photon dose calculation performance of treatment planning systems used in a clinical setting”, Rad Onc **60,** 203-213 (2001).

8. Brahme A, “Dosimetric precision requirements in radiation therapy”, Acta Radiologica Oncology **23**, 379 – 391 (1984).

9. Mijnheer B.J., Battermann J.J. and Wambersie A., “What degree of accuracy is required and can be achieved in photon and neutron therapy?”, Rad. Onc. **8**, 237-252 (1987).

10. Brahme A, Ed., “Accuracy requirements and quality assurance of external beam therapy with photons and electrons”, Stockholm, Acta Oncologica, ISBN 1100-1704 (1988).

11. Haryanto F., Fippel M., Laub W., Dohm and Nusslin F., “ Investigation of photon beam output factors for conformal radiation therapy – Monte Carlo simulations and measurements”, Phys. Med. Biol. **47**, N133-N143 (2002).

12. Arnfield M.R. , Siantar C.H., Siebers J., Garmon P., Cox L. and Mohan R., “The impact of electron transport on the accuracy of computed dose”, Med Phys **27**, 1266-1274 (2000).

13. Jones B., Aird E., Colyer H, Dobbs J, Harris R., Hoskins P., McKenzie A. and West C., “Commentary: United Kingdom Radiation Oncology 1 Conference (UKRO 1): Accuracy and uncertainty in radiotherapy”, Brit J Rad, **75**, 297–306 (2002).

14. Engelsman M., Damen E.M.F., Koken P.W., Van`t Veld A.A., Van Ingen K.M. and Mijnheer B.J., “Impact of simple tissue inhomogeneity correction algorithms on conformal radiotherapy of lung tumours”, Rad. Onc. **60**, 299 – 309 (2001).

15. Hurkmans C., Knoos T., Nilsson P., Svahn-Tapper G. and Danielsson H., “Limitations of a Pencil Beam approach to photon dose calculations in the head and neck region”, Rad. Onc **37**,74 – 80 (1995).

16. AAPM American Association of Physicists in Medicine “COMPREHENSIVE QA FOR RADIATION ONCOLOGY”, Report No. **40**, College Park, USA (1994).

17. Fraass B., Doppke K., Hunt M., Kutcher G., Starkschall G., Stern R. and Van Dyke J., “Quality assurance for clinical radiotherapy treatment planning”, AAPM American Association of Physicists in Medicine, Radiation Therapy Committee Task Group 53, Med. Phys. 25, 1773-1829 (1998).

18. Leszczynski K.W. and Dunscombe P.B., “Independent corroboration of monitor unit calculations performed by a 3D computerized planning system”, J. APPL. CLIN. MED. PHYS. **4**, 120-125 (2000).

19. Venselaar J., Welleweerd H. and Mijnheer B., “Tolerances for the accuracy of photon beam dose calculations of treatment planning systems”, Rad. Onc. **60**, 191-201 (2001).

20. Venselaar J. and Welleweerd H., “Application of a test package in an intercomparison of the photon dose calculation performance of treatment planning systems used in a clinical setting”, Rad Onc **60**, 203-213(2001).

21. Ahnesjö A. and Aspradakis M.M., “Dose calculations for external photon beams in radiotherapy”, Phys. Med. Biol. **44,** R99–R155 (1999).

22. ICRU Report 42, “Use of Computers in External Beam Radiotherapy Procedures with High Energy Photons and Electrons”, Bethesda, Maryland USA (1987).

23. Khan F.M., “The Physics of radiation therapy”, Lippincott Williams & Wilkens, Third Ed., Philadelphia, USA (2003).

24. Van de Geijn J. and Fraass B.A., “The net fractional depth dose: A basis for a unified analytical description of FDD, TAR, TMR, and TPR”, Med. Phys **11**, 784 – 793 (1984).

25. Johns H.E., Cunningham J.R., “The Physics of Radiology”, Charles C Thomas, Springfield, Illinois (1983).

26. Ahnesjö A. and Andreo P., “Determination of effective brehmsstrahlung spectra and electron contamination for photon dose calculations”, Phys. Med. Biol. **34**, 1451-1464 (1989).

27. Ahnesjö A., Andreo P. and Brahme A., “Calculation and application of point spread functions for treatment planning with high energy photon beams”, Acta. Oncol. **26**, 49-56 (1987).

28. Storchi P. and Woudstra E., “Calculation of the absorbed dose distribution due to irregularly shaped photon beams using pencil beam kernels derived from basic beam data”, Phys. Med. Biol. **41**, 637-656 (1996).

29. Ma C.M., Faddegon B.A., Rogers D.W.O. and Mackie T.A., “Accurate characterization of Monte Carlo calculated electron beams for radiotherapy”, Med. Phys. **24**, 401 – 416 (1997).

30. Jiang S.B., Kapur A., and Ma C.M., “Electron beam modeling and commissioning for Monte Carlo treatment planning”, Med. Phys. **27**, 180 – 191 (2000).

31. Deng J., Jiang S.B., Kapur A., Li J., Pawlicki T. and Ma C.M., “Photon beam characterization and modeling for Monte Carlo treatment planning”, Phys. Med. Biol. **45**, 411 – 427 (2000).

32. Fix M.K., Stampanoni M., Manser P., Born E.J., Mini R. and Ruegsegger P., “A multiple source model for 6MV photon beam dose calculations using Monte Carlo”, Phys. Med. Biol. **46**, 1407 – 1427 (2001).

33. Fippel M, “Fast Monte Carlo dose calculation for photon beams based on the VMC electron algorithm”, Med. Phys. **26**, 1466 – 75 (1999).

34. Kawrakow I., Fippel M. and Friedrich K., “3D electron dose calculation using a voxel based Monte Carlo algorithm (VMC)”, Med. Phys. **23**, 445 – 57 (1996).

35. Keall P.J. and Hoban P.W., “Super-Monte Carlo: a 3D electron beam dose calculation algorithm”, Med. Phys. **23**, 2023 – 34 (1996).

36. Lovelock D.M.J., Chui C.S. and Mohan R.A., “Monte Carlo model of photon beams used on radiation therapy”, Med. Phys. **22**, 1387 – 94 (1995).

37. Neuenschwander H. and Born E.J., “A macro Monte Carlo method for electron beam dose calculations”, Phys. Med. Biol. **37**, 107 – 25 (1992).

38. Sempau J., Wilderman S.J. and Bielajew A.F., “DPM, a fast, accurate Monte Carlo code optimized for photon and electron radiotherapy treatment planning dose calculations”, Phys. Med. Biol. **45**, 2263 – 391 (2000).

39. Rogers D.W.O., Faddegon B.A., Ding G.X., Ma C.M. and We J., “BEAM: a MC code to simulate radiotherapy treatment units”, Med. Phys. **22**, 503 – 25 (1995).

40. Mackie T.R., El-Khatib E., Battista J.J. and Scrimger J.W., “Lung dose corrections for 6- and 15-MV x-rays”, Med. Phys. **12**, 327 – 332 (1985).

41. Storchi P. and Woudstra E, “Calculation of the absorbed dose distribution due to irregularly shaped photon beams using pencil beam kernels derived from basic beam data”, Phys. Med. Biol. **41**, 637-656 (1996).

42. Mackie T.R., Scrimger J.W. and Battista J.J., “A convolution method for calculating dose for 15MV x-rays”, Med. Phys. **12**, 188 – 196 (1985).

43. Ahnesjo A., Saxner M. and Trepp A., “A pencil beam model for photon dose calculation”, Med. Phys. **19**, 263 – 273 (1992).

44. Mohan R. and Chui C., “Use of fast Fourier transforms in calculating dose distributions for irregularly shaped fields for three-dimensional treatment planning”, Med. Phys. **14**, 70 – 77 (1987).

45. “External Beam Modelling Configuration Manual”, CadPlan 6.2, (Varian Medical Systems, Inc., Palo Alto, CA 94304) (2000).

46. Ulmer W., Pyyry J. and Kaissl W., “A 3D photon superposition/convolution algorithm and its foundation on results of Monte Carlo calculations”, Phys. Med. Biol. **50**, 1767–1790 (2005).

47. Cunningham J.R., “Tissue inhomogeneity corrections in photon beam treatment planning”, Progress in Medical Radiation Physics, Chapter 2; Ed. Colin G Ortin, 103 – 131 (1982).

48. Boyer A.L. and Mok E.C., “Calculations of photon dose distributions in an inhomogeneous medium using convolutions”, Med. Phys. **13**, 503 – 509 (1986).

49. Ahnesjö A. and Andreo P., “Determination of effective brehmsstrahlung spectra and electron contamination for photon dose calculations”, Phys. Med. Biol. **34**, 1451-1464 (1989).

50. Ahnesjö A. and Trepp A., “Acquisition of the effective lateral energy fluence distribution for photon beam dose calculations by convolution models”, Phys. Med. Biol. **36**, 973 – 985 (1991).

51. Ahnesjö A., “Analytic modeling of photon scatter from flattening filters in photon therapy beams”, Med. Phys. **21**, 1227-1235 (1994).

52. Mackie T.R., Scrimger J.W. and Battista J.J., “A convolution method of calculating dose for 15MV x-rays”, Med. Phys. **12**, 188 – 196 (1985).

53. Mohan R., Chui C. and Lidofsky L., “Differential pencil beam dose computation model for photons”, Med. Phys. **13**, 64-73 (1986).

54. Ahnesjö A., “Collapsed cone convolution of radiant energy for photon dose calculation in heterogeneous media”, Med. Phys **16**, 577 – 592 (1989).

55. Storchi P.R.M., van Battum L.J. and Woudstra E., “Calculation of a pencil beam kernel from measured photon beam data”, Phys. Med. Biol. **44**, 2917–2928 (1999).

56. Cunningham J.R., “Scatter-Air Ratios”, Phys. Med. Biol. **17**, 42 – 51 (1972).

57. Sontag M.R. and Cunningham J.R., “The equivalent tissue-air ratio method for making absorbed dose calculations in a heterogeneous medium”, Radiology **129**, 787 – 794 (1978).

58. Siddon R.L., “Calculation of the radiological depth”, Med. Phys **12**,84 – 87 (1985).

59. CadPlan 6.0 (Varian Medical Systems, Inc., Palo Alto, CA 94304), External Beam Modelling Physics Manual (1999).

60. du Plessis F.C.P. and Willemse C.A., “Monte Carlo calculation of effective attenuation coefficients for various compensator materials” Med. Phys. **30**, 2537-2544 (2003).

61. Sethi A., Leybovich L., Dogan N. and Glasgow G., “Effectiveness of compensating filters in the presence of tissue inhomogeneities” J. Appl. Clin. Med. Phys. **4**, 209 – 216 (2003).

62. Ahnesjö A., Weber L. and Nilsson P., “Modeling transmission and scatter for photon beam attenuators” Med. Phys. **22**, 1711-1720 (1995).

63. Castellanos M.E. and Rosenwald J.C., “Evaluation of the scatter field for high energy photon beam attenuators”, Phys. Med. Biol. **43,** 277-290 (1998).

64. Papiez E. and Froese G., “The calculation of transmission through a photon beam attenuator using sector integration” Med. Phys. **17**, 281-290 (1990).

65. Metcalf P.E., Hoban P.W., Murray D.C. and Round W.H., “Modeling polychromatic high energy photon beams by superposition”, Aust. Phys. Eng. Sci. Med. **12**, 184 – 194 (1989).

66. Aspradakis M.M., Morrison R.H., Richmond N.D. and Steele A., " Experimental verification of convolution/superposition photon dose calculations for radiotherapy treatment planning", Phys. Med. Biol. **48**, 2873-2893 (2003).

67. Boyer A., and Mok E., "A photon dose distribution model employing convolution calculations", Med. Phys. **12**, 169 – 177 (1985).

68. Weber L., "Photon dose calculations in a fluence based treatment planning system", Ph.D Thesis, Lund University, Sweden (2003).

69. Hasenbalg F., Neuenschwander H., Mini R. and Born E.J., "Collapsed cone convolution and analytical anisotropic algorithm dose calculations compared to VMC++ Monte Carlo simulations in clinical cases", Phys. Med. Biol. **52**, 3679–3691(2007).

70. Wieslander E., Knoos T., "A virtual accelerator for verification of treatment planning systems", Phys. Med. Biol. **45,** 2887-2896 (2000).

71. Chui C, Mohan R, "Off-center ratios for three dimensional dose calculations", Med. Phys. **13**, 409-412 (1986).

72. Milan J. and Bentley R.E., "The storage and manipulation of radiation dose data in a small digital computer", Br. J. Radiol. **45,** 115-121 (1974).

73. Storchi P. and Woudstra E., “Calculation models for determining the absorbed dose in water phantoms in off-axis planes of rectangular fields of open and wedged photon beams”, Phys. Med. Biol. **40**, 511-527 (1995).

74. Lam W. and Lam K., “Error in off-axis treatment planning for a 4MeV machine”, Med. Phys. **10**, 480 – 482 (1983).

75. Schwarz M., Bos L., Mijnheer B.J., Lebesque J.V. and Damen E.M.F., “Importance of accurate dose calculations outside segment edges in intensity modulated radiotherapy treatment planning”, Rad. Onc. **69**, 305–314 (2003).

76. Worthley B., “Equivalent square of rectangular fields”, Br. J. Radiol. **39,** 559 (1966).

77. Attix F.H., “Introduction to radiological physics and radiation dosimetry”, John Wiley, New York (1986).

78. Sontag M.R., Battista J.S., Bronskill M.J. and Cunningham J.R., “Implications of computed tomography for inhomogeniety corrections in photon beam dose calculations”, Radiology **124**, 143-149 (1977).

79. Du Plessis F.C.P., Willemse C.A., Lötter M.G. and Goedhals L., “The indirect use of CT numbers to establish material properties needed for Monte Carlo calculation of dose distributions in patients”, Med. Phys. **25**, 1195 – 1201 (1998).

80. Battista J.J. and Sharpe M.B., “True three dimenstional dose computations for megavoltage x-ray beams”, Australas. Phys. Eng. Sci. Med. **15**, 159-178(1992).

81. Kornelsen R.O. and Young M.E.J., “Changes in the dose profile of a 10MV x-ray beam within and beyond low density material”, Med. Phys. **9**, 114 – 116 (1982).

82. Batho H.F., “Lung corrections in Cobalt 60 beam therapy”, J. Can. Assoc. Radiol. **15**, 79-83 (1964).

83. Cunningham J.R., “Scatter-air-ratios”, Phys Med Biol **17**, 42-51 (1972).

84. Beaudon L., M.Sc. Thesis, University of Toronto (1968).

85. Wong J.W., Henkelman R.M., “A new approach to CT pixel based photon dose calculations in heterogeneous media”, Med. Phys. **10**, 199 – 208 (1983).

86. Robar J.L. and Clark B.G., “The use of radiographic film for linear accelerator stereotactic radiosurgical dosimetry”, Med. Phys. **26**, 2144-2150 (1999).

87. Cheng C.W. and Das I.J., “Dosimetry of high energy photon and electron beams with CEA films”, Med. Phys. **23**, 1225-1232 (1996).

88. Duggan L., Hood C., Warren-Forward H., Haque M. and Kron T., “Variations in dose response with x-ray energy of LiF:Mg,Cu,P thermoluminescence dosimeters: implications for clinical dosimetry” Phys. Med. Biol. **49**, 3831 – 3845 (2004).

89. McDermott P.N., He T. and De Young A., “Dose calculation accuracy of lung planning with a commercial IMRT TPS”, J. Appl. Clin. Med. Phys. **4,** 341 – 351 (2003).

90. Du Plessis F.C.P., Willemse C.A., Lötter M.G., Goedhals L., “The indirect use of CT numbers to establish material properties needed for Monte Carlo calculation of dose distributions in patients”, Med. Phys. **25**, 1195 – 1201 (1998).

91. Ma C.M., Faddegon B.A., Rogers D.W.O. and Mackie T.A., “Accurate characterization of Monte Carlo calculated electron beams for radiotherapy”, Med. Phys. **24**, 401 – 416 (1997).

92. Niemierko A., “Reporting and analyzing dose distributions: A concept of equivalent uniform dose”, Med. Phys. **24**, 103 – 110, (1997)

93. Stavreva N., Stavrev P., Warkentin B. and Fallone B.G., “Derivation of the expressions for γ_{50} and D_{50} for different individual TCP and NTCP models”, Phys. Med. Biol. **47**, 3591 – 3604 (2002).

94. Warkentin B., Stavrev P., Stavreva N., Field C. and Fallone B.G., “A TCP-NTCP estimation module using DVHs and known radiobiological models and parameter sets”, J. Appl. Clin. Med. Phys. **5**, 50 – 63 (2004).

95. Alber M. and Nüsslin F., “A representation of an NTCP function for local complication mechanisms”, Phys. Med. Biol. **46**, 439–447 (2001).

Chapter 3

Monte Carlo Simulations

3.1. Overview

Originally Monte Carlo MC codes were developed to study nuclear disintegrations produced by high-energy particles[1]. It was later applied to study shower productions by following the fate of particles in passing through intervals of lead thickness by spinning a "wheel of chance"[2] which eventually lead to more applications to calculate radiation shielding thickness requirements [3,4] for gamma radiation in large accelerators.

Monte Carlo codes as applied in the field of medical dosimetry simulate the transport of ionizing radiation such as photons, electrons, protons and neutrons in any medium of any composition and state. This makes it one of the most accurate methods of determining absorbed dose distributions in complex geometries. It is used widely as a golden standard to provide benchmark data for dose calculations in radiotherapy. Absorbed doses are calculated in small scoring regions (voxels) from the first principles of radiation physics[5,6]. MC dose calculation is based on the random sampling of dynamic parameters constructed using cross section data to determine interaction probabilities from probability density functions to model radiation transport.

The transport of photons and electrons with a very wide range of energies (from a few keV to hundreds of GeV) can be simulated with some codes such as EGSnrc. Due to the stochastic nature of radiation a large number of particle histories must be simulated to reduce the statistical variance in small voxels (scoring regions) to increase dose distribution accuracy. Unfortunately this leads to long simulation times. This problem can however be addressed today as MC simulations can be carried out on relatively fast personal computers and inexpensive cluster systems.

3.2. Accuracy of MC simulations

It has been shown that MC can be used to determine the absorbed dose in any medium with a high level of accuracy[5-15]. Many authors have been able to reproduce measured beam data of linear accelerators with MC simulations within low uncertainty values. This has also proven the MC dose calculation technique to be general enough to handle existing and future radiation treatment techniques. Although it is still time consuming, the computers[16,17] that are available today along with the development of variance reduction techniques have enabled MC simulations to be used for routine dose calculation. The potential for MC techniques to improve treatment planning is enormous, specifically considering the degree of accuracy achieved, and that this level of accuracy is better than the current state-of-the-art kernel techniques[12,13,17-27].

The EGS-group of MC codes simulate photon and electron transport based on basic physical processes to obtain particle trajectories. These particle trajectories are a faithful simulation of physical reality where particles lose energy and others are created by interaction processes. The transport of such an individual particle is modeled either until its energy is exhausted or it has left the geometry of interest. This is called a particle history. Each transport step in the particle history is determined by a random selection of dynamic variables such as its energy and direction through sampling from probability distributions. During the simulation the particle transport parameters are stored in a stack of variables. This means that after each step, the stack will be updated.

Once the stack has been updated, the most recent particle will be transported and the random sampling process starts again to determine its dynamic variables. There are different types of particle interactions that can take place[29] and these are chosen through random sampling according to the branching ratio method. The probability of an interaction occuring is governed by the energy of the particle as well as the medium through which the particle is transported. E.g. for Compton interactions the new direction of the scattered photon transport is determined from the Klein-Nishina cross section data tables. Depending on the type of interaction that was selected, new particles can also be created (example: pair production) and their position, direction and energy are added to the stack and each of their steps are also simulated until they have deposited all of their energy or left the medium of interest.

MC transport simulations are usually divided into batches where each one contains the same number of histories. The absorbed dose or other quantities of interest that are scored, are the average value of the batches. In EGS4, the uncertainty in dose is given as a percentage of the mean dose per batch. If say, 1 million histories were simulated, ten batches of 100 000 histories will be used and the average value of the batches will be used to calculate the uncertainty. As the simulation is based on random sampling, there is an associated statistical variance with the scored values e.g. the calculated absorbed dose in a region. In order to minimize the variance in dose, a large number of histories have to be simulated.

The EGSnrc codes have been developed to incorporate many different geometries that can be specified by the user for various radiation transport applications. It is a general purpose package for the simulation of coupled electron and photon transport. It is based on the EGS4 code system but includes a variety of enhancements on condensed history implementation. It has been extensively used for the study of Co-60 gamma-ray beams and high energy linear accelerators[7-11,13-15,18,19]. Some researchers have used it in other dosimetric applications to study the properties of dosimeters in specific radiotherapy measurements[29-31]. Because of the time constraints associated with its use, some have done quantitative benchmarks to evaluate the speed of simulations on various hardware and software platforms[16].

One of the main improvements from EGS4 to EGSnrc is the history by history method[32] for estimating uncertainties. This method replaced the EGS4 method of using statistical

batches. The new method groups scored doses (or other quantities of interest like fluence) by primary history and determines the root mean square standard deviation according to primary history grouping. It reduces the uncertainty in the uncertainty estimate by also correlating between particles stored in certain regions in the accelerator geometry during the simulation and their subsequent transport until dose calculation.

The EGSnrc system also forms the basis for transport simulation in several derivative codes like DOSXYZnrc, DOSRZnrc, FLURZnrc, CAVRZnrc, and the BEAMnrc code. DOSXYZnrc calculates 3D dose distributions in a Cartesian co-ordinate system while DOSRZnrc uses a cylindrical system. The BEAMnrc code is used for the simulation of radiotherapy treatment machines, but can also be used to score dose in a cylindrical system. In this chapter the basic operation and requirements for Monte Carlo codes will be discussed with the emphasis on the EGSnrc codes BEAMnrc and DOSXYZnrc.

The MC codes BEAMnrc and DOSXYZnrc are well benchmarked and are used widely in the medical physics environment in dosimetric applications[5,14,21]. In codes such as DOSXYZ and DOSXYZnrc, as well as MCSIM and MCDOSE, the geometry can be represented in a Cartesian space so that energy deposited can be scored in a three-dimensional array. It also enables the user to make use of CT-generated data to represent real patient geometries[5,14,33]. Radiation treatment machines on the other hand, can be accurately modeled with the MC codes BEAMnrc, MCBEAM and MCNP[5,14,15,34-39].

The main components of the EGSnrc system will now be discussed:

3.3 PEGS4 and the user codes

PEGS4 is a preprocessor code for the generation of cross section data[5,37]. Interaction cross section data is essential for the realistic and accurate simulation of coupled photon and electron transport. This program generates material dependant parameters such as scattering cross sections, mean free paths and electron stopping powers for user-defined energy ranges.

By making use of the data tables produced through the PEGS4 preprocessor a number of different processes can be simulated and the data is read in via the subroutine $HATCH in the user code before the simulation begins. These tables include cross section data on brehmstrahlung x-ray production, pair annihilation, Moliere multiple (coulomb) scattering, Møller and Bhabha scattering, pair production, incoherent (Compton) and coherent (Thompson) scattering, photoelectric absorption, continuous energy loss of electrons and radiational and collisional electron interactions. The data can be generated for user selected energies over large energy ranges.

Various materials can be specified for cross section data generation. The atomic compositions, physical density and energy range over which data must be generated for photons and electrons, are supplied by the user through input files. The diversity of this processor allows data to be generated for gasses, solids (mixtures or compositions) or

liquids. An input file is required for each material through which transport simulations are to be carried out. Output data sets used in the simulations contain a fixed number of intervals over the energy ranges required for the simulation to be done. The range should be as small as possible due to the fact that interpolations are performed over smaller interval widths.

3.4. Random numbers

The likelihood that a particular value for a dynamic variable will be chosen for e.g. a photon step length or electron scattering, etc., depends on a probability distribution determining the outcome of the event. It is important to ensure that efficient random numbers can be generated to model the stochastic nature of photons and electron transport. In a single history a very large number of simulation steps are involved and an equally and larger number of random numbers must be available with a large sequence so that the random numbers do not repeat. Computers cannot generate infinite arrays of random numbers but can generate pseudo random numbers. This means that an array of random numbers is deterministically calculated which repeats itself after a large number of steps. As long as the numbers are not re-used in such an array, the numbers will be random[40]. The EGS4 code makes use of a multiplicative congruential type of random number generator where the n-th random number is found through:

$$X_n = (aX_{n-1})_{\mathrm{mod}\ 2^k} \tag{3.1}$$

where k is the integer word size of the computer and a is a constant multiplier.

The first number in the sequence (X_0) is given by the user and is known as the random generator seed[5] which is an integer between 0 and 100. With twos-complement integer arithmetic, the random numbers range from $-2^k/2$ to $2^k/2-1$. This number is converted to a floating point number in the range 0.0 to 1.0 by multiplying by 2^{-k} and the result added to 0.5. In order for the random number generator to be of long sequence, the choice of a is important. The length of the array of numbers is determined by it and can give up to $2^{k-2} = 2^{30} \approx 10^9$ numbers on a 32-bit computer where k=32 and a = 663608941.

EGSnrc is supplied with a random number generator, RANLUX. It is a generator which comes with a variety of "luxury levels" ranging from 0 to 4 and a period of greater than 10^{165}. RANLUX is completely portable, producing the same sequences on different machines. It can be initialized and guaranteed to produce a random number sequence which is independent from other sequences and requires two initial seeds. This is very useful for doing runs in parallel on multiple machines. By default the RANLUX random number generator requires no initialization (user selected initial seed). However, to use a luxury level different from the default of 1, or a different initial seed, one must specify not to use the default values. The value of the initial seed is from 1 to 1073741824 (2^{30}), however, the initial seed values are restricted to 0 < I seed < 31328 and 0 < J seed < 30081 and 0 values are set to defaults.

As the code makes use of several variables for different functions of particle transport, it is required that this method of random sampling must be able to generate unambiguous results. Cross section generating functions involving scatter and energy loss of different particles in EGSnrc utilize a mixed method of composition and rejection techniques[30] for sampling.

3.5. Photon interactions

High energy photons, as described in the literature[28], interact with absorbing media through twelve possible types of interactions, of which five are regarded as major interaction types. Absorption and attenuation of photons are dominated by the photoelectric effect, Compton scattering and pair production. In order of decreasing energies the following photon interactions can occur in matter: Pair production interactions is the mechanism by which a photon materializes into an electron-positron pair. The photon has to travel through the electromagnetic field of the nucleus of an atom or its surrounding atomic electrons because pair production cannot occur in free space. Incoherent (Compton) scattering is a process where the photon has an interaction solely with loosely bound (free) atomic electrons, while photoelectric absorption takes place when the energy of the photon is transferred to an orbital electron and it gains enough energy to be regarded as a free electron. Lastly, coherent (Rayleigh) scattering is a process where a low energy photon has an interaction with the molecules (or atoms) of

the medium in which it finds itself. The photon only changes direction in an elastic collision process, such as the scattering of visible light photons.

At high photon energies (several MeV), pair production interactions dominate and has a cutoff of 1.022 MeV. Below this energy pair production is not a possibility because the respective rest mass of an electron or positron is 0.511 MeV. In tissue equivalent materials and at low energies up to 100 keV, the photoelectric effect dominates. Incoherent scattering interactions are the most frequent interaction type from 100 keV up to a few MeV in water. The medium on which the photons are incident also with specific energy contribute in determining the interaction type[28]. E.g. in high-Z (lead) materials the photoelectric interaction can occur at high energies compared to low-Z materials (water).

3.6. Electron interactions

Electrons undergo different interactions in materials than photons. They lose energy through radiative and collisional interactions with atomic electrons. Brehmstrahlung interactions are processes where radiative loss of energy takes place. Another process of radiative losses is through positron annihilation where the energy is actually converted back into photons and leads to the coupling of the electron and photon radiation fields. Once photons create secondary charged particles in the patient being irradiated, lower energy electrons are set in motion and they predominantly have collisional interactions. These interactions at low energies are very frequent, hundreds to thousands of times more

than the number of interactions photons undergo per unit path length. During these interactions the electrons change direction with almost no loss in energy over very short distances.

Inelastic electron collisions and the photon interactions with atomic electrons lead to excitations and ionizations of atoms where these particles have interactions along the path they travel. When the electrons in outer shells fall back to the inner shells after such excitations, photons and electrons with characteristic energies are emitted such as Auger electrons.

3.7. The Monte Carlo simulation process

3.7.1. Photon transport

3.7.1.1. Pathlength selection through random sampling

The decision on how far a photon can travel in a medium before it has an interaction is controlled by a suitable probability density function on which the number of free pathlengths can be randomly sampled.

In this case, the probability density function is normalized such that its area is unity and then integrated to give a cumulative density function that has a maximum value of 1.0.

The probability that a photon will interact is described by the total linear attenuation coefficient (μ), which in turn influences the mean free path for the particle with its current energy. In the specific medium of concern the mean free path can be described by λ, and has a relation to the linear attenuation coefficient[42], μ = 1/λ. This relation has the consequence that the smaller the total linear attenuation coefficient, the smaller the probability for any type of interaction and therefore the photon travels larger distances before it interacts with the medium. The probability density function can be given by

$$f(x) = \mu e^{-\mu x} \tag{3.2}$$

Integrating this function gives the cumulative density function

$$F(x) = 1 - e^{-\mu x} \tag{3.3}$$

where the value of F(x) ranges between 0 and 1 as x goes from 0 to infinity. This function allows sampling the distance traveled in the medium up until an interaction will take place. This unit interval is the interval over which random numbers are generated. It can be seen that the probability for any interaction to take place will increase as the photon travels larger distances, for example more than one mean free pathlength.

If a random variable is chosen between 0 and 1, the probability that the corresponding value of x will lie between x and x + dx is proportional to the gradient of F(x), being equal to f(x). This has the effect that when a pathlength is randomly selected, the

probability of an interaction being chosen decreases exponentially with x. Equation 3 therefore means that when a particle's traveled distance becomes larger (approaching infinity), the probability for an interaction to occur would approach unity.

To solve the value of x (distance to be traveled) through direct sampling of F(x) with the use of an already produced random number, r (within the interval [0,1]), equation 3.3 is written as:

$$x = -\left(\frac{1}{\mu}\right)\ln(1-r) \tag{3.4}$$

But, r and thus (1 – r) is also a random number, x is solved through:

$$x = -\left(\frac{1}{\mu}\right)\ln(r) \tag{3.5}$$

Once the value of r is known, x is determined and this is the distance traveled by the particle until the next interaction takes place.

The cross sectional data produced by the PEGS4 preprocessor is energy and material dependent and the larger the energy of the particle, the longer the mean free pathlength since μ is getting smaller. This can be observed in equation 3.5.

Once the random position of interaction has been selected through the use of the mean free pathlength, the type of random interaction is selected through the use of interaction cross section tables.

3.7.1.2. Choosing an interaction type

When a photon interaction type is to be chosen, the relative probabilities or branching ratios for each interaction are used. The branching ratio, for interaction type i, is expressed in terms of the total atomic cross section σ_t. If the range of real numbers over the closed interval [0,1] is divided into intervals of length equal to each branching ratio, the likelihood of a random variable between 0 and 1 falling in an interval corresponding to interaction i is equal to the branching ratio $\frac{\sum_i \sigma_i}{\sigma_t}$. Here, the summation over the cross section symbolizes all the interaction types that can be found when photons have atomic interactions and is normalized by the total atomic cross section.

The interaction type is therefore chosen by sampling a random number between 0 and 1 and finding the interval to which it corresponds. In this interval a random number (r) can be sampled through the inequality relation:

$$F(i-1) < r < F(i) \qquad (3.6)$$

When a random number r is sampled and the condition in 3.6 is reached, stepping through the values of *i*, the various interaction types are all possible. The different values of *i* are representative of the different types of interactions which would satisfy the equation, determining in turn the interaction type[14].

An example of determining such an interaction is when a photon with energy $h\upsilon$ has a Compton interaction by colliding with a "free" electron and transferring some of its energy, E_{tr}, to the electron. The photon is scattered during the interaction and leaves the interaction site with energy $h\upsilon - E_{tr}$. The energy transferred, photon scattering angle and initial direction of the recoil electron are determined by sampling from the Klein-Nishina probability function.

3.7.2. Electron transport

From a previous discussion on electron interactions the simulation of electron transport uses the largest amount of calculation time and it is very important to simulate it efficiently. Electrons loose their energy in the medium through collisional losses while the photon would be transported another distance before another interaction type will take place.

When charged particles, like electrons, pass in the neighborhood of a nucleus, it undergoes a change in direction through Coulomb force interactions. The appropriate scatter angle is sampled from electron elastic multiple-scattering distribution functions

like the Molière multiple scattering distributions[1,28]. The MC code makes use of complex electron interactions and the use of transport parameters are discussed in detail in the literature[41-43].

In MC simulations electrons are mostly simulated to loose their energy in a continuous way and not discretely as photons. In such an energy loss step the electron would loose a certain fraction of its energy and a discrete interaction is sampled with a new scatter angle to give an overall random path for the transported electron. Electrons are transported until they reach a user defined cutoff energy, named ECUT. ECUT is user defined and is often specified to have a value of 0.521 MeV which is the total energy of an electron in this case. This corresponds to a kinetic energy 10 keV. The energy lost by an electron in a single step is actually the product of the stopping power of the medium and the length of the step. Random sampling is again used to determine the scattering angle influenced by the scattering power and step length at a discrete interaction event such as Môller scattering.

3.7.2.1. Electron-step algorithms

The electron-step algorithm used in EGSnrc determines the algorithm that will be used to calculate lateral and longitudinal corrections which accounts for elastic scattering in a condensed history electron step. The user has an option of two algorithms, PRESTA-II (the default) and PRESTA-I. PRESTA-II is more accurate and only available in EGSnrc,

while PRESTA-I is the original PRESTA algorithm of EGS4 with some modifications. PRESTA-I has shown to underestimate lateral deflections and underestimates longitudinal straggling of electrons. It also produces a singularity in the distribution describing the lateral spread of electrons in a single condensed history.

Another variable, ESTEPE, can also be specified which is a limiting variable on the maximum fractional energy loss an electron can experience in a single step. Appropriate values should be selected for ESTEPE, not too high so that electrons will not be allowed to traverse boundaries they should, and not too low. The lower this value, the more accurate the simulation would be, but this will lead to unacceptably long simulation times. The boundary crossing algorithms employed in EGSnrc are called EXACT and PRESTA-I. PRESTA-I forces a multiple scatter event when an electron reaches a boundary. The default algorithm is EXACT which transports electrons in single elastic scattering mode as soon as they are within a distance from the boundary given by the EGSnrc input parameter, Skin Depth for boundary crossing algorithm (BCA).

If the boundary crossing algorithm is chosen to be PRESTA-I, then the Skin Depth for BCA is the perpendicular distance (in elastic mean free paths) from the boundary at which lateral pathlength corrections are turned off and the particle is transported in a straight line until it reaches the boundary. EGSnrc automatically calculates the distance at which lateral corrections are switched off. If the BCA is chosen to be EXACT, the Skin Depth for the BCA determines the perpendicular distance (in elastic mean free paths) to the region boundary at which electron transport will go into single elastic scattering

mode. A skin depth of 3 elastic mean free paths has been found to give peak efficiency in this case and is used as the default value. If the BCA is EXACT and Skin Depth for BCA is set to a very large number (eg. $1x10^{10}$), then the entire simulation will be done in single scattering mode.

PRESTA-I is however more efficient than EXACT and can be used at higher (therapy range) energies where electron fluence singularity effects (as a cause of forced multiple scattering) are small since elastic scattering is weak. It is recommended that this algorithm should not be used for low energy applications such as kV unit simulations.

The electron transport method of fractional energy loss across the volume of interest is known as a continuous slowing down approximation (CSDA). It has the potential of speeding up the simulation rather than simulating each individual electron through all of its transport steps. There is however a reduction in the randomness of such a simulation, but the EGSnrc code allows for user definable variables which allow realistic simulations within a certain energy range, and below those values the simulation will follow the CSDA. The threshold value for discrete (photon like) collisions is called AE, while the radiative energy losses threshold is the AP value. It can be understood that the lower these values, the more randomized would the simulation be. These values have to be used very carefully as their influence can be significant on the outcome of simulation results.

3.7.2.2. Electron spin algorithm

The simulation of spin effects allows elastic scattering cross-sections that take into account relativistic spin effects used in electron transport. If spin effects are switched off during the simulation, screened Rutherford cross-sections are used for elastic scattering of electrons. Results are more accurate when spin effects are simulated and is particularly important if good backscatter calculations are to be obtained. These effects can be seen in calculated depth-dose curves. Small underestimations of depth dose data can be made when backscatter through spins effects is not simulated.

3.8. EGSnrc MC user codes

3.8.1. BEAMnrc

In the EGSnrc system the user specifies the geometry of the accelerator and patient/phantom in which radiation dose needs to be calculated, or simply transported through. The BEAMnrc code can be used to model the x-ray production and collimating systems of linear accelerators by providing an input file which specifies these structural variables, as well as their composition. The code uses these input files to realize the geometry and materials for the transport simulation. In these files, planes can also be identified anywhere in between two different linear accelerator parts (or CMs) where a dataset can be generated which contains all the dynamic variables (energy, direction,

type, etc.) of each particle being transported through that plane in a phase space file. Phase space files are very large, in the range of several gigabytes. The position, energy and direction of each particle can be saved in a PSF for use in further simulations.

PSFs can also be re-used to continue the simulation of particles past the plane where they were stored in the plane of interest. As an example, a PSF can be created above a CM of the linac and it can be used as an input source of particles for several simulations of different linac treatment head configurations in subsequent simulations. All the particles coming from the accelerator treatment head can be recorded in these PSFs.

3.8.2. DOSXYZnrc

The Cartesian geometry used in DOSXYZnrc can represent a 3D dose distribution which is similar to that found in most treatment planning systems. Superimposing these 3D dose distributions on CT datasets shows the dose distribution through the use of several isodose lines on a patient CT or that of a phantom. Phantoms are constructed by specifying voxel sizes (x,y,z) and outer boundaries of the phantom in a DOSXYZnrc input file. The media for these voxels are also specified along with transport parameters, the radiation source (which can be a phase space file) and the radiation beam coordinates with respect to the position of the phantom. If patient CT models are used in these simulations, the dataset is specified in this input file along with the transport parameters, radiation source and beam coordinates.

3.9. Limitations of the MC code

The usage of large amounts of disk space and the continuous extraction of data from PSFs that have driven researchers to seek methods of speeding up the simulation process. Multiple source models have been developed needing less disc storage space, as well as variance reduction techniques to simplify particle transport and speed up simulation times. The problem of simulation speed or time used to simulate can also be overcome by making use of computer clusters to perform parallel processing in what is sometimes called a “super computer”. Some authors have achieved great success in overcoming the demand for storage space through the use of very accurate multiple source models[7-10] and variance reduction techniques which will be discussed later[11-13,18,19,47].

The use of MC in the clinical environment has been limited previously by long computation times to achieve reasonable statistical accuracy. This is especially true in the case of photon beam simulation. However, in the last couple of years there has been major development and steadfast improvements in the production of fast computers and adapted MC methods[11-13,18,19,47] which have enabled MC treatment planning in routine clinical use. These methods rely on compressed history and fast electron transport algorithms and ray tracing techniques[18] combined with detailed characterization of the beam. Some of these MC methods are 15 – 20 times faster in simulation speed than EGSnrc/PRESTA[18].

3.10. Efficiency and variance reduction

Variance reduction techniques can be used to speed up the simulation while still performing accurate transport through some assumptions. The efficiency of the simulation can be increased by reducing the variance associated with the energy deposition over a shorter time interval.

Some variance reduction techniques are achieved through the deposition of all the kinetic energy of an electron in a voxel when it does not have enough energy to be transported out of the voxel. The $HOWFAR subroutine is also used in this way to determine whether a particle would cross a voxel boundary during a single step or not. This probing method is however used in conjunction with $DNEAR, which is a variable storing the closest distance of the particle to a boundary and allows $HOWFAR to be called only when a particle is close to a boundary, before the rest of the simulation of that particle continues. The principle here is not to simulate events that are not needed, or that would not influence the final result.

Another method of performing variance reduction is through the assumption that central axis depth dose for a broad beam can be obtained by using a very narrow pencil beam and scoring the energy deposition within a radius equal to that of the broad beam. The same energy will be scored in the small volume element with an incident broad beam as would be deposited in a large volume element with an incident pencil beam. The variance reduction comes from the fact that most particles that are incident within a large radius on

the surface will not contribute to the central axis dose. On the other hand, particles incident from the narrow beam will almost all contribute to the dose within a coaxial region of larger radius. This is known as the reciprocity technique and can be used for efficiency improvements when depth dose curves, for example, are generated. This technique is not built into the code, but is a method the user can employ.

Range rejection is a method used to save computing time during simulations. The range of a charged particle is calculated and its history can be terminated (depositing all of its energy at that point) if it cannot leave the current region with its current energy. Its energy at this stage of transport must be larger than a value ECUTRR. ECUTRR is the range rejection cutoff energy which may vary from region to region depending on the type of range rejection that is implemented. To determine the range to ECUTRR, BEAMnrc calculates the range from ECUTRR to AE for each region at the beginning of the simulation. This range is equal to zero if ECUTRR is equal to AE. Once the stack has been updated and the next step of a charged particle is to be simulated, the range is subtracted from the particle's range to AE. Ranges are calculated using restricted stopping powers and, thus, represent the longest possible ranges to ECUTRR.

Range rejection introduces an approximation because, in terminating a charged particle's history and depositing all of its energy in the current region, it is assumed that any bremsstrahlung photons that would have been created by the particle, do not leave the current region. Such inaccuracies can be minimized by defining a variable representing the maximum charged particle energy (in MeV) at which range rejection is considered.

The choice of this variable (ESAVE_GLOBAL) depends on the incident beam energy and the materials that it is passing through.

Photons can also be forced to interact in specified CMs during the simulation. This option, called photon forcing, improves statistics of scattered photons when photon interactions are sparse (eg. in thin slabs of material or in materials with low density). Photons forced to interact in a CM are "split" into a number of scattered photons whose weight is equal to the probability of interaction and an unscattered photon carrying the remaining weight. The unscattered photon proceeds as if an interaction did not take place and it cannot be forced to interact any more within the specified forcing zone. Once the unscattered photon exits the forcing zone, it may interact again depending on the sampled pathlength. The scattered photon can be forced again in the forcing zone depending on how many interactions are allowed to be forced.

Bremsstrahlung photon splitting is an option which improves the statistics of bremsstrahlung photons resulting from electron interactions. BEAMnrc offers two bremsstrahlung splitting techniques, uniform bremsstrahlung splitting (UBS) and selective bremsstrahlung splitting (SBS). Both of these splitting techniques have been optimized in BEAMnrc with the addition of the Russian Roulette feature. In UBS each bremsstrahlung event produces a number of brehmsstrahlung splitted photons (NBRSPL), each having a weight equal to 1/*NBRSPL* times the weight of the electron that underwent the bremsstrahlung event. The energies and directions of each photon is sampled individually according to the relevant probability distributions. The energy of the primary

electron is decremented by the energy of just one of the photons. This must be done in order to preserve the effects on energy straggling but it does mean that energy is not conserved on a given history (the energy would have to be decremented by the average energy of the photons created) but it is conserved “on average” over many histories.

SBS is a more efficient method of bremsstrahlung splitting and can increase the efficiency by up to an additional factor of 3-4 compared with UBS, but this will vary with accelerator and end point being calculated. In contrast to UBS, in which the bremsstrahlung splitting number is fixed, SBS uses a varying bremsstrahlung splitting number. At the beginning of a simulation, an array of probabilities that a bremsstrahlung photon will be emitted into the treatment field (defined by FS and SSD) is calculated for different electron directions and energies (calculation of this array typically takes less than a minute).

Following all of the secondary charged particles created by the “split” photons increases the CPU time required for simulations. If the primary interest is in secondary electrons or their effects (eg. dose deposition), the extra computing time is obviously acceptable. But if, as is often the case, the main interest is in the bremsstrahlung photons themselves, one can reduce the CPU time while still preserving the variance reduction advantages of bremsstrahlung splitting by using a Russian Roulette technique with any charged particles generated by the split photons. Russian Roulette is implemented by giving secondary charged particles resulting from split photons a survival threshold. The survival threshold is always the inverse of the photon splitting number. Thus, in the case

of UBS, the threshold is fixed and is equal to 1/*NBRSPL*, while in the case of SBS, the survival threshold is 1/*NBR*, where NBR is the variable splitting number. Then a random number is chosen for each charged particle. If the random number is less than the survival threshold, the charged particle survives, and its weight is increased by a factor of NBRSPL (for UBS) or NBR (for SBS). Otherwise, the charged particle is eliminated. Secondary charged particles subject to Russian Roulette are electrons resulting from Compton events and photoelectric events and electrons and positrons resulting from pair production. Note that if Russian Roulette is turned on, then higher-order bremsstrahlung and annihilation photons are also split. This is because any charged particle surviving Russian Roulette has a weight higher than the photon that created it. If radiative products from this surviving charged particle are not split, then their high weight may interfere with the statistics of the original split bremsstrahlung photons. Also, splitting of higher-order bremsstrahlung and annihilation photons does not greatly increase computing time when Russian Roulette is on because most of the secondary charged particles have been eliminated.

3.11. Role of MC simulations in this study

As MC simulations have proven to be accurate in reproducing dose distributions from various linear accelerator simulations and various beam energies, it was decided to use this dosimetric tool for production of reference data with which the CadPlan TPS could be evaluated. The flexibility of the MC codes makes it possible to evaluate the TPS in all

possible treatment geometries which would otherwise have been difficult or even impossible to perform. The reference dataset could be used for the same study on other TPS as well and could be kept as a benchmarking dataset.

References

1. Goldberger M.L., “The interaction of high energy neutrons and heavy nuclei”, Phys. Rev. **74**, 1269 – 1277 (1948).

2. Wilson R.R., “Monte Carlo study of shower production”, Phys. Rev. **86**, 261 – 269 (1952).

3. Nelson W.R., Hirayama H. and Rogers D.W.O., “The EGS4 Code System” Stanford Linear Accelerator Center Report SLAC-265 (Stanford Calif) (1985).

4. Bielajew A.F., Hirayama H., Nelson W.R. and Rogers D.W.O., “History, overview and recent improvements of EGS4”, National Research Council of Canada, Report NRC-PIRS-0436 (1994).

5. Metcalf P., Kron T. and Hoban P., “ The Physics of Radiotherapy X-Rays,” Medical Physics Publishing, Madison, Wisconsin, (1997).

6. Haryanto F., Fippel M., Laub W., Dohm O. and Nusslin F., “ Investigation of photon beam output factors for conformal radiation therapy – Monte Carlo simulations and measurements”, Phys. Med. Biol. **47**, N133-N143 (2002).

7. Ma C.M., Faddegon B.A., Rogers D.W.O. and Mackie T.A., “Accurate characterization of Monte Carlo calculated electron beams for radiotherapy”, Med. Phys. **24**, 401 – 416 (1997).

8. Jiang S.B., Kapur A. and Ma C.M., “Electron beam modeling and commissioning for Monte Carlo treatment planning”, Med. Phys. 27, 180 – 91 (2000).

9. Deng J., Jiang S.B., Kapur A., Li J., Pawlicki T. and Ma C.M., “Photon beam characterization and modeling for Monte Carlo treatment planning”, Phys. Med. Biol. **45**, 411 – 27 (2000).

10. Fix M.K., Stampanoni M., Manser P., Born E.J., Mini R. and Ruegsegger P., “ A multiple source model for 6MV photon beam dose calculations using Monte Carlo”, Phys. Med. Biol **46**, 1407 – 1427 (2001).

11. Lovelock D.M.J., Chui C.S. and Mohan R.A., “Monte Carlo model of photon beams used on radiation therapy”, Med. Phys. **22**, 1387 – 94 (1995).

12. Neuenschwander H. and Born E.J., “A macro Monte Carlo method for electron beam dose calculations”, Phys. Med. Biol. **37**, 107 – 25 (1992).

13. Sempau J., Wilderman S.J. and Bielajew A.F., “DPM, a fast, accurate Monte Carlo code optimized for photon and electron radiotherapy treatment planning dose calculations”, Phys. Med. Biol. **45**, 2263 – 391 (2000).

14. Rogers D.W.O., Faddegon B.A., Ding G.X., Ma C.M. and We J., “BEAM: a MC code to simulate radiotherapy treatment units”, Med Phys **22**, 503 – 25 (1995).

15. Paena J., Franco L., Gomez F., Iglesias A., Lobato R., Mosquera J., Pazos A., Pardo J., Pombar M., Rodriguez A. and Sedon J., “Commissioning of a medical accelerator photon beam Monte Carlo Simulation using wide-field profiles”, Phys. Med. Biol **49**, 4929 – 4942 (2004).

16. Bielajew A.F. and Rogers D.W.O., “A standard timing benchmark for EGS4 Monte Carlo calculations”, Phys Med **19**, 303-304 (1992).

17. Linthout N., Verellen D., Van Acker S., Voordeckers M., Bretz A. and Storme, G, “Evaluation of dose calculation algorithms for dynamic arc treatments of head and neck tumors” Rad. Onc. **64**, 85–95 (2002).

18. Fippel M., “Fast Monte Carlo dose calculation for photon beams based on the VMC electron algorithm”, Med . Phys. **26**, 1466 – 75 (1999).

19. Kawrakow I., Fippel M. and Friedrich K., “3D electron dose calculation using a voxel based Monte Carlo algorithm (VMC)”, Med. Phys. **23**, 445 – 57 (1996)

20. Bielajew A.F. and Rogers D.W.O., “PRESTA – The parameter reduced electron step algorithm for electron Monte Carlo”, PIRS No 042, National Research Council of Canada, Ottawa (1986).

21. Ahnesjö A. and Aspradakis M.M., “Dose calculations for external photon beams in radiotherapy”, Phys. Med. Biol. **44**, R99 – R155 (1999).

22. Engelsman M., Damen E.M.F., Koken P.W., Van`t Veld A.A., Van Ingen K.M. and Mijnheer B.J., “Impact of simple tissue inhomogeneity correction algorithms on conformal radiotherapy of lung tumours”, Rad. Onc. **60**, 299 – 309 (2001).

23. Vergote K., De Deene Y., Claus F., De Gersem W., Van Duyse B., Paelinck L., Achten E., De Neve W. and De Wagter C., “Application of monomer/polymer gel dosimetry to study the effects of tissue inhomogeneities on intensity-modulated radiation therapy (IMRT) dose distributions”, Rad. Onc. **67**, 119–128 (2003).

24. Irvine C., Morgan A., Crellin A., Nisbet A. and Beange I., “The Clinical Implications of the Collapsed Cone Planning Algorithm”, Clin. Onc. **16**, 148–154, (2004)

25. Nisbet A., Beange I., Vollmar H.S., Irvine C., Morgan A. and Thwaites D.I., "Dosimetric verification of a commercial collapsed cone algorithm in simulated clinical situations" Rad. Onc. **73**, 79–88 (2004).

26. Scholz C., Schulze C., Oelfkea U. and Bortfeld T., "Development and clinical application of a fast superposition algorithm in radiation therapy", Rad. Onc. **69**, 79–90 (2003).

27. Hurkmans C., Knoos T., Nilsson P., Svahn-Tapper G. and Danielsson H, "Limitations of a Pencil Beam approach to photon dose calculations in the head and neck region", Rad. Onc **37**, 74 – 80 (1995).

28. ICRU Report 28, "Basic Aspects of high energy particle interactions and radiation dosimetry", Washington, D.C., USA (1978).

29. Higgins P.D., Sibata C.H. and Paliwal B.R., "Determination of a contamination-free build-up for ^{60}Co", Phys. Med. Biol. **30**, 153-162 (1985).

30. Rogers D.W.O., Bielajew A.F. and Nahum A.E., "Ionchamber response and A_{wall} correction factors in a ^{60}Co beam by Monte Carlo simulations", Phys. Med. Biol. 30, 423-443 (1985).

31. Hubbell J.H. and Seltzer S.M., “Table of X-ray Mass Attenuation Coefficients and Mass Energy-Absorption coefficients 1 keV to 20MeV for elements Z = 1 to 92 and 48 Additional Substances of Dosimetric Interest”, NISTIR 5632, U.S. Dept. of Commerce (1995).

32. Walters B.R.B., Kawrakow I. and Rogers D.W.O., “History by history statistical estimators in the BEAM code system”, NRCC Report PIRS-0791, NRC Canada (2002).

33. Du Plessis F.C.P., Willemse C.A., Lötter M.G. and Goedhals L., “The indirect use of CT numbers to establish material properties needed for Monte Carlo calculation of dose distributions in patients”, Med. Phys. **25**, 1195 – 1201 (1998).

34. Wilson R.R., “Monte Carlo study of shower production”, Phys. Rev. **86**, 261 – 269 (1952).

35. Chaney E.L., Cullip T.J. and Babriel T.A., “A Monte Carlo study of accelerator head scatter”, Med. Phys **21**, 1383 – 1390 (1994).

36. Ebert M.A. and Hoban P.W., “A Monte Carlo investigation of electron-beam applicator scatter”, Med. Phys **22**, 1431 – 1435 (1995).

37. Nelson W.R., Hirayama H. and Rogers D.W.O., “The EGS4 Code System” Stanford Linear Accelerator Center Report SLAC-265, Stanford Calif (1985).

38. Lewis R.D., Ryde S.J.S., Seaby A.W., Hancock D. A. and Evans C.J., “Use of Monte Carlo computation in benchmarking radiotherapy treatment planning system algorithms”, Phys. Med. Biol. **45**, 1755–1764 (2000).

39. Lewis R. D., Ryde S. J. S., Hancock D. A. and Evans C. J., “An MCNP-based model of a linear accelerator x-ray beam”, Phys. Med. Biol. **44,** 1219–30 (1999).

40. Raeside D.E., “Monte Carlo Principles and applications”, Phys. Med. Biol. **21**, 181-97 (1976).

41. Li X.A. and Rogers D.W.O., “Electron mass scattering powers: Monte Carlo and analytical calculations”, Med Phys **22**, 531 – 541 (1995).

42. Simpkin D.J. and Mackie T.R., “EGS4 Monte Carlo determination of beta dose kernel in water”, Med. Phys. **17**, 179-186 (1990).

43. Rogers D.W.O., Ma C.M., Walters B., Ding G.X., Sheikh-Bagheri D. and Zhang G., “BEAMnrc users Manual”, NRCC Report PIRS-0509 (2002).

47 Keall P.J. and Hoban P.W., “Super-Monte Carlo: a 3D electron beam dose calculation algorithm”, Med. Phys. **23**, 2023 – 34 (1996).

Chapter 4

Methods

4.1. Introduction

As mentioned in the previous sections, the TPS requires parameters and radiation beam input data characteristic to the linac of interest for implementation in treatment planning and dose calculations. The commissioning process must be done with utmost accuracy as the calculated dose distributions and monitor unit settings should reflect dose delivery with the linac during patient treatment. Normally the input data set consists of measurements done in a waterbath which usually includes percentage depth dose curves, crossline and inline profiles at predefined depths and diagonal profiles at preferred depths. The depth dose and profile data are collected for a range of field sizes, while the diagonal profiles are usually measured for the largest possible field. The specifications for such a dataset differs between TPS models, but almost all of them require the mentioned beam data including requirements for wedged and blocked beam data.

In this study the linac specific commissioning data as required by the CadPlan TPS was generated with Monte Carlo (MC) simulations of a generic linac based on a Siemens MD2 model. This methodology was chosen because MC simulations are regarded as the golden standard for radiotherapy dose calculations and can provide a set of benchmarking beam data. The MC simulations allow all degrees of freedom, similar to the real

accelerator, to produce dose distributions as would be found in practice. The advantages of this method lie in the fact that beam instability is avoided and measuring equipment instability leading to measurement inconsistencies or electronic drifts in measuring equipment is circumvented. Equipment positioning errors are excluded.

Uncertianties in dose calculations should be kept below 3% in order to correlate treatment outcome with prescribed dose. Evaluation of TPSs should thus be done with appropriate measuring equipment that can themselves be accurate within 3%, or preferably less. It is already known[1] that ionchambers reach accuracy levels that are acceptable and are used as reference detectors for dose determination and specification. Ionchambers show a very stable response over a very wide range of x-ray energies. In comparison, TLDs are easy to use in the sense that they can provide reliable data in a stable form and are easily positioned in phantoms for dose measurements. These detectors, however, have shown under responses for lower energies (between 10 and 800 keV)[2]. TLDs also require very delicate handling and are subject to fading due to light and heat exposure. Nevertheless, some studies have shown that they can point out dose differences between planned dose distributions and calculated dose distributions of larger than 5% and have good spatial resolution, depending on the TLD design. TLDs are also limited in that they measure dose at a point and cannot provide continuously sampled spatial distributions of dose.

Radiographic film can be used to verify conformal dose distributions and have a high spatial resolution and allows recording of dosimteric information in two dimensions.

Optical densities on the film can be digitized using scanning densitometers, but these detectors have also shown film emulsion sensitivity on depth within the phantom. The dependence is caused by a relative increase with depth in the population of lower energy scattered photons in the spectrum and the subsequent photoelectric absorption of these photons by the film emulsion. This is especially pronounced in the energy region below approximately 400keV. The mass attenuation coefficient at these energies for the emulsion increases rapidly leading to film over response.

The following procedure was followed to evaluate the CadPlan TPS calculated absorbed dose distributions: Section 4.2 describes the construction of a 6 and 15 MV generic accelerator. It is shown here how the master phase space files (PSFs) were produced above the top plane of the collimating jaws. These PSFs could then be used in further simulations for different field sizes as required for linac characteristic commissioning data and treatment plan requirements for clinical cases. The second set of PSFs were generated at SSDs of 90 cm for TPS commissioning data and 50 cm for clinical planning cases. Section 4.3 discusses the procedure used to calculate the absorbed dose in a water phantom for commissioning data from the PSFs generated in section 4.2. The use of the DOSXYZnrc MC code is explained here. The commissioning procedure of the TPS is described in section 4.5. The calculated dose profiles and depth dose data from the DOSXYZnrc simulations was imported to the TPS and validated. Verification of the dose calculation results in a homogeneous medium in the TPS was done through comparison of the MC dose calculations with the CadPlan calculated doses. Section 4.4 explains the procedure followed in which patient CT based models were converted to discrete data

matrix format that could be used for MC simulation and dose determination with DOSXYZnrc as addressed in section 4.6. 3D dose distributions were calculated for prostate, breast, lung, head and neck, brain and esophagus patient models. The breast case also included cerrobend shielding blocks. The same treatment plans were constructed in section 4.7 on the CadPlan TPS to allow the comparison and evaluation of its dose calculation algorithms for clinical cases in section 4.8. The different dose distribution evaluation tools used in the study are also explained in this section.

4.2 Construction of a Siemens MD2 based generic accelerator

The MC constructed accelerator was based on a Siemens MD2 linac. Its basic components are shown in figure 4.1. The simulations were carried out with the BEAMnrc MC code (2002) installed on a 3 GHz Pentium 4 PC with 1 GByte RAM and an 80 GByte IDE hard drive on a Linux Red Hat version 7 platform. The geometric and material composition and density specification for construction of the generic accelerator components were acquired from Siemens Medical Solutions USA Inc. (4040 Nelson Avenue Concord, CA 94520).

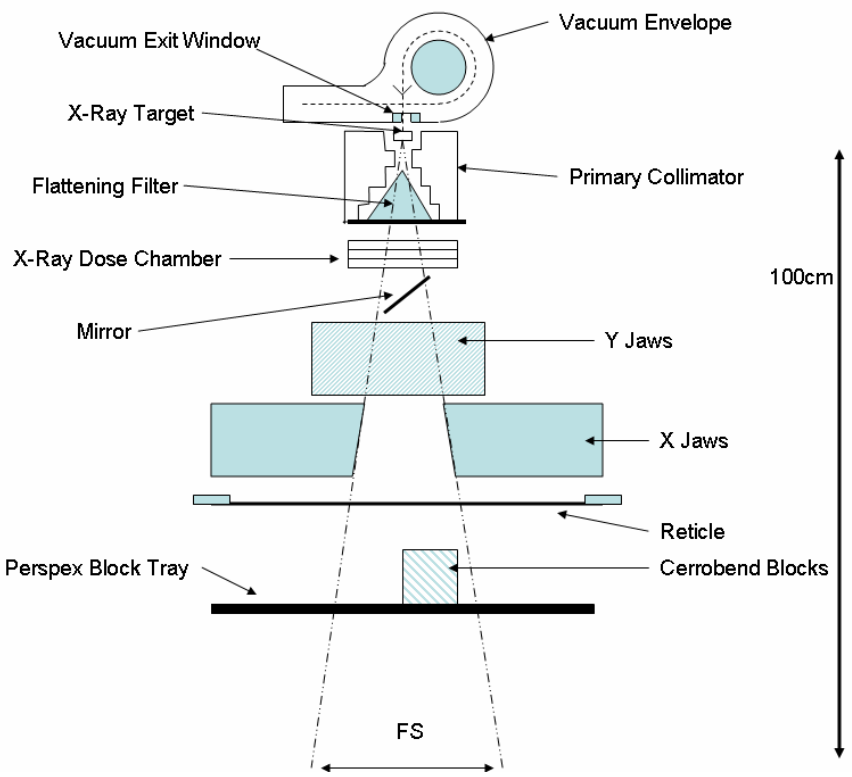

Figure 4.1. Schematic representation of a Siemens MD2 generic accelerator with accesories. The master PSF was generated beneath the mirror, just above the y-jaw position. This was done by simulating brehmstrahlung photons generated with electrons with known energies through the x-ray target, primary collimator, flattening filter, dose monitor chamber and mirror. Further simulations could be carried out for various field sizes and blocked fields by using the master PSF as an input radiation source and transporting the particles through the collimating jaws, reticle, blocks and the block tray.

The first steps of BEAMnrc MC simulation involves specifying and compiling the CMs that were used to construct the linac. The maximum possible optimization level was selected for compilation. The first simulation stage involved 4 CMs namely: FLATFILT for the target that includes eight slabs, consisting of different sections of stainless steel, gold (the brehmstrahlung target itself), carbon and water for cooling of the target. The tungsten primary collimator and the stainless steel flattening filter were contained in a

single CM called FLATFILT as the flattening filter is positioned inside the opening of the primary collimator (fig. 4.1.) for both 6 and 15MV modes. The flattening filters though were different for 6 and 15 MV. The CHAMBER CM represented the dose monitor chamber consisting of 5 thin alumina slabs. The MIRROR CM represented the oblique silicon oxide and aluminum mirror. The master PSF was generated at the back of the MIRROR CM.

A mono-energetic parallel electron beam of 6 MeV and 12 MeV was used to generate the dual energy brehmstrahlung photon spectra emerging from the gold target. The radius of the incident electron beam was 0.2cm. The number of histories were 30 million for 6 MV and 50 million for 15 MV. Variance reduction techniques were employed through the use of brehmstrahlung splitting and Russian Roulette which lead to an increase in the photon yield by a factor of 50. These options saved considerable CPU time and the generated PSF showed a particle yield of 817% and 556% with respect to the number of primary histories for 6 and 15 MV respectively. The total disk space occupied by the two PSFs was in the order of 8GByte each containing the dynamic parameters of approximately 270 million photons. Simulation rates were in the order of 2 million histories per hour and 1.2 million histories per hour for the 6 and 15MV beams respectively.

For the second stage of simulations of the accelerator the master PSF was used as a PSF input source and the simulation could be carried out for the remaining part of the treatment head. The second set of PSFs were generated at an SSD of 90 cm. This allowed water bath dose determinations to be done at 90 cm SSD which is required by some

TPSs. This second part of the linac simulation involved using the following CMs: JAWS for the X and Y collimating jaws, SLABS for the reticle used for light field and cross-hair projection and SLABS for the air gap up to 90cm SSD where the secondary PSF was located

Range rejection was utilized during this part of the simulation by setting the local transport parameters for the electron cutoff energy of particles entering the jaws. This value was selected as 2 MeV for both photons and electrons so that only those particles that could clear the jaw aperture were transported for each field size. The result was a simulation rate of approximately 380 million and 260 million histories per hour for the 6 and 15MV beams respectively. No brehmstrahlung splitting or photon forcing was selected for this part of the simulation. As required by the CadPlan TPS, PSFs were generated for square fields of side lengths 4, 6, 8, 10, 12, 15, 20, 25, 30, 35 and 40 cm. Each of these PSFs could then be used as beam input sources for simulation with DOSXYZnrc. To make this dataset flexible for use in future on other TPSs, some extra field size PSF data were simulated. It included 2, 3, 5 and 7 cm side length square fields.

The third stage of accelerator head simulation involved the modeling of shielding blocks. This required the same CMs as in stage 2 for the collimating jaws and reticle, but the remaining air gap to 90 cm SSD was thinner to make room for the BLOCK CM. This CM described the size and shape of the cerrobend blocks. Also included was the SLABS CM to represent the perspex block tray. This simulation was done for 10 and 25 cm side

length square fields. No brehmstrahlung splitting or photon forcing was invoked during this part of the PSF generation.

4.2.1 Modeling of the accelerator components

4.2.1.1 The brehmstrahlung target

The ‘FLATFILT’ CM was used for modeling of the target with a radius of 1.575 cm and a thickness of 1.473 cm. The target was modeled as a set of coaxial cones consisting of different layers of stainless steel, gold, air and water. The CM started at a distance of 0.0 cm in the z plane. The different layers of materials are part of the stainless steel cooling system which surrounds the gold brehmstrahlung target. The photon and electron cut-off energies for this CM were set to PCUT = 0.010 MeV and ECUT = 0.700 MeV respectively for both 6 and 15 MV beams.

4.2.1.2 The primary collimator and flattening filter

The ‘FLATFILT’ CM was also used to model the primary collimator and the flattening filter. The CM extended from the z = 1.590 cm to the z = 9.972 cm plane for the 6MV beam. The values were z = 1.590 cm to z = 9.781 cm for the 15 MV beam. The primary collimator extended over this height, while the flattening filters for 6 MV only starts at z

= 7.798 cm and z = 4.905 cm for 15 MV. The medium in-between the tungsten primary collimator and the fattening filter was air.

The flattening filters consisted of stainless steel for 6 MV and a mixture of C, Mn, P, S, Si, Cr, Ni and Fe for 15 MV. The radius of the CM was 3.772 cm and the thickness 8.382 cm for 6 MV and 8.191cm for the 15 MV CM. The photon and electron cut-off energies for this CM ware set to 0.010 and 0.700 MeV respectively for both 6 and 15 MV beams.

4.2.1.3 The ion chamber

The ‘CHAMBER’ CM was used to model the ion chamber which consisted of three layers of alumina with air in-between these layers. The chamber had a radius of 3.81 cm and a total thickness of 0.825 cm. Each of the alumina layers had thicknesses of 0.152 cm and the CM started at z = 10.503 cm. The photon and electron cut-off energies for this CM ware set to 0.010 and 0.700 MeV respectively for both 6 and 15 MV beams.

4.2.1.4 The mirror

The ‘MIRROR’ CM was used for modeling of the accelerator mirror composed of silicon oxide and aluminum. It consisted of two slabs with a total thickness of 0.165 cm. The half length of the mirror was 4cm and started the z-plane located at 11.45 cm. The photon

and electron cut-off energies for this CM ware set to 0.010 and 0.700 MeV respectively for both 6 and 15 MV beams.

4.2.1.5 The collimating jaws

The ‘JAWS’ CM was used to model the collimating jaws. The jaws consisted of two upper (Y) and two lower (X) jaw pairs. The radius of the CM was set to 10.482 cm and the CM started at z = 20.3 cm. The jaw thicknesses were 6.5 cm and both pairs consisted of tungsten. The top of the X jaws started at z = 28.1 cm leaving a small air gap inbetween the two sets of jaws. The aperture formed by jaws could be specified by considering the distance from the source to the upper and lower edge of both jaw pairs along with beam divergence down to the isocenter. The bottom of the jaws was at 34.6 cm and the photon and electron cut-off energies for this CM were set to 0.010 and 0.700 MeV respectively for both 6 and 15 MV.

4.2.1.6.The reticle

The ‘SLABS’ CM was used for modeling of the PMMA reticle with a thickness of 0.2997 cm. The radius of the CM was set to 8.636 cm and the CM started at z = 40.0 cm. The photon and electron cut-off energies for this CM were set to 0.010 and 0.700 MeV respectively for both 6 and 15 MV.

4.2.1.7 The cerrobend blocks

The ‘BLOCK’ CM was used for modeling of the cerrobend shielding blocks. The radius of the CM was 14.0 cm and the CM started at z = 47.01 cm. The blocks had a thickness of 8.989 cm. The photon and electron cut-off energies for this CM were set to 0.010 and 0.700 MeV respectively for both 6 and 15 MV.

4.2.1.8 The block tray

The ‘SLABS’ CM was used for modeling of the PMMA shielding block tray. The radius of the CM was 50 cm and the CM started at z = 56.01 cm. The tray had a thickness of 0.635 cm. The photon and electron cut-off energies for this CM were set to 0.010 and 0.700 MeV respectively for both 6 and 15 MV.

4.2.1.9 Air gaps

Relevant air gaps were simulated with the ‘SLABS’ CM. The radii of all these gaps were set to 50 cm. Photon and electron cut-off energies for these air gaps were set to 0.010 and 0.700 MeV respectively for both 6 and 15 MV.

4.2.1.10 Variance reduction

In the incident beam simulation, the EGSnrc options and settings used to generate the PSFs were: AE = ECUT = 0.700 MeV, AP = PCUT = 0.010 MeV and no photon forcing or Rayleigh scattering was invoked. The electron range rejection technique was used to increase the simulation speed. The value of IREJCT_GLOBAL was set to 2 allowing range rejection to be performed on a region-by-region basis. The value for ESAVE_GLOBAL (defining the maximum charged particle energy (in MeV) at which range rejection is considered) was set to 2 MeV. This provided a factor of 2-3 increase in speed and ignored only 0.1% of photons[3,4] which reached the phantom surface. These "lost photons" would have been produced by brehmstrahlung interactions in the accelerator head model due to the use of electron range rejection.

Range rejection was turned off in the target to provide the most accurate model for brehmstrahlung production. Selective brehmstrahlung splitting (SBS) was also used for speed increase. Ding[4] reported that performing both range rejection and SBS during a simulation and repeating the simulation with both turned off showed results that were the same within the known variance. However, the simulation with SBS turned on was much faster (almost two orders of magnitude) than when it was switched off. The number of histories simulated in this study was large enough to ensure statistical uncertainties of less than 1%. Spin effects were switched on so that elastic scattering cross-sections that take into account relativistic spin effects were used in electron transport. Spin effects do increase calculation time, however, results are more accurate.

The only CM that had transport cut-off energies of the electrons and photons set to a higher level (2 MeV) was the jaws of the accelerator. The transport cut-off energies in all other CMs were set to 0.700 MeV (ECUT) and 0.010 MeV (PCUT). This decreased the simulation time since the electron transport is terminated and all its residual kinetic energy is locally deposited when the electron has a kinetic energy of equal or less than 189 keV. The 700icru PEGS4 data file was used for cross section data supply.

The PRESTA algorithms were utilized during electron transport simulation. PRESTA-I was set for the boundary crossing algorithm and PRESTA-II as the electron step algorithm. Since the dimensions of the accelerator components are much larger than the average step length of electrons, the use of these algorithms result in decreased simulation time. This is because PRESTA-I allows electron transport in larger steps when the particle is not close to a CM boundary to deposit more energy than utilizing smaller electron step sizes.

The simulations were carried out in three stages of which the first was the longest. After generation of the master PSF beneath the mirror, just above the jaws, the PSF could be re-used for the second and third stages of simulation. The advantage of this method is that simulation time is decreased drastically because the first stage of simulations did not have to be repeated for all simulated field geometries.

4.2.2. Cross section data for the flattening filter mixture of materials

The flattening filters of the 6 and 15 MV beams were different in composition. The 521icru.pegs4dat and 700icru.pegs4dat files contain cross section data for use by the preprocessor code PEGS4 and contains data for electron cut-off kinetic energies of 0.01 MeV and 0.189 MeV respectively. These data files contain the interaction cross section data for the stainless steel used to model the 6 MV flattening filter, but had to be extended to include the cross section data for the 15 MV flattening filter which is composed of a number of elements. The PEGS4 preprocessor was supplied with a suitable input file to generate this data. Table 4.1. provides the physical parameters for this mixture:

Mixture	SST303 (C Mn P S Si Cr Ni Fe)
Density: (g/cm^3)	8.19
Composition by percentage:	0.1 : 2 : 0.045 : 0.03 : 1 : 18 : 9 : 69.825

Table 4.1. List of the physical parameters for the 15 MV flattening filter which was supplied to the PEGS4 pre-processor for cross section data generation.

All the cross section data contained in the PEGS4 cross section data files had lower electron and photon energy bounds of AE = 0.700 and AP = 0.010 MeV. The upper energy bounds were set to UE = 55.51 and UP = 55.0 MeV. The flattening filter of the 15MV beam was defined as a mixture and the APRIM (empirical correction factor in brehmstrahlung cross section) was set to a value of 1. A piecewise linear fit (PWLF)

option was chosen for interpolating between tabulated energy values for the appropriate cross section data together with the DECK option. IUNRTS was set to zero to use the restricted stopping power.

4.3. Calculation of absorbed dose in a water phantom using DOSXYZnrc

As mentioned before, the CadPlan TPS requires percentage depth dose data for a number of square fields, profiles at different depths for these same field sizes and diagonal profiles for the largest possible field size at different depths for commissioning purposes. The required beam model data was generated from the PSF data from the generic linear accelerator by calculating the absorbed dose in a water phantom using the DOSXYZnrc MC code. The simulations were done by using the PSFs discussed in 4.1. as the beam source. The characteristic beam data was extracted from the DOSXYZnrc created 3D dose files with a program called STATDOSE (supplied with the EGSnrc package) and other suitable programs that were written in the FORTRAN language to extract relevant data. The STATDOSE program is limited to profile and depth dose data extraction in the three main axis (x,y,z) directions. Diagonal profiles or volumetric data extraction is not a possibility and that is why an extra FORTRAN program was written. Both programs had the capability of normalizing the dose to any desired point. The TPS uses 5mm grid spacing for depth dose and 2.5 mm for profile data import. The simulations were done

with a smaller resolution grid to ensure accurate representation of the regions where steep dose gradients are found. The CadPlan TPS interpolates between the beam data points.

4.3.1. Construction of the water phantom

The water phantom voxel dimensions were set up according to the different field sizes. It is recommended in most dosimetry protocols[1] that the phantom in which accurate measurements are done should extend at least 10 cm laterally and in depth from the point of measurement. This methodology was used during the water phantom dose calculations. The largest field size simulated was a 40x40 cm^2 field and the phantom size was 60x60x40 cm^3 to satisfy this requirement. The 40 cm depth of the phantom was kept constant for all simulations and allowed depth dose measurements of up to 30 cm in depth.

The radiation isocenter from the BEAMnrc construction was chosen 10 cm beneath the water surface at z = 10 cm in the origin of the horizontal x-y plane located at the beam central axis. The number of voxels varied in the x-y plane according to the resolution requirements in the penumbra regions, the inner part of the geometrical field and the required resolution outside the penumbra region. The phantom was constructed so that the inner part of a beam profile, where the flatness and symmetry seldom changes by more than 2-3%, had maximal voxel dimensions in the x-y plane of 5 mm. Closer to the penumbra region the voxel dimensions were changed to reach at least 2 mm in the x-y

plane and 2 cm outside the penumbra region the voxel dimensions were allowed to reach 5 mm. The voxel dimensions in the y-direction were 1cm, centered over the depth at which profiles were calculated. The voxel specification was done in such a way that one voxel was always found centered in the phantom which corresponded with the position of the CAX for profile generation. For depth dose measurements, the voxel dimensions in the z-direction had increments of 2 mm up to 3 cm beyond the buildup region to allow accurate determination of the surface dose and position of maximum dose. Where the dose gradient became less steep the voxel depths were changed to 3 mm, 4 mm and 5 mm and at larger depths 1 cm to achieve shorter simulation times with the PRESTA-I boundary crossing algorithm employed. Calculations were done for PDDs with voxel sizes of 5 mm and 1 cm in depth from 3 cm beyond the position of maximum dose to investigate the effect of different voxel depths. The results showed that no distinction could be made between the different PDDs within the statistical variance of the data. The radiation source was aligned with the isocenter and the beam direction parallel to the z-axis. The boundaries of the phantom varied according to the field size used for simulation.

4.3.2 Transport control parameters for the water phantom

The photon and electron energy cut-offs were selected to be 0.010 MeV and 0.700 MeV respectively and the 700icru PEGS4 data file was used for the supply of cross section data for water. Spin effects were enabled for this simulation and no range rejection was

employed as the ESAVE_GLOBAL value was equal to ECUT. The boundary crossing algorithm was PRESTA-I and the electron step algorithm was selected to be PRESTA-II. The incident radiation beam source was selected to be the PSFs generated by the BEAMnrc simulation during stages 2 and 3 with the ISMOOTH option selected for the re-use of open field PSF data only. This option was not used where shielding blocks influenced the particle fluence in the third stage of PSF generation.

The material outside the water phantom was selected to be air. The number of histories was chosen so as to reduce the percentage error to less than one percent in all voxels inside the field. Five hundred million particle histories were followed for small field sizes to more than 1 billion for larger field sizes. The simulation rate was in the order of 20 million histories per hour. Electron cut-off energies were kept at 0.700 MeV, although simulations with higher cut-offs showed no distinguishable results within the known variance in 5mm voxels with an ECUT value of 0.85 MeV. The lower value was preferred (although the simulation time was longer) so as to not introduce simulation artifacts in the dose calculations.

4.3.3 Data analysis

Simulations with DOSXYZnrc result in the production of 3D dose files that contain the different boundaries of all the voxels in the phantom, along with their particle weighted absorbed dose values and associated statistical errors. This file is a text formatted file and

can be read and manipulated by writing suitable subroutines. The STATDOSE code was used in combination with locally developed FORTRAN based analyses tools to normalize the dose to the dose maximum (or any other desired point) in this 3D dose array and to express it in terms of percentage dose values. Percentage depth dose data were extracted from the voxel array centered on the beam CAX (z-direction). The beam profiles were also extracted at depths of dose maximum (d_{max}), 5, 10, 20 and 30 cm in the x-direction. Dose data were extracted for open and blocked fields. Data conversion was performed with the developed tools into a format suitable for import to the CadPlan TPS machine. The FORTRAN based tool extracted beam profiles and PDDs from the DOSXYZnrc 3D dose files and wrote the data into ASCII file format that contain the measurement specifications in the header of the file. PDDs were normalized to 10 cm depth and the profiles by the corresponding depth dose value on the central axis.

Before any data was imported to the TPS, the PDDs and profiles were compared to the original commissioning water bath scans for a Siemens MD2 (6 and 15 MV x-ray beams) to verify that the dose distributions were actually realistic. Although the aim of this study was not to replicate an existing accelerator, the data should be representative of a typical linac. Comparisons of this data showed deviations in the order of 2% maximum in regions of low dose gradients and 2mm maximum deviation in regions were the dose gradient was high.

4.4. Commissioning of the TPS input data

The characteristic beam data were imported directly into the TPS. The beam data is then used by the TPS (as explained in chapter 2) to generate pencil beam kernels for the convolution dose calculation process. The CadPlan TPS normalizes all profile data to 100% at the central axis, while PDDs are extrapolated to 40 cm depth and normalized to 100% at d_{max}, or to 100% at the d_{max} of a reference field. Before the dose calculations on patient CT models on the TPS could be carried out, the TPS had to be validated by comparing the dose data as calculated by the pencil beam convolution model with the original DOSXYZnrc calculated dose profiles. If the MC beam dataset corresponds to the TPS dose calculations for open and blocked beams then MC and TPS dose calculations on the same CT models can be used to evaluate the TPS accuracy. The convolution process is done in a water equivalent patient representative medium and corrected for inhomogeneities through the Batho and ETAR algorithms.

4.4.1. Water phantom dose calculations

For the validation of the TPS dose calculations a water phantom was constructed on the TPS with a relative electron density of one to make it equivalent to a water medium. This medium was uniform. The validation process required that the convoluted dose profiles on the TPS should be the same as the initial commissioning dose profiles created with DOSXYZnrc. Dose distributions for fields with side lengths of 2, 5, 10, 15, 20, 30, and

40 cm were used in this process. This was done for open and blocked fields. The data consisted of PDDs and the five profiles at different depths as mentioned previously.

The validation process was based on the recommendations of tolerances for the accuracy of photon beam dose calculations by Venselaar et al[5]. This methodology covers both simple and more complex dose distributions. They proposed to express the difference between calculated and measured dose values as a percentage of the dose measured locally. Normalization to this local dose (D) is preferred instead of to the maximum buildup dose (D_{max}) as the local dose eventually determines the success of a radiation treatment of a tumor and is therefore clinically more relevant.

Deviations between results of calculations and measurements can be expressed as a percentage of the locally measured dose according to:

$$\delta = \frac{100\% \times \left(D_{calc} - D_{meas}\right)}{D_{meas}} \qquad (4.1)$$

They proposed different tolerances for δ for different regions in the beam which can be distinguished. These regions include:

δ_1 : for data points on the central beam axis beyond the depth of D_{max}

δ_2 : for data points in the build-up region, in the penumbra, and in regions close to interfaces of inhomogeneities. This criterion can be applied in the region between the phantom surface and the depth of the 90% isodose surface, as well as in the penumbra

region. As an alternative, it is often proposed to use the shift of isodose lines expressed in mm. A large dose gradient is generally defined as being larger than 3% per mm.

δ_3 : for data points beyond d_{max}, within the beam but outside the central beam axis: again this region is a high dose and small dose gradient region.

δ_4 : for data points off the geometrical beam edges and below shielding blocks, generally beyond d_{max}: the region is a low dose and small dose gradient region, for instance below 7% of the central ray normalization dose.

δ_4 is applied in low dose regions where the dose calculations are inherently less accurate and it is not useful to relate deviations between calculations and measurements in such cases to the value of the locally measured dose. Equation 4.1. can be replaced by:

$$\delta = \frac{100\% \times \left(D_{calc} - D_{meas}\right)}{D_{meas,CAX}} \qquad (4.2)$$

in which the deviation for points outside the beam is related to the dose measured at a point at the same depth as the point under consideration, but on the CAX ($D_{meas,CAX}$). The same approach can be applied for points where the dose is very low, such as below shielding blocks.

Venselaar and co-workers have also recommended two other quantities to compare results of isodose calculations and profiles, especially for the reproduction of the basic beam data by the treatment planning system.

RW_{50}: the radiological width, defined as the width of a profile measured at half its height compared to the value at the beam axis.

δ_{50-90} : the distance between the 50% and the 90% point (relative to the maximum of the profile) in the penumbra (also called the beam fringe).

Treatment planning systems working with direct input data and utilizing interpolation algorithms should be able to reproduce data with a very high accuracy. Recommendations for tolerances $\delta_1 - \delta_4$ are summarized in table 4.2. from Venselaar et. al.

Table 4.2. Tolerance values for δ for application in different configurations

Tolerance	[1] Homogneous, Simple geometry	[2] Complex geometry (inhomogeneity, blocks)	[3] More Complex geometries (combinations of [2])
δ_1	2%	3%	4%
δ_2[a]	2 mm or 10%	3 mm or 15%	3 mm or 15%
δ_3	3%	3%	4%
δ_4	3%[b] (30%)	4%[b] (40%)	5%[b] (50%)
RW_{50}	2 mm or 1%	2 mm or 1%	2 mm or 1%
δ_{50-90}	2 mm	3 mm	3 mm

[a] These values are preferably expressed in mm. A shift of 1 mm corresponding to a dose variation of 5% is assumed to be a realistic value in the high dose, large dose gradient region
[b] This percentage is applicable to equation (4.2.); the percentages between brackets refer to equation (4.1.)

They also recommended the use of a confidence limit (Δ) for a set of data points. It is based on the determination of the mean deviation between the calculation and measured

dose points and the standard deviation (SD) of the difference. The confidence limit Δ is defined as:

$$\Delta = |\text{mean deviation}| + 1.5 \times SD \quad (4.3)$$

It was recommended to use a multiplication factor of the standard deviation of 1.5 which corresponds with a one-sided confidence probability P = 0.065.

An adequate number of dose points should be selected to obtain statistically relevant conclusions. It might sometimes be necessary in this case to combine data of different field sizes and beam qualities. Dose points included in the analyses must be representative of the specific study, e.g. dose profiles. Different regions of investigation may be subject to separate investigations, e.g. penumbra and central regions. In this way one can judge the performance of a dose calculation algorithm including its implementation in a TPS with only one parameter for a specific test situation.

4.5 Conversion of CT based patient models into a suitable DOSXYZnrc format

For radiotherapy treatment planning purposes patient model data is usually found in CT format. These data sets consist of a number of CT slices and each pixel in the CT image

has an associated CT number. These CT numbers need to be converted to relative electron densities by the TPS for use in dose calculation algorithms.

For a CT image based patient model to be used in the DOSXYZnrc code, each of its CT slice volume elements (voxels) have to be converted to a specific material. This material should be included in the PEGS4 data file. CT numbers can be associated with various tissues of known atomic composition and density through their relative electron densities. There exists a bilinear relationship between CT numbers and relative electron densities through which specific CT numbers can be associated with specific electron densities. In turn, the relative electron densities can be associated with a mixture of materials with the same electron densities.

For DOSXYZnrc transport simulation, the patient CT data have to be converted to tissue data representing the physical characteristics of the different tissues using the code CTCREATE. The CT phantom file can be created from the CT dataset since all the required material information is specified through a CT number to electron density conversion ramp function. The additional information that the user is required to provide are the CT data format, voxel dimensions for the phantom, and the transport parameters. The CT dataset can also be “clipped” to remove some data not required for patient dose calculations, like the surrounding air in the CT image or the couch top on which the patient is positioned during the CT scan.

A CT to material conversion tool was developed using the Interactive Data Language (IDL) patform. The IDL based program allows the user to create his/her own CT ramp (ie function for converting CT data to the densities and materials required for the DOSXYZnrc phantom). The ramp function converts CT numbers to materials and linear density scaling is applied over a material interval as shown in table 4.3.

Table 4.3. The materials with their associated CT number and density intervals for the default CT ramp.

Material Name	**CT upper bound**	**Density lower bound**	**Density upper bound**
AIR700ICRU	50.0	0.001	0.044
LUNG700ICRU	300.0	0.044	0.302
ICRUTISSUE700ICRU	1125.0	0.302	1.101
ICRPBONE700ICRU	3000.0	1.101	2.088

The conversion ramp requires the ramp parameters (material ct upper bound, material density lower bound and material density upper bound). The file created by the IDL program or CTCREATE is an ASCII file used as input for DOSXYZnrc to simulate the CT phantom and for the display program, MCSHOW, to display the density information.

The ASCII file contains information such as:

1. The number of media in the phantom
2. The names of the media
3. The ESTEPE value for each medium (now a dummy input)
4. The number of voxels in the X, Y and Z directions
5. A list of the voxel boundaries in the X direction
6. A list of the voxel boundaries in the Y direction
7. A list of the voxel boundaries in the Z direction

8. For each Z slice, an X-Y array containing the medium number in each voxel

9. For each slice in the Z direction, an X-Y array containing the densities in each voxel.

4.6 Preparing and executing DOSXYZnrc with compatible patient models for absorbed dose calculations

Once the CT data files had been converted to *.egsphant files an input file could be produced for DOSXYZnrc simulation and dose determination based on patient data.

4.6.1 Patient study cases

A selection of typical patient studies encountered in the clinical radiotherapy treatment department was used for the evaluation of the CadPlan TPS. These studies consisted of the following: Head and Neck, Oesophagus, Breast, Lung, Brain and Prostate cases.

For head and neck cases the treatment sites are typically associated with missing tissue geometries and air cavities inside the treatment volume. There is also a complex geometrical distribution of soft tissue and bone structures. This geometry is ideal to evaluate the performance of convolution algorithms in combination with heterogeneity correction based algorithms since a variety of tissue inhomogneities are present.

Oesophagus: this treatment site contains large parts of lung having very low densities, but still larger than that of air. Also, these low density regions are situated close to the PTV. The influence of low density regions in close proximity of the larger density PTV can thus be evaluated. This is of major concern as inaccuracies can typically lead to under- or overdosage.

Breast: this treatment site is known to have associated inaccuracies in dose determination using kernel based algorithms due to interface effects of electronic disequilibrium, missing tissue geomtries and partial beam absorbtion. The low density lung volumes that sometimes get quite close to the PTV lead to lower doses inside the thin chest walls due to scatter from inside the PTV to outside the patient tissue, thus reducing the dose. The effects of wax bolus could also be investigated for these cases, as well as the use of shielding blocks.

Lung: although the effects of low density tissue could be evaluated in the oesophagus plan, the lung plan allows evaluation of the calculated dose in a low density medium which can be compared with the prescribed dose. In this case, dose is prescribed to low density tissue with reduced absorbtion and enhanced scatter effects.

Brain and Prostate cases: these treatment sites are more homogeneous than the others, but the effects of bone and small air cavities could be evaluated.

4.6.2. CT data conversion from TPS to egsphant files

For external beam treatment planning the CT data is transferred via a network to the TPS. Once the CT data is received by the TPS it is converted to CART image format and stored in the patient database. The CART format is a direct-access binary file and the CT data consists of a 256x256 image matrix for every single CT slice. From the patient database, the CART format images could be transferred via network for conversion into the *.egsphant format required by DOSXYZnrc for dose calculation. Conversion could be done on a Linux based PC with CTCREATE or on a Windows based PC with the IDL program.

The IDL and CT create programs have the capacity to swap the bytes in the CART files as the HP MOTOROLA based microprocessor of the CadPlan system stores data in “big-endian” format, while the PC stores data in “little-endian” format. The CART files are composed of 269 records with length of 512 bytes. Record one is an administrative block and records 2 to 13 are user blocks. Records 14 to 269 contain the CT image data stored as a 2 byte integer array[6]. The CT numbers are represented as {Hounsfield Number} + 1000. The CT image data could thus be extracted, converted to media numbers and densities and stored as separate sequential access ASCII files on the PC, as mentioned earlier.

4.6.3 The DOSXYZnrc input file

The CT dataset for each clinical case was converted to the *.egsphant format. The data contained in these files represent the patient model for DOSXYZnrc simulations to be carried out. The x,y and z coordinates of the radiation beam isocenter was selected to be the same as what was used on the CadPlan TPS. Slice thicknesses were 1cm for all the cases. The pixel sizes in each of the CT slices varied according to the size of the field of view that was selected during the CT scan. Pixel sizes were the same in the x and y directions.

4.6.4 DOSXYZnrc simulations

MC simulations, especially with DOSXYZnrc, are very unforgiving. If a small error in the simulation setup was not detected at first, the wrong result can be obtained after many simulation hours. Quick simulation checks had to be done before the actual full scale treatment plan simulation. This was done by simulating a small number of histories (typically 1-10 million) with large energy cut-off values to verify that the beam and patient coordinate systems corresponded with the setup used on the CadPlan TPS. Once the simulations were complete, the dose distribution could be displayed with the MCSHOW software which displays the patient CT and a superimposed, slice specific dose distribution. The software has the capability of allowing not only transverse slices, but also coronal and sagital CT slices with their associated dose distributions. This

software program further has the option of drawing in structures like target volumes and organs at risk and allows computation of dose volume histograms (DVHs).

An IDL program was written to extract the 3D dose distribution data from the CadPlan dose files. These dose distributions are represented in a 160x112 matrix for each slice and had to be resampled for superimposing on the 256x256 image matrices on MCSHOW so that comparisons of dose distributions could later be made. This also corresponded to the DOSXYZnrc dose calculation grid.

The CadPlan planar dose files were converted into a 3D dose grid, the same format in which DOSXYZnrc dose files are stored. Byte swapping on the PC was also performed. The CadPlan dose calculation grid can be varied from 1.25 mm to 5 mm and this influences the way in which the dose distribution is resampled by the IDL program through pixel dimension calibration factors. All the clinical cases in this study though, were calculated with a dose grid size of 2.5mm and then resampled to a 256x256 matrix. The dose values are stored in the CadPlan format as direct-access binary files containing 256 records each of length 512 bytes. A similar method as described for image manipulation was followed to access the dose values in these files.

4.6.5 DOSXYZnrc transport control parameters

4.6.5.1. Open fields

The cut-off energies for photons and electrons were set to 0.010 and 0.700 MeV respectively. The boundary crossing algorithm for the simulations was PRESTA-I and PRESTA-II for the electron step algorithm. The dose in air was set to zero. The ISMOOTH option was invoked for the re-use of open field PSF data. ESAVE_GLOBAL was set to 0.700 MeV resulting in no range rejection being implemented. Photon splitting was turned off and spin effects were switched on. The number of histories was chosen so as to reduce the statistical uncertainty to less than one percent standard deviation in all voxels in a field. This number varied between 60 million for a 2x2 cm^2 and 1 billion for a 20x8 cm^2 field sizes. The simulation rate was in the order of 20 million histories per hour for the head and neck case with voxel dimensions of 1.31x1.31x10 mm^3. There was a slight increase in the simulation rate for patient models with larger voxels (e.g. prostate: 1.96x1.96x10 mm^3). The simulations were carried out on the same PC as for the BEAMnrc simulations.

4.6.5.2. Blocked fields

The evaluation of blocked fields in the breast case was done by using the specific PSF from the BEAMnrc simulations that included shielding blocks. The number of histories

in this case was determined in the same way as the open fields, regardless of the block. The transport parameters for the simulation was exactly the same as for the open fields, but the ISMOOTH option was switched off as any rotation of the PSF file through 180° would result in inconsistencies in the shielded part of the beam. Block and block tray transmission factors were calculated since the TPS had to be commissioned with these values for each of the two energies. This was done according to the procedure stipulated in the CadPlan manual by calculating the dose at d_{max} with DOSXYZnrc for open beams, beams with the whole (10x10 cm^2) field blocked and beams with only the perspex tray influencing the calculated dose. The ratio of blocked or Perspex tray fields to the open fields gave the transmission factors.

4.7 Absorbed dose calculations for clinical cases on the TPS

4.7.1 Absorbed dose calculations

Treatment planning was performed with the generic accelerator beam data that was discussed in sections 4.2. and 4.3. Absorbed dose distributions were calculated for the clinical cases mentioned in 4.5.1. The field sizes varied over a large range from 2x2 cm^2 for a small brain field to a 20x8 cm^2 for the breast plan. Normalization of the dose distribution was done according to the ICRU 50[7] guidelines for multiple beam plans. Dose could be prescribed to isodose lines where necessary to achieve good tumor

coverage as the PTVs and GTVs used were the same for the TPS and MC dose distributions.

Head and Neck: A seven beam arrangement with multiple isocenters was planned for this case. The normalization point was selected according to the ICRU[5] criteria and involved two 6x7 cm^2, two 4x14 cm^2, two 4x7 cm^2 and a 7x12 cm^2 field size. The gantry angles were 234.4° and 132.3° for the 6x7 cm^2 fields, 180° for both 4x14 cm^2, 0° for both 4x7 cm^2 and 180° for the 7x12 cm^2 fields. Collimator angles for all fields were 90°. The couch angles in all beams were 0°.

Breast: Firstly two 100cm SSD beams with gantry angles at 112° and 292° and field sizes of 20x8 cm^2 were used. Collimator angles were selected to be 197° and 343° for the two gantry angles respectively. The couch angles in both beams were 0°. The patient model also incorporated a paraffin wax bolus of approximately 2 cm on the left chest wall.
Secondly, to investigate the effect of planning without bolus, the same patient model was used, but in this case treatment of the other breast was planned. This involved two SSD beams with gantry angles at 60° and 250° and field sizes of 20x6 cm^2. Collimator angles were selected to be 170° and 190° for the two gantry angles respectively. The couch angles in both beams were 0°. These two cases allowed for comparisons of the dose close to the skin surface in the bolus and non-bolus plans.

Lung Case A: The same patient model used for the breast case was also used for the lung case. This plan involved two 4x3 cm^2 isocentric fields at gantry angles 9° and 293°.

Collimator angles were selected to be 90° for both beams, while the couch angles were 0°. The isocenter was situated inside the tumor volume and dose was normalized to the ICRU reference point (the isocenter).

Case B: A dose distribution for a 2x2 cm^2 field was also produced to study the effects of electronic disequilibrium in lung for small fields. The gantry angle selected for the single field dose distribution was 293°.

Brain: Two isocentric beams with beam gantry angles at 270° and 90° and field sizes of 14x8 cm^2 and 14x11 cm^2 respectively. Collimator angles were selected to be 0° for both beams. The couch angles were 0° for the first beam angle and 270° for a vertex field with gantry angle of 90°. The ETAR inhomogeneity correction algorithm could not be employed for vertex fields due to calculation restrictions in the sense that the effective coalesced slice can not be calculated for vertex beams, or beams directed along the patient z-axis. Dose was normalized according to the ICRU criteria.

Prostate: A five beam isocentric prostate plan arrangement was planned here with beam gantry angles at 0°, 120°, 75°, 295° and 300°. The field size was 8x7 cm^2 for all fields. Dose normalization was done in a similar way as for the brain plan. Collimator angles were selected to be 0° for all beams and the couch angles also 0°.

Esophagus: A three beam isocentric plan arrangement was opted for with beam gantry angles at 0°, 285° and 75°. The field size was 8x7 cm^2 for all fields. Dose normalization

was done in a similar way as for the brain plan, but also ensuring that the reference point was not selected in a region of low density or close to such interfaces. Collimator angles were selected to be 0° for all beams and the couch angles also 0°.

In this study the treatment planning system was evaluated for 6 and 15 MV x-ray beams for both the double pencil beam and single pencil beam models. More focus fell onto the single pencil beam model as this is the preferred method for dose calculations. Combinations of Batho and ETAR inhomogeneity correction algorithms were utilized in this study.

4.8 Comparison of DOSXYZnrc and TPS calculated dose distributions

4.8.1. Normalization of the dose distributions calculated with DOSXYZnrc

Once the dose distribution had been calculated with the TPS and DOSXYZnrc they could be compared on the same patient CT model. To achieve this, the dose distributions in both cases where normalized to the ICRU reference point as explained before for multiple beams, and to a depth of interest (with the depth deeper than d_{max}) for single beam comparison. The dose at d_{max} was not chosen as small errors in this position lead to large differences between the two calculated distributions. The normalization point dose consisted of the average dose in the voxel corresponding to the position of the point and

the 8 voxels surrounding that particular voxel on the CT slice of interest. This was done to reduce the noise on the data. Absolute dose comparison was possible in this way.

4.8.2. Evaluation of treatment plans with dose volume histograms

Treatment planning optimization for 3DCRT will provide maximal tumor control probability (TCP) and an acceptable normal tissue complication probability (NTCP). Tumor dose will be maximized in this case with no normal tissue tolerance being compromised and treatment plans are evaluated with this criterion. The difficulty in this evaluation is associated with the large amount of data contained in a 3D dose distribution. Areas or volumes of under- and overdosage can be identified through visual inspection of the dose distribution, but due to the size of all these dose calculation points such an interpretation alone is very difficult, especially when comparing two different plans.

To aid the user in the interpretation of the 3D data and getting an easily representable relationship between dose distributions and the associated delineated volumes receiving the dose, dose-volume-histograms (DVHs) are often used for this purpose. DVHs are graphical representations of organ dose versus the volume of the delineated organ of interest. On this data plot the volume receiving dose greater than or equal to each dose level as a function of the dose interval in the expected dose range, is represented. This graphical presentation of 3D dose distributions summarized on a 2D graph allows quick assessment of the degree of dose uniformity and non-uniformity of dose distributions.

DVHs are 2D representations of 3D data over the entire scanned volume. Dose uniformity and non-uniformities can thus be identified on DVHs, but their exact position within the whole volume of interest can only be identified on the CT slices with their isodose lines. DVHs may give some additional information that may not be readily apparent when using the isodose distributions. High dose regions on the DVH may represent a high dose region related to a single CT slice or may represent a contiguous region related to adjacent CT slices, or even a number of discreet high dose regions related to the same or different CT slices. Only isodose lines can be used to identify the location of high dose regions and thus DVHs must be used in conjunction with isodose distributions for treatment plan evaluation.

The DVH data was obtained from the MCSHOW software by analyzing the 3D dose distributions for each organ or tumor that was delineated and after manipulation could be plotted on a graph for comparison. The TPS and MC generated plans were also compared based on the Equivalent Uniform dose (EUD).

4.8.3 Evaluation of treatment plans with the Equivalent Uniform Dose (EUD)

The EUD according to the proposal by Niemierko[8] was calculated for all OARs and delineated tumor volumes. Although this phenomenological concept can potentially provide a method of comparing inhomogeneous dose distributions, it does have some limitations, especially where very cold spots in tumor volumes are calculated in

combination with hot spots elsewhere. This simplified form of the EUD is not sensitive enough for low dose areas in the tumor and more comprehensive TCP models have been developed.

Further development of NTCP models expressed in terms of EUD have been reported[9] and may be simpler to use than the well known Lyman[10] equation. An investigation into the sensitivity of the EUD concept and TCP model to dosimetric heterogeneity has shown that both indices provide distinctions between dose distributions of varying nonuniformity[11]. It has also shown that EUD is insensitive to its parameters (both spatial and temporal) relative to the more particular index of TCP. It was found that in light of uncertainty regarding in vivo radiobiological parameters, within the limitations imposed by variations in dose distribution, EUD provides a more stable and less deceptive indicator of relative effect. This would allow the EUD indice to be used favorably in certain applications, like:

_ intercomparison of dose distributions when radiobiological parameters are uncertain;

_ incorporation as an objective (or part of an objective) in optimization routines. EUD overcomes many of the deficiencies of geometric indices (e.g. linear or least-squares comparisons) by incorporating the nonlinear dose–response into calculation of a scalar dose indicator; and

_ for multicentre reporting of dose distributions using alternative irradiation techniques.

By considering these factors, it was decided to use the EUD application in its simplest form.

However, Ebert[11] pointed out that the insensitivity of EUD to model parameters can be a disadvantage if parameters are accurately known and definitive comparison of alternative irradiation strategies is required. In such cases, the sensitivity of TCP would be an advantage since it would accurately and adequately distinguish potentially successful and unsuccessful techniques.

$$EUD(Gy) = D_{ref} \frac{\ln\left[\sum_{i=1}^{N} v_i \cdot (SF_2)^{D_i / D_{ref}}\right]}{\ln(SF_2)} \qquad (4.4)$$

Equation 4.4 was used for the EUD calculation in this study. The various biological parameters used during the calculations are indicated in chapter 5. The simplest model was used during these calcualtions, in other words, no absolute volume effects, non-uniform spatial distribution of clonogens, dose-per-fraction effects, cell proliferation effects and inhomogeneity of patient populations was incorporated. The dose volume histogram data from the CadPlan and DOSXYZnrc distributions were used for calculation of the EUD in the clinical cases.

References

1. IAEA International Atomic Energy Agency, “Absorbed dose determination in external beam radiotherapy: An international code of practice for dosimetry based on standards of absorbed dose to water”, Technical Report Series no. **398**, IAEA, Vienna (2001).

2. Duggan L., Hood C., Warren-Forward H., Haque M. and Kron T., “Variations in dose response with x-ray energy of LiF:Mg,Cu,P thermoluminescence dosimeters: implications for clinical dosimetry” Phys. Med. Biol. **49**, 3831 – 3845 (2004).

3. Sheikh-Bagheri D., Rogers D.W.O., Ross C.K. and Seuntjens J.P., “Comparison of measured and Monte Carlo calculated dose distributions from the NRC linac”, Med. Phys. **27**, 2256 – 2266 (2000).

4. Ding G.X., “Energy spectra, angular spread, fluence profiles and dose distributions of 6MV and 18MV photon beams: results of Monte Carlo simulations for a varian 2100EX accelerator”, Phys. Med. Biol. **47**, 1025 – 1046 (2002).

5. Venselaar J., Welleweerd H. and Mijnheer B., “Tolerances for the accuracy of photon beam dose calculations of treatment planning systems”, Rad. Onc **60**, 191-201 (2001)

6. CadPlan 6.0 (Varian Medical Systems, Inc., Palo Alto, CA 94304), External Beam Modelling Physics Manual (1999).

7. International Commission on Radiological Units and Measurements. “Prescribing, Recording and Reporting Photon Beam Therapy,” ICRU Report **50**. Bethesda, MD: ICRU (1993).

8. Niemierko A., “Reporting and analyzing dose distributions: A concept of equivalent uniform dose”, Med. Phys. **24**, 103 – 110, (1997)

9. Luxton G., Keall P.J. and King C.R., “A new formula for normal tissue complication probability (NTCP) as a function of equivalent uniform dose (EUD)”, Phys. Med. Biol. **53**, 23–36 (2008)

10. Lyman J.T., “Complication probability as assessed from dose–volume histograms”, Radiat. Res. **104**, S13–19 (1985)

11. Ebert M.A., “Viability of the EUD and TCP concepts as reliable dose indicators**”,** Phys. Med. Biol. **45,** 441–457 (2000)

Chapter 5

Results and Discussion

5.1. Introduction

Chapter 4 addressed the methods that were employed for the evaluation of the CadPlan TPS dose calculations against MC simulations. In this chapter the results found during these evaluation tests will be shown and discussed in detail.

5.1.1. Analysis of the BEAMnrc generated PSFs for open and blocked beams

During the first stage of accelerator simulation with the BEAMnrc code, the generic accelerator was built and compiled with the CMs as set out in chapter 4. Thereafter the master PSFs were generated beneath the MIRROR CM for 6 and 15 MV photon beams. The master PSFs were used as input for simulations with different jaw settings leading to PSFs for various field sizes. The fluence and spectral distributions of the master PSFs (generated just above the jaws) and for a second PSF generated for a 10x10 cm^2 field are shown in figures 5.1 and 5.2 respectively. The second stage PSFs for the TPS beam characteristic commissioning data were generated at 90 cm SSD. The PSFs used during patient model dose calculations with DOSXYZnrc were generated at 50 cm SSD to allow them to be used for any further stage simulations.

The SSD at which the particles in the PSF were scored determines the distance between the 50% intensities of the fluence profile due to beam divergence. The PSF analysis was done with the BEAMDP code.

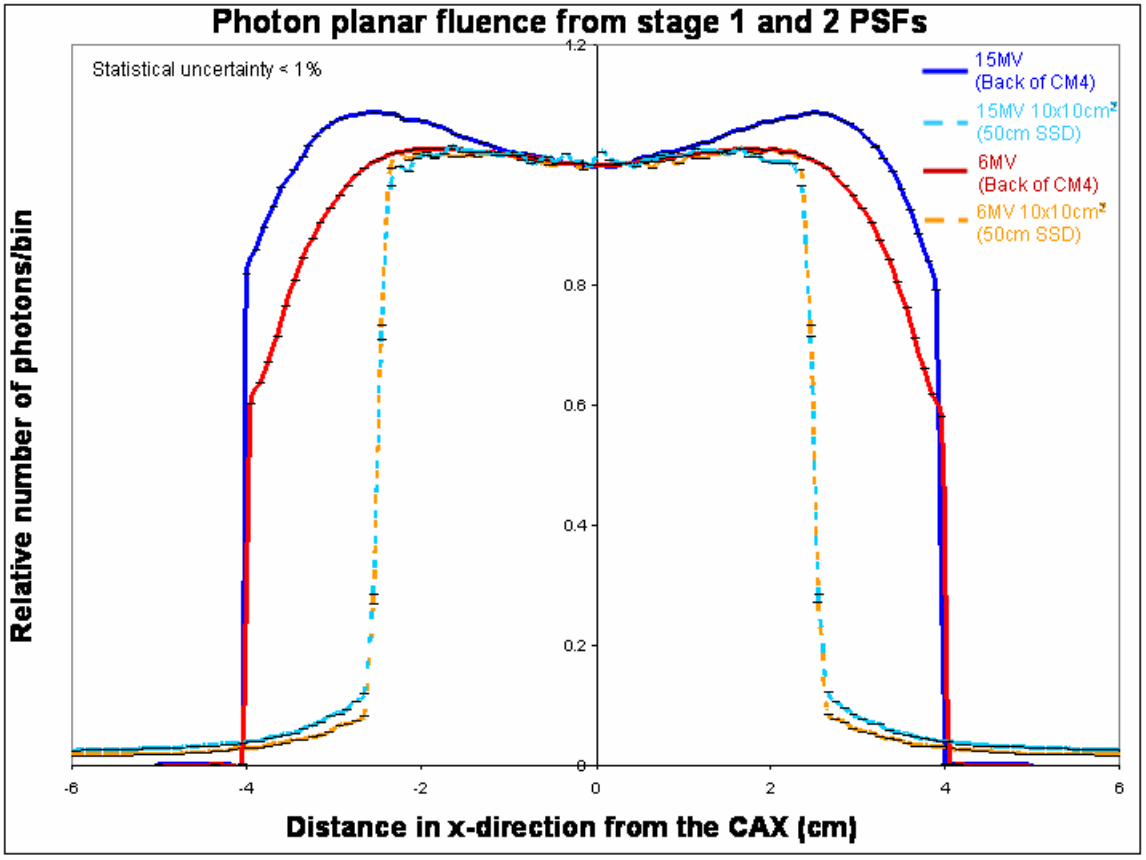

Figure 5.1 The photon fluence distribution of the master PSFs (solid lines) of the 6 and 15 MV beams in the x-direction, as well as the corresponding fluence distribution of PSFs generated at 50 cm SSD (broken lines) for 10x10 cm^2 field sizes. The data was scored in 100 bins with a width of 1 mm each in the x-direction. The error bars have sizes comparable to the line thicknes.

From figure 5.1 the increase in the photon fluence in the master PSFs with off axis distance until a maximum is reached at approximately 3 cm from the CAX defined at the plane above the jaws. A local minimum fluence value in the open part of the beam is found on the CAX due to the effect of the conical shape of the flattening filter. The thick

central part attenuates the forward peaked brehmstrahlung fluence from the target more than on the peripheral regions. Between 3 and 4 cm from the CAX, the primary collimator starts to attenuate and absorb some of the photons leading to a reduction in the fluence. Beyond 4cm most of the photons are absorbed inside the primary collimator. The fluence profile is symmetric with the statistical uncertainty smaller than 1%. The error bars on the graph are not discernable.

The planar fluence profile has an important effect on the dose profiles calculated with DOSXYZnrc. If the fluence is higher in the center of the beam for the master PSF, the corresponding dose profiles will show a peak in the center of the beam. On the other hand, if the peak is closer to the edge of the fluence profile, the dose profiles will show increased dose towards the edges of the radiation beam.

The incident electron beam energies of 6 MeV and 12 MeV were chosen to simulate the photon beams. The resulting fluence distributions played an important role in selecting the appropriate incident electron energy. The 6 MeV electron beam resulted in a fluence profile that lead to a flat dose profile at 10 cm depth in a water phantom. For the 15 MV beam however, an incident electron energy of 15 MeV was initially selected. This resulted in a fluence profile that was peaked in the center and the resulting dose profiles for the largest field size also showed a peak on the central axis. The incident electron energy was subsequently decreased in steps of 0.5 MeV until the dose profiles were found to be comparable with the commissioning data of a real Siemens MD2 accelerator. However, as large changes in the dose profile shape were seen when varying the incident

electron energy, the PDDs showed less variation over the incident electron energy range in these trial runs. These findings showed good agreement with the literature where it was found that incident electron energy with the resulting brehmstrahlung energy spectra has much larger influences on dose profile shapes than on PDD data. Pena et. al[1] concluded that depth–dose profiles are not sensitive enough to produce two different PDDs for a 0.5 MeV nominal energy change in any of the configurations they studied for the NRC linac. Sheikh-Bagheri and Rogers[2] came to similar conclusions for various accelerators. Sheikh-Bagheri et. al[3] reported that when the nominal beam energy is varied by 3% at 10 MV and 5% at 20 MV, it is observed that, unlike the peripheral dose (dose outside the penumbra), the dose distribution inside the field and in the penumbral region are sensitive to such variations. The beam energy impacts the depth-ionization distribution and the calculations show that, for example, increasing the electron energy from 20 to 21 MeV changes the value of relative ionization at 10 g/cm^2 depth slightly (from 0.788±0.001 to 0.796±0.001 for their simulations).

In comparison to the fluence distribution for the stage 1 simulation, the 10x10 cm^2 fluence profiles are clipped by the accelerator jaws. The shapes of the profiles are approximately maintained in the open part of the field compared to the master PSF. However, the effect of scattered radiation outside the field is clearly seen for the fluence profiles at 50 cm SSD.

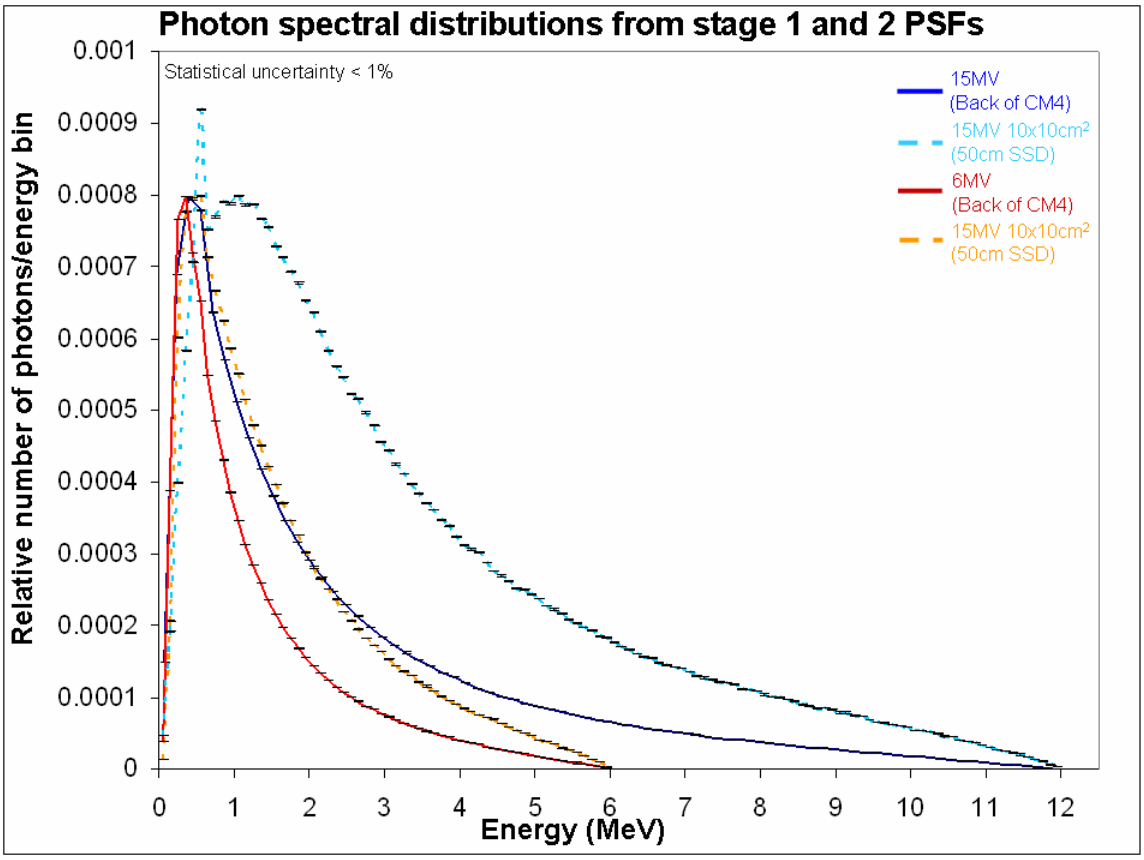

Figure 5.2 The photon energy spectrum distribution of the master PSFs (solid lines) and at 50 cm SSD for a 10x10 cm^2 field size (broken lines). These are the energy spectra for the photons produced by the brehmstrahlung target and scattered by the flattening filter of the accelerator. The error bars again have sizes comparable to the line thicknesses. Data was scored in 60 and 120 bins with widths of 100 keV each in the x-direction for the 6 and 15 MV beams respectively.

The spectral data was generated in a rectangular region of 10x10 cm^2 for the master PSFs, while this region was set to 20x20 cm^2 for the data at 50 cm SSD. The width of the energy bins were 0.1 MeV and the statistical uncertainty was less than the 1% level. The peak energy of the photon fluence in the master PSFs was 0.35 MeV for the 6 MV beam without any collimation and 0.4 MeV for the 15 MV beam. When the field size was clipped to 10x10 cm^2 for these two energies, the effective energy of the beam is increased

since the peripheral part of the fields contain relatively more low energy photons due to soft beam transmission of the thinner part of the flattening filter. The peak energies changed to 0.4 MeV and 1.05 MeV for the 6 and 15 MV beams respectively. The 15 MV beam also showed a peak at 0.550 MeV resembling the annihilation photons produced during pair production interactions.

Figure 5.3 shows the fluence for an irregularly shaped block field for both energies. The block thickness was 9 cm on the beam axis and the PSF was generated at 60 cm SSD. The reduced fluence intensity at 2.4 cm is caused by the collimating effect of the jaws. In the positive x-direction the sudden decrease in intensity is due to the cerrobend block photon absorption. However, due to the shape of the block getting thinner in the positive y-direction, some scattered photons still reach the scoring plane underneath the block. As the distance from the central axis increases, the number of photons in the fluence profile bins decrease. The number of photons in this plane also includes all photons that were transmitted through the cerrobend block. The photon fluence outside the beam edge is also less than the number in the same position in the negative x-direction due to more scattered photons being absorbed by the shielding block.

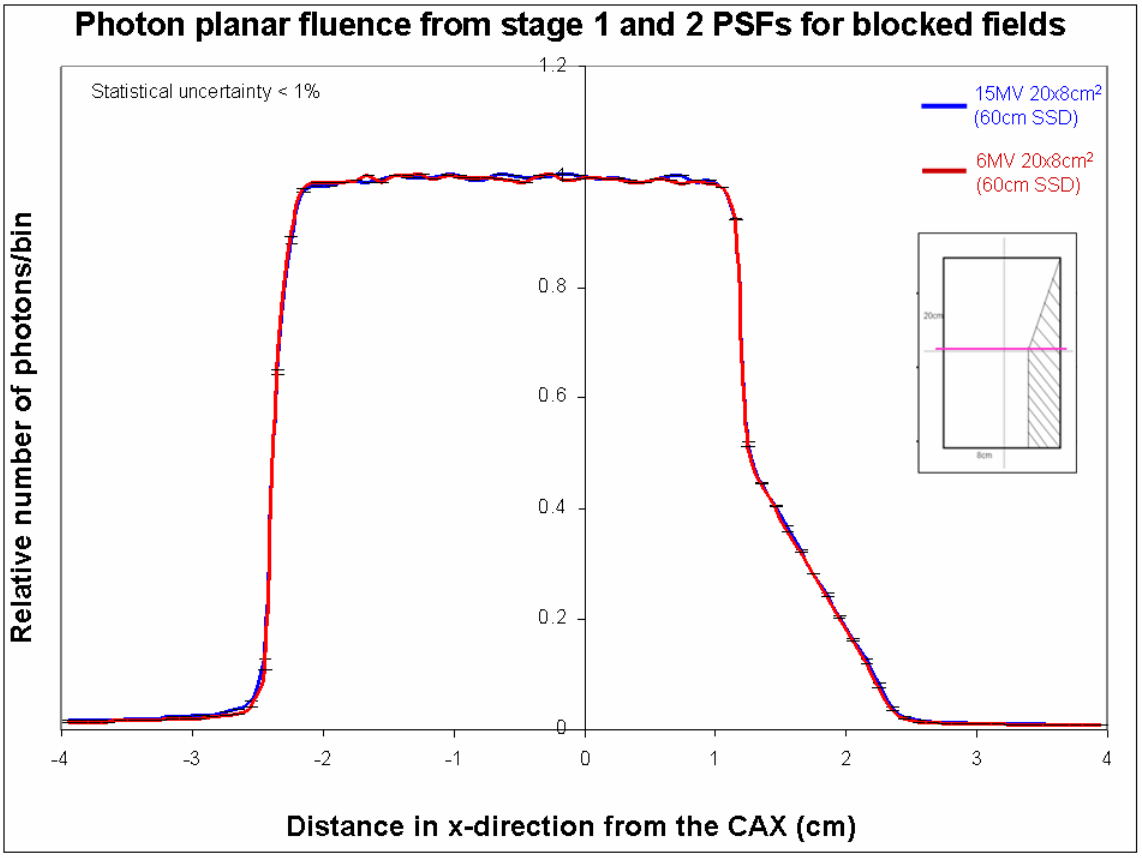

Figure 5.3 The photon fluence distribution of 6 and 15 MV beams in the x-direction of an irregularly blocked 20x8 cm^2 (defined at 100 cm SSD) field with the PSFs at 60 cm SSD. The insert shows the shape of the shaded blocked region superimposed on the field at the phantom surface and the line the position where the fluence profile was sampled. The data was scored in 80 bins with a width of 1 mm each in the x-direction. The error bars have sizes comparable to the line thickness.

5.1.2. Input beam data for the CadPlan TPS generated with DOSXYZnrc

5.1.2.1. Open Fields

The evaluation of the TPS involved the generation of a commissioning dataset for 6 and 15 MV x-ray beams. The commissioning was done with dose distributions of various

field sizes, similar for both energies. Additional field size beam data was produced and used during the treatment unit characterization (TUC) process to allow these datasets to be used for commissioning of other TPSs as well.

The DOSXYZnrc generated dose profiles to import to the TPS are shown in figures 5.4 to 5.15 for the 6 MV dataset. The voxel sizes were chosen for each field size to produce accurate dose distributions. Voxel widths of less than 3 mm near large dose gradients were used. Larger voxels were used where the dose gradients are small, or outside the beam penumbra.

The commissioning beam data was sampled from the resulting .3ddose files generated with the DOSXYZnrc simulations. The depth dose data was normalized to 10 cm depth and the profiles normalized to the corresponding central axis percentage dose. Only the diagonal profiles of both energy datasets were normalized to unity on the CAX at the depth of maximum dose. Once the data was imported to the TPS, it was re-sampled (through interpolation) into 0.25 cm grid spacing for the profile data and 0.5 cm spacing for PDDs by the TPS. PDDs and profile data were generated for the following field side lengths: 2, 3, 4, 5, 6, 7, 8, 10, 12, 15, 20, 25, 35, 40 cm and 40 cm diagonal profiles. The profiles were generated at depths of d_{max} (of the 10x10 cm^2 field), 5, 10, 20, and 30 cm and are largely influenced by the photon fluence in the PSFs.

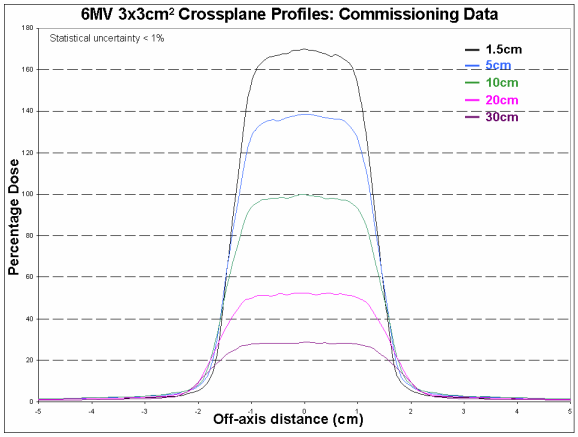

Figure 5.4

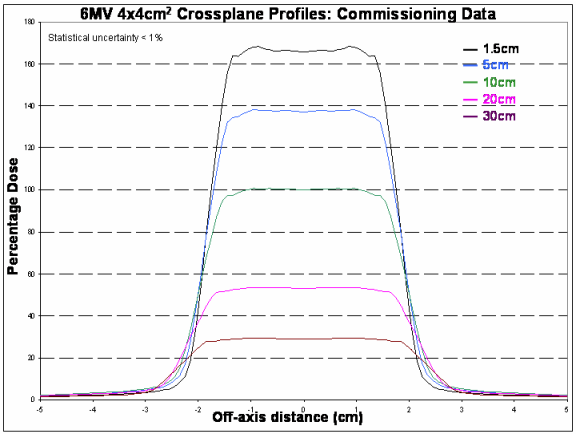

Figure 5.5

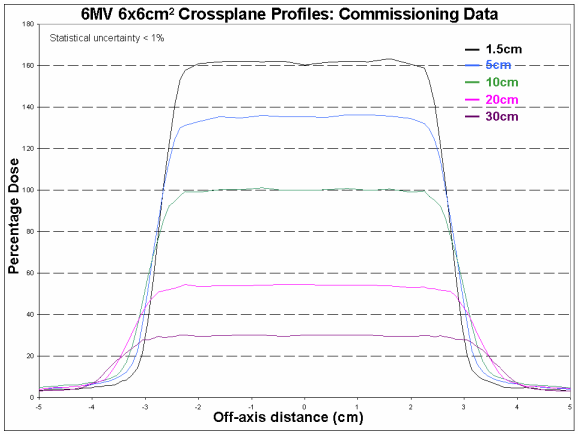

Figure 5.6

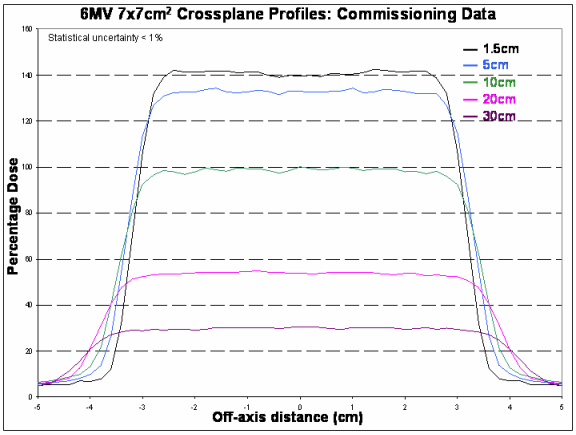

Figure 5.7

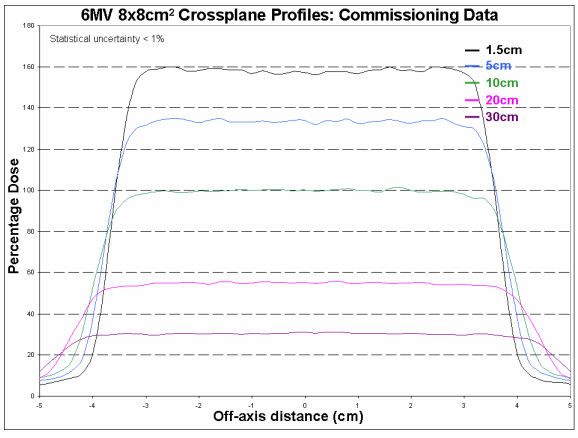

Figure 5.8

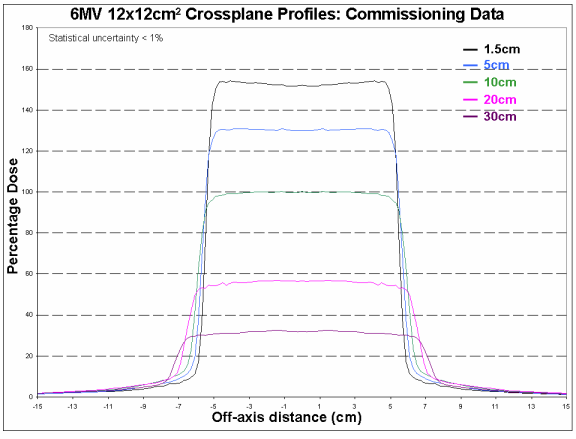

Figure 5.9

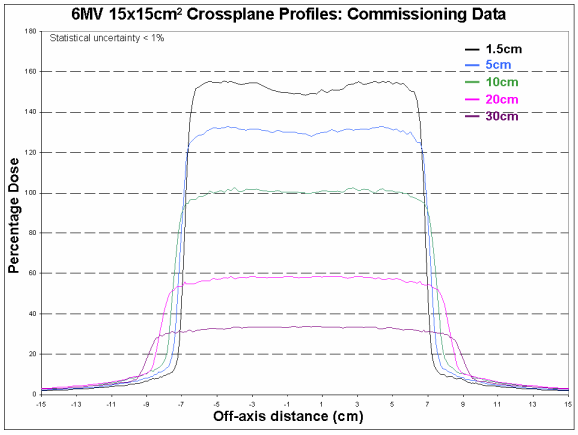

Figure 5.10

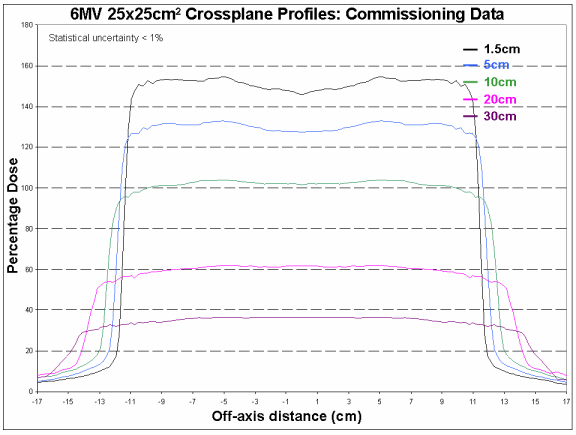

Figure 5.11

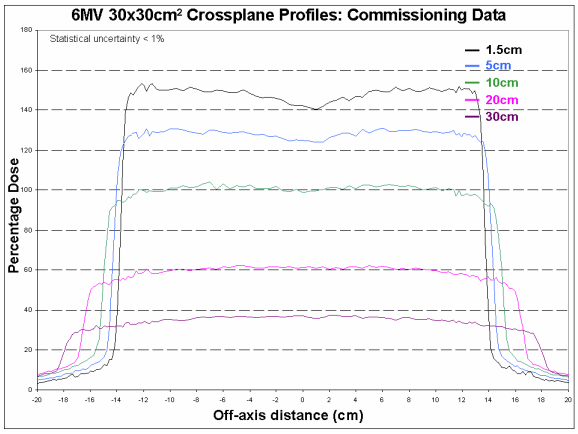

Figure 5.12

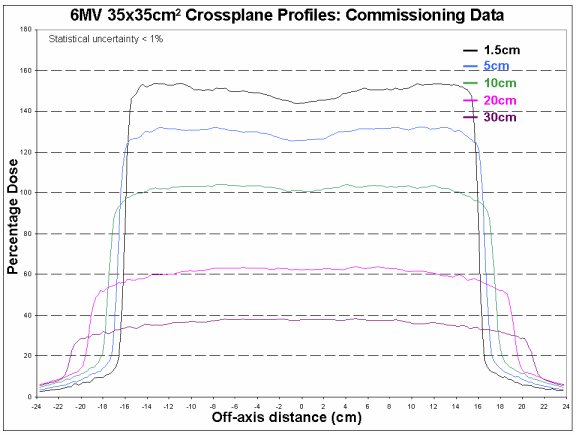

Figure 5.13

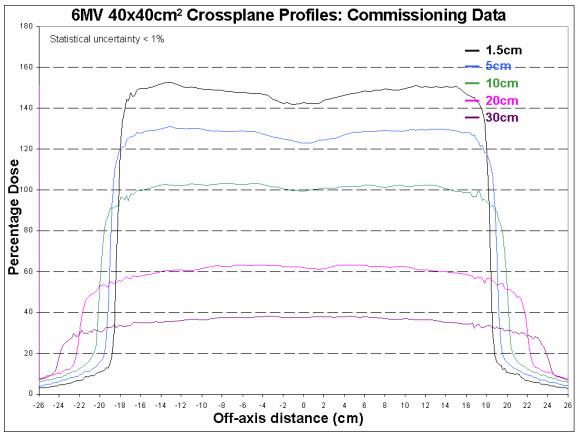

Figure 5.14

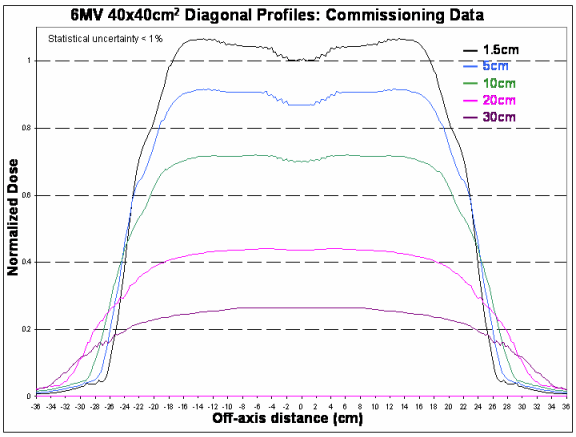

Figure 5.15

Figures 5.4 – 5.15 DOSXYZnrc generated profile import data.

The increased statistical variation, though the variance is smaller than 1%, can be seen by close inspection of regions close to the beam penumbra or where it was deemed necessary to have accurate representations of fast changing dose gradients. It is more evident for larger field sizes. This can e.g. be observed for the 30 cm depth profile in figure 5.14 between 16 and 24 cm from the CAX.

The TPS should be able to replicate the original imported beam data once the validation of the input data has been done and beam characteristic parameters for dose calculation use have been generated. The TPS calculated dose distributions should agree to within a certain tolerance value of the original measured data for evaluation of the TPS algorithm accuracy. Profile data showing the comparison of MC simulated and TPS calculated dose distributions are shown in figures 5.16 to 5.17. The graphs include a small expanded region selected in the penumbra to make comparison of the dose distributions clearer.

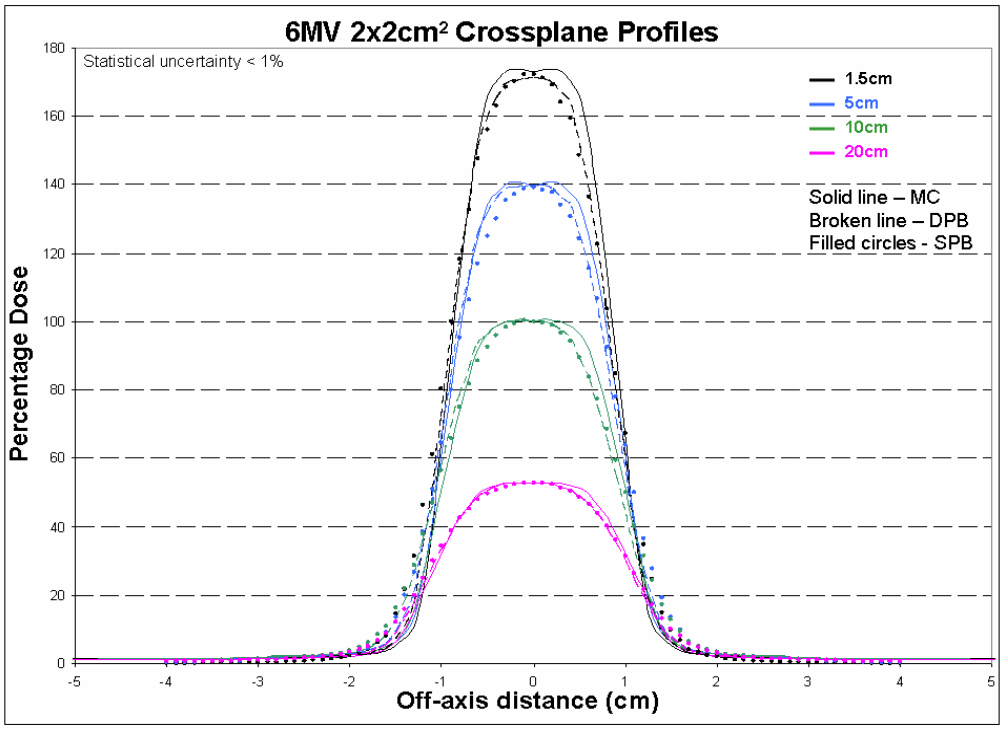

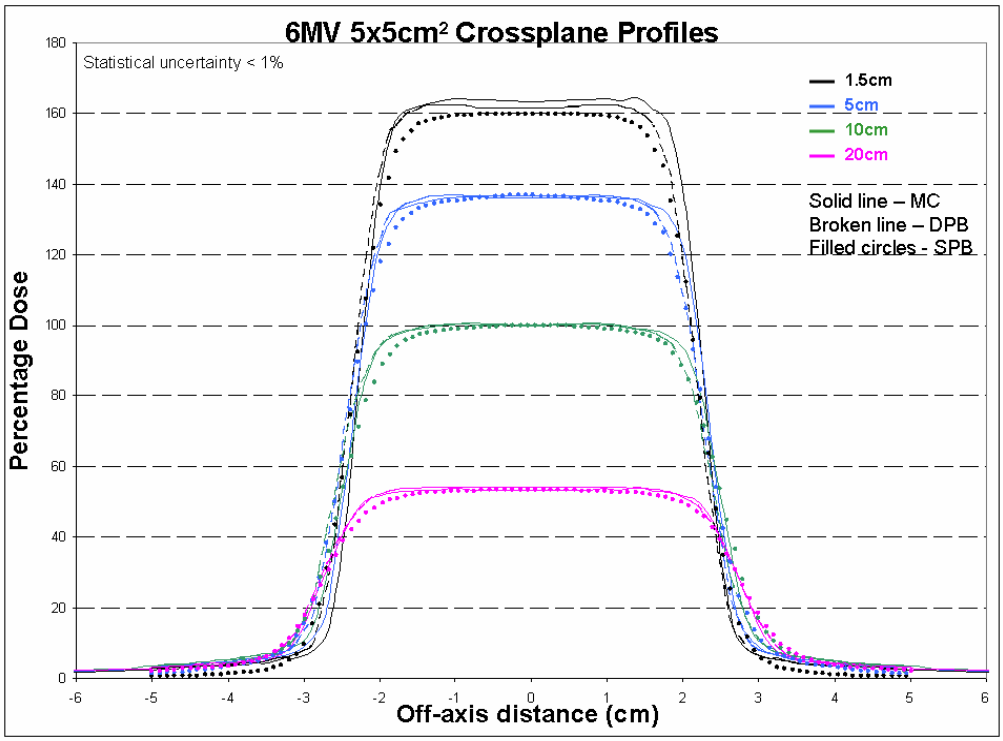

Figure 5.16 Comparison of the MC (solid lines) calculated dose distributions for a 2x2 cm^2 and 5x5 cm^2 field with the Double Pencil Beam (DPB; broken line) and Single Pencil Beam (SPB; filled circle) algorithms at depths of d_{max} (1.5 cm for 6 MV), 5, 10 and 20 cm.

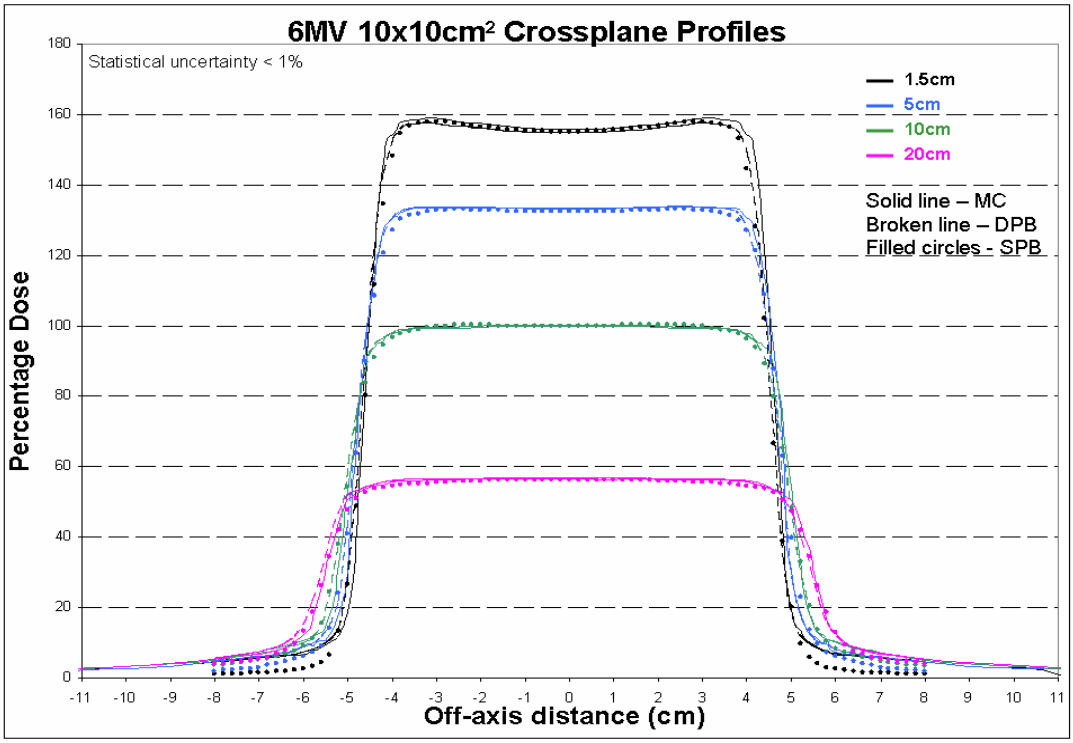

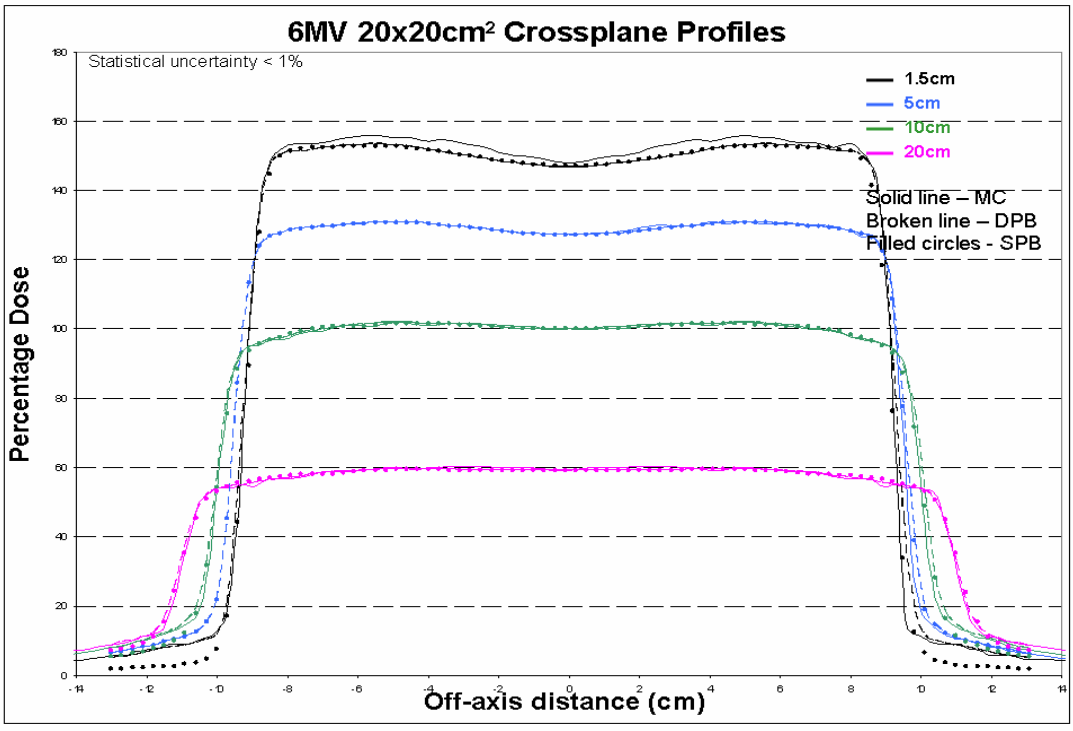

Figure 5.17 Comparison of the MC (solid lines) calculated dose distributions for a 10x10 cm^2 and 20x20 cm^2 field with the DPB (broken line) and SPB (filled circle) algorithms at depths of d_{max}, 5, 10 and 20 cm.

The 6 MV MC depth dose data are shown in figures 5.18 to 5.19 for the open fields, while MC and TPS comparative data are shown in figure 5.20. The PDD data were normalized to the dose value at the isocenter (10 cm depth) for each field.

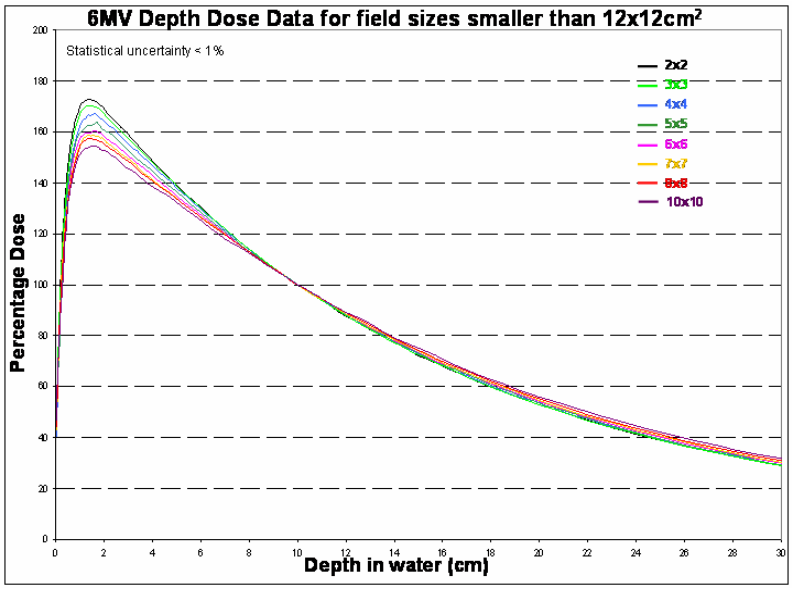

Figure 5.18

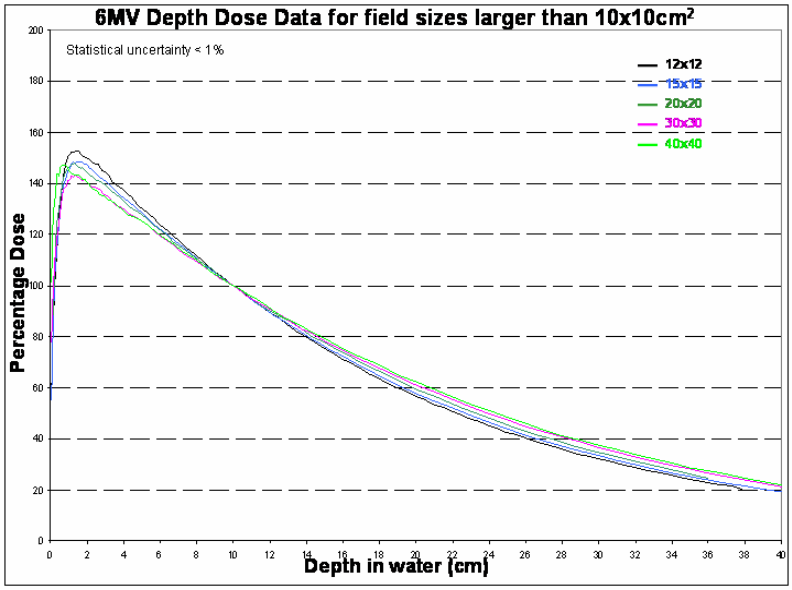

Figure 5.19

Figures 5.18 and 5.19 Depth dose data for the MC simulations used for TPS commissioning

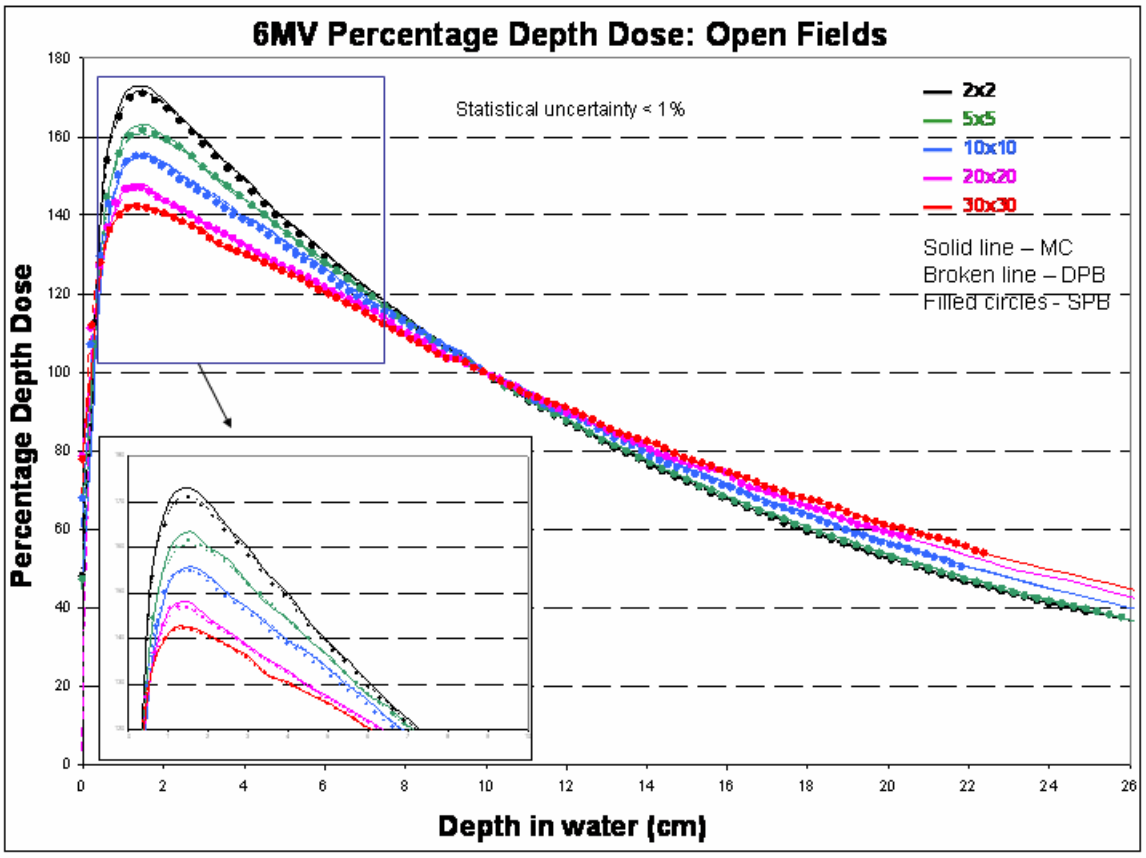

Figure 5.20.: Comparison of the MC (solid lines) calculated dose distributions with the DPB (broken line) and SPB (filled circle) algorithms for field sizes of 2x2, 5x5, 10x10, 20x20 and 30x30 cm^2. The curves are normalized to 10 cm depth. An expanded insert of the region surrounding the depth of maximum dose buildup is shown.

It can be seen on the PDD curves that larger field sizes show increased dose with depth in the phantom compared to the same depth position in smaller field sizes. This is a result of increased phantom scatter towards the CAX leading to a "lift" in the tail of the PDD curve. The effective energy of the beam is somewhat field size dependant due to more soft x-rays contained in larger fields, but this energy dependence is not nearly as pronounced as the phantom scatter effects. This is evident from the lower d_{max} value when PDDs are normalized to 10 cm depth as a result of higher doses in the exponential

tail of the PDD curve beyond the position of maximum dose. With an increase in phantom scatter with field size comes an increase in dose with depth.

The TPS imported MC dose profiles for the 15 MV dataset are shown in figures 5.21 to 5.34. PDDs, profile data and diagonals were generated for the same field sizes as for the 6 MV dataset. The profiles were generated at depths of d_{max} (of the 10x10 cm^2 field), 5, 10, 20, and 30 cm.

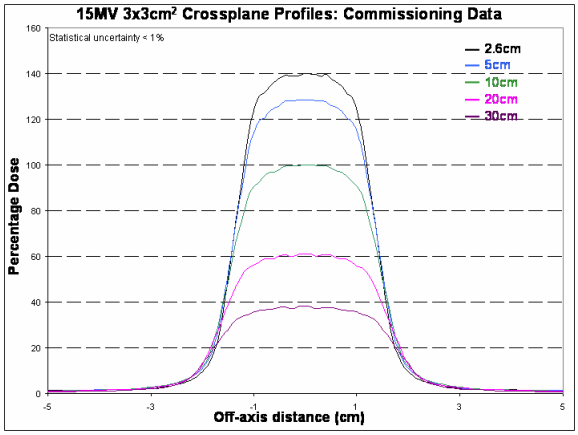

Figure 5.21

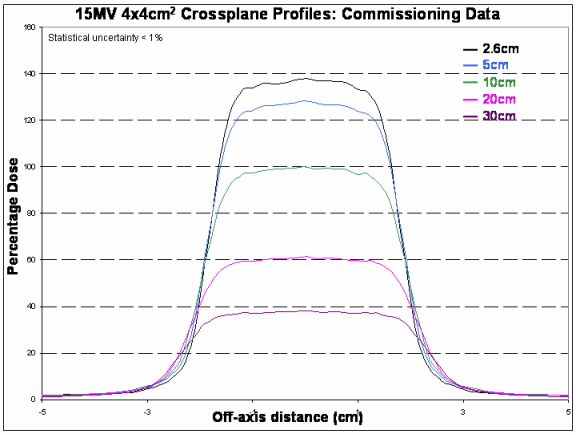

Figure 5.22

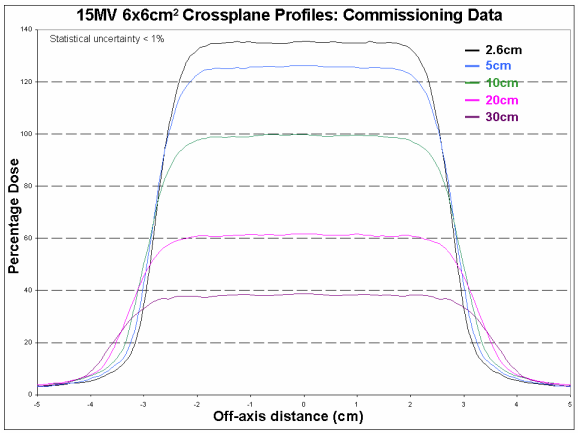

Figure 5.23

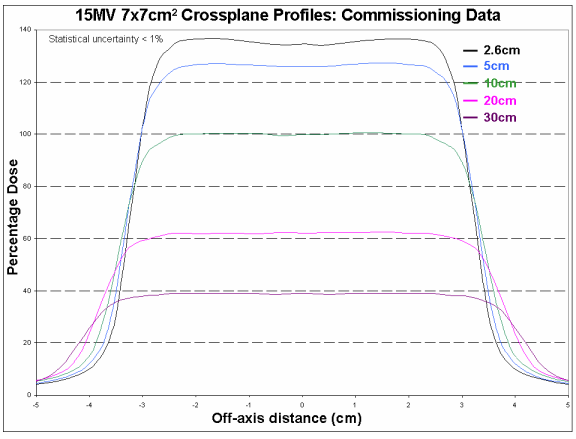

Figure 5.24

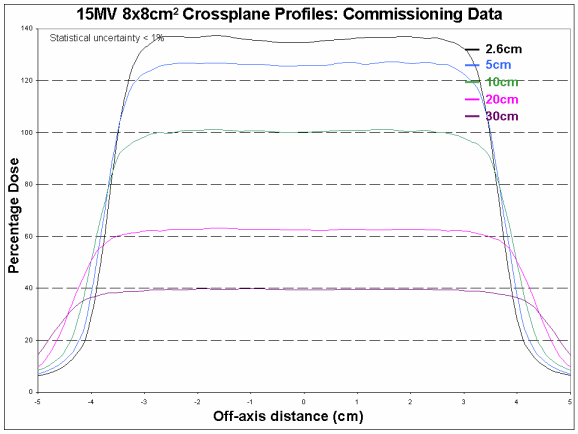

Figure 5.25

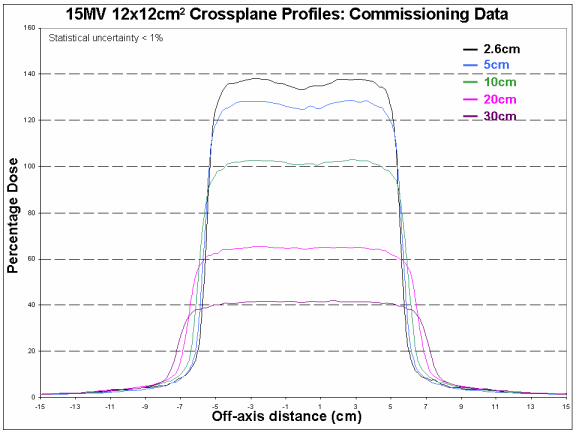

Figure 5.26

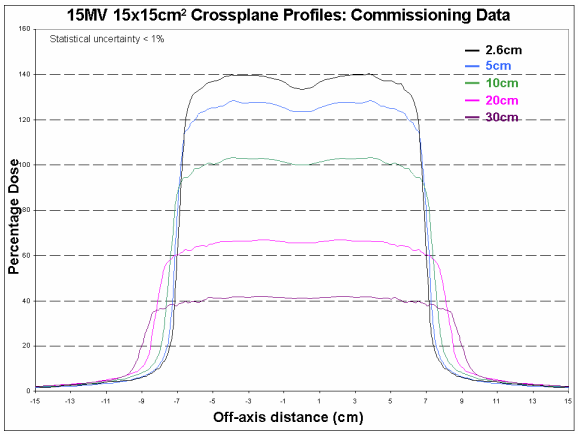

Figure 5.27

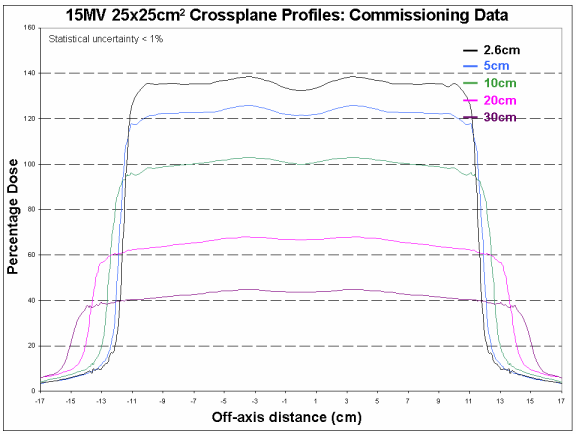

Figure 5.28

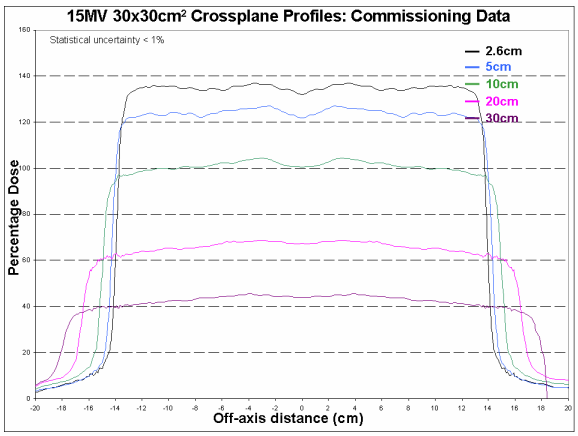

Figure 5.29

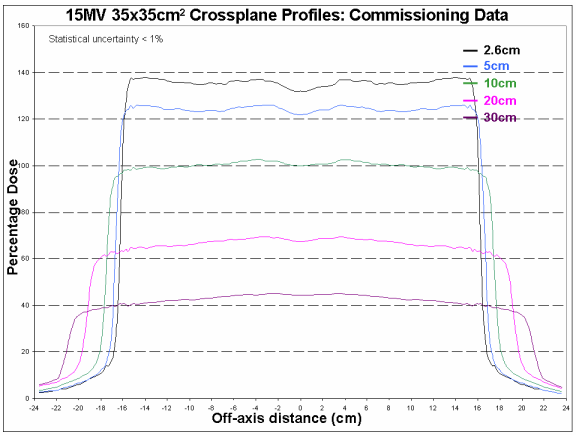

Figure 5.30

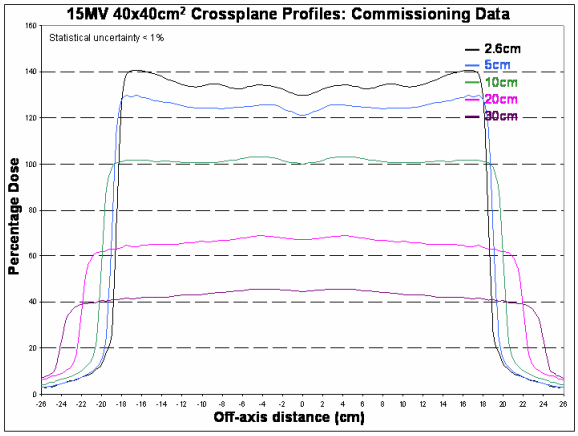

Figure 5.31

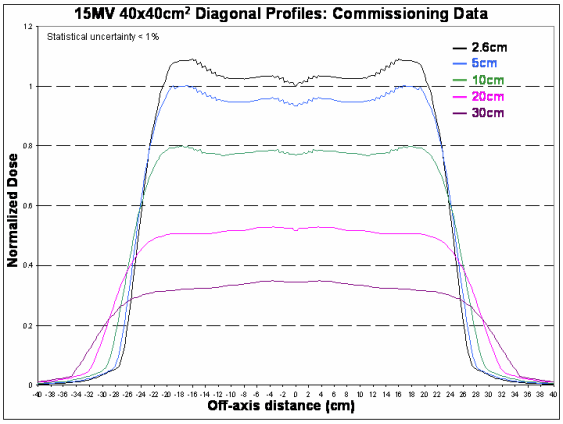

Figure 5.32

Figures 5.21 – 5.32 DOSXYZnrc generated profile import data.

Similarly to the 6MV data one can see by close inspection an increase in statistical noise in regions close to the beam penumbra or where it was deemed necessary to have accurate representations of fast changing dose gradients by utilizing smaller voxel sizes.

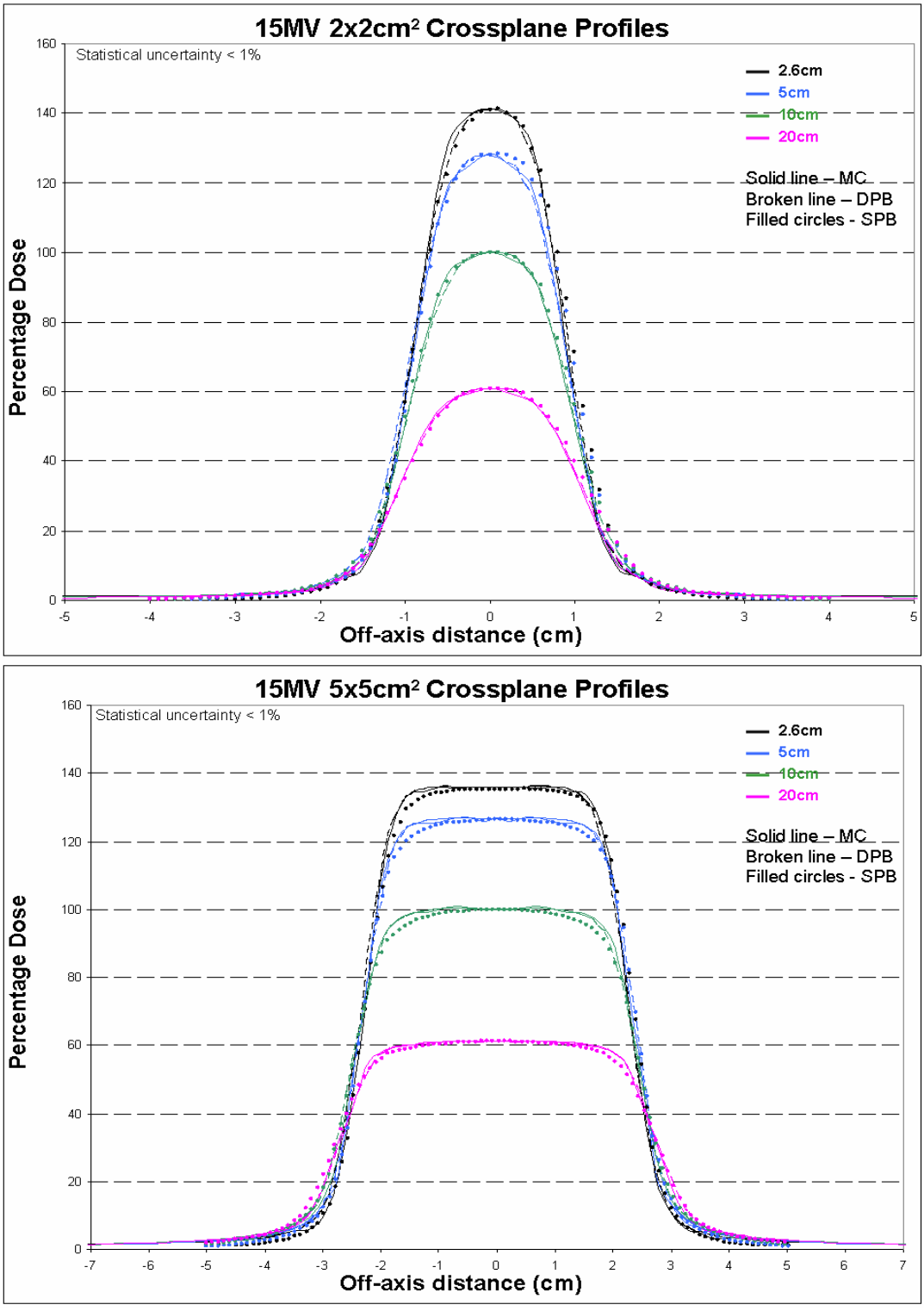

Figure 5.33 Comparison of the MC (solid lines) calculated dose distributions for a 2x2 cm^2 and 5x5 cm^2 field with the Double Pencil Beam (DPB; broken line) and Single Pencil Beam (SPB; filled circle) algorithms at depths of d_{max} (1.5 cm for 6 MV), 5, 10 and 20 cm.

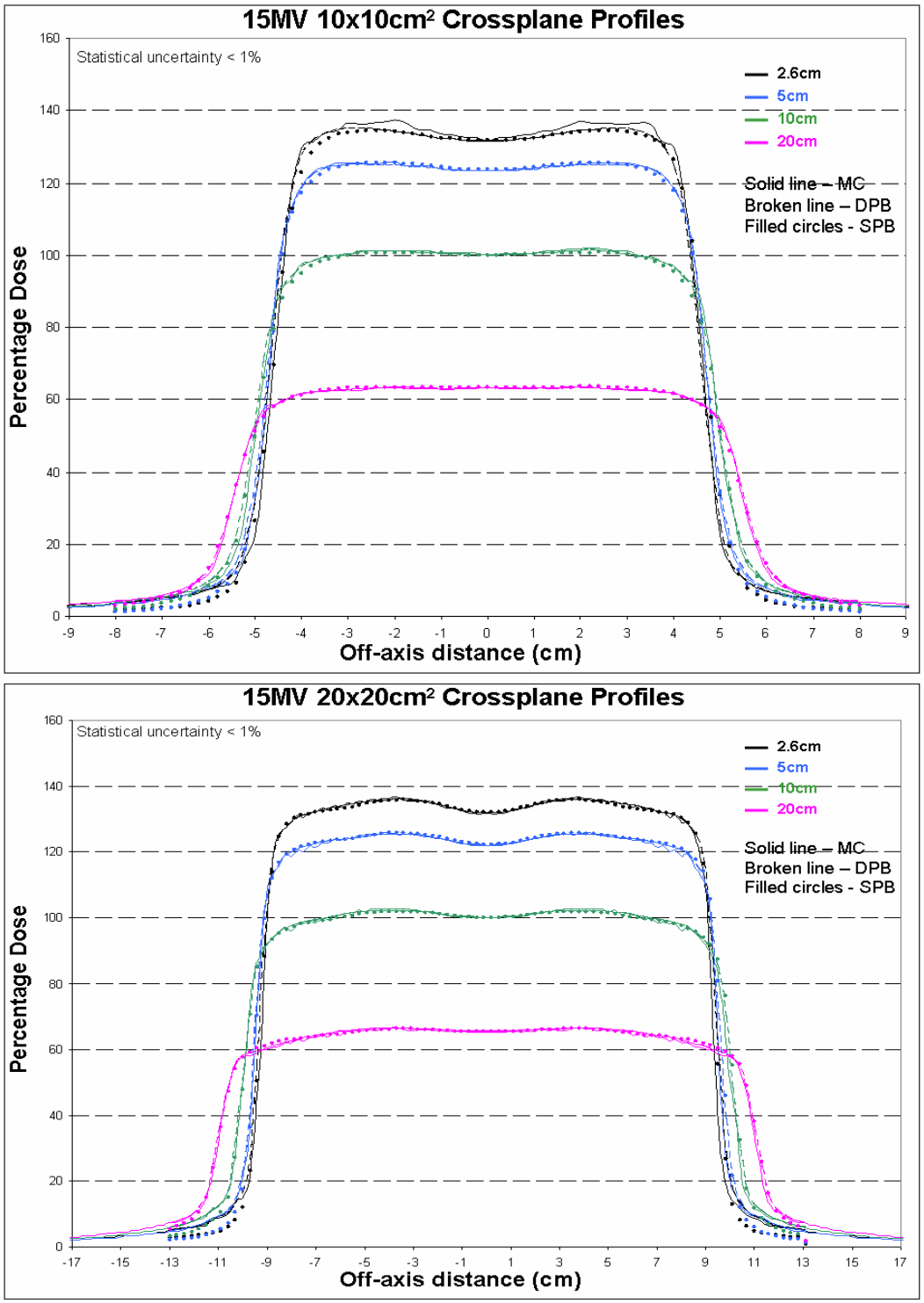

Figure 5.34 Comparison of the MC (solid lines) calculated dose distributions for a 10x10 cm^2 and 20x20 cm^2 field with the DPB (broken line) and SPB (filled circle) algorithms at various depths.

The 15 MV MC depth dose data are shown in figures 5.35 to 5.36 for the open fields. MC and TPS comparative data are shown in figure 5.37. The PDD data was normalized to the dose value at 10 cm depth for each field.

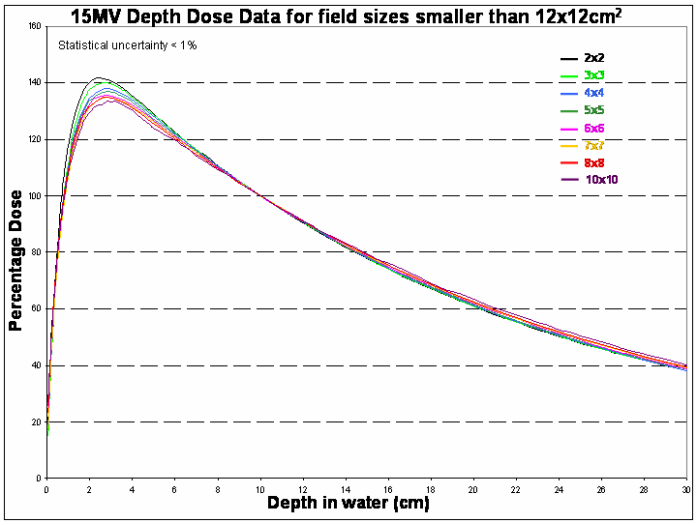

Figure 5.35

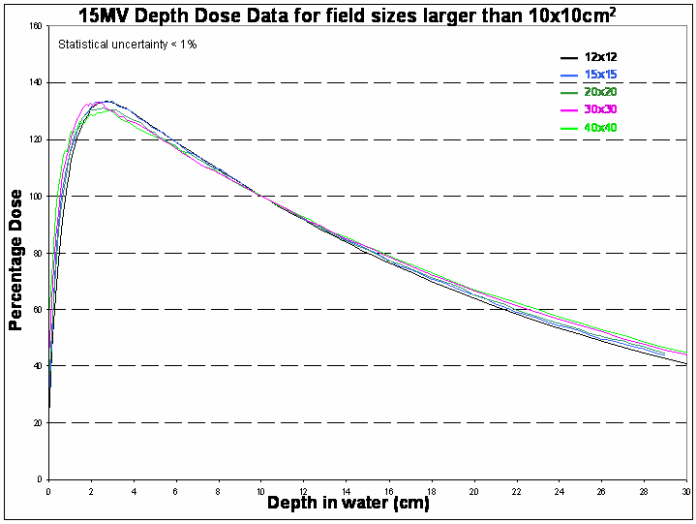

Figure 5.36

Figures 5.35 and 5.36 Depth dose data for the MC simulations used for TPS commissioning

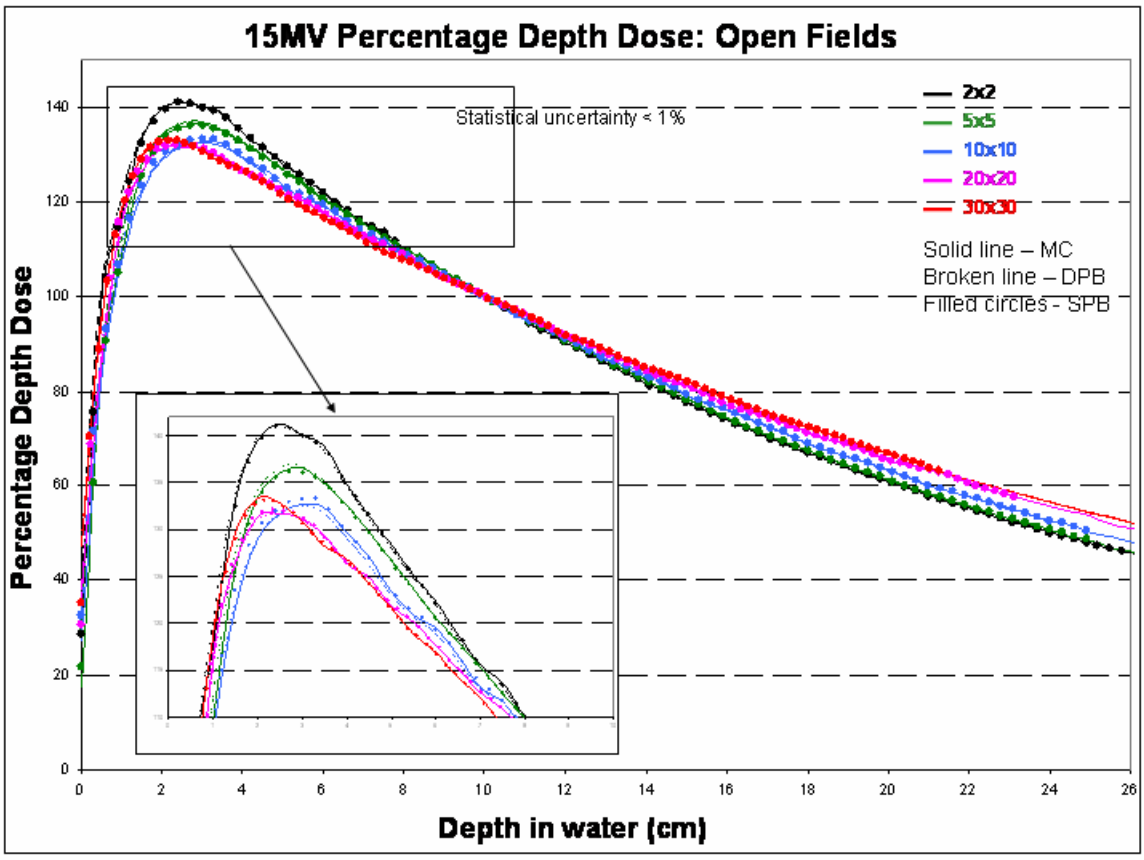

Figure 5.37 Comparison of the MC (solid lines) calculated dose distributions with the DPB (broken line) and SPB (filled circle) algorithms for field sizes of 2x2, 5x5, 10x10, 20x20 and 30x30 cm^2. The curves are normalized to 10 cm depth. An expanded insert of the region surrounding the depth of maximum dose buildup is shown.

The same trend is seen in the 15 MV input dataset results than for the 6 MV dataset. The PDD curves show a less steep tail for larger field sizes compared to smaller field sizes.

5.1.2.2. Blocked fields – CadPlan transmission and beam penumbra dose modeling

Profile data was generated with DOSXYZnrc simulations for partially blocked fields with side lengths of 10 and 25 cm. The profiles were generated at depths of d_{max}, 5, 10, and 20

cm. Two block shapes were investigated: a large cerrobend block that shields half of the radiation beam and a spinal cord block (1 cm width) to shield a thin section of the beam. Transmission factors for the cerrobend blocks and the PMMA block tray were calculated by taking the ratios of blocked and unblocked field dose values at d_{max} (as described by the CadPlan user's and dose calculation manual). Transmission factors are used during dose and MU calculations for treatment planning. The relevant data for the 6MV modality is shown in figures 5.38 to 5.39 and figures 5.40 to 5.41 for 15 MV. Some of the profiles also include the SPB and DPB data for comparison with MC simulations and TPS calculations.

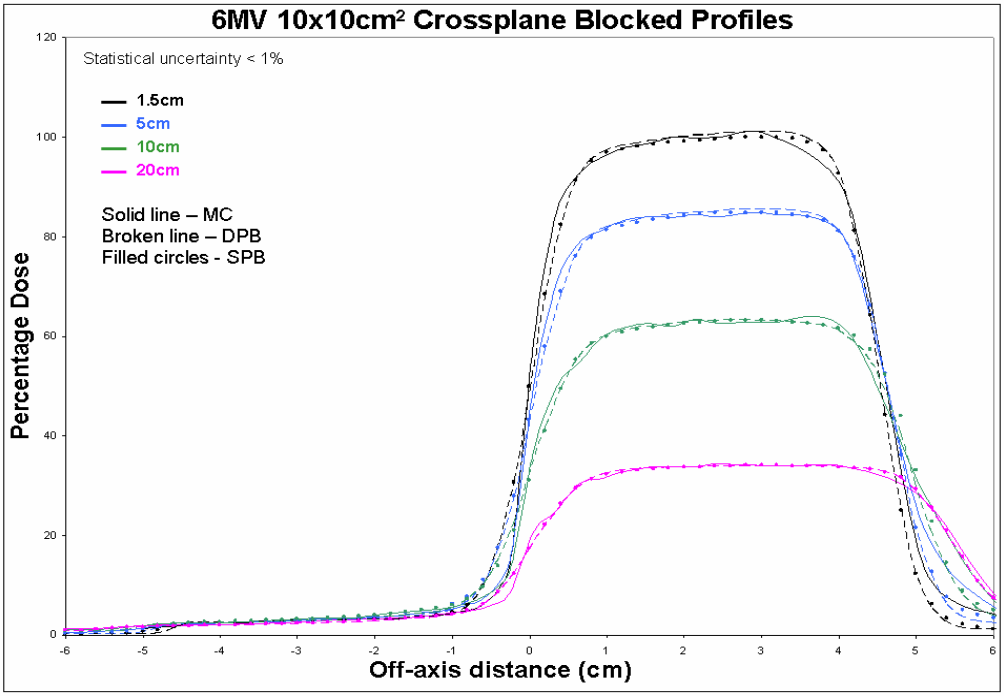

Figure 5.38 Comparison of the MC (solid lines) calculated dose distributions for a 10x10 cm^2 half blocked field with the DPB (broken line) and SPB (filled circle) algorithms at the indicated depths. The profiles are normalized to d_{max} of the effective axis depth dose curve.

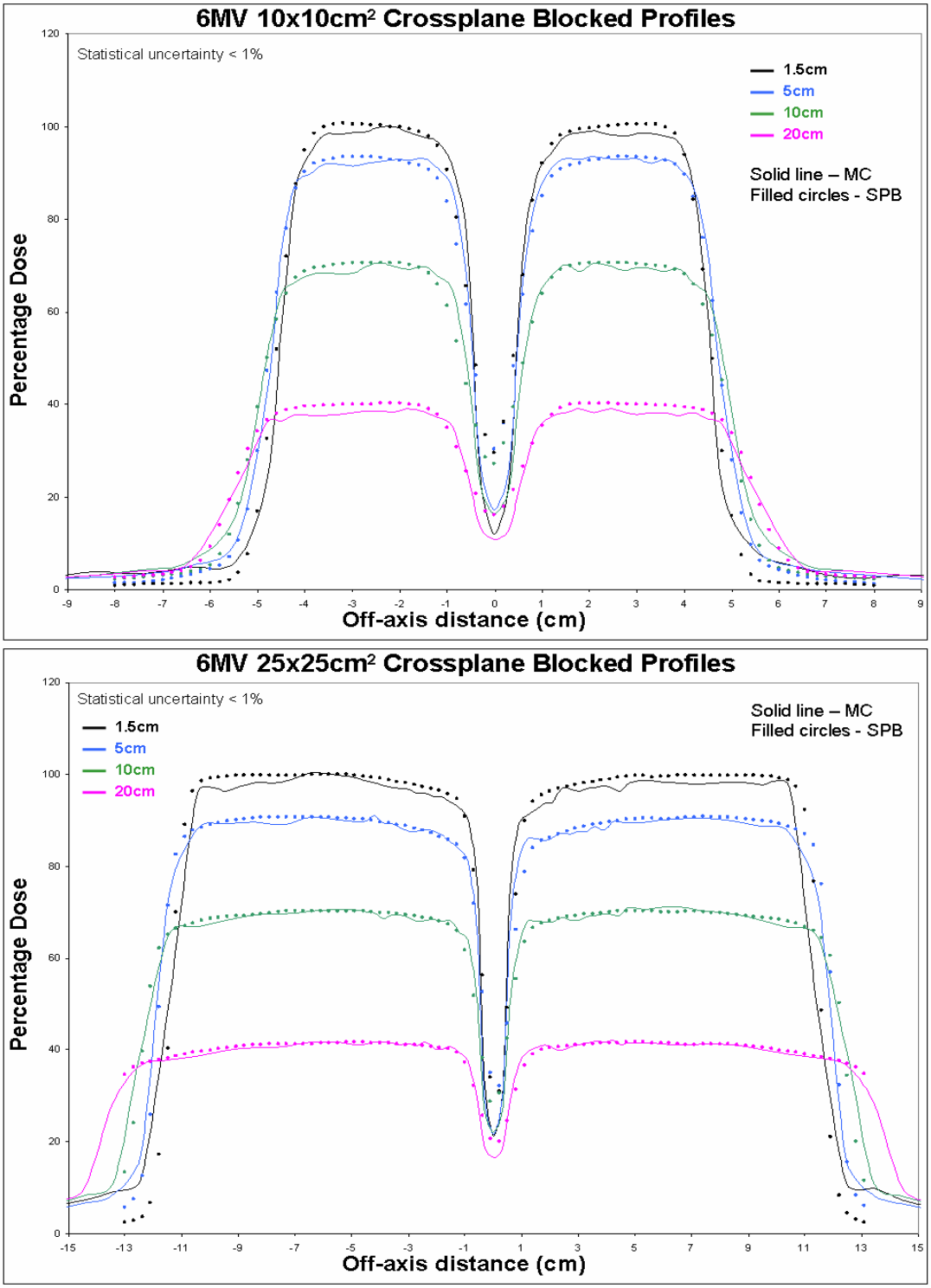

Figure 5.39 Comparison of the MC (solid lines) calculated dose distributions for a 10x10 cm^2 and 25x25 cm^2 spine blocked field with the SPB (filled circle) algorithm at the indicated depths. The profiles are normalized to d_{max} of the effective axis depth dose curve.

The same field sizes were used for the evaluation of blocked field calculations for 15 MV. The profiles were generated at depths of d_{max} (of the effective axis depth dose axis), 5, 10, and 20 cm.

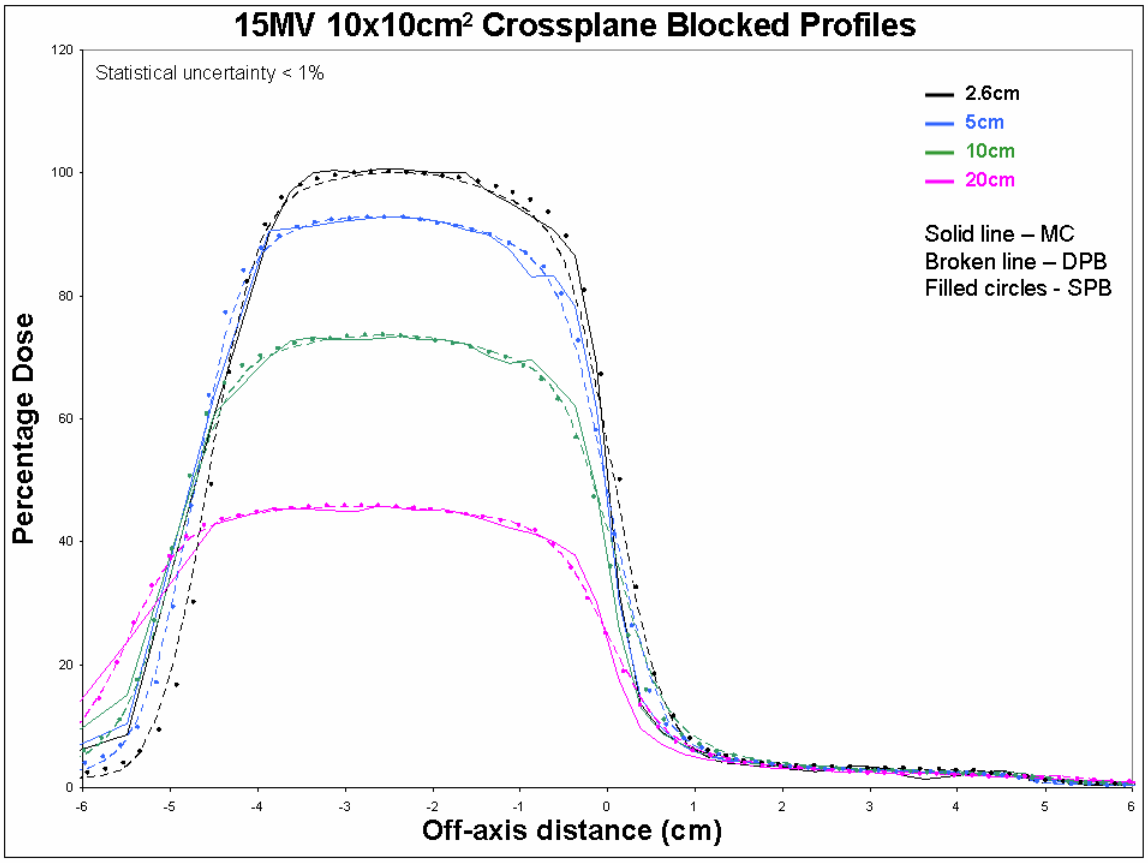

Figure 5.40 Comparison of the MC (solid lines) calculated dose distributions for a 10x10 cm^2 half blocked field with the DPB (broken line) and SPB (filled circle) algorithms at the indicated depths.

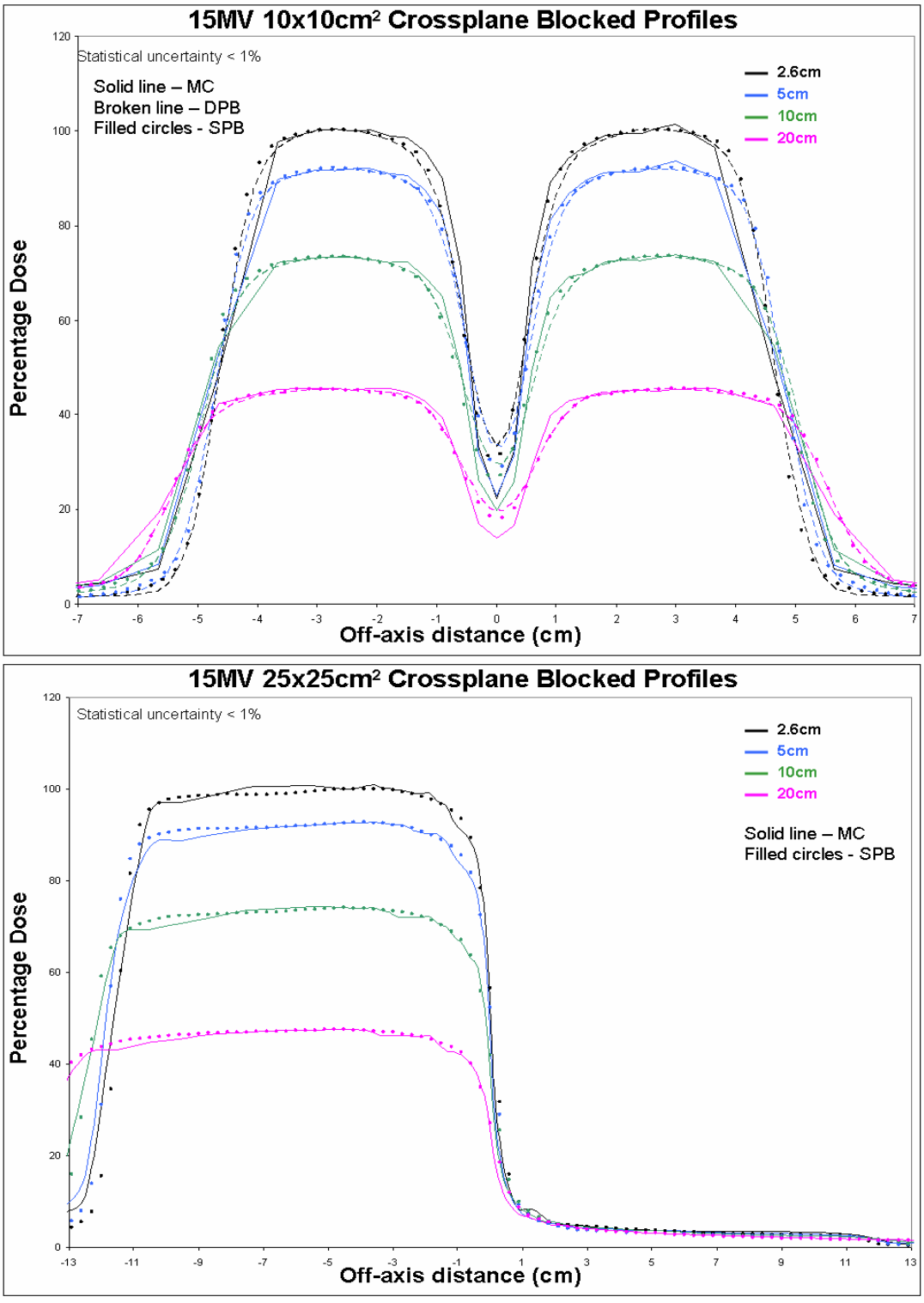

Figure 5.41 Comparison of the MC (solid lines) calculated dose distributions for a 10x10 cm^2 spine blocked and 25x25 cm^2 half blocked field with the DPB (broken line) and SPB (filled circle) algorithms at the indicated depths. The profiles are normalized to d_{max} of the effective axis depth dose curve.

The cerrobend block transmission factors implemented in the TPS for the two energies were 0.22 and 0.31 for 6 MV and 15 MV respectively. The block tray factors were 1.031 and 1.027 for the two energies respectively. The block transmission factor is used in the dose distribution calculation underneath the blocks, but the block tray factor is only used in MU calculations.

5.1.3. Evaluation of the TPS dose calculations accuracy in a homogeneous water equivalent phantom

The TPS uses the imported beam data to generate radiation machine beam specific parameters and variables. These parameters are used during dose calculations employing convolution methods. TPS acceptance and QA tests ensure that the imported data were entered correctly. Evaluations of the calculation algorithms ensure accurate dose calculations by the TPS when compared to the original input data.

Various field sizes are typically used in clinical treatment planning procedures and dose distributions should be evaluated for a representative set of these field sizes. This ensures that all possible discrepancies between measured and calculated dose distributions can be accounted for. Comparative water phantom data generated by DOSXYZnrc and the TPS for open fields are shown in figures 5.16 to 5.17 and 5.20 for 6 MV and figures 5.33 to 5.34 and 5.37 for 15 MV. The comparative water phantom data for blocked fields are

shown in figures 5.38 to 5.39 for the 6 MV data and figures 5.40 to 5.41 for the 15 MV data.

Tables 5.1 to 5.2 show the results of the 6 MV data analyses where confidence limit values were calculated with detailed verification of the TPS dose calculations for open field PDDs, profiles and blocked profiles. These confidence limit values can be compared with the tolerance criteria in the last column of the tables. The data summarizes the open and blocked field data for all the field sizes simulated and calculated in this study, except the 3x3, 6x6, 12x12 cm^2 and diagonal fields which where not deemed necessary. Venselaar et. al[4] have proposed to calculate a single δ value that is descriptive of the accuracy performance of the TPS, considering deviations in calculated dose distributions from the measured ones for all points in the dose datasets.

In this study, however, the different evaluated regions described for PDD and profile data were reported separately to clearly outline regions where inaccuracies were found. The reason for not reporting a single δ value is because an acceptable representative single value can be found for a TPS algorithm evaluation, but it does leave the opportunity for regions where large discrepancies are found, not being pointed out. This could have serious consequences where, for example, the spinal cord in a treatment plan is to be shielded off and the TPS dose deviates by 10% from the measurement data just outside the field. In such a case the spinal cord could potentially receive 10% higher dose than what was planned leading to paralyses if the tolerance dose was breached. A single δ value, if all other regions showed small deviations, will not point this fact out.

Table 5.1 Summary of the test procedures done on the CadPlan commissioning dataset for the 6 MV Double Pencil Beam (DPB) calculations. Calculated values are shown for the different tests for various geometries and regions, which include the number of points, the mean deviation of the points from the MC data, the standard deviation of the calculation points from the MC data and the confidence limits for the calculated data.

Description of geometry	Tolerance (δ)	Number of points	Mean deviation	Standard deviation	Confidence limit	Tolerance
Square fields	δ_1	268	0.79%	0.263%	1.19%	2%
Square fields	δ_2	72	< 2 mm		< 2 mm	2 mm
Square fields	δ_3	1312	-0.33%	1.17%	2.08%	3%
Square fields	δ_4	226	0.91%	1.22%	2.74%	3%
Square fields	RW_{50}	150	0.68 mm	0.11 mm	0.85 mm	2 mm
Square fields	δ_{50-90}	384	-0.62 mm	0.25 mm	0.99 mm	2 mm
Block field	δ_3	264	2.16%	0.63%	3.11%	3%
Block field	δ_4	56	1.83%	2.92%	6.21%	3%
Block field	δ_{50-90}	46	1.53 mm	0.64 mm	2.49 mm	2 mm

Table 5.2 Summary of the test procedures done on the CadPlan commissioning dataset for the 6 MV Single Pencil Beam (SPB) calculations. Calculated values are similar to table 5.1.

Description of geometry	Tolerance (δ)	Number of points	Mean deviation	Standard deviation	Confidence limit	Tolerance
Square fields	δ_1	268	1.08%	0.19%	1.38%	2%
Square fields	δ_2	72	< 2 mm		< 2 mm	2 mm
Square fields	δ_3	1312	1.66%	0.281%	2.08%	3%
Square fields	δ_4	226	-0.03%	2.27%	3.73%	3%
Square fields	RW_{50}	150	1.56 mm	0.99 mm	2.32 mm	2 mm
Square fields	$\delta_{50\text{-}90}$	384	-1.57 mm	1.13 mm	3.26 mm	2 mm
Block field	δ_3	264	0.70%	1.37%	2.75%	3%
Block field	δ_4	56	4.31%	2.13%	7.5%	3%
Block field	$\delta_{50\text{-}90}$	46	0.21 mm	0.57 mm	1.07 mm	2 mm

Tables 5.3 to 5.4 show the results of the 15 MV data analyses where confidence limit values were calculated with detailed verification of the TPS dose calculations for open field PDDs, profiles and blocked profiles.

Table 5.3 Summary of the test procedures done on the CadPlan commissioning dataset for the 15 MV DPB calculations. Calculated values are similar to table 5.1.

Description of geometry	Tolerance (δ)	Number of points	Mean deviation	Standard deviation	Confidence limit	Tolerance
Square fields	δ_1	308	0.60%	0.24%	0.96%	2%
Square fields	δ_2	128	< 2 mm		< 2 mm	2 mm
Square fields	δ_3	1398	-0.37%	0.84%	1.62%	3%
Square fields	δ_4	310	0.37%	0.897%	1.71%	3%
Square fields	RW_{50}	152	0.40 mm	0.07 mm	0.51 mm	2 mm
Square fields	δ_{50-90}	374	0.94 mm	0.64 mm	1.45 mm	2 mm
Block field	δ_3	282	-0.16%	2.13%	3.35%	3%
Block field	δ_4	68	2.30%	1.21%	4.12%	3%
Block field	δ_{50-90}	80	0.83 mm	0.37 mm	1.38 mm	2 mm

Table 5.4 Summary of the test procedures done on the CadPlan commissioning dataset for the 15 MV Single Pencil Beam calculations. Calculated values are similar to table 5.1.

Description of geometry	Tolerance (δ)	Number of points	Mean deviation	Standard deviation	Confidence limit	Tolerance
Square fields	δ_1	308	0.56%	0.24%	0.92%	2%
Square fields	δ_2	128	< 2 mm		< 2 mm	2 mm
Square fields	δ_3	1398	-0.86%	1.29%	2.79%	3%
Square fields	δ_4	310	-0.20%	1.85%	2.97%	3%
Square fields	RW_{50}	152	0.90 mm	0.16 mm	1.14 mm	2 mm
Square fields	δ_{50-90}	374	0.51 mm	1.57 mm	2.87 mm	2 mm
Block field	δ_3	282	-0.37%	0.896%	1.71%	3%
Block field	δ_4	68	1.87%	1.41%	3.98%	3%
Block field	δ_{50-90}	80	0.98 mm	0.64 mm	1.93 mm	2 mm

From the compared PDD data (δ_1 and δ_2) it was found that the two algorithms displayed acceptable accuracy in reproducing the original MC input data for both energies. The only deviations found were in the buildup region with differences of more than 20% dose, but using the distance to agreement criteria in these regions showed that the tolerance of 2 mm was maintained. This criteria is used because the dose gradient change is more than 3% / mm. Calculated confidence limit values were less than 2 mm in distance which is acceptable. In the region beyond d_{max} the confidence limit values were well within tolerance. This correspondence is clear from the comparative PDD graphs and the overall performance of the TPS in producing the PDDs is very good. Similar results were found for the 6 and 15 MV PDD data.

The profile results for open beams showed good agreement in the open, central part of the beam (80% of the geometrical field size). Discrepancies of up to 3% are found in the beam fringe (distance from the 50% to the 90% dose points). Both pencil beam algorithms underestimate the dose in these regions with the SPB showing the largest deviations. The DPB algorithm shows better agreement compared to the SPB that breaches the tolerance value when the confidence limit values are evaluated.

Deviations get smaller with increased field size, but overall the SPB fails in these regions ($\delta_{50\text{-}90}$) even when considering the 1% variance on the MC data. Consequences of these deviations may be that larger field sizes are used for tumor dose coverage than that actually required. In the 6 MV SPB case field sizes should thus be chosen to be slightly larger than what is currently chosen, while the 15 MV SPB case requires field sizes that

should actually be smaller. This is especially true for small radiation fields. The 6 MV DPB plans will also require a smaller field size selection for tumor dose coverage. The fact that larger fields will be selected during planning with the SPB algorithm results in OARs in close proximity of the tumor volume receiving higher doses than what will be calculated by the TPS. The problem lies in the fact that tolerance doses can be breached for OARs although the tumor volume may actually receive a more uniform dose with good coverage. This is quite a concern as the pencil beam algorithms, especially the SPB underestimates the dose underneath the jaws (δ_4) as will be seen in later discussions. This will lead to an additive underestimation of OAR dose close to the target volume.

Outside the geometrical field boundaries the TPS consistently underestimates the dose. Although the penumbra widths show less than 2 mm deviations from the input data and RW_{50} (radiological width; width of the profile measured at half the height of the CAX dose) deviates less than 2 mm for all but the 6 MV SPB data. The TPS calculated dose for the SPB decrease at a higher rate just outside the penumbra region resulting in large dose underestimation. The confidence limit values show that the inaccuracy for both algorithms is larger for the 6 MV data than 15 MV. The SPB just passes the tolerance criteria for the 15 MV data, while the DPB results are well within tolerance for both energies.

The 6 MV data evaluation shows that underneath the jaws the SPB and DPB algorithms underestimate the dose for small fields. This underestimation decreases with off-axis distance and with depth. The maximum deviation is found for the profile at d_{max}. With

increasing field size, the deviations become larger and it is clear from figures 5.16 and 5.17 that the SPB deviations are much larger than the DPB deviations. Again the trend in off axis distance and depth is repeated with the deviations decreasing in the same way. Local differences of more than 50% have been calculated, but as the dose is very low in these regions the deviation should be expressed in terms of dose on the central axis. This was found to vary from 3-4% depending on the field size between 2x2 cm^2 and 5x5 cm^2.

With field size increasing from 5x5 cm^2 to 10x10 cm^2, the SPB dose underestimation increases to 5-6% underneath the jaws, while the DPB deviations vary from 2-3% expressed as a percentage difference relative to the central axis dose. Deviations still decreased with off-axis distance and depth. For field sizes larger than 10x10 cm^2 the same trend was maintained and the SPB showed deviations from 5 to 8% while the DPB deviations actually start to decrease to 1-2%. These DPB differences may not statistically be significant as the uncertainty in the MC data is in the order of 1%. SPB deviations again decreased with depth and off-axis distance.

The DPB algorithm calculates depth dose values for irregularly shaped fields at different depths by utilizing the dose due to primary radiation and phantom scatter under conditions of electronic equilibrium. Off-axis ratios which modulate the depth dose are produced by the product of the envelope and boundary functions. The depth dose and boundary functions were computed by the convolution of a field intensity function and a scatter kernel and boundary kernel respectively. This convolution process leads to a depth dose value arising from a field intensity function convolved with a full phantom scatter

kernel and boundary function. The boundary function at specific off-axis points and different depths determines the shape of the penumbra region of the field, while the envelope profile considers the non-flatness of the beam. The primary radiation intensity function changes to transmission values underneath blocks and becomes zero underneath the jaws, resulting in only phantom scatter contributions to dose underneath the jaws.

The SPB utilizes only a single pencil kernel convolution with a similar field intensity function as was used in the DPB model. A correction factor is also used in combination with the pencil beam kernel that takes into account the variation of the primary photon fluence as a function of depth and off-axis distance. The scatter kernel from the phantom scatter at a reference depth is calculated for at least a 4x4 cm^2 field by differentiation of the scatter dose on the central axis of the beam. The intensity profile and scatter kernel is assumed to have rotational symmetry which changes a 2D integration to a 1D integration for calculation speed increase. The scatter kernel is computed with the intensity profile. As the intensity profile is more of a scatter profile (while the envelope profile is more a fluence modulating profile), the situation might arise where the scatter profile does not adequately account for the photon intensity close to the beam edge, or the scatter from the inside of the field to the outside is simply overestimated in this way. The intensity profile calculation seems reasonable and can probably be excluded in assessing the deviations found when comparing MC dose distributions with the SPB calculations. A possible reason for these differences underneath the jaws could be the combination of the scatter – and boundary kernels. As it is assumed that the boundary profile, corrected for photon scatter, is the result of the convolution of the missing part of the pencil beam kernel

(referred to as the boundary kernel) with a uniform square field (1 inside and 0 outside the field), the dose underneath the jaws may certainly be underestimated. As the non-uniformity of the field is already taken into account by the scatter profile, it seems like the generation of this profile leads to the underestimated dose in the beam fringe region while the boundary kernel could possible be over-correcting for phantom scatter.

Some of the consequences for these discrepancies for the SPB would typically be dose underestimations to OARs that lie just outside the geometrical field edge. These situations can again potentially be very serious when the OAR tolerance dose is in fact transgressed and the dose distribution data do not reflect the actual situation. Keeping in mind that, due to beam fringe dose underestimation and thus selection of larger field sizes during treatment planning, the total underestimation beneath the jaws can be an additive effect.

The result of dose discrepancies underneath the jaws can also be attributed to the fact that both the pencil beam models do not take extra-focal radiation into account as it does not explicitly simulate scattered radiation from the jaws and the flattening filter. The pencil beam algorithm calculates the dose outside the field due to phantom scatter only. Storchi et al[5] have stated discrepancies up to 3% outside the field at depths of 1.5 cm for a 6 MV beam and the error becomes less at deeper depths due to the fact that the effective source of the scattered photon is lower than the normal focus and is more diffuse. The mean energy of the scattered radiation is also lower than the mean energy of the beam and thus the contribution at greater depths outside the field becomes rapidly smaller.

The 15 MV SPB and DPB discrepancies underneath the jaws are very similar to the 6 MV discrepancies. Small field analyses show the same trends in decreased deviations with off-axis distance and increased depth. The trend is seen for all fields from the 2x2 to 10x10 cm^2 data. RW_{50} tends to be larger for the SPB algorithm compared to the MC and DPB data due to the wider penumbra of 1-2 mm. The discrepancies underneath the jaws are however smaller than those found in the 6 MV data analyses. Intermediate field sizes from 10x10 cm^2 and larger show differences in dose relative to the central axis dose of 3% for the SPB and 1-2% for the DPB. Considering the variance on the MC data, the DPB discrepancies for small and intermediate field sizes are not really discernable. Large field size data from 15x15 cm^2 and bigger show discrepancies of 5% underneath the jaws for the SPB and 1-2% for the DPB. As the beam size increases, the beam fringe in contrast to dose underneath the jaws and especially for the SPB which has the largest discrepancies, improves along with the width of the penumbra.

The blocked fields were also evaluated with the criteria as mentioned for the open fields. The intermediate sized 6 MV spine blocked fields showed some large discrepancies underneath the blocked region. The SPB analyses turned up with 18% overestimations of dose underneath the block for the profiles at d_{max}. These values decrease slightly to 17 and 16% at 5 and 10cm depth. Considering that spinal cords, eyes, optical chiasms, and other shallow situated OARs are found between 1 and 6 cm depths, the dose to these organs can thus be overestimated by the SPB. The DPB was found to be worse for these situations with more than 20% discrepancies for the same block setup. The beam fringes

and penumbras at the open-block interface were found to be slightly wider for the SPB than MC data and 2-3 mm for the DPB. Similar results for the fringes were found for half blocked intermediate and large field sizes for 6 MV, but the dose underneath the blocks were much more accurate and differences were not distinguishable within the variance of the MC dose data. Large spine blocked fields showed similar results as those of intermediate field sizes for the SPB which was evaluated here, being reported[5] to be more accurate than the DPB. Dose underneath the blocks were overestimated by the SPB resulting in wider beam fringes and penumbras. Overestimation of the dose was in the order of 10% underneath the block and a slight decrease in this error is found with increasing depth, mostly because the MC dose is "pulled" towards the surface due to scatter from the open part of the beam, and not due to scatter modeling of the SPB algorithm. On the dose profile graphs for blocked fields it might seem that there are large deviations in the penumbra regions on the beam edges between the MC and TPS data, but these regions were not analyzed for the blocked fields and thus their voxel sizes in those regions were large compared to the block penumbras so that simulation speed could be increased.

For the 15 MV intermediate half blocked field size the SPB and DPB algorithms show similar results compared to the MC data. Both deviate by just less than 2% underneath the blocked region. The blocked penumbra is larger for the TPS algorithms than for the MC penumbra. This is attributable to the fact that the pencil beam algorithms calculate an overestimated scatter or lateral fluence contribution due to the usage of the field intensity functions that changes in this region rather than a boundary profile forcing the penumbra.

Also, the block is situated closer to the water phantom in the MC simulation than the changed intensity distribution backprojected to the target for the pencil beam algorithms. The closer the block is to the water phantom, the sharper the penumbra due to the radiation source size and beam divergence. Again the penumbra regions on the outer field edges are not addressed here due to the larger voxel sizes used for increased simulation speed.

The spinal block for intermediate sized 15 MV fields showed penumbras wider by 2-3 mm in the open-block interface. Similar to the 6MV results, the dose is largely overestimated underneath the blocks by the TPS. The beam fringe is also overestimated by the pencil beam algorithms with the DPB being less accurate than the SPB. Errors seem to slightly decrease with depth. Dose differences underneath the blocks were 12.6% for the DPB and 8% for the SPB algorithm.

The results for large spine and half blocked fields of 15 MV beams were found to be very similar to the intermediate sized fields. Overall the SPB seemed to perform consistently with more accuracy than the DPB algorithm. Errors decreased with depth in the phantom in a similar way as the 6 MV data due to more phantom scatter dose calculated underneath the blocks with the MC method.

Storchi et al[5] have tested the SPB and DPB algorithms for a number of open and blocked photon field profiles in a water phantom, measured with ionization chambers. For small field sizes diodes were used as they have better resolution. They have stated that the

discrepancies between measured and calculated profiles have not exceeded 2% in the open part of the fields and 2 mm in isodose shift in the penumbra regions. However, they have found that the discrepancy exceeds 2% outside the field for depths smaller than 10 cm.

The DPB algorithm utilizes the intensity function convolved with a full scatter kernel and boundary kernel, while these are transformed to one kernel for the SPB algorithm. Only the field intensity function considers the fluence of the open region, while scatter and boundary kernels were calculated for open symmetric fields. The use of these kernels could lead to an explanation for the discrepancies in dose underneath blocks and close to the penumbra of the open-block interface. No electron contamination from the blocks, block scatter or scattered dose contribution from the open part of the fields is considered in such a method (although it is known that scattered dose contributions are quite low).

Another important aspect is that boundary profiles for both algorithms are determined from jaw positions of open symmetric fields. Block boundary profiles use these same jaw boundary profiles. When evaluating the MC blocked profiles, one realizes that the block position during the BEAMnrc simulation is much closer to the DOSXYZnrc phantom than the jaws. This is not considered by the two pencil beam algorithms and they only consider the boundary profiles for the jaws along with transmission factors for the blocks. Thus the pencil beam algorithms cannot reproduce the sharp penumbra of the blocks due to consideration of the x-ray source size, block SSD, phantom SSD and beam divergence. Due to the fact that the spinal block is quite thin, a small overestimation of the penumbra

in the open-block interface will lead to large overestimations of dose underneath the blocks.

Storchi et al[5] have also shown that the single pencil beam algorithm is much better than the double pencil beam algorithm and this is evident from their measurements and calculations of large asymmetric fields. They state that the extra-focal radiation outside the field seems to be dependant on the jaw position as, from their results in testing the algorithm, the contribution is less underneath a jaw near the CAX than one displaced far from it and the calculation also takes the phantom scatter into account.

The verification of their SPB algorithm in a water phantom for smaller field sizes (2x2 and 3x3 cm^2) showed some discrepancies, especially in the penumbra region. They do refer to the fact that the instruments used to measure the data play an important role in the measurement results. This fact, however, can be investigated if MC simulations are used to generate input datasets as the resolution of the voxels in these penumbral areas can be set to increase the accuracy (resolution) of the profile. They state that a detector with a resolution of better than 0.25 cm might improve the fit to the measured data. This was tested with MC simulations where voxel dimensions in the high dose gradient regions were set smaller than 0.25 cm. The higher resolution did improve the fitting of the inner part of the profile before the large dose gradient change near the penumbra, and the calculation of the boundary kernel seemed to be more accurate.

Further evaluation of the model by them included irregularly shaped fields where cerrobend blocks were used to evaluate the calculation and influence of the boundary kernel. They also found the dose underneath the jaws being underestimated. The lack of extra focal radiation not included in the calculation was prominent here again. They stated that the same effect leads to underestimation of the dose under a block in the center of a field and the discrepancy gets smaller at depths larger than 10 cm. However, in their study the block width was much larger than the one used in this study and thus the lack of extra focal radiation as a reason for the discrepancies may form only a part of the explanation for this phenomenon.

The consequences of these discrepancies could be summarized as follows:

Wider penumbra and RW_{50} – Better coverage of the PTV is found during treatment planning leading to marginal underdosage of the tumor during treatment. Treatment margins should thus be considered carefully.

Beam fringe underdosage – The SPB algorithm will require larger field sizes for PTV coverage when compared to the DPB and MC data. This could result in unnecessary overdosage of nearby OARs

δ_4 dose underestimation – The SPB algorithm will calculate doses to the OARs outside the geometrical field that are lower than will actually be received. The potential for transgressing dose tolerance is thus a reality. The situation is turned around when

evaluating dose under thin blocks as both algorithms show overestimation of the dose to shielded areas underneath blocks. Although the SPB is more accurate in this case than the DPB, dose to OARs will be overestimated leading to lower total doses that can be delivered to the PTV because of OAR tolerance.

5.1.4 Transformation of CT based patient models into a format suitable for DOZXYZnrc

Patient models are constructed from CT slice data. The CT images are converted to relative electron density matrices by the TPS with the use of a bi-linear graph relating CT number and relative electron density for soft tissues and high density bone. These equations are straight line fits to experimental data measured with a suitable phantom that have inserts with different relative electron densities.

The DOSXYZnrc code requires density of different tissues along with their cross-sectional PEGS4 data. The IDL program discussed in section 4.4 was able to extract CT numbers from the patient data file and convert them to relative electron densities. PEGS4 media of each voxel in the image dataset in the *.egsphant files were created from this data. The dimensions of all voxels are specified in the *.egsphant file along with the outer dimensions of the dataset. DOSXYZnrc could combine the radiation beam coordinate system with the patient CT model as set up in the egsphant file for dose calculations.

EGSnrc contains a code called CT create that can also produce *.egsphant file for a set of CT slices. Both codes allowed for the resizing and resampling of CT patient models so that objects like the CT scanner couch top could be excluded from the model. This was a requirement due to the fact that the patient contours defined on the TPS exclude these objects and are not considered during dose calculation. The only times these objects were included in the patient model for DOSXYZnrc simulations were for the case where the object was downstream of the patient surface. Patient immobilization devices were included in both the TPS and DOSXYZnrc patient models.

Immobilization devices outside the patient outline were excluded for dose calculations. The DOSXYZnrc dose calculations were done for the inclusive patient CT model. Any dose dicrepancies as a result of this can also be related to patient outline delineation differences between DOSXYZnrc and the TPS.

5.1.5. Comparison between the dose distributions calculated by DOSXYZnrc and the TPS for the SPB and DPB dose calculation algorithms in combination with the BATHO and ETAR inhomogeneity correction algorithms

5.1.5.1. Open field percentage depth dose and profile data for various clinical cases

In this section the differences between the dose calculations performed with DOSXYZnrc and the TPS Batho and ETAR inhomogeneity correction algorithms in combination with

the SPB and DPB convolution algorithms will be discussed. The focus is mainly on the SPB algorithm as this is the preferred method used for dose calculation. According to previous studies it has superior accuracy compared to the DPB algorithm and is recommended by the TPS vendors[5]. Various field sizes were used and they vary according to the clinical situation at hand in each of the different plans. The results of comparisons of the open fields in the clinical cases as mentioned in section 4.6.1, will be discussed.

5.1.5.1.1. Head and Neck plans

The head and neck cases involved the evaluation of 6 and 15 MV dose distributions. Although 15 MV x-ray beams will seldom be used for the planning and treatment of 3DCRT head and neck cancers, they were included in this study for dosimetric comparison. The evaluation of the head and neck cases consisted of single beam dose distribution comparisons using of PDDs and beam profiles, as well as 3D dose distribution analysis that includes dose volume histograms. The center figure in fig 5.48 shows a CT slice of the patient along with an indication of the beam angles that were used to produce the 3D dose distributions.

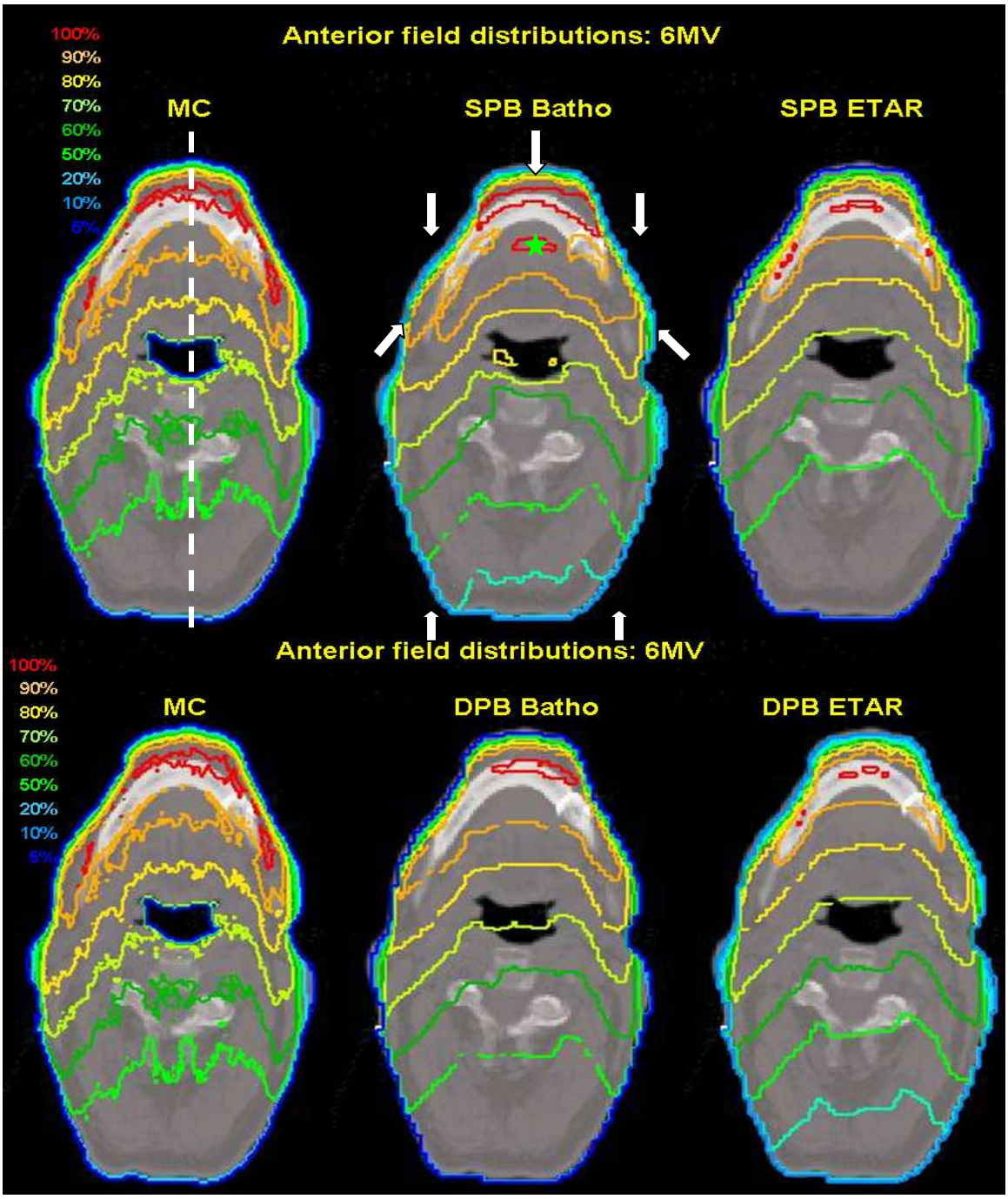

Figure 5.42 Comparison of the anterior 6 MV photon beam dose distributions on a dataset with missing tissue and inhomogeneity regions. The Monte Carlo (MC) distribution is shown along with the single pencil beam (SPB) and double pencil beam (DPB) dose distribution in combination with the Batho and ETAR inhomogeneity correction algorithms. The arrows illustrate the beam angles that were used to produce the combined beam dose distributions. The broken line is the position at which PDD curves were sampled for all cases shown.

Figure 5.43 shows a set of percentage depth dose curves sampled between two points as indicated by the white broken line on the upper left image in figure 5.42. The PDD data were extracted using a locally developed FORTRAN routine. The dose distributions in figure 5.42 were normalized to the dose at d_{max}, however, the PDDs in figure 5.43 are normalized to the ICRU reference point (position of the green star in fig 5.42).

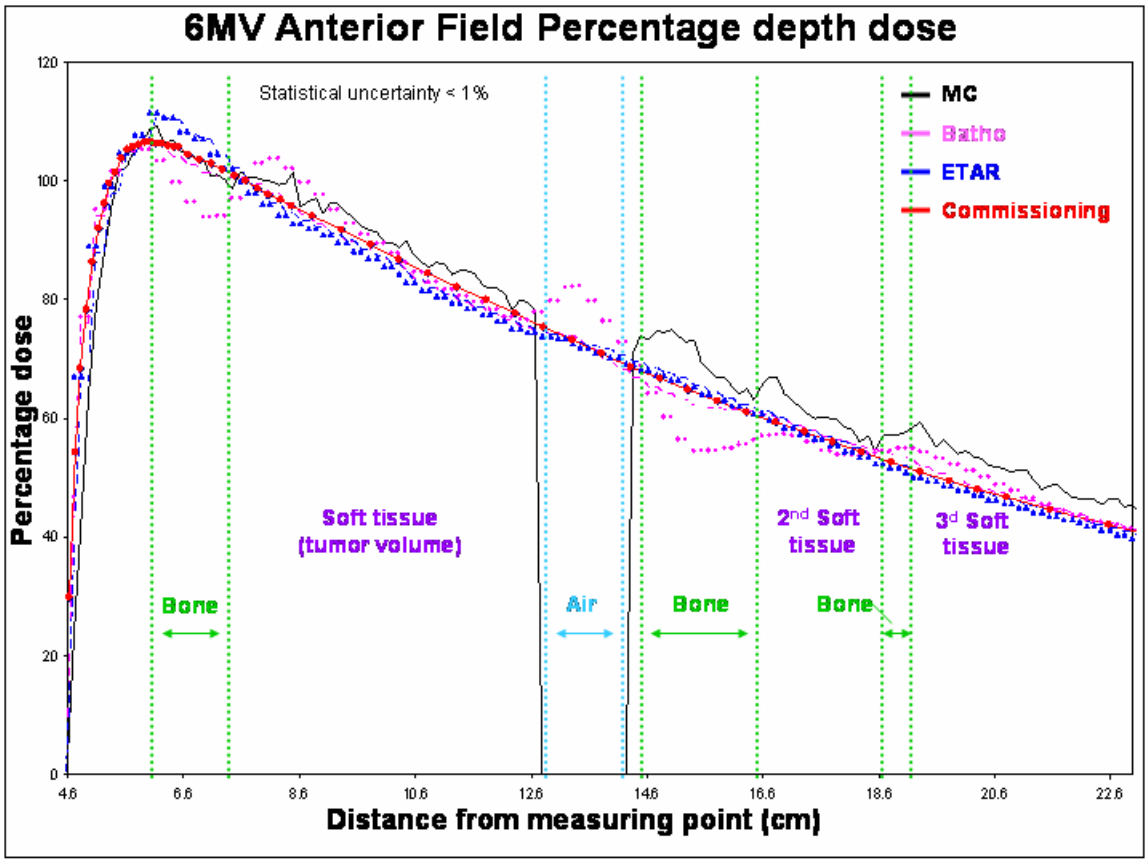

Figure 5.43 Percentage depth dose curves for the dose distributions in figures 5.42. The MC PDD curve (black line) has statistical uncertainty within 1%. The pink filled circles represent the SPB in combination with the Batho algorithm and the pink broken line the DPB Batho combination. The blue filled triangles is SPB in combination with the ETAR algorithm, the blue broken line the DPB ETAR combination and the red filled circle line is the same open field that was used during commissioning in a water equivalent medium.

In figure 5.43 the x-ray beam is perturbed by a series of bone regions. This apparently leads to hardening of the beam with depth as seen in the more penetrative power of the beam in the soft tissue region. This dose discrepancy may also be linked with the normalization dose value of the ICRU reference point. These beam effects are not accounted for by the pencil beam algorithms, even in combination with their heterogeneity correction algorithms and results in a slightly lower dose with depth in the soft tissue regions and particularly after the air cavity. Increasing discrepancies can be noticed with an increase in depth. MC shows a prominent increase in the absorbed dose after the air cavity since no beam absorption takes place here. Thus the fluence is higher leading to higher absorbed dose after the air cavity. The DPB and SPB algorithms do not account for this.

In the first bone region (jaw), the DPB algorithms overestimate the dose absorbed by the higher density bone, while the SPB Batho combination shows a reduced absorbed dose calculation. The deviations are in the order of 4% overestimation and 10% underestimation in this region compared to MC. Just in front of the bone region there seems to be small increase in dose as shown by the MC which can be a result of backscatter from the higher density bone. Once the beam passes through the bone and reaches the soft tissue, the MC curve has slightly higher dose values than the commissioning data which may be attributed to some beam hardening in the jaw. The SPB batho combination overestimates the dose at the entrance to the soft tissue region by approximately 4%. This can be due to a power law correction factor larger than 1. The ETAR algorithm in combination with both pencil beam (PB) algorithms underestimates

the dose in this soft tissue region due to an overestimation of the absorption of primary photons in the bone region.

As the depth increases until the oral cavity in the mouth is found, the MC curve shows a sudden drop to zero dose inside the air cavity. This dose in air was set to zero during the DOSXYZnrc simulation. The SPB Batho combination again overshoots in this air filled region. The ETAR algorithm in combination with the PB algorithms and the Batho in combination with the DPB algorithm acts as if this region is near water equivalent and shows little deviation from the commissioning data. Beyond the air cavity, the MC curve shows a re-buildup of dose in the spinal column. None of the combinations of the other algorithms realized the re-buildup of dose in this region. The SPB Batho combination largely underestimates the dose absorbed in this region. MC shows a small dose peak in the first centimeter or so of the 2nd soft tissue region. This is possibly due to scattered photons in the head that enhances the dose at this point on the PDD profile axis and the shape of the vertebrae. The ETAR PB algorithms follow the water curve from here on, while the SPB Batho combination shows an increase in dose when the final bone region is reached. In this region the MC curve again shows a rise in the absorbed dose with a further dose increase once soft tissue is reached in the third soft tissue region. This is possibly due to cumulative beam hardening and more primary photons reaching these regions due to less absorption in the oral cavity compared to the other algorithm models.

The dose distribution in the 2nd soft tissue region falls over the spinal column and brainstem. It is clearly seen that the PB algorithms all underestimate the dose to this

highly sensitive critical organ which may lead to paralysis if the tolerance dose is transgressed in such a treatment plan. Deviations vary from 5 to almost 15% local dose for the SPB Batho and SPB ETAR respectively.

In-between the jaw and oral cavity, where the tumor volume is found, the dose is underestimated by the SPB ETAR combination by 6 to 7 %, while the Batho algorithm combinations underestimate the dose by 4-5%. None of the TPS algorithms account for the loss of dose just in front of the air cavity. This is potentially a very serious deviation as the dose to tumors in close proximity decreases as no electrons are backscattered from the cavity. Underdosage can thus be found, especially at lower energies and may result in tumor recurrence. Difference in the MU calculations are 7% too high for the ETAR SPB combination, 6% too high for both DPB combinations and 3% for the SPB Batho combination. These MUs are compared to the MUs required to reach a certain dose at the ICRU point using the MC isodose data.

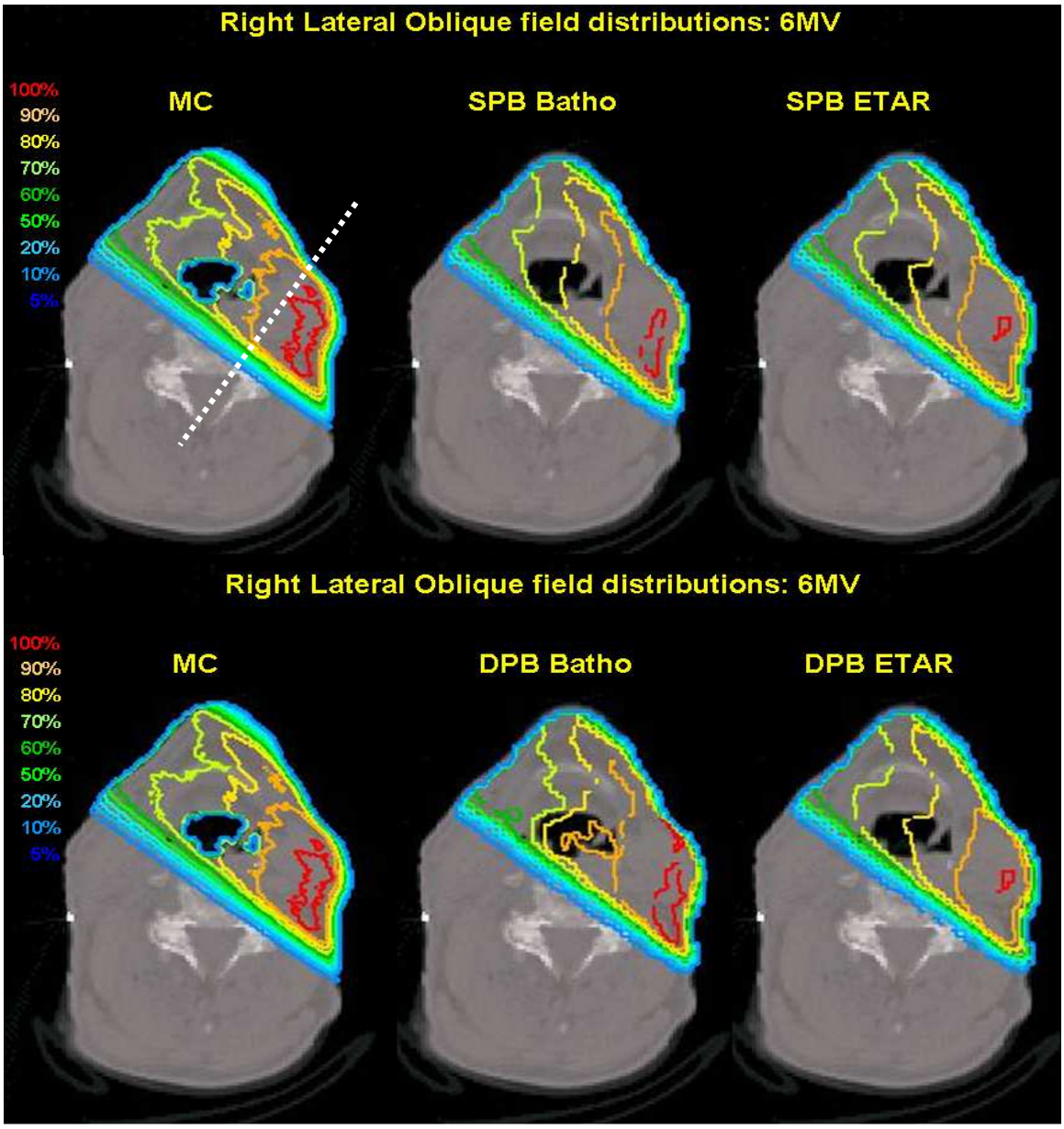

Figure 5.44 Comparison of the right lateral oblique 6 MV photon beam MC distribution, the SPB and DPB dose distributions in combination with the Batho and ETAR inhomogeneity correction algorithms.

Figure 5.44 shows the dose distributions of the right lateral oblique fields having one beam edge passing right along the skin surface of the patient. It is expected that secondary electron scatter from inside the skin surface to outside the patient would lead to a decrease in the dose close to the skin surface. It can be seen that the MC isodose

lines, especially the 70% and 80% isodose lines, tends to curve inward leading to lower doses close the skin surface. In comparison, the PB algorithms assume water equivalent media during the convolution process and the Batho algorithm does not consider lateral extent of inhomogeneities which lead to higher doses and incorrect scatter modeling in regions close to the skin surface.

The effect of the oral cavity is seen in a similar way as in the anterior field dose distributions. As no absorption takes place in the cavity, the x-ray fluence reaching the tissue downstream of the air is higher leading to higher absorbed dose values compared to a situation where no air was involved. The MC dose distribution shows this increased dose downstream of the air cavity and the ETAR algorithm also accounts for it. Only the SPB Batho combination corrects for this change in fluence while the DPB Batho fails in that respect.

The combination of all 7 fields (see figure 5.42 top center) leads to a distribution as depicted in figure 5.45. The PTV and GTV for this plan are also shown. DVHs were calculated for both these volumes and OARs defined for the the spinal cord and left parotid gland. The DVHs are shown in figure 5.46 and are the results of using 6 MV x-ray beams.

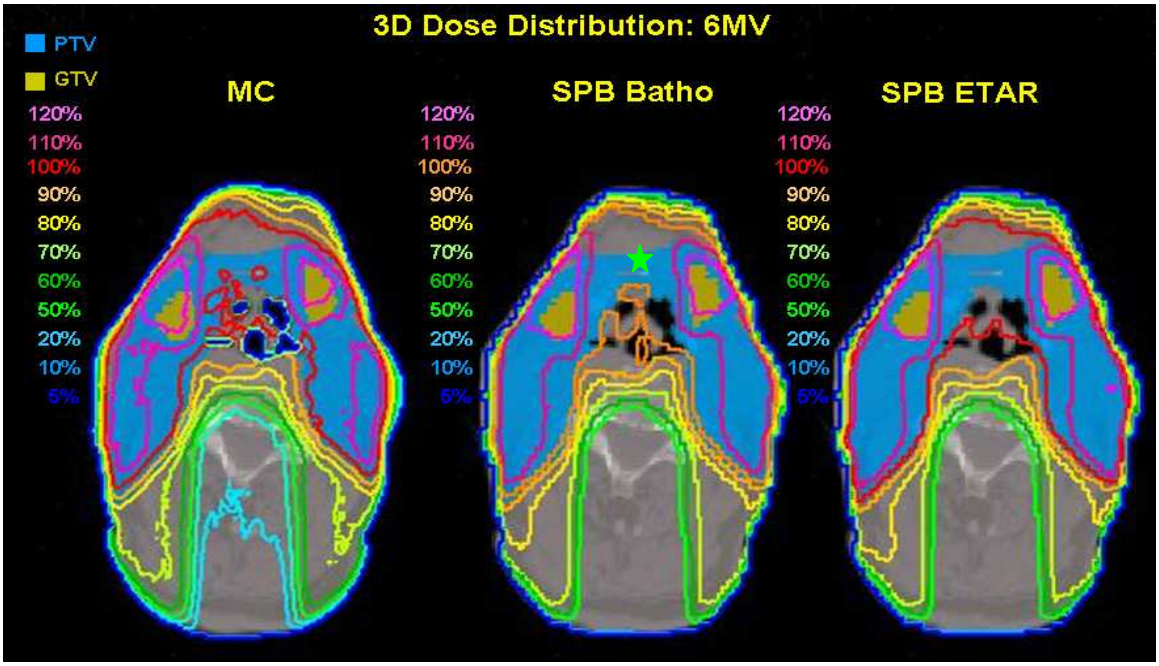

Figure 5.45 Comparison of the dose distributions of all seven beams for the 6 MV head and neck case. Dose volume histograms could be calculated from the delineated GTV (yellow) and PTV (blue). The OARs were not delineated on these images for clarity of isodose lines. The ICRU reference point is indicated by the green star.

The DVH was used to calculate the equivalent uniform dose (EUD) for each of the volumes. A total dose of 70 Gy was prescribed to the PTV, 84 Gy to the GTV (integrated boost) and the tolerance doses as shown in table 5.5.

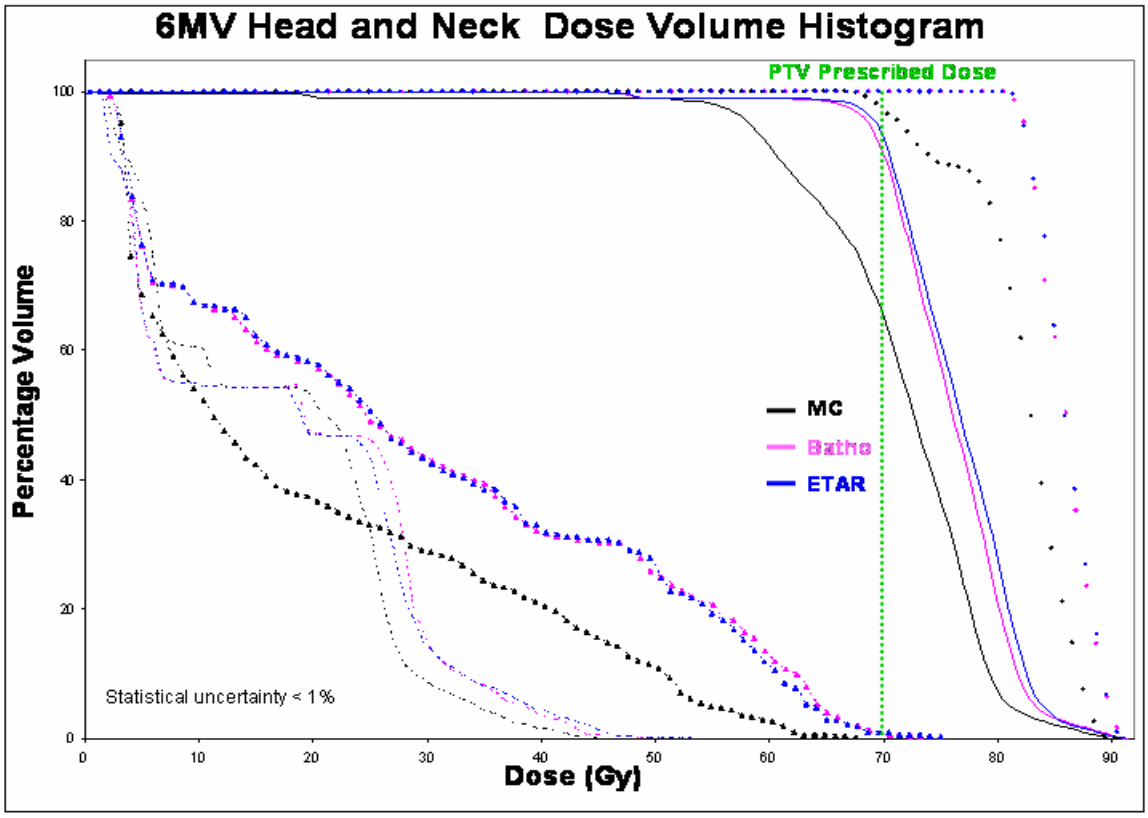

Figure 5.46 Dose volume histograms of the GTV (filled circles), PTV (solid lines), spinal cord (broken lines) and right parotid gland (filled triangle with broken line) for the MC (black) and SPB in combination with the Batho (pink) and ETAR (blue) algorithms in the head and neck case.

Table 5.5. Summary of the seven field 3D dose distributions for the 6 MV head and neck case in terms of EUD values. Prescribed and tolerance doses are also supplied.

Volume	**Prescribed dose (Gy)**	**Tolerance dose TD(5/5) (Gy)**	**EUD* (Gy)**		
			MC	Batho	ETAR
GTV	84.0		83.7	87.5	87.9
PTV	70.0		70.7	75.3	76.0
Spine		46.0	16.1	16.5	15.4
Parotid		45.0	18.2	26.6	26.6

* Survival Fractions were chosen as 0.55 for the GTV dose per fraction of 2.4 Gy, and 0.6 for the other organs and volumes.

Although the EUD values are within the tolerance for the OARs, the spinal cord has a serial functional sub unit architecture. This means that when one of the groups of cells in this organ is eradicated the whole organ loses its function. One must rather report the maximum dose to the spinal cord. In this case, the maximum doses were 44.9 Gy for the MC distribution, 51.4 Gy and 53.2 Gy for the Batho and ETAR algorithms respectively. If the maximum dose were used as a dose limiting factor then according to the TPS the dose to the tumor would have been lowered by 5-7% which might be clinically significant. According to the MC data this dose was within the tolerance limit.

The same procedure was followed in analyzing the 15 MV dose distribution. Figure 5.47 shows the anterior field dose distribution consisting of data for the SPB and DPB in combination with the two inhomogeneity correction algorithms. It was found that there are virtually no differences between the SPB and DPB dose distributions. Small differences between the Batho and ETAR methods compared to the MC data exist. The dose is underestimated in the tumor region and the total effect of reduced absorption in the oral cavity is not well modeled by the PB algorithms. This leads to a higher spinal dose as shown by the MC distribution. The dose on the patient's cheeks, close to the skin surface, is also lower in the MC calculated distribution. This is due to electronic disequilibrium not considered by the PB convolution technique and by either of the inhomogeneity corrections. Some dose buildup due to backscatter is found in front of all the bone regions and is not addressed by the PB algorithms.

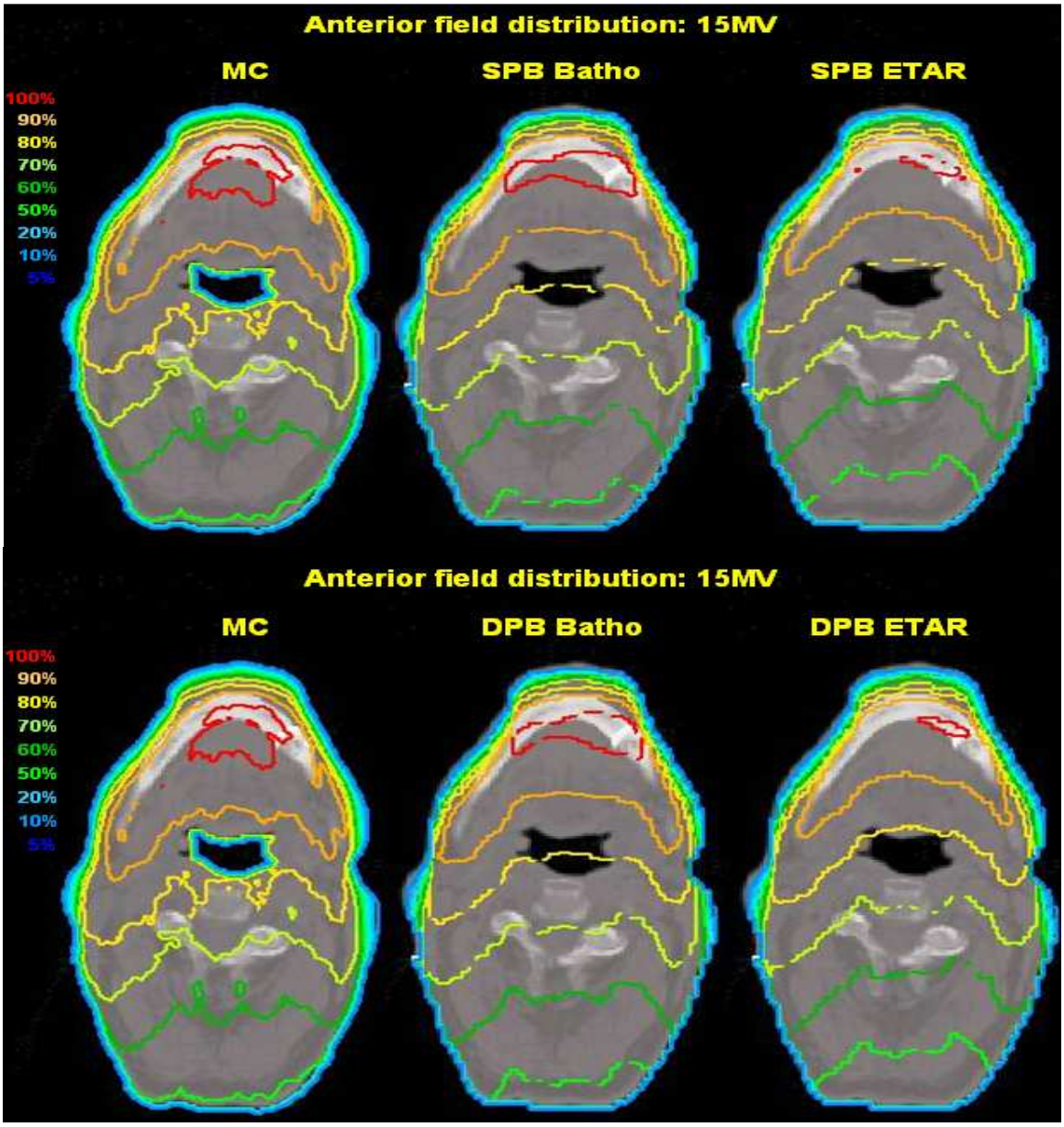

Figure 5.47 Comparison of the anterior 15 MV photon beam MC distribution and the SPB and DPB dose distributions in combination with the Batho and ETAR inhomogeneity correction algorithms.

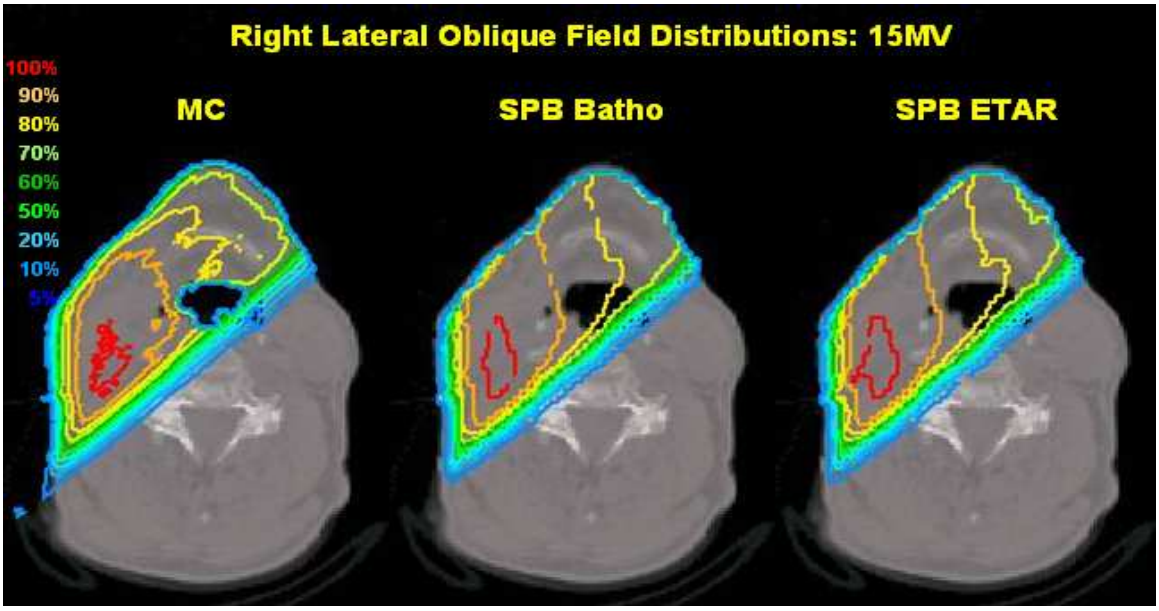

Figure 5.48 Comparison of the anterior 15 MV photon beam MC distribution and the SPB and DPB dose distributions in combination with the Batho and ETAR inhomogeneity correction algorithms.

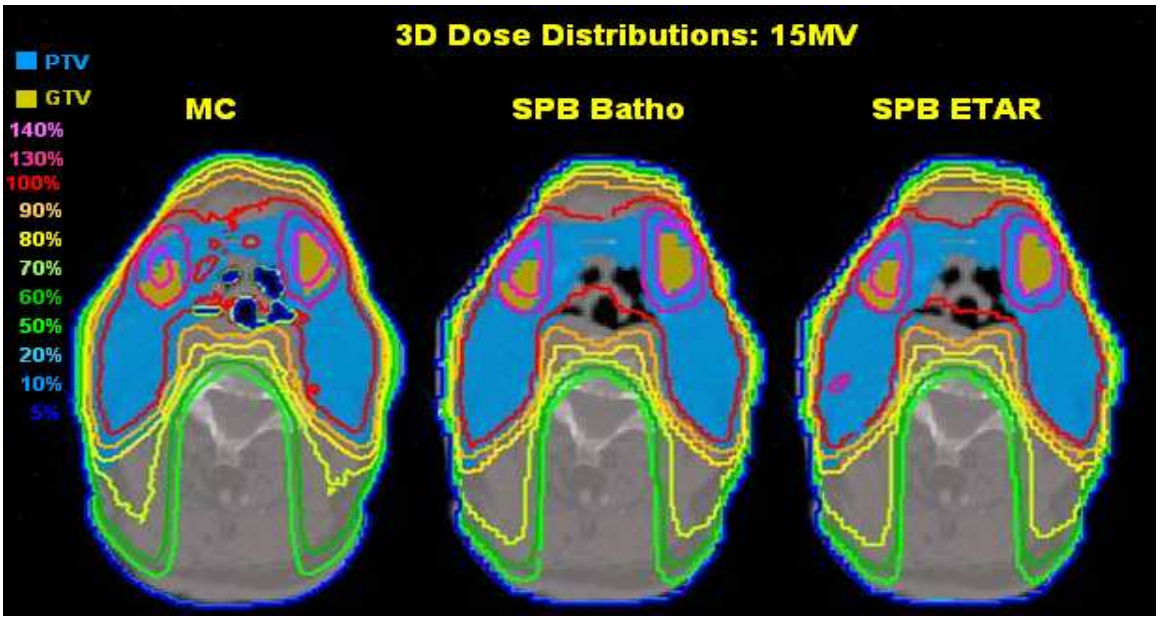

Figure 5.49 Comparison of the dose distributions of all seven beams for the 15 MV head and neck case. Dose volume histograms could be calculated from the delineated GTV (yellow) and PTV (blue). OARs are not delineated not these images for clarity of isodose lines.

The effect of lateral scatter in a situation where electronic equilibrium exists is illustrated in figure 5.48 for 15 MV x-rays. The effect of the oral cavity causes more penetration in the 15 MV x-ray beam that is not modeled by the TPS dose calculation algorithms. A secondary smaller cavity causes penumbra widening that is also not modeled by the TPS. The effect is however small.

Figure 5.49. shows the total dose distribution as a result of the combination of the 7 fields for the 15 MV case. On evaluation of the volumes located near the left and right cheek one can see that the TPS dose fit the volumes on this slice. The MC data clearly indicates that these structures are not fully covered in terms of the delivered dose. The dose is overestimated by the PB algorithms on this particular CT image as shown in the DVHs for the 3D dose dataset in figure 5.50.

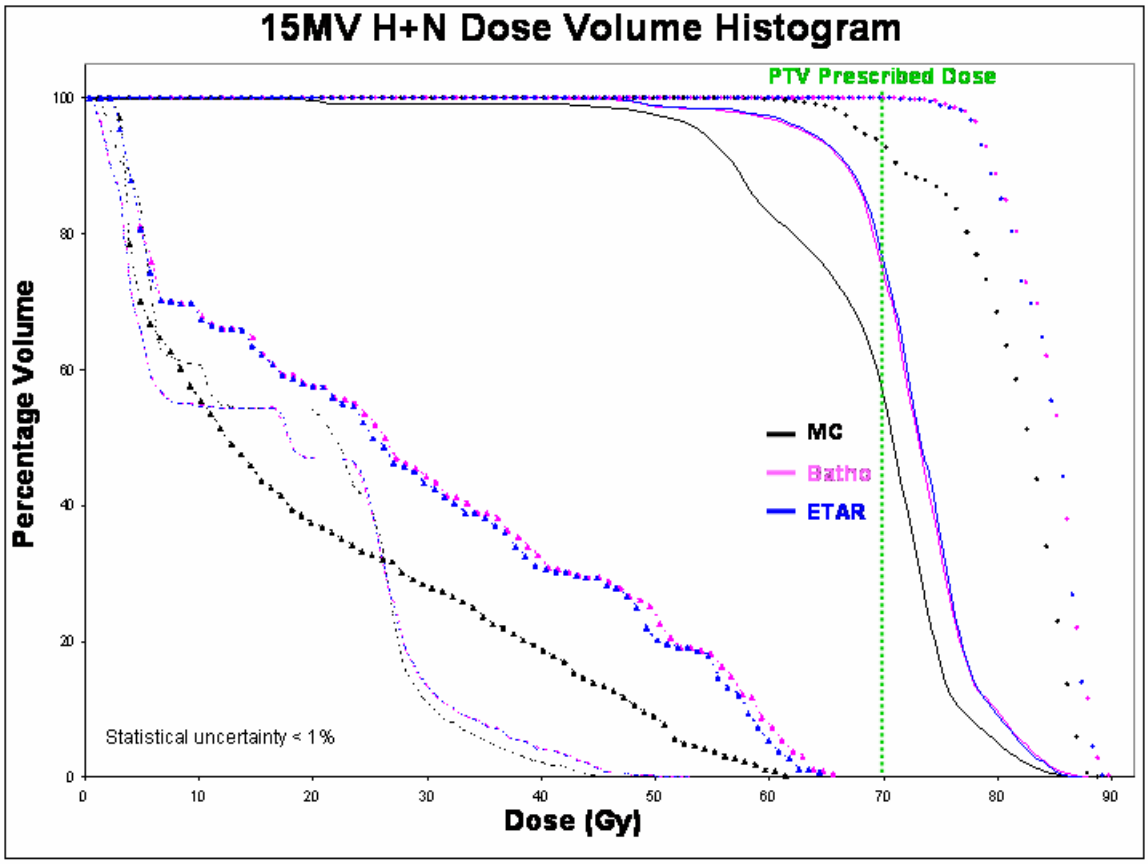

Figure 5.50 The DVH of the GTV (filled circles), PTV (solid lines), spinal cord (broken lines) and right parotid gland (filled triangle with broken line) for the MC (black) and SPB in combination with the Batho (pink) and ETAR (blue) algorithms in the 7 field head and neck case.

The DVH shows similar results to what was found in the 6 MV case. There are very few differences between the two inhomogeneity correction methods, but MC results show overestimation of dose to all the structures. There are some regions where the dose to the spinal column is underestimated by the TPS due the presence of the oral cavity upstream of the spine. These differences seem to be larger in the 6 MV case compared to the 15 MV case. Table 5.6 gives a summary of the EUD values calculated for the seven field 15 MV case.

Table 5.6. Summary of the seven field EUD values for the 15 MV head and neck case 3D dose distributions in terms of EUD values. Prescribed and tolerance doses are also supplied.

Volume	**Prescribed dose (Gy)**	**Tolerance dose TD(5/5) (Gy)**	**EUD* (Gy)**		
			MC	Batho	ETAR
GTV	84.0		82.6	86.1	91
PTV	70.0		67.9	72.1	72.5
Spine		46.0	16.5	15.8	15.8
Parotid		45.0	18.2	26.3	25.9

* Survival Fractions were chosen as 0.55 for the GTV dose per fraction of 2.4 Gy, and 0.6 for the other organs and volumes.

According to the results in tables 5.5 and 5.6, the PB algorithms overestimate the dose for the head and neck cases in the PTV and GTV. The MC based DVHs show that the dose distributions in the delineated regions are actually much less uniform than what was predicted by the TPS according to the EUD calculation. The following assumptions were made: Survival fractions were set to 0.55 associated with the tumor type and 0.6 for the OARs. The dose per fraction was set at 2.4 Gy for the GTV and 2 Gy for the PTV. For the 6MV case this leads to an overestimation of total dose to the GTV of 3.5 and 3.9 Gy for the SPB Batho and ETAR algorithms respectively. This is equivalent to approximately 1.5 fractions of treatment that will not be delivered according to TPS results. The PTV dose showed even larger discrepancies leading to approximately 2.5 to 3 fractions of dose equivalent actually given less than was planned. The results for the 15MV plan were similar; dose equivalent fractions were less by 1 to 3 factions for the GTV and 1 to 2.5 fractions for the PTV in the SPB Batho and ETAR cases respectively. From the 15 MV DVH data the maximum spinal dose was found to be 45.5Gy for MC,

53.1 Gy Batho and 52.8 Gy ETAR. This means that the spinal cord dose is again overestimated meaning that lower doses need to be given to the tumor volumes due to overestimated spinal cord dose when compared to the MC dose. A higher dose could have been delivered to the spinal cord leading to higher PTV and GTV doses. The implication of these dose discrepancies in the clinical situation strongly depends on the tumor stage. The effects of underdosage may not be as evident for early stage tumors, but underdosage of late staged tumors in this way could potentially lead to tumor recurrence.

5.1.5.1.2. Breast plans

The breast case involved the evaluation of 6 and 15 MV dose distributions. 15 MV x-ray beams are seldom used for the planning and treatment of 3DCRT breast cancers. However, it was included for dosimetric comparisons to evaluate dose calculations for both energies in regions where electronic disequilibrium exists. The evaluation of these two breast cases consisted of single beam dose distribution comparisons through the use of PDDs and profiles, as well as 3D dose distribution analysis.

The evaluation also involved the use of two tangential fields for the treatment of the left breast. A paraffin wax bolus was placed on the patient's surface to establish electronic equilibrium close to the skin surface. The plan was devised for 6 and 15 MV x-ray beams at 100 cm SSD. Figure 5.51 shows the dose distribution of the anterior tangential field for

the SPB algorithm in combination with the Batho and ETAR inhomogeneity correction algorithms, as well as the MC dose distribution.

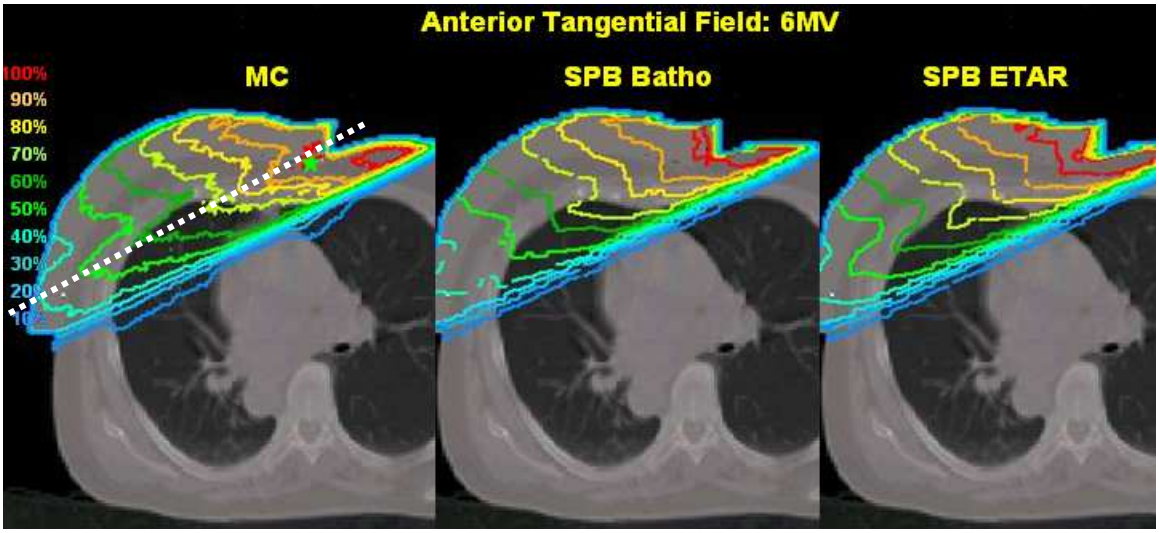

Figure 5.51 Dose distributions of the anterior tangential field of the breast plan for MC, SPB Batho and SPB ETAR calculations. The normalization point is represented by the green star.

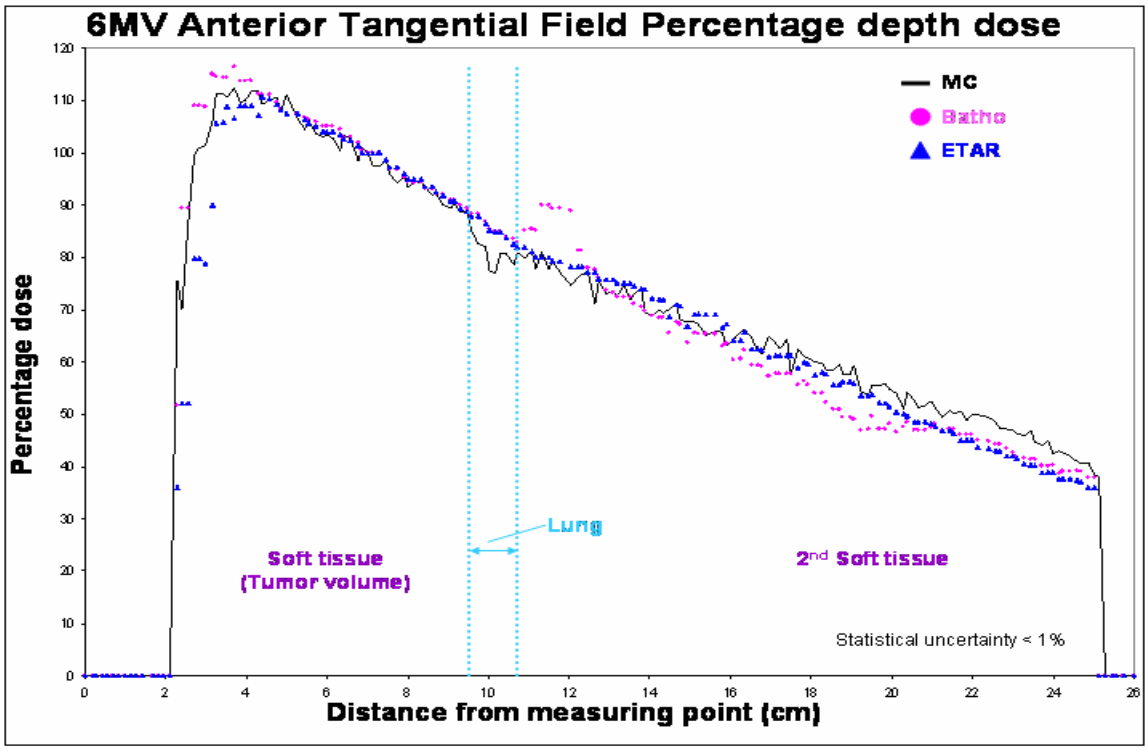

Figure 5.52 Percentage depth dose curves for the anterior tangential field dose distributions in figure 5.51. Data is shown for the MC (black line; with statistical uncertainty within 1%), SPB Batho combination (pink filled circles) and SPB ETAR combination (blue filled triangles).

PDD data were generated along the broken line depicted on the left image in figure 5.51 for all three dose distributions. The normalization point in the figure was selected to be at d_{max} of the 6 MV beam. The PDD curves are displayed in figure 5.52 and were re-normalized to 5 cm depth inside the breast tissue as that is the depth at which the tumor and the ICRU reference point is found.

For the same dose at the ICRU reference point, the TPS calculates 3% too few MUs for the ETAR distribution and 3% too many MUs for the Batho distribution, which is acceptable given the variance on the MC data being of the order of 1%. Dose differences on the ray line are generally within 2-3%, except in the buildup region. According to the distance to agreement criteria the discrepancies are 5 and 3 mm respectively for the ETAR and Batho dose values. Only the dose at d_{max} shows deviations of 3% overestimation (Batho) and 3% underestimation (ETAR) in the first soft tissue region.

Larger deviations are found where a small region of lung is intercepted by the line. MC shows a dose deficit because of a loss of lateral electronic equilibrium from the lung volume irradiated by the beam. The MC dose value quickly drops by 12% here. Changes in the ETAR and Batho values in this lung region are negligible. Once electronic equilibrium is re-established, the MC curve shows a small buildup region, but the Batho algorithm totally overestimates this re-buildup due to calculation of too large a correction factor. This overestimated correction factor is applied over approximately 2 centimeters in depth.

In the second soft tissue region the SPB Batho underestimates the dose by up to 10%, increasing to a local difference of 15% at 6 centimeters from the exit skin surface. The implications in a fully planned tangential field dose distribution for breast treatment are that the opposing field could “compensate” for this deviation and depending on the normalization point selection, could lead to approximately 7% underdosage in the lateral part of the breast in the final plan.

The ETAR PDD deviates less from the MC data until 5cm from the exit surface. Local deviations in this region reach 13% for a single field. These deviations require that normalization and dose prescription points be carefully selected. These points should be selected in a region where dose uniformity is found and not in high or low density regions where dose calculation algorithms may have large calculation errors. If the normalization is done in a region where the errors are quite large, the rest of the dose distribution will be affected accordingly.

The deviation of the two TPS algorithms at depths of greater than 20 cm on the PDD graph is mainly attributable to increased dose contribution from the primary photon fluence only partially attenuated in the lung tissue leading to more primary photons on the side of the field where more homogeneous breast tissue is found (second soft tissue region). This is not considered by the PB algorithms. These enhanced dose effects can be seen from the more penetrative MC isodose lines in figure 5.51 after the lung region.

Neither the pencil beam convolution applied with the Batho nor the ETAR correction algorithm makes any correction for the increased photon and secondary electron pathlengths in low density lung tissue. They cannot model the widened penumbra trend in lung tissue as seen in the MC dose distribution. This is even more evident from the combined effect of two tangential fields shown in figure 5.53. The accompanying DVHs are displayed in figure 5.54.

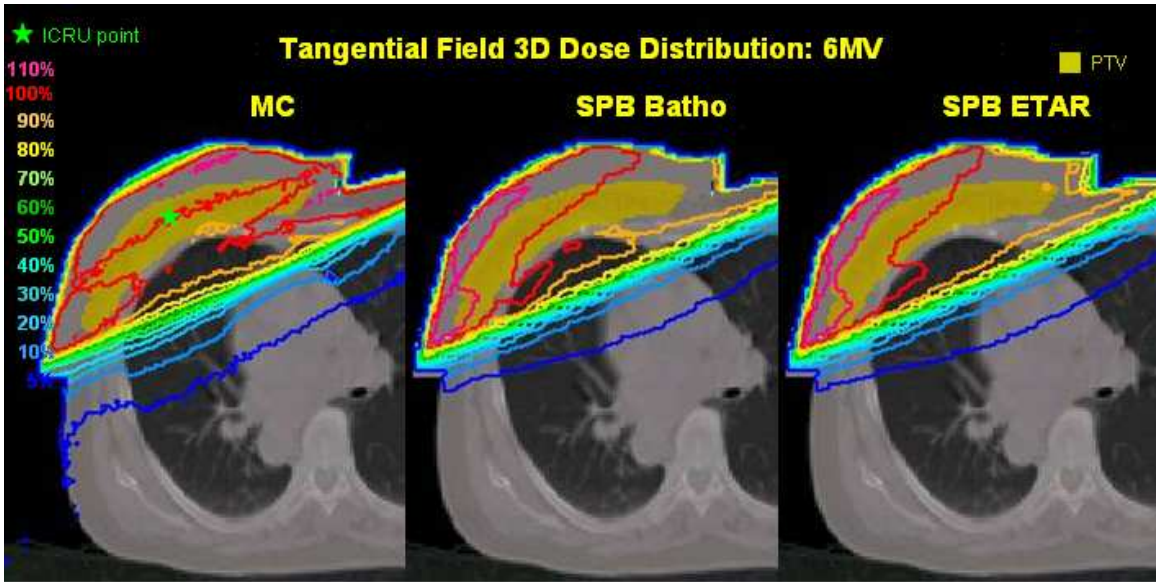

Figure 5.53 Comparison of the dose distributions from two opposing tangential fields for the 6 MV breast case. Dose volume histograms were calculated from the delineated tumor region and the OARs (not delineated on these images for clarity of isodose lines).

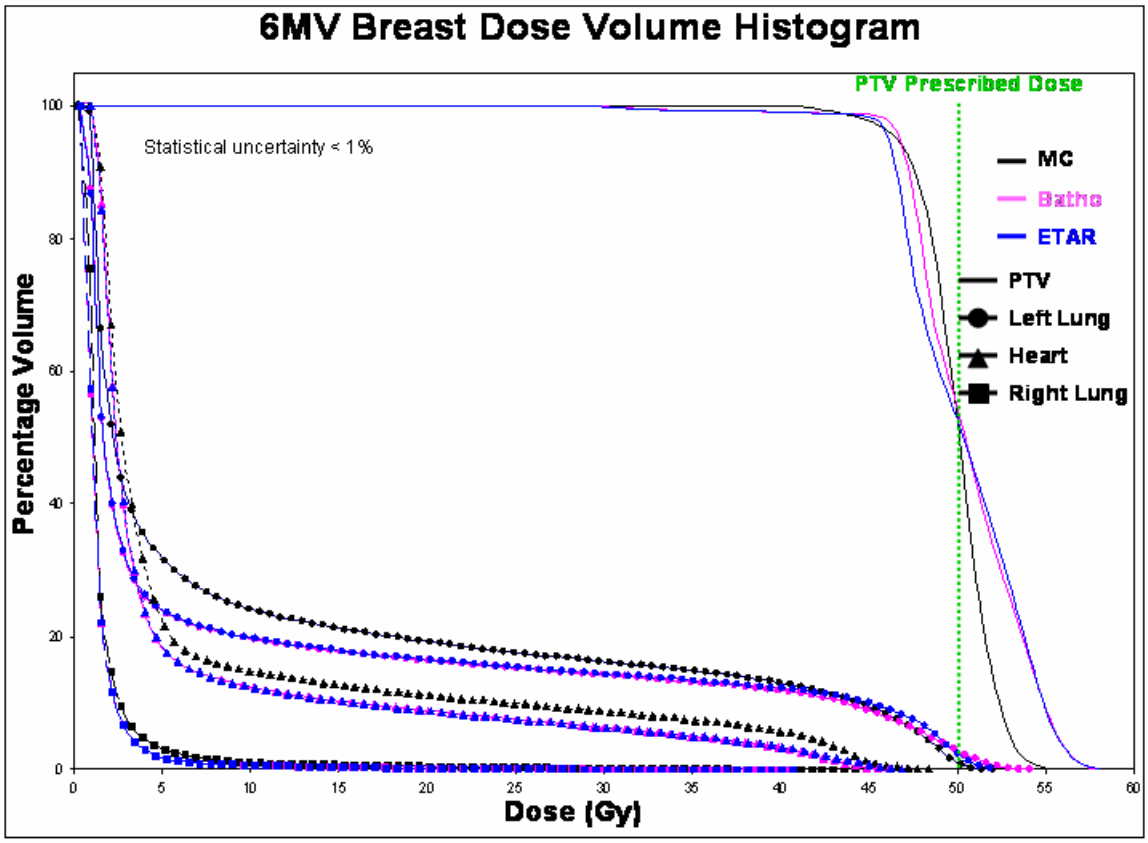

Figure 5.54 Dose volume histogram of the PTV, left lung, heart and right lung for the MC and SPB in combination with the Batho and ETAR algorithms in the 6MV breast case.

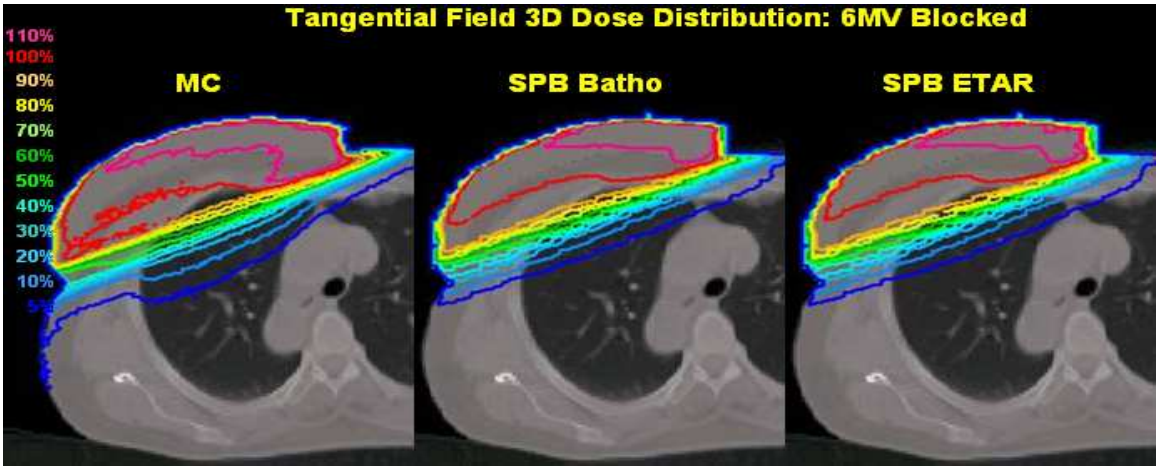

Figure 5.55 Comparison of the dose distributions from both partially blocked tangential fields for the 6 MV breast case. Dose volume histograms were calculated from this data. The ICRU reference point was situated on a different CT slice.

For the opposing tangential field plan shielding blocks were also added to evaluate the dosimetric effects of partially blocked fields. The left lung was shielded from primary radiation in this way. The block shape is shown in figure 5.3. Dose distributions are shown in figure 5.55 and the DVH for the different structures are shown in figure 5.56.

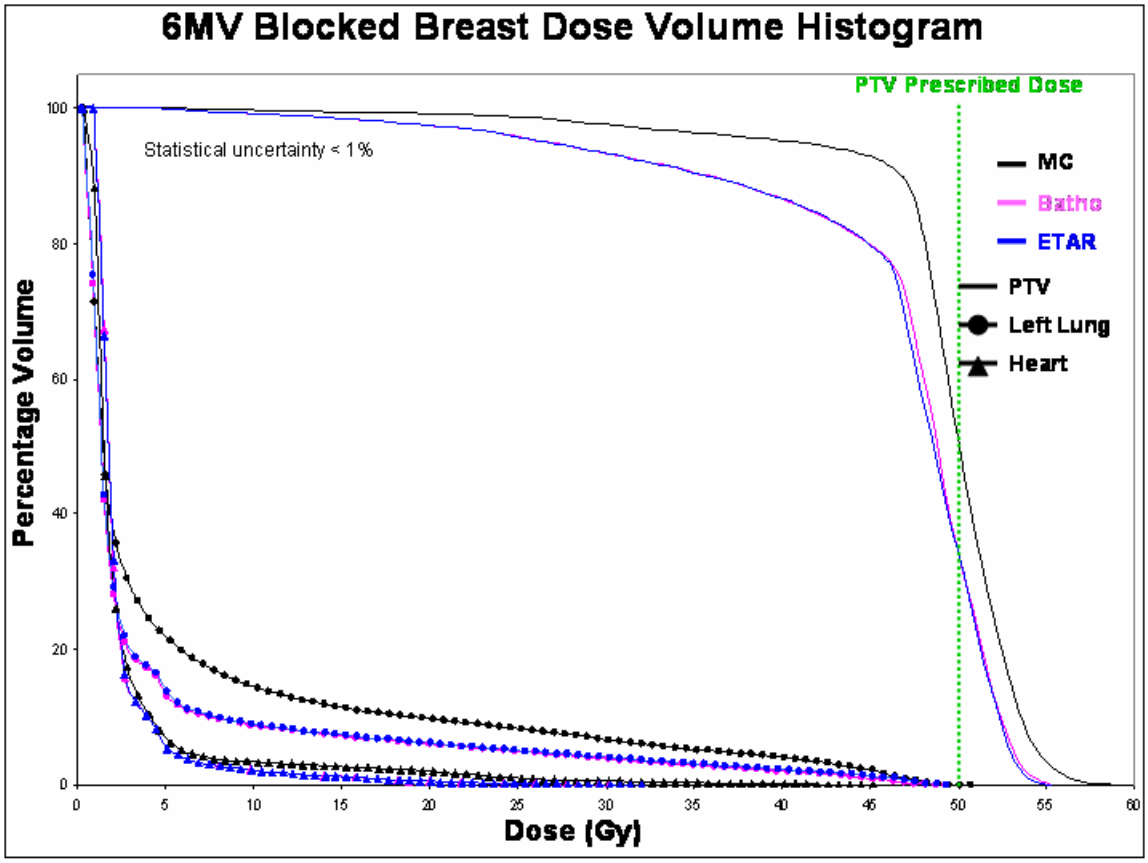

Figure 5.56 Dose volume histograms of the PTV, left lung and heart for the MC and SPB in combination with the Batho and ETAR algorithms in the 6 MV blocked field breast case.

Evaluation of the DVH for the blocked fields shows that the blocks had the desired effects of reducing OAR dose. The magnitude of the differences between MC and TPS calculated dose seems to be relatively similar to what was found in the open beam case.

When comparing the dose distributions one can see a wider penumbra in the left lung. The larger beam fringe ($\delta_{50\text{-}90}$) at the open-block interface leads to SPB dose underestimation in the volume of lung. The PB algorithm also largely underestimates the dose in the open part of the beam traversing the wax bolus. This is a combined effect of block boundary modeling and electronic disequilibrium. The dose in the PTV is underestimated by the Batho and ETAR algorithms in comparison with the MC data. Both PB combination algorithms correctly calculate a reduction in OAR dose.

Similar effects can be seen in the partially blocked 15 MV breast case. Due to the longer electron range in low density lung for 15 MV beams the 90% isodose line pulls towards the denser breast tissue. As the distance into the lung increases, the isodose lines start to bulge outward leading to widening of the penumbra. Again the PB algorithm fails to account for these phenomena.

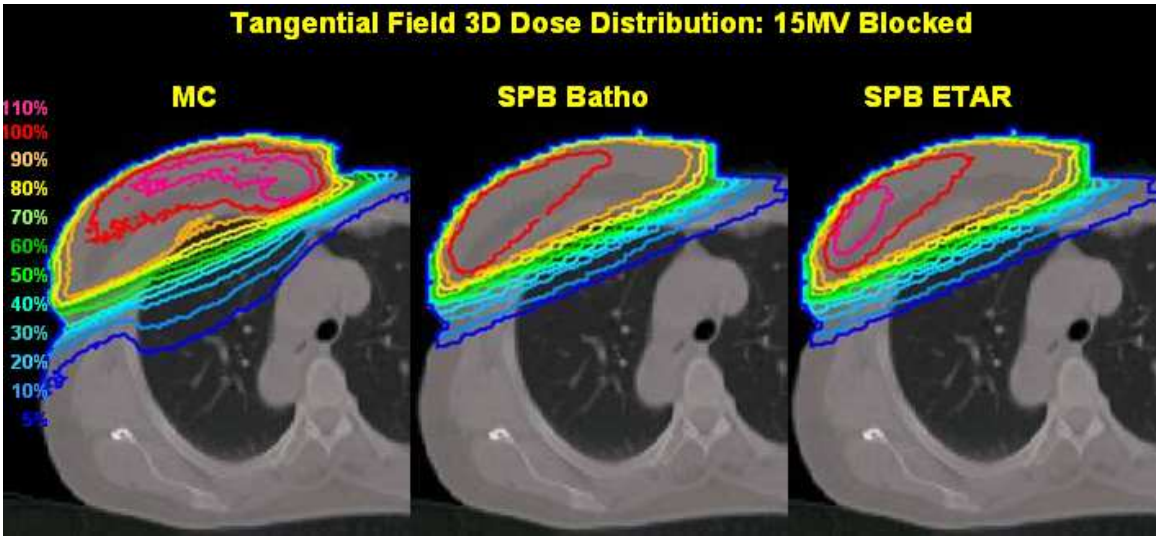

Figure 5.57 Comparison of the dose distributions from both blocked opposing tangential fields for the 15 MV breast case. Dose volume histograms were calculated from this data. The ICRU reference point was situated on a different CT slice.

Table 5.7. Summary of the EUD values for the 6 MV breast case 3D dose distributions for both tangential fields. Prescribed and tolerance doses are supplied along with the calculated equivalent uniform dose (EUD) and maximum doses for each volume.

Volume	**Prescribed dose (Gy)**	**Tolerance dose TD(5/5) (Gy)**	**EUD* (Gy)**			**Maximum dose (Gy)**		
			MC	Batho	ETAR	MC	Batho	ETAR
R Lung		30	1.3	1.0	1.0	44.2	40.5	40.7
L Lung		30	9	7.5	7.8	52.0	54.1	51.8
Heart		40	6.3	5.3	5.3	48.4	46.9	46.1
PTV	50		49.8	50.3	50.0	55.6	57.8	58.0

* Survival Fractions were chosen as 0.6 for the PTV dose per fraction of 2 Gy, and 0.6 for the other organs and volumes.

Table 5.8. Summary of the EUD values for the 15 MV breast case 3D dose distributions for both tangential fields. Prescribed and tolerance doses are supplied along with the calculated equivalent uniform dose (EUD) and maximum doses for each volume.

Volume	**Prescribed dose (Gy)**	**Tolerance dose TD(5/5) (Gy)**	**EUD* (Gy)**			**Maximum dose (Gy)**		
			MC	Batho	ETAR	MC	Batho	ETAR
R Lung		30	1.3	0.8	0.8	44.0	42.0	42.9
L Lung		30	9.0	7.5	7.5	53.3	51.3	52.3
Heart		40	6.0	5.0	5.0	49.5	47.5	48.4
PTV	50		49.5	49.8	49.8	54.4	54.6	55.0

* Survival Fractions were chosen as 0.6 for the PTV dose per fraction of 2 Gy, and 0.6 for the other organs and volumes.

The data from tables 5.7 and 5.8 support the fact that the 6 MV dose distribution is more heterogeneous than the 15 MV case because of the slightly larger deviations of maximum dose from the EUD. E.g. for ETAR the difference is 55 Gy maximum dose compared to 49.8 Gy EUD. At 6 MV this changes to 58 Gy against 50 Gy EUD. These deviations are smaller in the 15MV case. Although the EUDs for the OARs are similar, one can see that they receive higher dose in some regions where the dose maximum far exceeds the EUD value. This is good motivation for not relying on single EUD values, or even 2D DVH data. But one must also consider the 3D dose distribution in combination with these evaluation tools in treatment planning.

The effect of missing tissue on the dose at the anterior region of the breast was investigated by planning the treatment of the right breast without any bolus material. Figure 5.58 shows the distributions for all TPS and MC calculation methods for two opposing tangential fields.

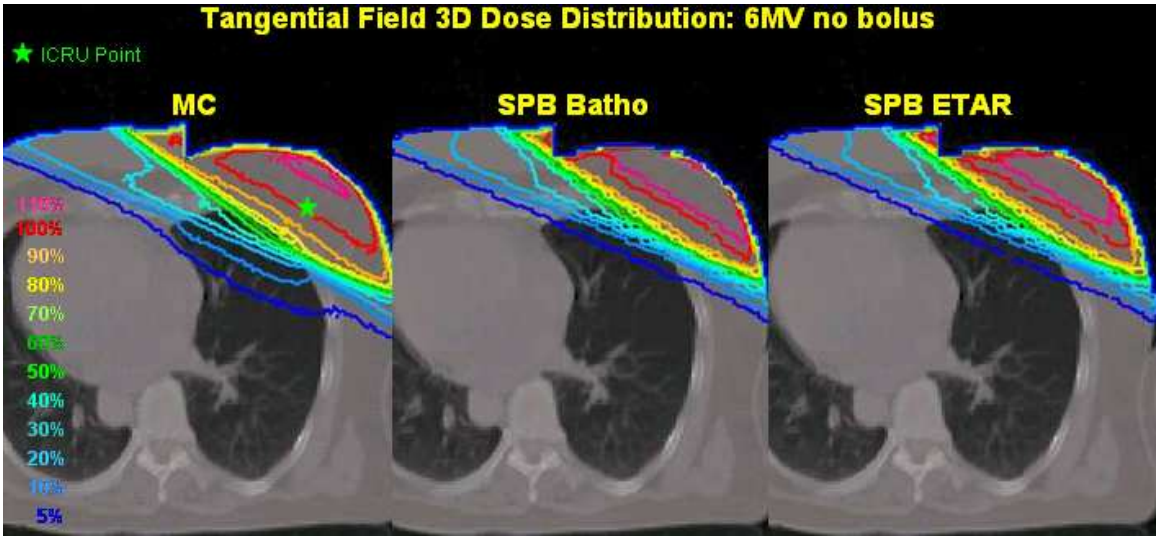

Figure 5.58 Comparison of 6 MV 3D dose distributions of the right breast without wax bolus consisting of the same field sizes as the left breast case. The ICRU reference point is indicated by the green star.

It is clear from figure 5.58 that the missing tissue geometry results in lower doses to the first few millimeters of the bolus free anterior breast tissue. The pencil beam convolution model cannot account for this as the scatter kernels and boundary functions are determined in water equivalent media and the calculated penumbras are based on these parameters. The Batho inhomogeneity correction algorithm does not consider lateral inhomogneities and utilizes only a forward calculation by assuming a heterogeneous slab. Compared to the ETAR dose one can see very few differences. The position of heterogeneities is considered by the ETAR method, but the use of an equivalent “scatter generating slice” for slice-by-slice dose calculation does not prove to be successful enough as the results are found to be similar to the Batho method.

However, considering the total volume encompassed by the 100% isodose line, the SPB in combination with the Batho and ETAR corrections overestimates it as well as the 110% isodose volume. This causes an overestimation of the absorbed dose to the PTV.

5.1.5.1.3. Lung plans

The lung plans were based on the same CT dataset that was used for the breast case. Both 6 and 15 MV plans were constructed consisting of two beams that intersect in the lung. The evaluation of the two cases consisted of single beam dose distribution comparisons with PDDs, as well as 3D dose distribution analyses.

The treatment plan consisted of an anterior and lateral oblique isocentric field setup. The beams intersected at the PTV located inside the lung. The normalization point was selected in the center of the PTV. The combined dose distributions from the two fields are shown in figure 5.59 and 5.62 for 6MV and 15 MV respectively.

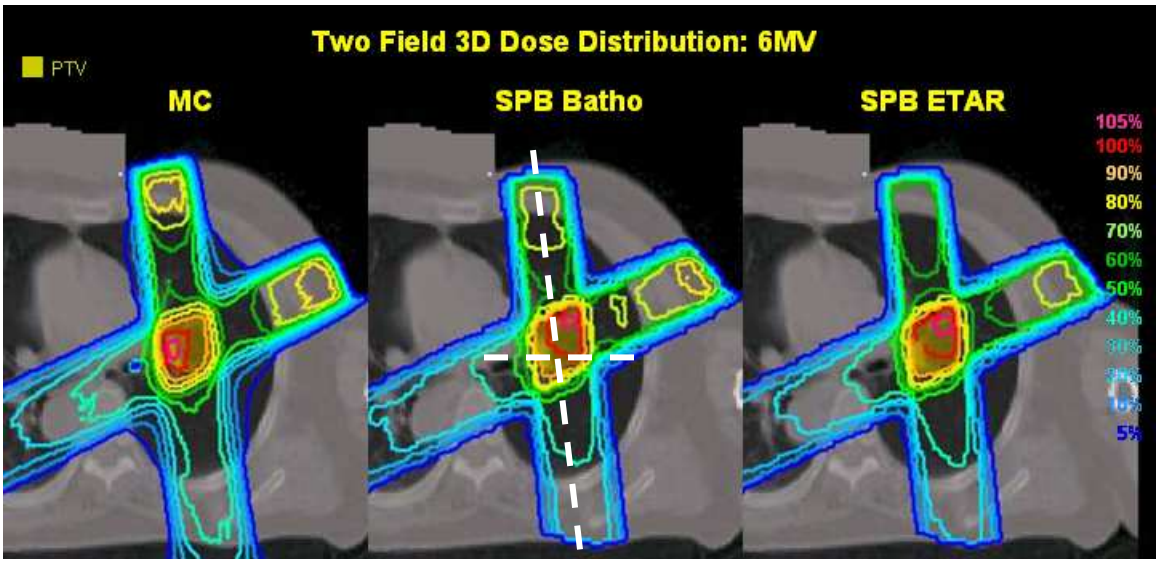

Figure 5.59 Comparison of 6 MV dose distributions of the lung case. The ICRU reference point is located in the center of the PTV.

A PDD was generated along a line through the beam axis of the anterior field for all three distributions. A profile was also generated in the center of the PTV for this field. The normalization point for both these dose profiles was at the ICRU reference point. The PDD and Profiles are shown in figures 5.60 and 5.61 respectively. From figure 5.60 it is seen that the MUs differ markedly between MC and the PB combinations for this field. The Batho algorithm underestimates the absolute dose to the normalization point by 7%, while the ETAR algorithm underestimates the dose by 17%, leading to a calculation of 7% and 17% too many MUs for the two algorithms respectively.

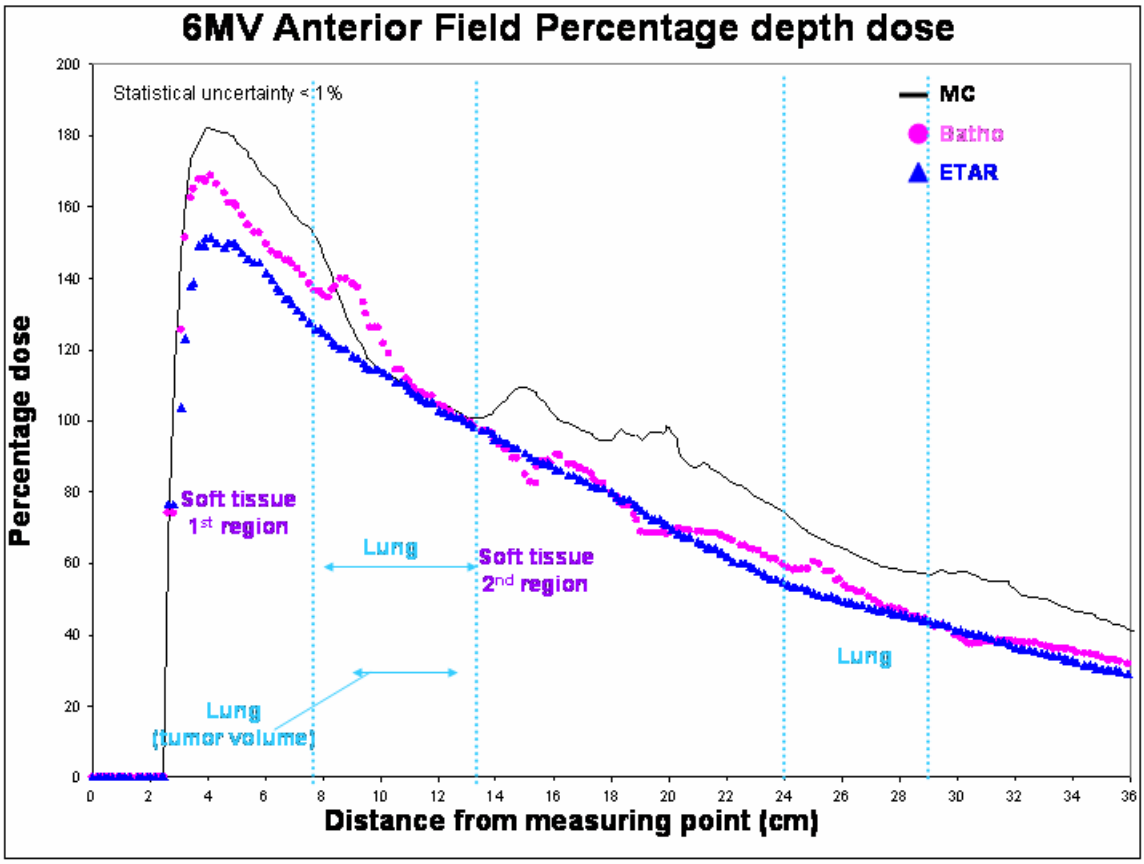

Figure 5.60 Percentage depth dose curves for the 6 MV lateral oblique field dose distributions in figure 5.59. The dose is normalized to the ICRU reference point in the center of the PTV.

Relative to the dose normalization point the dose differences in the buildup region are within 2 mm until a depth of more than 6mm where the MC PDD increases rapidly. Here the ETAR dose starts to reach the d_{max} position. This underestimation of dose at the normalization point is due to the reduced photon absorption inside the lung not being modeled correctly by the pencil beam in combination with the ETAR and Batho methods. The ETAR algorithm overestimates the lung dose and normalization inside the lung causes the large discrepancies in the buildup region. The Batho method follows nearly the same trend as the ETAR method. The correction factor calculated in the lung region

should be smaller than 1 as a result of reduced photon absorption, but the algorithm incorrectly calculates an increase in absorption first and then shows reduction in dose inside the PTV. Because of this first calculated increase the dose in the low density PTV is still overestimated by the Batho algorithm. The MC profile shows an immediate decrease in absorbed dose inside the lung requiring more MUs than the PB algorithms to obtain the prescribed dose at the ICRU reference point.

As the beam exits the PTV it passes through some more lung tissue until the large blood vessels, oesophagus and spinal column is reached. A sharp buildup region is found here where the increased photon fluence is absorbed in the higher density media. Both the PB algorithms do not show any change in dose here and the Batho algorithm shows a decrease in dose a few centimeters downstream. As the ETAR method uses a coalesced scatter CT slice for dose calculations, its inability to handle sharp changes in density correctly can probably be explained by the fact that such a coalesced scatter slice is more of an averaging effect of various densities leading to a loss of explicit density change considerations at inhomogeneity interfaces.

In the second soft tissue region the Batho method basically shows dose increases and decreases in direct contrast to the MC data, resulting in a regular variation of discrepancies with depth.

The profile data in figure 5.61 emphasizes the lack of scatter modeling in low density media in the penumbra regions as the dose outside the field is underestimated by the PB algorithms.

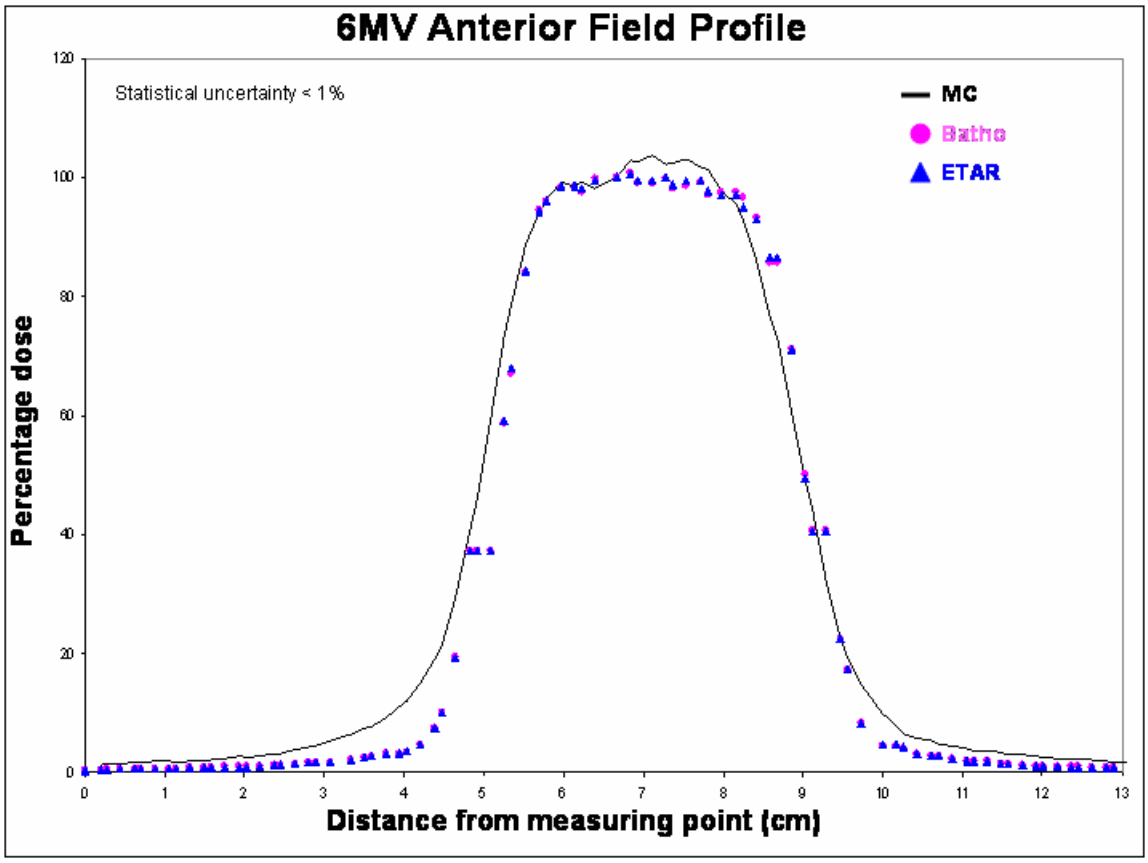

Figure 5.61 Dose profiles for the 6 MV anterior field dose distributions in figure 5.59. The dose is normalized to the ICRU reference point in the center of the PTV. The position of the ray line where the profile was sampled is shown by the white broken line in the center image of figure 5.59.

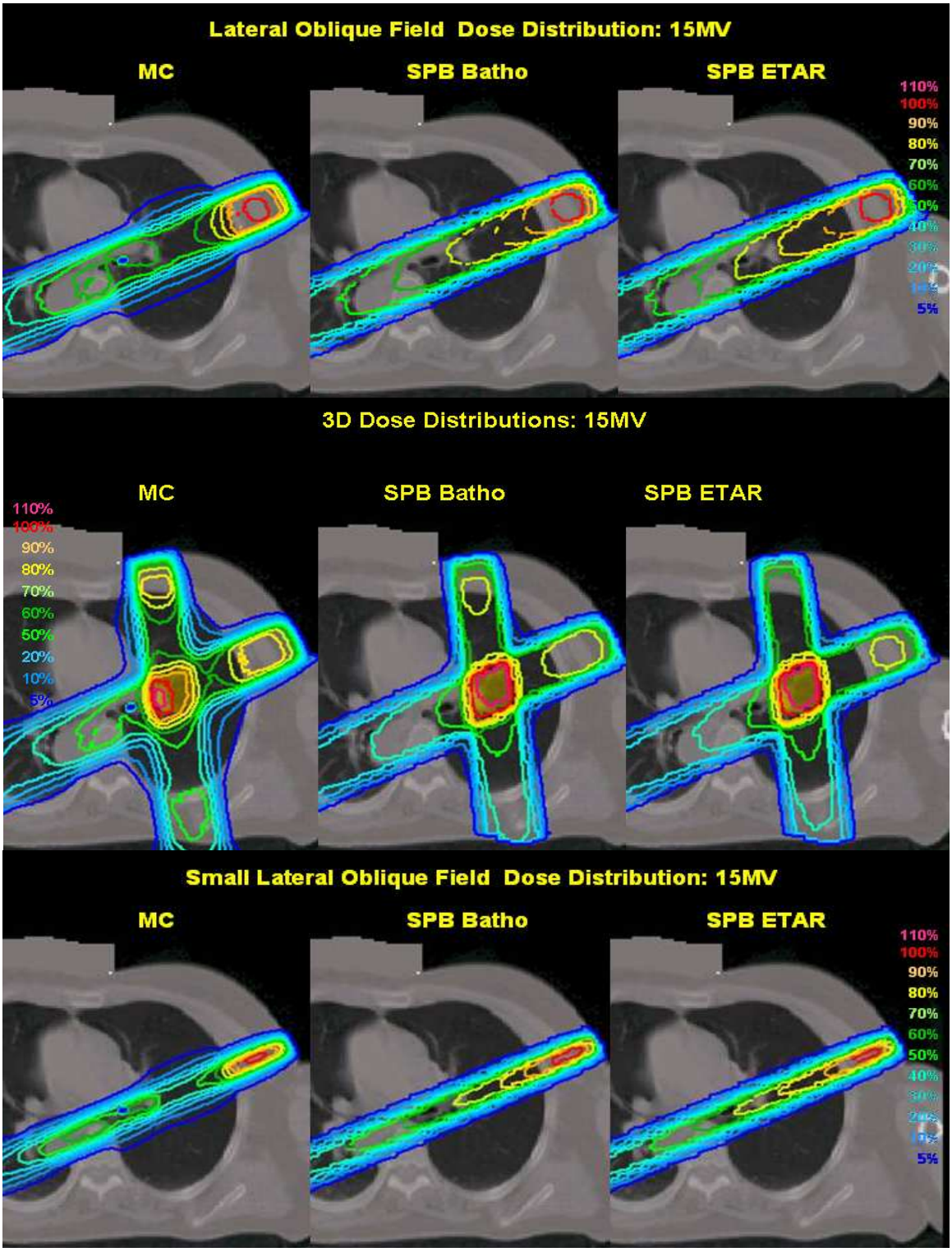

Figure 5.62 Comparison of 15 MV 3D dose distributions of the lung case. The ICRU reference point is located in the center of the PTV for the two beam plan. Single field dose distributions were normalized to d_{max}.

The dose distributions for the 15 MV case are shown in Figure 5.62 and they include the lateral oblique field distribution, the total dose from the two beams and a distribution of a single 2x2 cm^2 field. The small field shows the emphasized penumbra widening not considered by the PB algorithms and is appropriate evidence to recommend that small fields should not be used to plan dose distributions for lung tumors, unless MC algorithms are available.

Due to normalization in the low density PTV the MU discrepancy for the 15 MV lateral oblique beam is 28% for the Batho algorithm and 33% for the ETAR. These discrepancies are seen in figure 5.63. For the higher energy beams through lung, the discrepancies in the Batho and ETAR data are larger and both methods show almost total disregard for the changes in absorbed dose in the regions set out in figure 5.63. The MC data shows a dose reduction in lung, a dose buildup in the 2^{nd} soft tissue region, an increase in the absorption of photons in the higher density spinal column and a reduction of photon absorption in the adjacent lung region. Figure 5.63 includes the PDD of the 2x2 cm^2 showing that larger dose discrepancies are found for smaller fields in lung for 15 MV. The variation of the PB algorithms on the small field data is a result of the 160x112 dose matrix expansion in combination with the large dose gradient changes of small fields at oblique angles to the dose grid.

The DVHs of the 6 and 15 MV two field plans are shown in figure 5.64. The MC dose distribution is seen to be more heterogeneous than the PB distributions, leading to a lower EUD value in table 5.9.

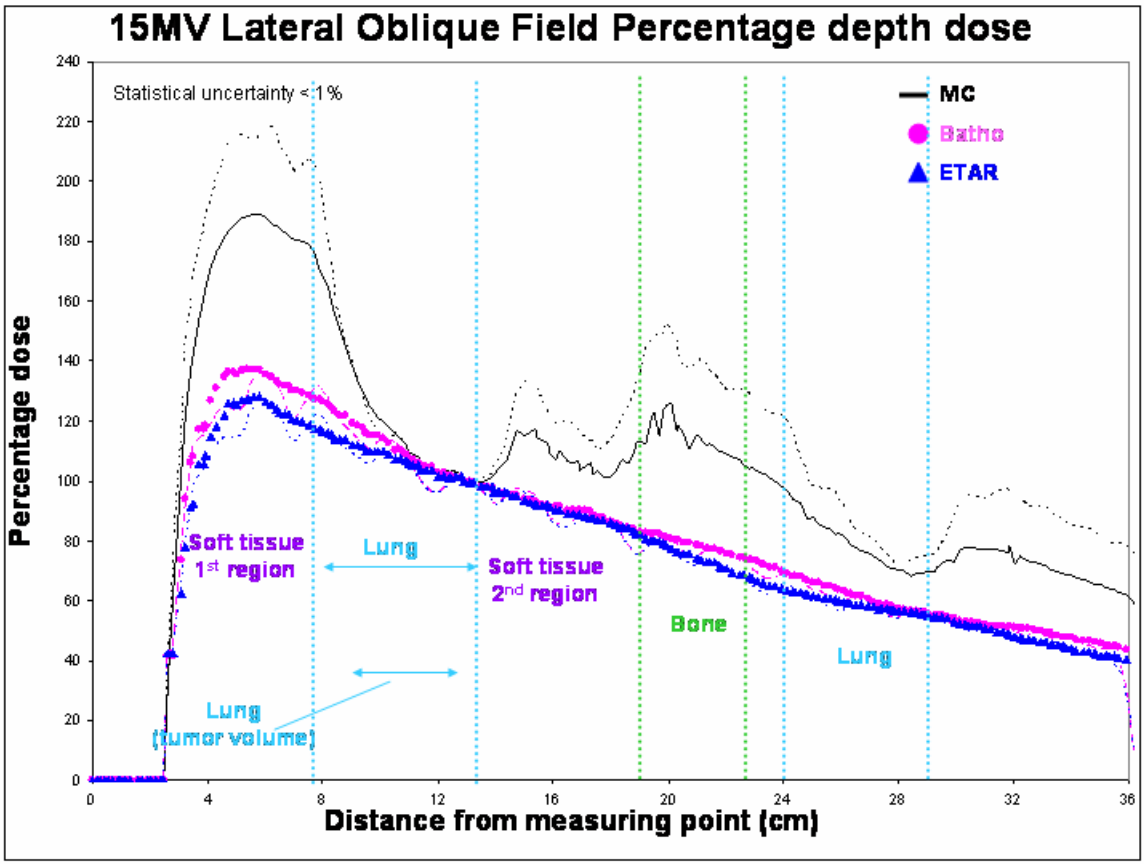

Figure 5.63 Percentage depth dose curves for the 15 MV 4x3 cm^2 lateral oblique field dose distributions and a 2x2 cm^2 field (represented by the broken lines) from figure 5.62. The dose is normalized to the ICRU reference point in the center of the PTV.

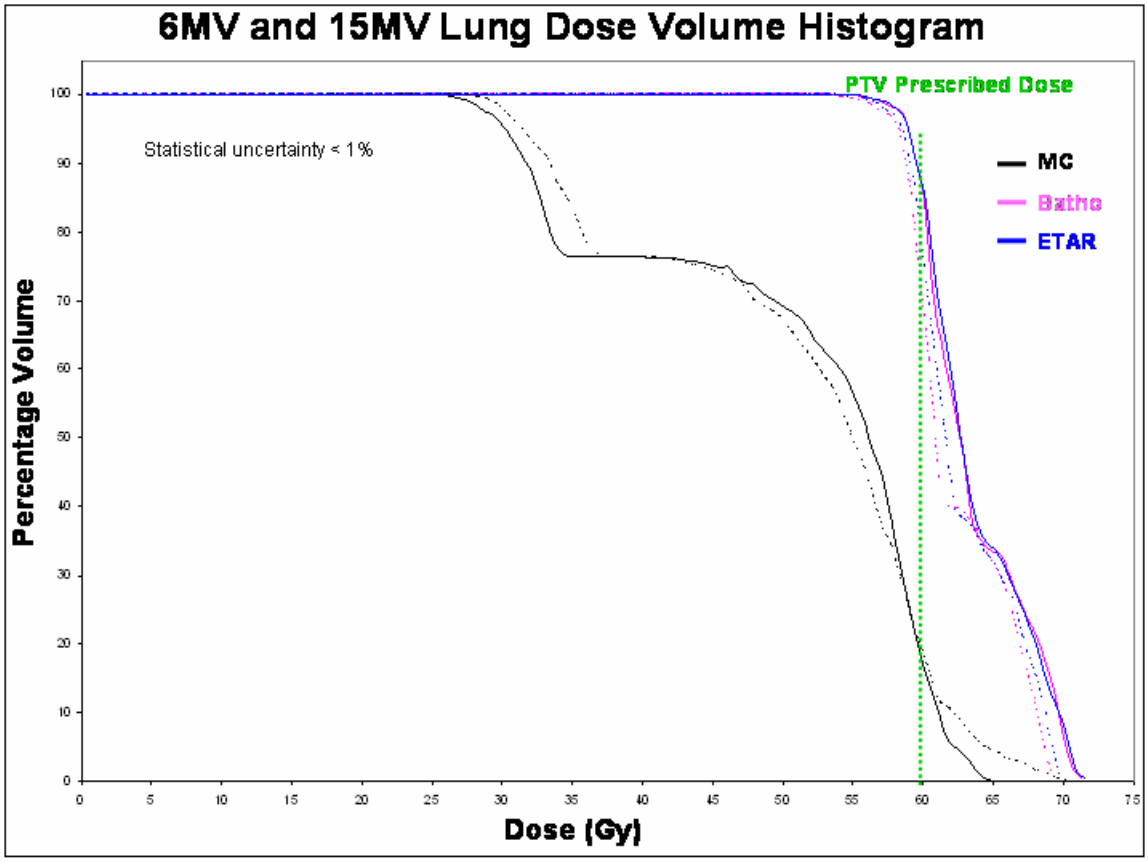

Figure 5.64 DVH of the PTV for the MC and SPB in combination with the Batho and ETAR algorithms in the 6 MV and 15 MV lung cases. The solid lines represent the 6 MV data and the broken lines the 15 MV data.

Table 5.9 Summary of the 6 and 15 MV lung case 3D dose distributions EUD values. Prescribed doses are supplied along with the calculated equivalent uniform dose (EUD) for each volume.

Volume	**Prescribed dose (Gy)**	**EUD* (Gy)**		
		MC	Batho	ETAR
6MV PTV	60	50.1	63.3	63.3
15MV PTV	60	50.1	62.1	62.4

* Survival Fractions were chosen as 0.55 for the PTV dose per fraction of 2 Gy.

According to table 5.9, the PB algorithms overestimate the dose to the PTV compared to MC data. The EUD values show that the actual total tumor dose is significantly less than the dose calculated by the TPS. The overestimation is so high that almost 5 fractions of 2Gy are not actually delivered. The EUD calculations are based on the assumptions of the survival fractions, reference dose and clonogen densities. Although prognostic factors are not good for most lung cancer patients treated at this institute due to the majority being very late staged cancers, this overestimation of dose could be linked to the outcomes of treatments and low TCP.

5.1.5.1.4. Prostate plans

The prostate case was planned with 5 isocentric 15 MV beams. The prostate plans usually contain fewer heterogeneous regions consisting mostly of the femoral heads and air cavities in the rectum. The rest of the tissues are usually quite uniform and near water equivalent. The normalization point was selected in the center of the PTV where the dose is uniform. Figure 5.65 show the dose distributions from the 5 fields for the MC and PB algorithms and the resultant DVHs are shown in figure 5.66.

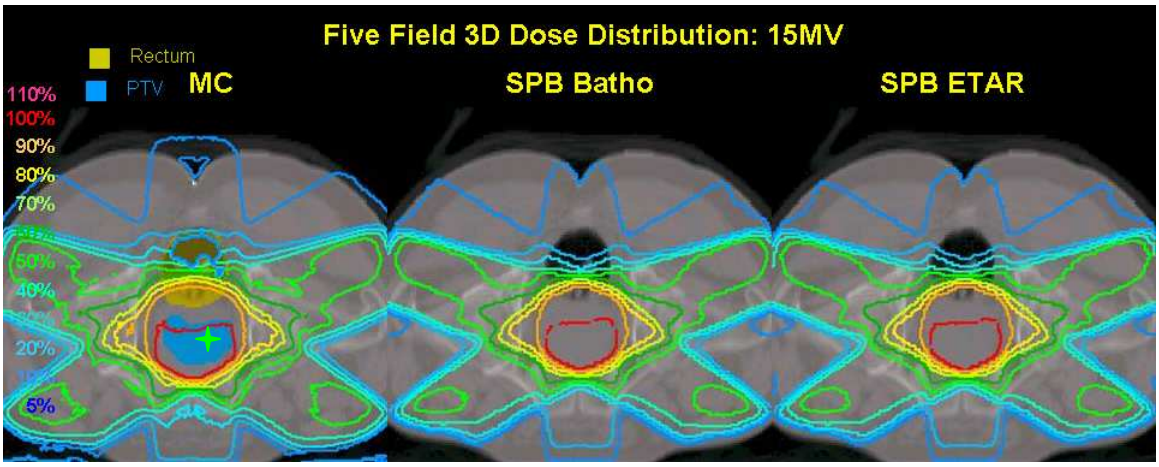

Figure 5.65 Comparison of 15 MV dose distributions of the prostate case. The ICRU reference point is located in the center of the PTV for the 5 beam plan. The green star indicates the ICRU reference point.

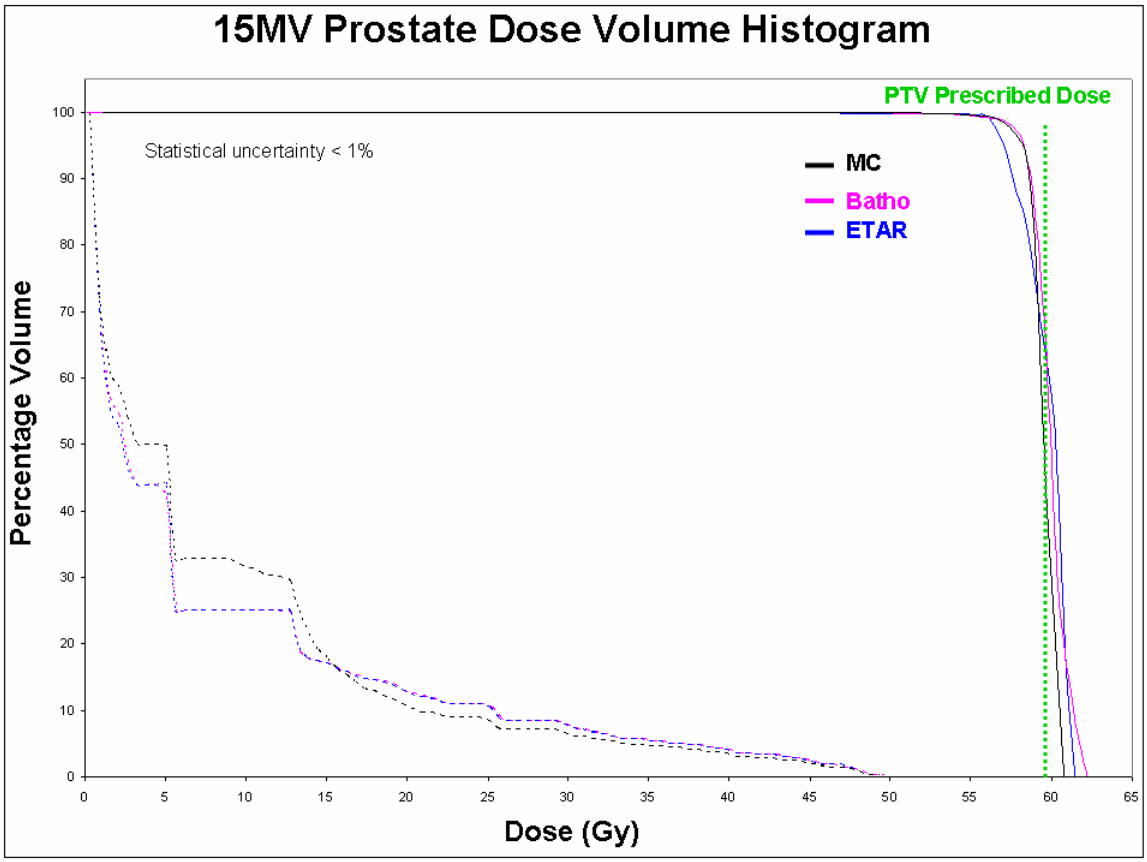

Figure 5.66 Dose volume histogram of the PTV and rectum for the MC and SPB in combination with the Batho and ETAR algorithms in the 15 MV prostate case. The solid lines represent the PTV and the broken lines the rectum data.

Table 5.10 Summary of the 15 MV prostate case EUD values. Prescribed doses are supplied along with the calculated equivalent uniform dose (EUD) for each volume.

Volume	**Tolerance dose TD(5/5) (Gy)**	**Prescribed dose (Gy)**	**EUD* (Gy)**		
			MC	Batho	ETAR
PTV		60.0	60.3	59.4	59.4
Rectum	55		7.5	6.9	6.9

* Survival Fractions were chosen as 0.6 for the PTV dose per fraction of 3 Gy.

Table 5.10 provides a summary of the dose distributions in the prostate case. The prescribed dose calculated with the Batho and ETAR algorithms correspond well with the MC data. The largest deviations are found in the rectal dose due to incorrect modeling of the photon fluence through the air cavity by the PB algorithms. As only a small part of the two lateral oblique and anterior oblique fields experience this change in photon perturbation, the influence of the discrepancies on the total dose is small. The anterior field exit dose showed some discrepancies of the order of 7% for the two PB algorithms, but the dose in this region is low and discrepancies are small in comparison to the tumor and OAR dose.

The femoral heads show higher absorbed dose when the MC distribution is compared to the PB algorithms. These discrepancies are 5% for the ETAR and 6% for the Batho at most, but do not have a significant impact on the tumor dose. The PB algorithms show a 1% lower dose than the MC data, which is within the statistical variation on the MC dose.

5.1.5.1.5. Oesophagus plans

The inhomogeneities in oesophagus treatment plans are similar to the ones found in the lung case, although the ICRU reference point will be selected in higher density regions in the oesophagus plan. This has a marked influence on the discrepancies found between the MC calculated dose and the PB combination algorithms. The plans evaluated in this study consisted of three isocentric photons fields, one anterior and two anterior oblique fields. The anterior field passed through reasonably large soft tissue volumes, while the other two fields passed through large low density lung volumes. The ICRU reference point was selected in the center of the PTV. The dose distributions for the fields for both energies are shown in figure 5.67.

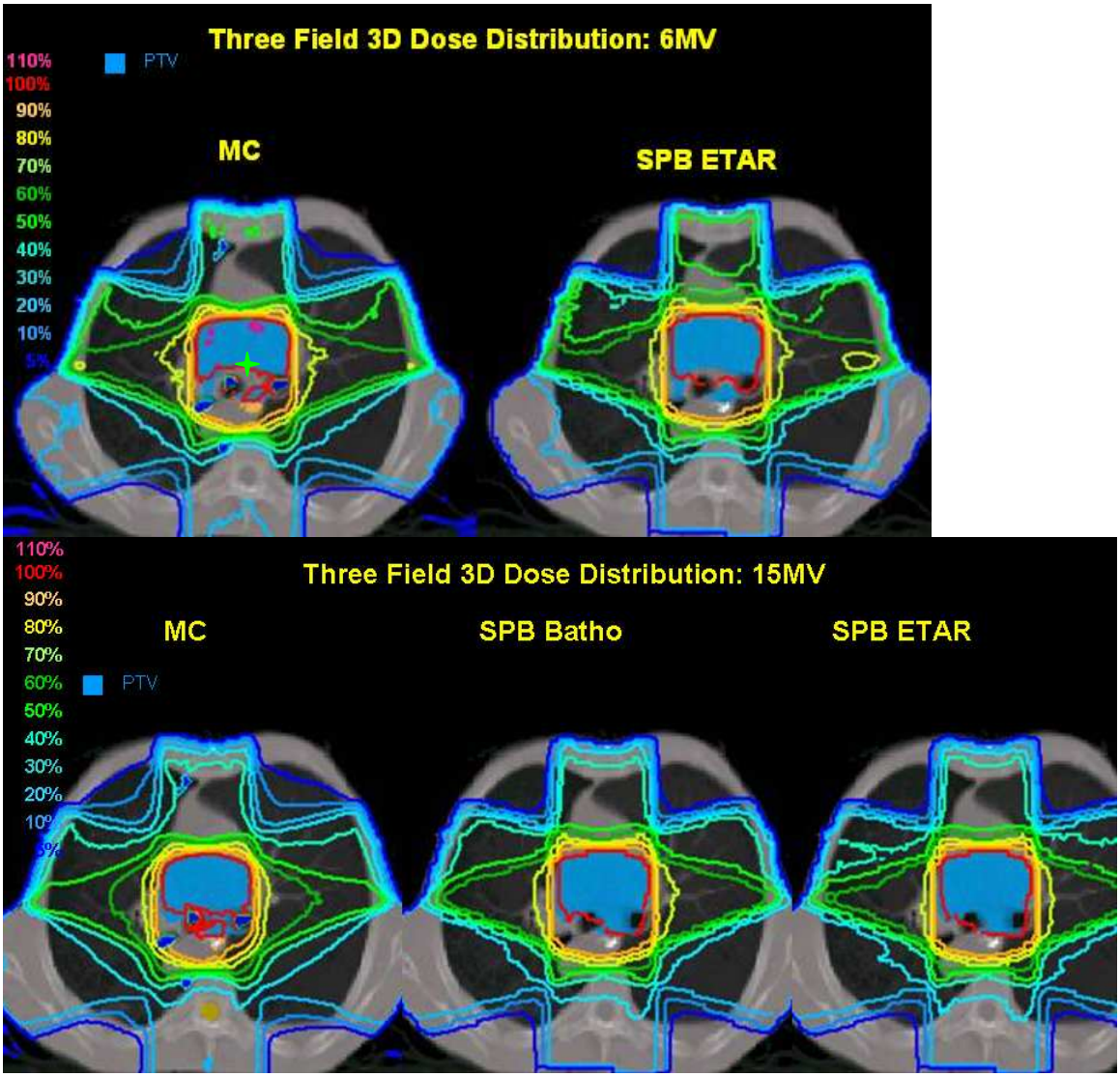

Figure 5.67 Comparison of 6 and 15 MV 3D dose distributions of the oesophagus case. The ICRU reference point is located in the center of the PTV for both plans.

From both sets of dose distributions it seems like the PB algorithms overestimate the dose to the PTV. The overestimation is possibly due to underestimation of the dose re-buildup region in the first couple of millimeters inside the PTV, being surrounded by low density lung. On the exit side of the PTV there is also reduced backscatter from the lung tissue leading to reduced dose in this volume. However, the overestimation of dose absorption

in the lungs by the Batho and ETAR algorithms seem to be counteracted in some way leading to a larger high dose volume than what is seen for the MC data. The fact that the field sizes in this case are larger than were used for the lung case also adds to a more accurate PB result in the oesophagus case. Larger fields allow electronic equilibrium to be established in the central part of the beam, although discrepancies will still be found closer to the beam edge as scattered photons and electrons have longer pathlengths in low density tissue. The dose distributions are depicted in the DVH data shown in figures 5.68 and 5.69.

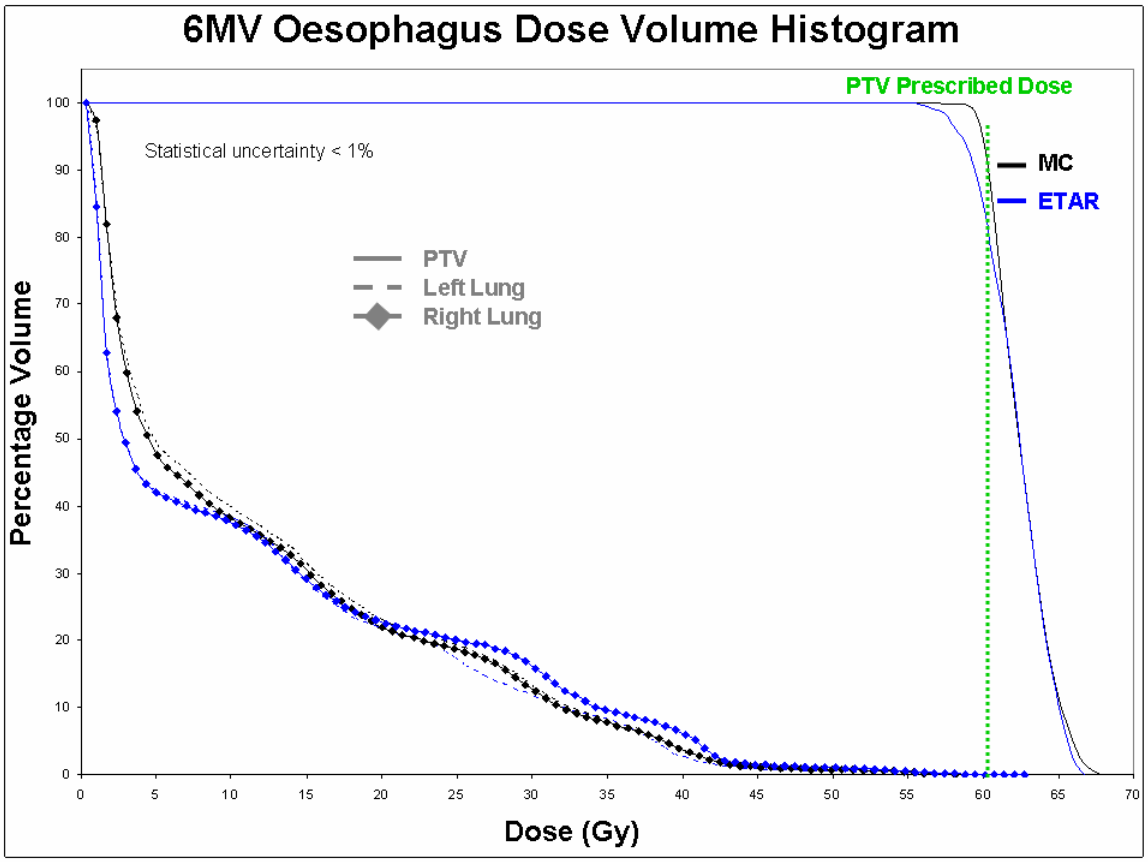

Figure 5.68 DVH of the PTV and lungs for the MC and SPB in combination with the ETAR algorithm for 6 MV.

Table 5.11 Summary of the 6 MV oesophagus case EUD values. Prescribed and tolerance doses are supplied along with the calculated equivalent uniform dose (EUD) and maximum doses.

Volume	**Prescribed dose (Gy)**	**Tolerance dose TD(5/5) (Gy)**	**EUD* (Gy)**		
			MC		ETAR
R Lung		30	10.8		9.6
L Lung		30	10.5		9.0
PTV	60		62.1		61.8

* Survival Fractions were chosen as 0.6 for the PTV dose per fraction of 2 Gy, and 0.6 for the other organs and volumes.

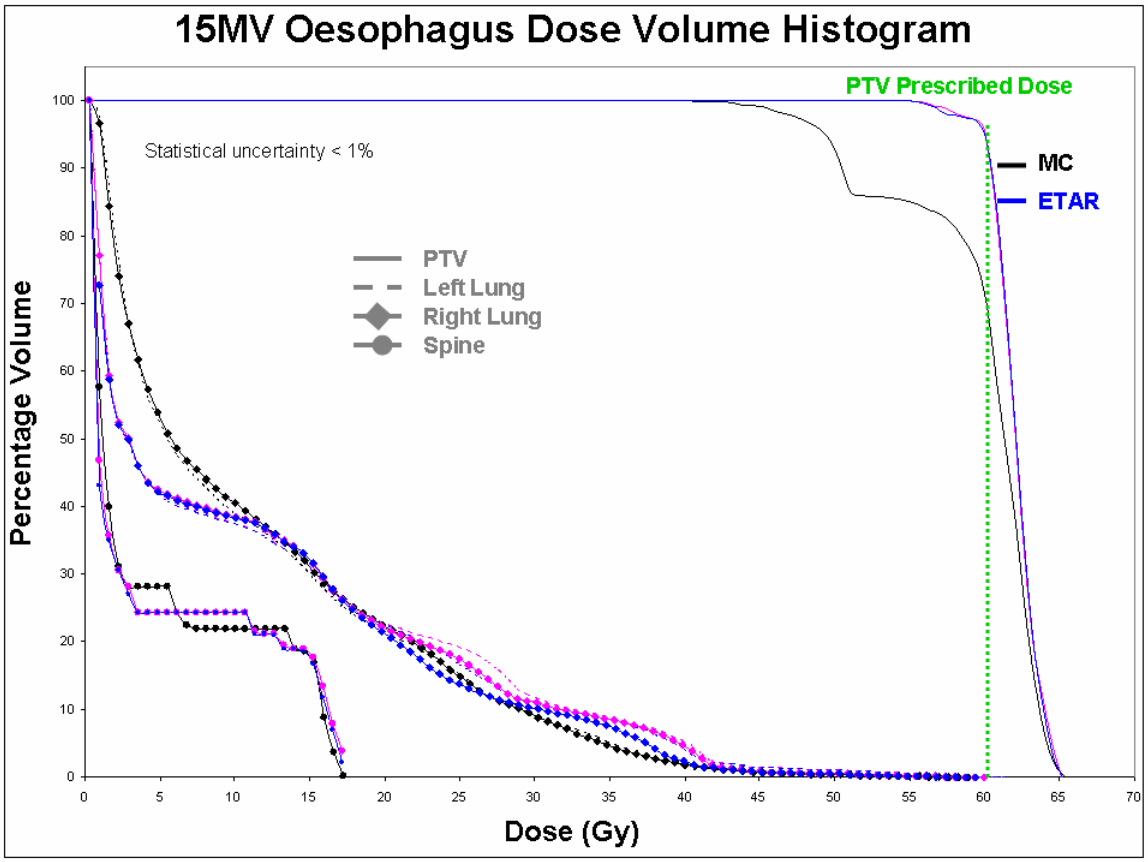

Figure 5.69 Dose volume histogram of the PTV, lungs and spinal cord for the MC and SPB in combination with the Batho and ETAR algorithms in the 15 MV oesophagus case.

Table 5.12 Summary of the 15 MV oesophagus case EUD values. Prescribed and tolerance doses are supplied along with the calculated equivalent uniform dose (EUD) and maximum doses.

Volume	**Prescribed dose (Gy)**	**Tolerance dose TD(5/5) (Gy)**	**EUD* (Gy)**			**Maximum dose (Gy)**		
			MC	Batho	ETAR	MC	Batho	ETAR
R Lung		30	10.5	9.9	9.3			
L Lung		30	10.2	9.9	9.6			
Spine		50	4.2	3.9	3.9	17.2	17.2	17.2
PTV	60		59.4	61.8	61.8			

* Survival Fractions were chosen as 0.6 for the PTV dose per fraction of 2 Gy, and 0.6 for the other organs and volumes.

Even though it is known and has been shown that the two PB algorithms have large discrepancies in dose calculations in low density tissues like lung, the oesophagus dose calculation evaluations showed good comparison with the MC simulations. The EUD values for the 6 MV data are almost the same and it can be seen from the DVHs that the dose distribution in the PTV is uniform for both MC and the SPB ETAR combination. The 15 MV data showed more non-uniformity in the PTV with some parts of the PTV receiving more than 10% lower doses than that calculated by the PB algorithms. This is most probably due to the effect of dose re-buildup on the entrance side of the PTV and reduced backscatter at the exit side of the PTV. This leads to an EUD of more than 2 Gy less than the TPS calculated dose and is equivalent to one less fraction. For late stage tumors a reduction in one fraction of dose could possibly lead to reduced tumor control and earlier recurrence in the form of oesophagus obstructions.

5.1.5.1.6. Brain plans

The brain case involved the use of two 6 MV isocentric fields with a large volume PTV located close to the skin surface. The plan consisted of a lateral and vertex field. The ICRU reference point, where the dose is normalized, was selected in the center of the PTV. Analyses of the dose distribution showed a non-uniform dose as only two fields were used to obtain tumor dose coverage. Figure 5.70 shows a comparison of the MC and SPB Batho combination dose distributions.

In figure 5.70 the MC dose distribution seems to have more variance compared to the images shown in other plans. The reason for this apparent increased variation is due to the vertex field dose distribution. As the CT slices are 1cm in thickness, a small dose variation along the beam direction is displayed as a large variation in the transverse plane of the CT dataset. The variance on these MC data was still within 1%.

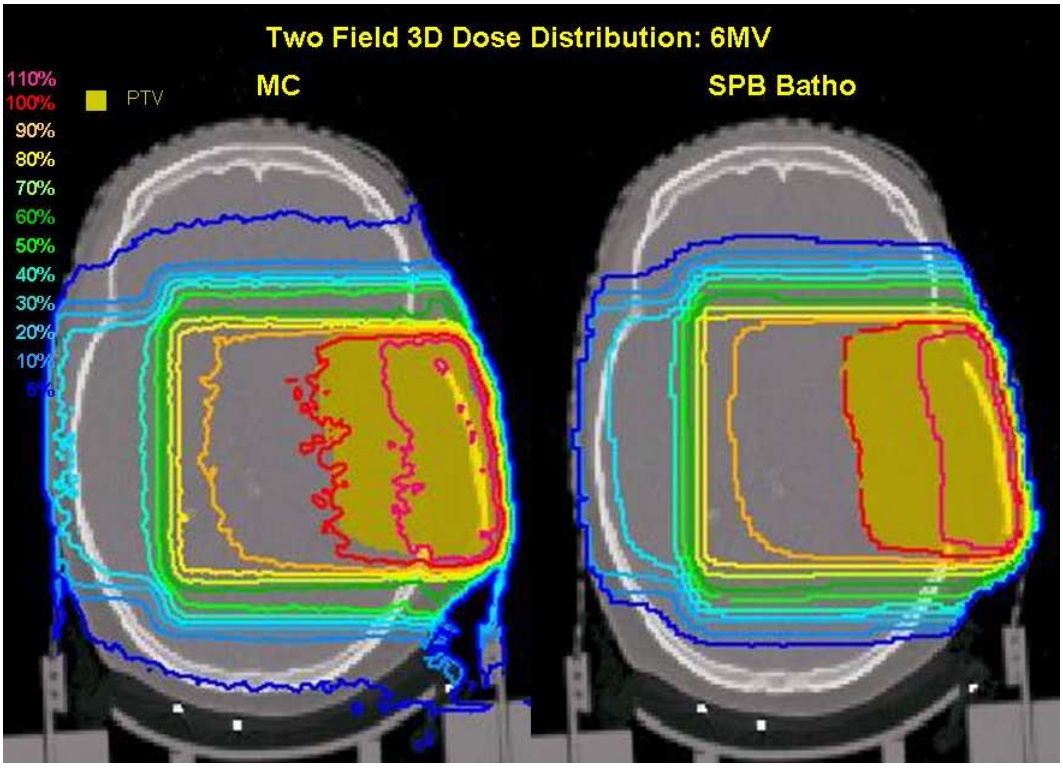

Figure 5.70 Comparison of 6 MV dose distributions of the brain case. The ICRU reference point is located in the center of the PTV for both plans and is located on a different slice.

The major differences between the two distributions are seen in the first few millimeters from the lateral side. The PB dose is higher closer to the skin surface as was seen in the head and neck and breast cases. This leads to reduced tumor coverage if bolus material is not used to establish electronic equilibrium. The MC distribution also shows higher absorption in the skull than what is seen in the PB distribution. As the scull thickness is only approximately 4 mm, this increased absorption does not have a major impact on dose distributions.

Volumes receiving scattered dose are larger in the MC case (although these are low doses regions) as was seen in all other cases studied as the TPS does not consider extra focal

radiation and the dose profiles outside the field are underestimated. This could be critical in treatment plans where small radiation sensitive organs are involved as the dose to these organs will be underestimated by the TPS. Figure 5.71 shows the DVHs for the two distributions.

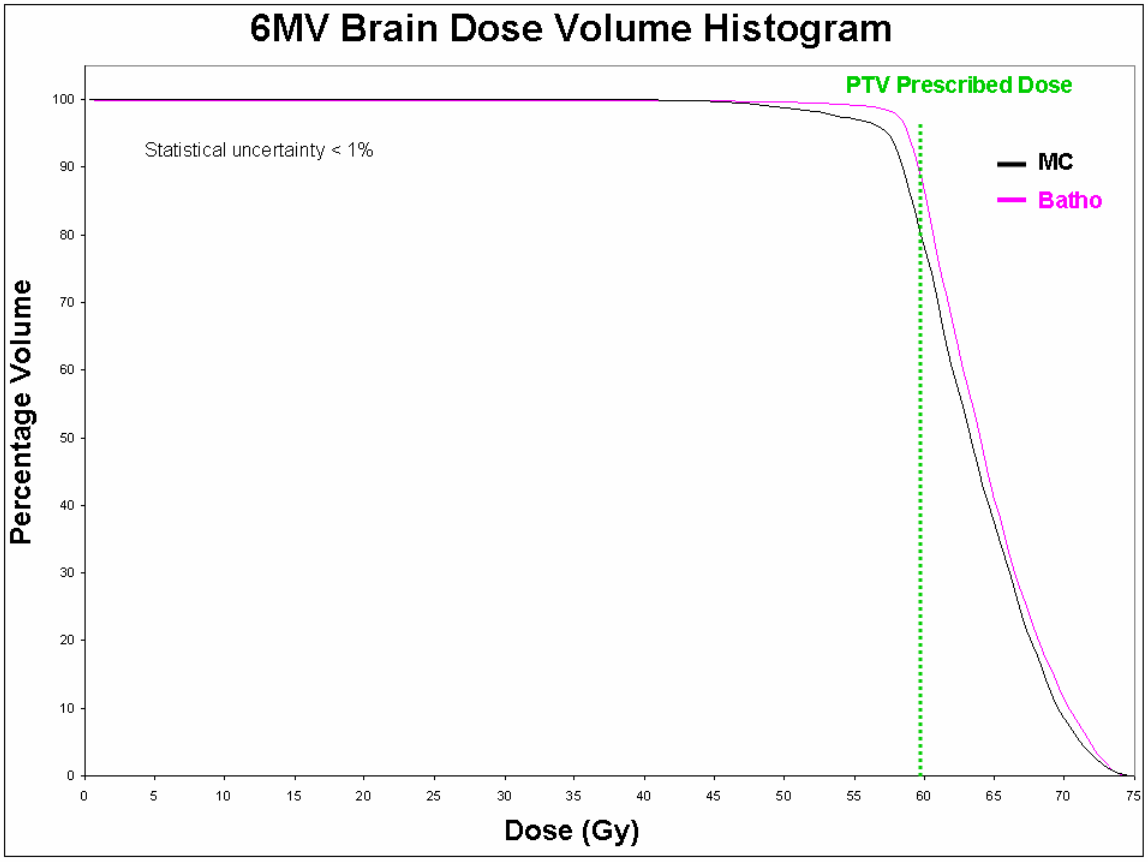

Figure 5.71 Dose volume histogram of the PTV for the MC and SPB in combination with the ETAR algorithm in the 6 MV brain case.

The DVH results show the overestimation of PTV dose due to the overestimation of dose close to the skin surface. As the outer brim of the PTV is located just under the skin surface, this overestimation is clearly pointed out in the MC data. The skin obliquity

leads to an inward bending of the MC isodose lines which is not modeled well by the ETAR algorithm, adding to the overestimation of dose to the PTV. Table 5.13 gives a summary of the EUDs calculated for the brain case.

Table 5.13 Summary of the 6 MV brain case dose distributions. Prescribed doses are supplied along with the calculated equivalent uniform dose (EUD) for each volume.

Volume	**Prescribed dose (Gy)**	**EUD* (Gy)**	
		MC	Batho
PTV	60	64.3	66.1

* Survival Fractions were chosen as 0.55 for the PTV dose per fraction of 2 Gy.

The EUD calculation confirms the overestimation of dose by the ETAR method, but also confirms that the dose distribution is non-uniform. The overestimation of dose by the TPS is equivalent to a reduction in dose by almost one fraction. Such a reduction in this case is not critical, but for curative treatments of other tumors where such geometries are planned, reduced tumor dose could result in recurrence or metastatic spread of the disease.

References

1. Paena J., Franco L., Gomez F., Iglesias A., Lobato R., Mosquera J., Pazos A., Pardo J., Pombar M., Rodriguez A. and Sedon J., "Commissioning of a medical accelerator photon beam Monte Carlo Simulation using wide-field profiles", Phys. Med. Biol **49**, 4929 – 4942 (2004).

2. Sheikh-Bagheri D., Rogers D. W. O., Ross C.K. and Seuntjens J.P., "Comparison of measured and Monte Carlo calculated dose distributions from the NRC linac", Med. Phys. **27** (2000).

3. Sheikh-Bagheri D. and Rogers D.W.O. "Sensitivity of megavoltage photon beam Monte Carlo simulations to electron beam and other parameters", Med. Phys. **29**, 379 – 390 (2002).

4. Venselaar J., Welleweerd H. and Mijnheer B., "Tolerances for the accuracy of photon beam dose calculations of treatment planning systems", Rad. Onc **60**, 191-201 (2001).

5. Storchi P.R.M., van Battum L.J. and Woudstra E., "Calculation of a pencil beam kernel from measured photon beam data", Phys. Med. Biol. **44**, 2917–2928 (1999).

6. International Commission on Radiological Units and Measurements. “Prescribing, Recording and Reporting Photon Beam Therapy,” ICRU Report 50. Bethesda, MD: ICRU (1993).

Chapter 6

Conclusion

The aim of this study was to evaluate a commercial treatment planning system in terms of dose calculation accuracy against Monte Carlo simulations. The CadPlan TPS was evaluated. It uses a combination of convolution algorithms (they are the Single and Double pencil beam algorithms) and the Batho and ETAR inhomogeneity correction methods for dose calculation.

In this study it was found that the BEAMnrc MC code can be used for the generation of realistic radiation beam specific data. The DOSXYZnrc code can be used for generation of commissioning data for any TPS that requires water phantom dose data for acceptance testing and commissioning. The combination of the EGSnrc codes allows the evaluation of any dose calculation algorithm in any geometry that can be replicated in the DOSXYZnrc code. The evaluation in this study was done for a one-dimensional convolution algorithm with inhomogeneity corrections on the TPS. The same can be achieved for 2 and 3D convolution/superposition algorithms. MC is independent of the TPS dose calculation methodology and is suitable for any comparative study where CT based patient models is used. The methods used in this study resulted in the development of a database of benchmark dose distributions that can be used for input in any TPS for evaluation purposes. It is certainly a valuable tool for any radiotherapy unit to evaluate

TPS dose calculation accuracy or to study individual effects that may not be well known or frequently seen on TPSs.

The TPS replication of water phantom input beam data exhibited some discrepancies in the SPB model calculated dose distributions. Discrepancies in dose outside the geometrical field in terms of the dose at the central axis were found to be in the order of 5-8% for the SPB algorithm, along with overestimation of the beam fringe by 2-3 mm. The discrepancies outside the geometrical field became smaller with depth and off axis distance. These errors in calculated dose could result in the selection of field sizes larger than necessary and, in combination with the underestimation of dose outside the field, could lead to overdosage of OARs. The DPB proved to have similar, but smaller discrepancies.

Dose calculation discrepancies in the TPS evaluation were found to be larger when shielding blocks are used in homogeneous water equivalent media. Large errors occured when dose underneath small or thin blocks was calculated. The TPS convolution model only approximates the modulation of the primary fluence with an intensity function convolved with scatter describing kernels. Extra focal and scattered radiation is not accounted for thus leading to overestimations of dose underneath the blocks and underestimations of dose outside the geometrical field. The DPB showed the largest discrepancies in the blocked field geometries of up to 20% in local difference of dose overestimation underneath spinal blocks. These discrepancies tended to be larger for

6MV beams as a result of more lateral scatter for the lower energies than forward scatter in higher energy beams in the water equivalent medium.

Comparison of dose distributions was possible through the normalization method which was similar in both the MC and PB distributions as recommended by international standards. Dose prescriptions to isodose lines were not problematic because exactly the same volumes for PTVs and GTVs were used in plan analyses and volume variability was thus circumvented. The ICRU guidelines were used here.

The evaluation of the TPS included geometries ranging from uniform water equivalent phantoms to a whole spectrum of complex treatment plans and sites. These consisted of a prostate case and complex geometries like the head and neck and lung cases. The effects of heterogeneities were studied for large low density regions like lungs and ranged to high density bone structures like the femoral heads and the spinal column.

In these clinical situations, the TPS algorithms displayed larger discrepancies in combination with the inhomogeneity correction algorithms than in a homogeneous medium. It was found that the Batho inhomogeneity correction algorithm exhibited the largest discrepancies while the ETAR algorithm did not show such large and frequent deviations in heterogeneous patient models. These discrepancies were found to be largest in the lung plan, especially because of the location of the normalization point in the low density lung. Normalization in these regions leads to large discrepancies in dose and MU calculations as a result of the limitations of the PB algorithms. The 15 MV data showed

that these discrepancies are larger compared to 6 MV as a result of total disregard for secondary scatter radiation by the TPS convolution algorithms.

The use of the EUD calculations proved to be a useful tool in evaluation of the effects of the discrepancies in dose calculations of the TPS. It was found that dose is mostly overestimated by the TPS where low density heterogeneities are present. High density heterogeneities, like the femoral heads in the prostate plan, did not result in large discrepancies in calculated dose.

The results from this study have shown that large errors in dose are associated with 1D convolutions combined with inhomogeneity correction algorithms. Other studies have shown that 2D and 3D convolution/superposition techniques result in similar, though smaller errors. Table 6.1 provides a summary of the largest errors found in this study, as well as the regions where the differences in MC calculated and TPS calculated doses were found.

Although there are different pencil beam (PB) algorithms available on commercial treatment planning systems (chapter 2), many authors have demonstrated similar results in studying the accuracy of such systems with variants of the pencil beam models and collapsed cone convolution (CCC) algorithms. Many of them have compared PB and CCC algorithm dose distributions in phantoms and on CT datasets with MC simulations, TLD-, ionization chamber- and film measurements. Comparitive studies and results will be discussed here.

Table 6.1 Summary of the largest errors calculated for the TPS dose calculations. The associated energy is shown along with the algorithm employed. The region where these errors were identified is also provided.

Treatment Plan	Expected dose errors	Energy	Algorithm	Region	Cause of discrepancies
H + N*	10% overestimation	15 MV	ETAR	Soft tissue close to cavity	Air cavities and missing tissue
Breast	10% overestimation	6 MV	ETAR	Lateral and anterior side of breast	Missing tissue, no bolus
Lung	33% underestimation	15 MV	ETAR	2/3 of PTV	Low densities, Small field
Oesophagus	10% overestimation	15 MV	Batho	Close to PTV boundaries	Low densities Surrounding tumor volume
Prostate	2% underestimation	15 MV	Batho	PTV	High density bone
Brain	4% overestimation	6 MV	Batho	Beneath skin surface, skull	Missing tissue

* Head and neck treatment plan

6.1. Similar studies on lung geometries

McDermott et al.[1] found an overall of 5% overestimation of CTV dose in a lung tumors planned with 6 MV IMRT fields. Some areas showed more than 10% lower dose with MC simulations and film measurements in comparison to the TPS which utilizes a finite

pencil beam algorithm (Nomos Corvus V4.6). It must be mentioned that their pencil beam algorithm is expected to be more accurate than the SPB algorithm as it utilizes a 2D kernel convolution, rather than a 1D kernel convolution as in the case of the CadPlan TPS. They found the greatest differences in the areas where the dose is highest and the electron density lowest, which supports the findings of this study. They also found that it does not seem possible to distinguish the TLD measured dose in a Rando phantom from either the TPS with a finite pencil beam algorithm or MC predictions within the accuracy of the TLD measurements (3-5%).

Wang et al.[2] used the MSKCC (Memorial Sloan Kettering Cancer Centre) pencil beam algorithm for 6 MV photon beams in lung plans. The pencil beam algorithm utilizes an equivalent pathlength heterogeneity correction method and they obtained similar results to McDermott et al.[1] The PTV in their case was underdosed due to larger electron ranges in low density media which is not accurately accounted for in the PB algorithm. Underdosage from the dose-volume indices they used was as high as 10%. These tests varied from TPSs using compensators for beam modifying devices to TPSs using MLCs. A plausible argument for the larger deviations found in this study is partly the use of a 1D pencil kernel convolution, combined with the restricted and sometimes incorrect modulation in terms of attenuation of the Terma through the use of the Batho and ETAR heterogeneity algorithms. Mean lung doses in their case were underestimated by up to 6%.

A study by Laub et al.[3] found good agreement between an adaptation of the EGS4 MC code and the KonRad TPS utilizing a (PB) algorithm, as well as measurements. A possible reason for their good agreement might be the use of non-coplanar beams that might suppress the disagreements. It is important to also investigate single fields that may obscure inaccuracies when combined in multiple field plans resulting in dose errors to OARs. The differences in terms of SPB and DPB underestimation of OAR dose from the present study is also attributable to the deviations in calculated dose outside the geometrical field.

Larger differences in similar co-planar plans were seen where Pawlicki and Ma[4] compared the EGS4 MC simulations with the Corvus TPS for an upper thoracic target. 8 4 MV co-planar beams were used in their study. Their results showed that a 9% lower mean dose to the target is found when the Corvus is compared with MC. The PB doses were higher in the target than MC because of the electron transport out of the target (surrounded by less dense tissue) into surrounding low density lung tissue. Similar to the algorithms investigated in the present study, the Corvus PB kernel is not laterally scaled to account for the changes in lateral electron transport due to inhomogeneities. The authors mentioned that in these studies with photons the target is usually not a real lung tumour representation and these tumours might have higher electron densities than normal lung, but the study by Wang et al.[2] was done on real patient CT data which suggests that the overestimations of target/CTV doses are insensitive to these electron density differences. The results from McDermott et al.[1] showed good agreement between the MCNP MC codes and measurements. The Corvus PB algorithm computed doses up

to 10% higher than MC with an average of 5% higher mean CTV dose in regions where the electron density is low and the dose high.

In another study based on phantom measurements, Cranmer-Sargison et al.[5] quantified differences between experimentally measured beam profiles and those calculated using both a commercial convolution algorithm and the MC method. It incorporated a vertical solid water-lung material interface parallel to the beam axis, irradiated by 6 and 18 MV photons. They studied a limited number of field sizes, namely 10x10 cm^2 and 4x4 cm^2 with the SPB algorithm of the CadPlan TPS, while the MC simulations were done with the EGSnrc package in a similar way as what was done in the present study.

Their results are an excellent confirmation that the CadPlan TPS has a substantial problem modeling the dose distribution in the lung region. They also demonstrated that the CadPlan profile differences increased in the lung region as the field size decreased and the beam energy increased. Worst case differences were more than 15%, again confirming the results seen in the present study. MC-film differences were not found to be affected by material density difference (differences were less than 2%). The TPS also utilized the modified Batho inhomogeneity correction algorithm. They found excellent agreement between MC and measured PDD data in a homogeneous phantom, and good agreement between profiles. However, the TPS 4x4 cm^2 profiles were not modeled as accurately as the 10x10 cm^2 profiles which is again similar to the results of the present study. It is clear from the combination of these results that the CadPlan SPB algorithm is very much inferior to even the PB algorithms of the other TPSs.

In the heterogeneous lung phantom, the CadPlan TPS failed to accurately model dose in the lung region. As beam energy increased and field size decreased, the differences increased, confirmed by the study of Cranmer-Sargison et. al.[5] Their conclusion was that the convolution algorithm was unable to model the effects of material heterogeneity. They have also studied the ETAR method, but the corresponding profiles showed even less agreement to their film and MC data in the lung region. Penumbral broadening was not at all addressed by the TPS in these regions. The empirical penumbral forming functions and laterally unscaled kernels lead to these discrepancies. Thus the convolution integral of the SPB model accounts well for depth dose and profile characteristics in water, but not at extreme material interfaces. As a result of lateral lung inhomogeneity not being accounted for by the SPB, the dose is overestimated in low density regions and regions of unit density surrounded by low densities. These effects are severely increased with decreasing field size.

Other investigators also pointed out that ignoring the impact of electron transport and photon scatter from heterogeneities lead to deviations from measured dose and MC simulations. Heterogeniety corrections based on the Batho method or 1D convoltions along beam paths applied in pencil beam systems stress the limitations found for these algorithms. Knöös et al.[6] showed that limitations in unit density media are not exploited and deviations from measured and MC simulated data are generally small. On the other hand, deviations in low density media increase with increasing beam energy from approximately 3% for 4 MV to 14% for 18 MV x-rays as a result of increased electron disequilibrium.

Other studies also confirm the results shown here, accept that the complex CT model geometries increase the discrepancies found, and a large contribution to the errors are the simplicity of the SPB dose calculation model. In the pencil beam approach by Ahnesjö et. al.[7] to calculate dose in heterogeneous media, the primary dose is calculated by choosing pre-calculated fitting-parameters at the radiological depth instead of the geometrical depth in a slab-like approximation. The scattered dose is firstly calculated in homogeneous water and then corrected using a 1D convolution along the beam path. The correction is governed by the linear attenuation coefficient for the primary photons. It is also clear from the data from Knöös et. al.[6] that using photon energies of more than 6 MV has the effect of totally underestimating the secondary electron range in low density tissue (like lung) in these algorithms. It is thus recommended that higher energy beams should not be used to treat sites where lung or similar types of tissues are involved. Wang et. al.[2] showed that even lung radiotherapy patients with plans of 15-18 MV x-rays that show deeper penetration and better tumor dose uniformity, should not be attempted as these higher energy recoil electrons cause lateral electronic disequilibrium and degrade target coverage. The 15 MV dose distributions and DVHs generated by the TPS were as good as, or slightly better than, those generated for 6 MV beams. But the Monte Carlo dose calculations showed increased penumbra widths for the higher energy photon beams that lead to a decreased lateral dose homogeneity for the 15 MV plans. The Monte Carlo calculations indicated that the tumor coverage was significantly worse for 15 MV than for 6 MV. On the other hand, the spinal cord and lung doses were clinically equivalent for the two energies. The lessons learnt from these studies are that, although the 15 MV pencil beam plans seem to be better than the 6MV plans, they are more inaccurate than

the 6 MV plans and should not be implemented in these clinical cases, even if the TPSs not utilizing MC simulations show better higher energy target conformance than 6 or 4 MV plans.

6.2. Similar studies on head and neck and missing tissue geometries

Head and neck fields are affected to different degrees by tissue inhomogeneities, depending on specific anatomy, especially the size and location of air cavities in relation to the beam orientation and field size. Wang et al.[2] have found in single plans up to approximately 10% differences between TPS and MC plans. Critical normal tissue DVHs differed by just less than 10% at high dose ends. Sakthi et al.[8] evaluated the accuracy of superposition /convolution dosimetric results by comparing the TPS dose calculations with MC dose calculations for head and neck IMRT patients. Although IMRT plans consist of smaller beam segments, weighted and summed to give a modulated intensity distribution which is influenced by a larger leaf transmission and interleaf leackage contributions, the general calculation of dose is still done in a similar fashion as for 3DCRT. They used the EGS4-based MC algorithms. EUDs for the plans were calcualted in the way proposed by Niemierko (Chapter 2 and 4). Differences were calculated relative to the dose computed by the superposition/convolution algorithm at the local point of interest. Their results showed higher doses to CTVs and GTVs when compared to the MC dose calculations and parotid gland dose was 10.4% lower than the MC dose. Similar results were found for the spinal cord and brainstem.

The larger deviations were found in areas where heterogeneity structures are present. The MC results predicted higher doses than the superposition/convolution algorithm. They identified a ~1.5% systematic error in superposition/convolution dose computation. In this evaluation of three plans MC doses were also less homogeneous than the superposition/convolution doses, while the MC data agreed better with film measurements. They also found that some target structures in some plans had >5% differences between superposition/convolution and MC.

6.3. Similar studies on breast and head and neck geometries

Breast plans demonstrate the deviations from expected dose distributions by the dose calculation algorithms with respect to missing tissue geometries, low density heterogeneities in close proximity to target structures and oblique beam incidence in combination with skin curvatures.

Venables et al.[9] investigated the absolute dose accuracy at the center of the breast, as well as the accuracy of the isodose distributions on various computer planning system in three dimensions. They used a water-filled breast phantom for ionchamber measurements. This was done for 36 sets of data from various treatment planning systems. 32 of the 36 TPSs overestimated the dose to the center of the breast with a mean measured/calculated ratio of 0.979 (SD 0.013). The relative dose within 2cm of the lung was also overestimated.

Only one TPS algorithm (the CCC algorithm) in their study was able to calculate the dose to the center of the breast correctly in tangential breast radiotherapy. The study involved, among others, the DPB and SPB algorithms of the CadPlan TPS. The collapsed cone absolute dose was within 0.2%, while most other TPSs overestimated the dose. Overestimation of breast dose is expected with 2D calculations if no attempt is made to compensate for the missing tissue above the breast. However, the PB algorithms also overestimated the dose.

They showed that maximal discrepancies in absolute dose in the breast from the two tangential fields from various planning systems was +12%. The minimum deviation was -10%. These were found at 7 cm inferior of the CAX and 7 cm superior of the CAX, respectively. The largest differences were found for 6 MV, while 4 and 8 MV were also evaluated. The CadPlan PB algorithms mostly showed overestimations of the dose in lung and soft tissue at specific measurement points. The TPS could not compensate for the lack of lateral scatter from the lung at a point < 2 cm from the lung and was energy dependant. This leads to overestimations of dose. The TPS overestimates dose to a point within 2 cm of the apex of the breast. This was due to inaccuracies in scatter dose calculations due to the presence of wedges, buildup at oblique incidence (containing not only the buildup from photons, but also from contaminating electrons scattered from accelerator structures), corrections for tissue obliquity, interpolation between calculation grid points and errors due to the continuing contribution from scatter after a pencil beam has excited the patient. The first two of these factors lead to calculated dose being less than expected. Others may cause the dose to be either higher or lower than expected.

Weber et al.[10] used a similar geometry as Knoös et al.[6] to study accuracy of the collapsed cone point kernel algorithm. They compared MC with the TPS and found CCC to be feasable for clinical use as calcualtions agreed to experimental data within 3% for most of the tested geometries, including missing tissue and lung. They proved that dose calcualtion problems associated with the invariant pencil kernel algorithm have been considerably improved in the implimented point kernel and should be beneficial in a number of clinical situations.

Hurkmans et al.[11,12] demonstrated the expected decreases in dose close to the phantom edges (simulating the missing tissue situations in H+N cases and breast cases) due to the loss of phantom-scattering and not head-scatter. Knoös et al.[13] found similar results. They also demonstrated that deviations from measured data in unit density volumes are small for convolution algorithms, while deviations in low density volumes increase with increasing beam energy. As the TPS is limited to consider changes in lateral scatter when heterogeneities are present, doses in typical mediastinal geometries where found to be overestimated by a factor of 1.02 to 1.05 for 18 MV and 4 MV respectively. This might explain why deviations differ for 6 and 15 MV in the results from this study (bony regions in the head and neck is an example). The 18 MV overestimations are lower because higher energies yield more forward-directed and less amount of scatter.

The study by Knoös et al.[13] showed differences in lung were significant and increased with energy due to a lower degree of lateral charged particle equilibrium. As the TPS does not model the decrease, the resulting calculated dose distribution will overestimate

the absorbed dose. Their measurements were done in phantoms. Thus only certain limitations, linked to the phantom geometry, played a role. In this study where patient CT models were used, the geometry is much more complex and involves intricate combinations of lung, bone, air cavities, missing tissue geometries, oblique beam angles and curved patient surfaces. It is understandable that some errors might thus be enhanced while others may be suppressed, especially when combined dose distributions from various fields are evaluated.

Linthout et al.[14] compared 3 algorithms, the Clarkson, PB and CCC with in phantom measurements for treatment of oropharynx dynamic arc stereotactic radiation therapy treatment with 6MV photons. They mostly found good agreement between the TPS and their measurements, accept in the PTV in and around the border of an air cavity. All algorithms overestimated the dose in the PTV in this region by 12, 10 and 7% for the three algorithms respectively. The Clarkson algorithm is not suited to handle heterogeneities and variations in density as scattered radiation is assumed to be constant regardless of the absorbing medium and utilizes a 1D pathlength correction.

The pencil beam algorithm also assumes that the photon scatter is implicit to the beam data measurements and that photon scatter does not vary significantly with depth in a medium. The incident beam in their case is divided into many small beamlets (PBs) for which an individual radiological pathlength correction is performed to take tissue inhomogeneities into account. These are polyenergetic PBs and give a 2D convolution with the fluence distribution of the beam. The convolution assumes that the PB kernels

are invariant in the lateral and longitudinal direction of the beam, leading to dose calculation discrepancies.

The CCC algorithm has been described in Chapter 2. In a study by Verellen et al.[15] similar results of 9% overestimation have also been found near cavities due to the PB limitations. Although the CCC is more accurate, it still fails to account for lateral multiple scattering effects in small volumes close to air cavities. The CCC convolution method for dose calculation is based on first principles. It is certainly superior to the Batho method[p]. The Batho method only calculates a correction factor and needs a separate model to calculate the homogeneous dose distribution, whereas the CCC calculates dose directly in absolute units. Ahnesjö[16] confirmed in his work that the algorithm calculates dose with somewhat less accuracy in situations of lateral charged particle disequilibrium and in low density regions and that comparisons with superposition algorithms have shown similar results.

A recent study by Krieger et al.[17] confirmed that even the superior CCC algorithm still shows deviations from expected doses in heterogeneous media. They have recommended that a careful investigation be done of the accuracy for dose calculations in heterogeneous media for each beam data set and algorithm. They investigated the errors in dose calculation caused by the approximations of the utilized calculation algorithm. Errors associated by PB algorithms are due to 1D density corrections which do not accurately model the distribution of secondary electrons in media of different density. Doses are mostly scaled according to the radiological depth along a ray line from the radiation

source to the calculation point, not accounting for the effects of side scattered radiation. They compared PB and CCC algorithms with MC simulations as a gold standard, along with absolute dose measurements with an ionization chamber. Their measurements were done in a multilayer phantom consisting of water-equivalent and low-density materials.

Dose calculations were performed on the Helax TMS v6.1a TPS for PB and CCC calculations. The xvmc[18] MC code was used for simulations. Important differences between the CCC and PB algorithms are that the energy deposition kernels in the CCC algorithms are corrected for the density variation along a set of rays originating from each voxel in a phantom. It should guarantee that that the contribution from single scattered photons to the dose is correctly modeled. However, the CCC algorithm approximates multiple scatter photons, which may cause discrepancies in the calculated dose.

They used a simple slab phantom for their measurements and stipulated that the PB algorithm is not suitable to predict dose in heterogeneous volumes with sufficient accuracy, confirming conclusions from the present study. It is clear from their results, as well as the present study, that neither the amount, nor the direction of the deviation from the true dose value is predictable and thus no global correction factor to correct the dose to e.g. the lung calculated with a PB algorithm can be implemented. They found the CCC algorithm more appropriate. However, the dose inside the low density regions of the phantom was underestimated by the CCC algorithm. They have recommended that MC calculations for photon beams be used if very high accuracy in heterogeneous volumes has to be achieved.

Dose in water-equivalent media, inbetween low density media, was within 3% for the CC and MC algorithms. PB deviations were up to 14% higher than the measurements. The lack of lateral scatter modeling leads to this result. They found 30% overestimations of dose for a 10x10 cm^2 field and 10% for a 20x20 cm^2 field, for both symmetric and asymmetric fields inside the low density medium. Test calculations with slightly oblique beam incidence lead to unrealistic spikes in the vicinity of the interfaces between unit- and low-density media. They also found that outside the geometrical beam, the dose in the low-density material was drastically underestimated. This was experienced because lateral transport is not accounted for by the PB algorithm.

Similar to the results in this thesis, they found that the magnitude of the artifacts is higher the less lateral charged particle equilibrium (CPE) exists. Large lung volumes, as found in the present study, will certainly increase discrepancies. This is because the true electron range does hardly affect the dose at a point where CPE is approximately established. These results are also similar to what Cranmer-Sargison et al.[5] found on the CadPlan TPS.

The CCC profile curves in their study were found to be closer to measurements. Excess lateral scatter into low-density material is modeled well by this algorithm. However, the absolute dose within the low density slabs was on average 10% (for the 10x10 cm^2 fields), respectively, 8% (for the 20x20 cm^2) lower than measured. This is due to multiple scatter not being modeled, as well as the sensitivity of the dose determination in low density media being influenced by the fact that these kernels were generated in water-

equivalent media. CPE is well established in water-equivalent media where deviations are hardly visible.

Lastly, Arnfield et al.[19] investigated the accuracy of dose predicted by a Batho power law correction, and two models which account for electron range: A superposition/convolution algorithm and a Monte Carlo algorithm. The results of these models were compared in phantoms with cavities and low-density inhomogeneities, representing a combination of anatomical heterogeneities. An idealized geometry was considered with inhomogeneities represented by regions of air and lung equivalent material. Measurements were performed with a parallel plate ionization chamber, thin TLDs and film. Dose calculations were done with a generalized Batho model, the Pinnacle collapsed cone convolution model, and the Peregrine Monte Carlo dose calculation algorithm. Absolute central axis and off axis dose data at various depths relative to interfaces of inhomogeneities were compared.

Results confirmed that for a Batho correction, dose errors in the calculated depth dose arise from the neglect of electron transport influencing re-buildup effects in depth dose calculations. This is found adjacent to airgaps and can be significant both in magnitude and spatial extent at 6 MV and above. The effects increase as the field size decreases, as the density of the inhomogeneity decreases and with the energy of incident photons. The CCC calculations were closer to measurements than the Batho model, but significant discrepancies remain. Monte Carlo results agreed with measurements within the

measurement and computational uncertainties. Deficits of the magnitude in this and other studies would be expected to have clinical consequences.

Their TLD results confirm reports that the extent of the dose deficit at an air– water boundary is hidden not only by conventional dose calculations, but also by ionization chamber measurements. They found discrepancies of approximately 30% at the distal surface of airgaps when comparing the CCC model and TLD measurements. Of the three calculation models in their study, only the MC model revealed the actual surface dose, although the CCC algorithm is obviously a considerable improvement over the Batho model. The CCC and the MC model accurately predicted the shape of the beam profile at distal air cavity interfaces, whereas the beam fringe of the Batho model was 5 mm smaller than the measured value. The beam fringe may be considered to typically represent the distance between the physical beam edge and the boundary of the target volume. If the beam fringe is significantly underestimated by the planning system, the result may be inadequate target coverage by the treatment planner. Since air cavities are prevalent in the head and neck region, these results suggest the MC method or the superposition method is appropriate for treatment planning in this area, especially when small fields are used. The complex geometry involving air, bone and soft tissue in the head and neck would be expected to further emphasize the advantages of MC versus other methods. In radiotherapy of lung cancer, tumors are frequently surrounded by or adjacent to lung tissue, leading to disequilibrium effects requiring inhomogeneity corrections. Not correcting distributions may lead to underestimating the risk of radiation pneumonitis.

As is evident from the present study, electron transport effects are greater at higher beam energies, since a larger number of secondary electrons deposit dose beyond the geometric boundary of the field. The results from Arnfield et al.[19] suggest certain general conclusions about the accuracy of the three calculation models for calculations involving lung inhomogeneities. The agreement between the Batho model and measurements proved consistent with the well-known accuracy of Batho corrections for 6 MV and low-density inhomogeneities. For lung at 18 MV, the Batho algorithm was not accurate in predicting the depth dose for either a 4x4 cm^2 or a 10x10 cm^2 field, but was particularly poor for the smaller field.

It is clear from these past studies and the present results that the Batho corrections are unreliable at high energies. Their Batho results have shown the same trend as Batho calculations for 15 MV, 5x5 cm^2 fields, in lung phantoms. They could not explain the discrepancies for the 6 MV CCC they found.

For the 18 MV, 4x4 cm^2 beam incident on a lung phantom, discrepancies between CCC and measurements were about 5%, over a distance of several cm in the proximal part of the lung. The CCC and MC results in this case are similar to superposition and MC calculations reported for a 5x5cm^2, 18 MV beam in a lung phantom. Such errors are consistent with the known behavior of superposition models based on the rectilinear scaling approximation, such as the CCC model. These models overestimate dose in a layer beyond a high-to-low density interface; correspondingly they underestimate dose following a low-to-high density interface. This occurs because the largest contribution to

lateral electron spread at a given depth is from scattering events furthest upstream, which is not accounted for by rectilinear density scaling. It is recognized that conventional algorithms such as the Batho model are inaccurate in some situations; such considerations have prompted the implementation of models with a sounder physical basis such as superposition models. The conclusion from the Arnfield et al.[19] results were that the CCC superposition algorithm is accurate over a wider range of conditions involving low-density inhomogeneities than the generalized Batho model. The many different models in use all involve approximations which lead to inaccuracies in some or other circumstances. The results of this paper confirm that MC produces satisfactory results in the cases studied.

The trend in advanced radiotherapy techniques is to employ methods that reduce dose to OARs and escalate dose to tumors requiring more accurate dose computations. Errors in TPS calculated dose also brings a discrepancy into clinical outcome analyses. Biological parameters derived from such data may be biased and could potentially have serious consequences in biologically optimized treatment planning.

Some MC dose calculation methods have been proposed for routine treatment planning and their use is certainly escalating. The availability of faster computer hardware and new variance reduction techniques result in simulation times suitable for this purpose.

References

1. McDermott P.N., He T. and De Young A., “Dose calculation accuracy of lung planning with a commercial IMRT TPS”, J. Appl. Clin. Med. Phys. **4,** 341 – 351 (2003).

2. Wang L., Yorke E. and Chui C.S., “Monte Carlo evaluation of 6MV intensity modulation radiotherapy plans for head and neck and lung treatments”, Med. Phys. **29**, 2705 – 2717 (2002).

3. Laub W.U., Bakai A. and Nusslin F., “Intensity modulated irradiation of a thorax phantom: comparisons between measurements, MC calculations and pencil beam calculations”, Phys. Med. Biol. **16**, 1695 – 1706 (2001).

4. Pawlicki T. and Ma C.M., “Monte Carlo simulation for MLC-based intensity-modulated radiotherapy”, Med. Dosim. **26**, 157 – 168 (2001).

5. Cranmer-Sargison G., Beckham W.A., Popescu I.A., “Modelling an extreme water-lung interface using a single pencil beam algorithm and the Monte Carlo method”, Phys. Med. Biol. **49**, 1557 – 1567 (2004).

6. Knoös T., Ahnesjö A, Nilsson P. and Weber L., “Limitation of a pencil beam approach to photon dose calculations in lung tissue”, Phys. Med. Biol. **40**, 1411 – 1420 (1995).

7. Ahnesjö A., Saxner M. and Trepp A., “A pencil beam model for dose calculation”, Med. Phys. **19**, 263 – 273 (1992).

8. Sakthi N., Keall P., Mihaylov I., Wu Q., Wu Y., Williamson J.F., Schmidt-Ullrich R. and Siebers J., “Monte Carlo based dosimetry of head-and-neck patients treated with SIB-IMRT”, Int. J. Radiat. Oncol. Biol. Phys., **64**, 968 – 977 (2006).

9. Venables K., Winfield E.A., Aird E.G.A. and Hoskin P.J., “Three dimensional distribution of radiation within the breast: An intercomparison of departments participating in the START trial of breast radiotherapy fractionation”, Int. J. Radiat. Oncol. Biol. Phys., **55**, 271 – 279 (2003).

10. Weber L. and Nilsson P., “Verification of dose calculations with a clinical treatment planning system based on a point kernel dose engine”, J. Appl. Clin. Med. Phys. **3**, 73-87 (2002).

11. Hurkmans C., Knoös T., Nilsson P., Svahn-Tapper G. and Danielsson H., “Limitations of a Pencil Beam approach to photon dose calculations in the head and neck region”, Rad. Onc **37**, 74 – 80 (1995).

12. Hurkmans C., Knoös T., Nilsson P., “Dosimetric verification of open asymmetric photon fields calculated with a treatment planning system based on dose-to-energy-fluence concepts”, Phys. Med. Biol. **41**, 1277 – 1290 (1996).

13. Knoös T., Ceberg C., Weber L. and Nilsson P., “The dosimetric verification of a pencil beam based treatment planning system”, Phys. Med. Biol. **39**, 1609 – 1628 (1994).

14. Linthout N., Verellen D., Van Acker S., Voordeckers M., Bretz A. and Storme, G, “Evaluation of dose calculation algorithms for dynamic arc treatments of head and neck tumors” Rad. Onc. **64**, 85–95 (2002).

15. Verellen D., Linthout N., Van den Berg D., Bel A. and Storme G, “Initial experience with intensity modulated conformal radiation therapy for treatment of the head and neck region”, Int. J. Radiat. Oncol. Biol. Phys., **38**, 99 – 114 (1997).

16. Ahnesjö A., “Collapsed cone convolution of radiant energy for photon dose calculation in heterogeneous media”, Med. Phys. **16**, 577 – 92 (1989).

17. Krieger T. and Sauer O.A., “Monte Carlo- versus pencil-beam-/collapsed-cone-dose calculation in a heterogeneous multi-layer phantom”, Phys. Med. Biol. **50**, 859-868 (2005).

18. Fippel M., “Fast Monte Carlo dose calculations for photon beams based on the VMC electron algorithm”, Med. Phys. **26**, 1466-1475 (1999).

19. Arnfield M.R., Siantar C.H., Siebers J., Garmon P., Cox L. and Mohan R., “The impact of electron transport on the accuracy of computed dose”, Med. Phys. 27, 1266 – 1274 (2000).

Acknowledgements

During the time I spent working on this thesis I have met numerous interesting and very talented people. I wish to express my gratitude to everyone who have contributed to this work, whether that be in exchanging ideas, jokes, tips and tricks, emotional support or pure academic insight. It is impossible to name everyone here who has played a tremendous role in helping me achieve this humble goal, but know that I am extremely grateful for these contributions.

Above all I give thanks to my Creator and Heavenly Father for giving me this opportunity and carrying me through and over the valleys and hills of life, for the blessings I have experienced and His mercy.

My sincerest gratitude goes to:

My promoter, Dr. Freek du Plessis, for the time and effort, however frustrating it sometimes was that he devoted to make this work possible. Thank you for the numerous discussions and solutions that come from them. Many of those may not have featured in this work, but they are certainly building blocks for future research.

My colleagues at the University and National Hospital: Prof. Casper Willemse for all the fruitful discussions and support. Proff. Andries van Aswegen and Thys Lötter for their valuable suggestions and support, as well as all the other staff that contributed in a personal supportive way.

My dear family for their steadfast love and support through all of this time. Without you none of this would have been possible. I am eternally grateful for all your enthusiasm, constant reminding that this needed to be done, your understanding and prayers.

To my friends for keeping from completing this study, but at the same time reminding me that it had to be finished. Thank you for your continual support and friendship, all the great times, long braais, cold beers, late nights, dark rum and rugby trophies. I would also like to acknowledge those I met through my studies and conferences who have enlightened my thoughts and given me ideas in the world of Medical Physics. These ideas sometimes get me carried away, but they are the foundations of wonderful prospects that will contribute to my calling in my profession.